Technische Universität Berlin

Model reduction of components and assemblies made of composite materials as part of complex technical systems to simulate the overall dynamic behaviour

vorgelegt von
Master of Science
Humberto Peredo Fuentes
geb. in Mexiko Stadt

von der Fakultät V – Verkehrs- und Maschinensysteme
der Technischen Universität Berlin

zur Erlangung des akademischen Grades

Doktor der Ingenieurwissenschaften
– Dr. –Ing. –
genehmigte Dissertation

Promotionsausschuss:

Vorsitzender: **PROF. DR. RER. NAT. VALENTIN POPOV**
Gutachter: **PROF. DR.-ING.HABIL. MANFRED W. ZEHN**
Gutachter: **PROF. DR.-ING. CHRISTIAN HÜHNE**

Tag der wissenschaftlichen Aussprache: 25. April 2017

Berlin 2017

I would like to dedicate this thesis to my loving families in both sides of the Atlantic ocean who supported me and gave me the strenght to finish my PhD.

Declaration

I hereby declare that except where specific reference is made to the work of others, the contents of this dissertation are original and have not been submitted in whole or in part for consideration for any other degree or qualification in this, or any other university. This dissertation is my own work and contains nothing which is the outcome of work done in collaboration with others, except as specified in the text and Acknowledgements.

Acknowledgements

First and foremost I would like to thank my advisor, Prof. Dr.-Ing. habil. Manfred W. Zehn, for his continuous encouragement, insights and guidance throughout the preparation of my dissertation. The supply of the composite component assembly was possible thanks to the cooperation and support of the Prof. Dr.-Ing. Michael Sinapius from DLR Braunschweig, without this composite assembly my dissertation would not be possible.

I would like also to take this opportunity to thank Dr. Dragan Marinkovik and Dr. Cesar Adolfo Ortega Vivas for their meticulous reading and assistance during my publication and Larry R. Paul for the final review and corrections to my dissertation. I wish to express my gratitude to Tobias Rademacher and Fabian Wesolowski for their assistance during my experimental work (SLDV).

To Dr. Gonzalo Ramos Lopez, Dr. Hernani Yee-Madeira from Mexico and Dr. Rafael Santillan Ortega, without whose emotional support, I would not have had the chance to do this PhD in Germany. A special mention to the DAAD-CONACYT, my family in Mexico, Gerardo Lerma Hernandez and Jana Heimhold for the financial support and trust to complete my PhD.

My study in model reduction of components and assemblies made of composite materials as part of complex technical systems to simulate the overall dynamic behavior was possible by a cooperation between the Technische Universität Berlin (Institut für Mechanik, FG Strukturmechanik und Strukturberechnung), the DLR Braunschweig and the DAAD-CONACYT, for which I am very grateful.

Abstract

Model reduction of components and assemblies made of composite materials as part of complex technical systems to simulate the overall dynamic behaviour

The composite components and model order reduction (MOR) methods are widely used to improve the weight/strength ratio and the computational time respectively in different areas of the industry. The objective of this research is to evaluate the dynamic behaviour applying a MOR method in a composite component assembly. A new mixed numerical-experimental technique (MNET) is developed to obtain accurate stiffness parameters in a composite component and then the Craig-Bampton model order reduction (CBMOR) method is applied in terms of a substructure/super element technique using the automatic multi-layer substructuring (AMLS) method. The MNET consists of a correlation between a composite component assembly using experimental measurements and a 2D finite element (FE) model using an equivalent single layer (ESL) homogenized laminate theory including transverse shear effects (discrete Mindlin Kirchhoff triangle (DMKT)). Curve-fitting algorithms are used to improve the accuracy of the correlation. The correlation is performed based on the modal assurance criterion (MAC) and the updating is calculated with a design of experiments (DOE). A DOE is a regression analysis used to obtain a simple mathematical model (transfer function/surface response) to update the stiffness parameters. The dynamic behaviour consists of the application of a CBMOR and AMLS methods to the FE model in the previous part. Different modal assurance criteria were applied to correlate experimental measurements versus the dynamic behaviour response of the FE models. For comparative purposes the stiffness parameters obtained in MATLAB-SDTools with the new MNET were used in MSC/NASTRAN, ABAQUS, and few mode shape expansion techniques respectively to validate the results. Based on the results, it can be concluded that the stiffness parameters obtained with the new MNET were fundamental for the validation, updating and accuracy applying the CBMOR and AMLS methods in a composite component.

Keywords: Craig-Bampton, AMLS, CFRP, DOE, MAC, COMACs, MNET, composites.

Abstract

Modellreduktion bei Verbundwerkstoffkomponenten und -baugruppen als Teil komplexer technischer Systeme zur Simulation des dynamischen Gesamtverhaltens

Komponenten aus Verbundwerkstoffen und Methoden zur Modellreduktion finden breite Anwendung in verschiedenen Bereichen der Industrie, um das Verhältnis zwischen Gewicht und Festigkeit zu verbessern beziehungsweise die Berechnungszeit zu verkürzen. Ziel der vorliegenden Arbeit ist die Auswertung des dynamischen Verhaltens einer Verbundwerkstoffkomponente unter Anwendung eines Modellreduktionsverfahrens. Eine neue gemischte numerisch-experimentelle Methode zur Ermittlung akkurater Steifigkeitsparameter sowie der Einsatz des Craig-Bampton-Verfahrens in Form einer Substruktur-/Superelement-Technik unter Verwendung der automatischen Multi-Layer-Substruktur-Methode. Der gemischte numerisch-experimentele Methode besteht aus einem Zusammenhang zwischen experimentellen Messungen an einer Baugruppe aus Verbundwerkstoffkomponenten und einem 2D-Finite-Elemente-Modell unter Anwendung einer homogenisierten äquivalenten Single-Layer-Laminattheorie einschließlich transversaler Schereffekte (diskretes Mindlin-Kirchhoff-Dreieck). Mithilfe von Kurvenanpassungsalgorithmen wird die Genauigkeit der Korrelation erhöht. Die Korrelation erfolgt auf der Grundlage des MAC-Kriteriums (Modal Assurance Criterion) und die Modelloptimierung wird durch eine Versuchsplanung ermittelt, eine Regressionsanalyse zur Erlangung eines einfachen mathematischen Modells (Übertragungsfunktion/ Systemantwort der Oberfläche) für die Aktualisierung der Steifigkeitsparameter. Der dynamischen Verhaltens besteht aus der Anwendung des Craig-Bampton-Verfahrens und der automatischen Multi-Layer-Substruktur-Methode auf das existierende FE-Modell. Für die Anpassung des dynamischen Verhaltens des FE-Modells an die experimentellen Messungen werden verschiedene COMAC-Kriterien (Coordinate Modal Assurance Criteria) benutzt. Zu Vergleichszwecken und zur Validierung der Ergebnisse werden die mit der neuen Methode in MATLAB-SDTools erhaltenen Steifigkeitsparameter in MSC/NASTRAN, ABAQUS beziehungsweise mit weiteren

Schwingungsformausbreitungstechniken verwendet. Auf Grundlage der Ergebnisse lässt sich folgern, dass die mit der neuen Methode ermittelten Parameter von wesentlicher Bedeutung für die Validierung, Optimierung und Genauigkeit bei der Anwendung des Craig-Bampton-Verfahrens und der automatischen Multi-Layer-Substruktur-Methode auf eine Verbundwerkstoffkomponente sind.

Keywords: Craig-Bampton, AMLS, CFRP, FEM, DOE, MAC, COMACs, MNET, Verbundwerkstoffe.

Table of contents

List of figures

List of tables

Acronyms/Abbreviations

ABAQUS Atmosferic Research Center xl, xlvi

AMLS Automatic Multi-Layer Substructuring xxxi, xxxiii, xlii, xliv–xlvi

ANOVA Analysis of variace xxxviii, xxxix

ANSYS Analysis System xxxvii

APDL ANSYS Parametric Design Language xxxvii

CBMOR Craig-Bampton model order reduction xxxii, xxxix, xl, xlii, xlvi

CFRP Carbon Fiber Reinforcement Polymers xxix–xxxi, xxxiii, xxxv, xxxix, xl, xlv, xlvi

CLT Classical Laminate Theory xxxvi

CMS Component Mode Synthesis xxx–xxxiii, xliii–xlv

COMAC Coordinate Modal Assurance Criterion xxxiv, xxxv, xlii, xliii, xlv, xlvi

COMAC-S Scale Coordinate Modal Assurance criterion xxxiv, xlii, xliii, xlv, xlvi

DLR Deutsch Luft and Raumfahrt xlv

DMKT Discrete Mindlin Kirchhoff triangle xlvi

DOE Design of Experiments xxx, xxxvi, xxxviii–xl, xlii, xliii, xlv

DOF Degrees of Freedom xxx, xxxii, xxxiv, xlii

eCOMAC Enhanced Coordinate Modal Assurance Criterion xxxiv, xlii, xliii, xlv, xlvi

EMA Experimental Measurement Analysis xl

ESL Equivalent Single-Layer xxxvii, xlvi

FBS Frequency-Based Substructuring xxxiii, xliii

FE Finite Element xxxi, xl, xlii–xlvi

FEM Finite Element Method xxix, xxx, xxxiii, xxxv, xxxvi, xxxviii, xxxix, xlv

FRF Frequency Response Functions xxxiii, xliii

FSDT First-order Shear Deformation Theory xxxvii–xxxix, xlv

HSDT Higher-order Shear Deformation Theory xxxvii, xxxviii

HTA High Tenacity-Faser xliv

IDRC Identification de rèsidus complexes xxxix, xlii, xliii, xlv

IDRM Identification de rèsidus multiples xxxix, xlii, xliii, xlv

IRS Improved Reduction System xxxii

K-MAC Stiffness weighted criterion xliii, xlvi

LSQI Least Square Quadratic Inequality xxxv

LWM Layer-Wise Models xxxviii, xlvi

MAC Modal Assurance Criterion xxxi, xxxiv, xxxv, xxxvii, xxxviii, xlii, xliii, xlv, xlvi

MACco Modal Assurance Criterion coordinate criterion xxxiv, xlii, xliii, xlv, xlvi

MAG Multi-Axial-Gelege xliv

MATLAB Matrix Laboratory xxxiii, xxxv, xl, xlii, xlvi

MCC Modal Correlation Criterion xxxiv

MDRE Minimum Residual Dynamic Expansion xxxv

MDRE-WE Minimum Residual Dynamic Expansion with Experimental also called called MRE-QI xxxv

M-MAC Mass weighted criterion xliii, xlvi

MNET mixed-numerical Experimental Technique xxx, xxxi, xxxiii, xxxv, xxxvii–xl, xlii, xliii, xlv, xlvi

MOR Model Order Reduction xxx–xxxiii, xlii–xlvi

MSE Mode Shape Expansion xxxiii, xxxv, xxxix, xlii–xlvi

MSF Modal Scale Factor xxxiv, xxxv

NASTRAN NASA Structural Analysis (Computer Program) xxxix, xlii, xlvi

PCOMP Property Layer Composite Element xxxix, xlii, xlv

PSDT P-order Shear Deformation Theory xxxvii

QSM Quasi-Static Mode Synthesis xxxii

ROM Reduced Order Model xxx, xxxiv, xlii

RTM Resin Transfer Moulding xl, xliv, xlvi

SDTools Structural Dynamic Toolbox xxxiii, xxxv, xl, xlii, xlv

SEREP System Equivalent Reduction Expansion Process xxxii, xliii

SLDV Scanner Laser Doppler Vibrometer xxxvi, xl

SVD Singular Value Decomposition xxxii

UFF Universal File Format xl

Introduction

Motivation

Nowadays composite materials, like carbon fibre reinforcement polymers (CFRP), are increasingly used in mechanical structures substituting the conventional materials more and more with the advantage of their strength and lightness in the aerospace industry [1]- [2]. The dynamic

Fig. 1 Composite component assemblies in Airbus 380 from [3].

analysis of these structures using the finite element method (FEM)[1] is essential to fulfill the time, cost and quality requirement process management in many companies. The FEM is a

[1]The first achievements of the FEM are reported in the works of Courant [5], Argyris and Kelsey [6] and Turner et al. [7] for the analysis of structures.

powerful numerical method used to perform analysis of a wide variety of complex and large component structures made of composite and conventional materials, (see Fig. 1).

Furthermore, the FEM can be used to solve large and complex components with component mode synthesis (CMS) introduced by Hurty [8], Craig and Bampton [9], MacNeal [11] and Rubin [12]. The CMS is divided in two parts: the finite element model order reduction (MOR) method and the dynamic substructuring. The MOR method consists of the generation of a compact set of equations of motion (reduced order model (ROM)) that possesses similar vibration characteristics with less degrees of freedom (DOF) compared to the full model. The dynamic substructuring consists of the division of the total structure into components or simple parts to find a solution on the interfaces of the combined domains. This division of the structure or *domain decomposition*[2] is controlled with interfaces and allowed to determine easily the dynamic behaviour of assembled structures.

The CMS method is well established in literature for conventional materials to obtain a good approximation using FEM [8]-[12]. However, the application of CMS on composite components is not well documented. Just a few results are found in the literature where CMS is applied to CFRP plates [4]. On one hand it seems to be a lack of adequate methodology to estimate directly the constitutive properties precisely (stiffness parameters), and on the other hand the selection of a CMS method based on the accuracy and performance is essential. The precision of the stiffness parameters and CMS is fundamental in this research and is one of the most challenging problems applied to CFRP components.

A number of indirect methods for material identification of CFRP, called mixed-numerical experimental techniques (MNET), are introduced to determine the stiffness parameters in mechanical structures [167]-[168]. Two main characteristics are reported in the literature using MNET: a regression analysis or transfer function based on experimental measurements of the CFRP structure to identify the stiffness parameters, and the application of a numerical method based on the FEM to correlate with the experimental measurements [13]- [48].

It is important to notice that recently MNET studies have reported high precision results using thick and thin CFRP plates by [32], [43], [44] and [45] including transverse shear effects. The MNET study using a design of experiments (DOE) by Rikards *et al.* in [32] is highlighted over other MNET studies because the DOE can be performed without knowing the form of the optimum regression equation. More recently, Cugnoni *et al.* [43], [44] and Matter *et al.*

[2]The *domain decomposition* is considered a kind of dynamic substructuring where the subdomains are the components of the total structure [121] [198].

[45] implemented an algorithm based on the modal assurance criterion (MAC) in order to update and optimize the stiffness parameters in CFRP plates with sufficient accuracy. The high precision results reported by Cugnoni and Matter were dependent on the selection of the theories including transverse shear effects[3][43]- [84],[94] - [96], Poisson's ratio values [44], the quality of the experimental measurements and the regression analysis [45]. All these characteristics have determined the accuracy and optimization of the structure response in CFRP plates and should be taken into consideration to apply MOR methods in a CFRP component. Furthermore, in all the reviewed MNET bibliography there is not mentioned the evaluation of Poisson's ratio ($\nu_{12}, \nu_{13}, \nu_{23}$) values during the volume phase transformation of polymer gels[4] in CFRP.

Firstly, it is proposed in this research to establish a MNET methodology to determine the stiffness parameters in a CFRP assembly to achieve sufficient accuracy in the non-reduced finite element (FE) model and secondly to perform a CMS with automatic multi-layer substructuring (AMLS) in terms of substructure/super-element technique. There is no literature that reports a multidisciplinary approach using a MNET methodology and the CMS with AMLS methods in terms of substructure/super-element technique applied to CFRP components. So, this thesis is motivated by the need to develop a MNET methodology to obtain the stiffness parameters based on the composite's characteristics and the parameters that affect the dynamic behavior. After obtaining the stiffness parameters, the application of the CMS method to CFRP can be included as an integral part with conventional materials in aeronautical applications.

Background of work

Model order reduction (MOR) methods

There is a great interest in applying MOR methods, especially the CMS method, to composite components in the aerospace and aeronautic industry.

The origin of the MOR development dates back to the first condensation MOR method for components and assemblies proposed by Guyan [108] and Irons [109]. This condensation MOR

[3] An excellent review of transverse shear effects in CFRP materials is elaborated by Carrera in [94] - [96].

[4] *CFRP materials, including fibrous composites, have directional elastic properties where $\nu_{12}, \nu_{13}, \nu_{23}$ can be close to zero or negative, leading to unusual or extreme behaviour (such as improved shear stiffness, self-adapting vibrational damping and shock absorption) as well as coupling between stretch and shear or bend and twist [97].*

is also known as STATIC condensation or Guyan method. The Guyan method is distinguished because the inertial terms contributing to the dynamic behaviour are ignored.

The condensation methods taking into account the inertial terms and the characteristics of the Guyan method are known as dynamic methods. These methods were developed by Leung [110], O'Callahan, Avitabile and Riemer [111], Kammer [112], and are known as Improved Reduction System (IRS), System Equivalent Reduction Expansion Process (SEREP) and similar to SEREP respectively[5]. However, a great success in the field of dynamic MOR is considered to be the CMS by Hurty [8] and Craig and Bampton [9], mentioned previously in the introduction.

The CMS method belongs to the category of substructure techniques and offers an advantage in the field of MOR over the other developed MOR methods: the model is divided into substructures and each substructure is solved with the CMS methodology. The CMS methodology is also known as Craig-Bampton model order reduction (CBMOR) method [9].

A detailed overview about most of all the CMS techniques using the CBMOR method, can be found in [113], [114] and [115] to obtain and improve reduced finite element models by reducing the orders of mass and stiffness matrices (less DOF).

Cunedioğlu *et al.* [116] suggested the need to classify the state-of-the-art MOR methods in four groups by their characteristics: direct reduction, modal methods, reduction with Ritz vectors and the CMS. The author highlighted, according to this classification, that the last two groups yielded the best results. The Ritz vectors improve the accuracy-cost ratio and the CMS combines the first three classes of methods [116], [117].

In addition Cunedioğlu *et al.* have published in [4] one of the first papers applying MOR methods based on CMS and quasi-static mode synthesis (QSM1 and QSM2) to cantilever beams elaborated with composite materials. The best achievement is reported using the QSM2 method. The author analyzed additionally the effects on the natural frequencies modifying the parameters such as fibre orientation, stacking sequence and ply thickness in the full model.

Balmès has reported a fundamental property of the MOR method based on the Rayleigh-Ritz method: The reduced model gives exact approximations if the results match in the range of the reduction basis [117]. Balmès has achieved important contributions applying a MOR method with Ritz vector basis using singular value decomposition (SVD) based on the strain and kinetic energy norms [117]. The SVD is a classical mathematical tool used to select important directions in a given subspace.

[5] Introduction by Koutsovasilis [114].

Thus, Balmès has documented that a Ritz vector basis can be used to compute the modes for various values of the specified parameters [118] in order to create a parametric family of reduced models with enough sensitivity, (see [119] and [120]). In addition Balmès has achieved a generalised interface using the CMS [118], [121], automatic multi-layer substructuring [201] (AMLS) and residual iteration [213] methods in [106]. A review is presented about the relationships between the MOR methods and Ritz vectors (including the CMS) regarding the optimization and accuracy of the reduced model in terms of substructure/super-element technique [118], AMLS and mode shape expansion techniques [122], [123], [124].

Moreover, other class of dynamic substructuring method in the frequency domain using measured data of the uncouples systems is named frequency-based substructuring (FBS) [200]. The FBS method presents an advantage over the other condensation algorithms because it is used the frequency response functions (FRF). The FRFs represent the physical behaviour of the structure whereas they cannot be described by CMS approaches. However, the FBS method is difficult to apply because it is needed an identification technique (curve-fitting algorithms) to determine the mass, damping and stiffness matrices of the components involving experimental data. This combination of theoretical results and experimental measurements are referred to in the literature as hybrid analysis [200].

Thus, it is documented that the CMS method with Ritz vector basis offers the best accuracy-cost ratio applied to conventional materials and the hybrid analysis gives the advantage of experimental substructuring using experimental measurements. Therefore, to achieve the required level of accuracy applying MOR methods to a CFRP component, it is proposed to use the CMS with Ritz vector basis and several mode shape expansion (MSE) techniques including experimental measurements once it is obtained the stiffness parameters with the MNET in order to fulfill the objetive of this work. The CMS and MSE including experimental measurements in terms of MOR are implemented in MATLAB-SDTools [106] by Balmès *et al.* and these methods will be applied to compare and validate the results.

Validation of model order reduction methods

Several studies in literature using the FEM and MOR method have reported the validation using quality assurance criteria with conventional materials [113], [114] and [115] to verify large structures with complicated geometries and multiple materials. The need to use different quality assurance criteria is critical to predict and validate the structural behaviour in composite

components. Most of these criteria are used to check quantitative and qualitative results of the full and reduced models.

The MAC was developed by Allemang [125] and it is one of the most common criteria used to correlate experimental modal analysis and FE models (as well as ROM). The MAC is defined as *a scalar constant that provides a measure of consistency between modal vector evaluations* [125]. A MAC value of 100% means a perfect correlation. If this value decreases below 80%, the correlation results must be checked. The MAC characteristics are most sensitive to the largest differences than the smallest differences between comparative values. The need to identify the differences of the comparative values with enough sensitivity applying the MAC has developed and implemented several quality assurance criteria per DOF.

The MAC per pair-sensor (MACco) criterion consists in the *sequential order of sensors that contribute most to the poor correlation* [126]. This modal correlation criterion (MCC) is known by different names: the MAC coordinate criterion [106] or the MAC variation technique [127]. The MAC per coordinates (MACco) implemented in [106] is used to lead to the best mean MAC for the paired modes selected. It is possible to obtain a direct indication using the MACco where there is located the poorest correlation per sensor/DOF.

The quality assurance criteria per DOF are known as the coordinate modal assurance criterion (COMAC) developed by Lieven and Ewins [128], the enhanced coordinate modal assurance criterion (eCOMAC) by Hunt [129] and the scale coordinate modal assurance criterion (COMAC-S) [106] applying the modal scale factor (MSF) respectively. The application of the MSF is reported in the literature for a variety of different analysis by Hatch [130], Schwarz [187], Allemang [125], Catbas [132], Ewins [131] and Balmés [106]. The different COMACs are known as an extension of the MAC to identify the differences between DOF locations that contribute negatively to a low MAC value [129]. In contrast to the MAC values, if lower COMAC, eCOMAC and COMAC-S values are obtained, then a better agreement per DOF will be achieved.

The COMAC is a sensitive method for detecting large and small motion of DOF. This particularity makes the interpretation of the COMAC difficult [129]. The application of the eCOMAC is used to overcome this particularity. Furthermore, a common problem with experimental modal vectors is the calibration scaling errors and/or sensor orientation mistakes [129]. The preferred usage of COMAC-S is when the spatial correlation of the implicit modal shapes require that mode shapes are similarly scaled [132]. For example, the particularity of the COMAC-S, applied by Hatch *et al.* [130], consists of a pre-scale second set of mode

shapes using the modal scale factor [125] (MSF) before being processed by the COMAC. Two requierements must be fulfilled in the application of these criteria: modes have to be normalized and there must be phase correlation between pairs of modes [129]. The application of these criteria implemented in [106] is proposed to confirm the use of the mode shape information in the identification process to improve the stiffness parameters in a composite component as well as to validate the MNET methodology.

As was introduced, one way to check quantitative and qualitative results of the full and reduced models is to compare different MAC and different COMACs. Another way to check the quality of the results is to use MSE techniques. The use of MSE techniques has become a good practice when the experimental components are large and complex, see [122], [123] and [124]. Several MSE techniques with basis on Ritz vectors have been developed by Balmès *et al.* [122], [123]. Those MSE techniques are: Guyan [108], SEREP [111], MODAL [112] and DYNAMIC [134], minimum residual dynamic expansion (MDRE) [135] and its extension using least square quadratic inequality (LSQI) [136] known as minimum residual dynamic expansion (MDRE-WE) with experimental results (called MRE-QI or MDRE-WE), see [122] and [123]. The last MSE technique using least square quadratic inequality (LSQI) or square quadratic inequality constraint methods has the best performance and can reliably predict mode shapes based on the MOR methods, even in very adverse situations according to Levine in [124]. Other reports proposed to use MSE techniques to enhance structural modifications, (see [137], [138]).

Thus, it is proposed in this thesis to apply the above quality modal assurance criteria and MSE techniques implemented in MATLAB-SDTools [106] to verify the dynamic behaviour accuracy of the FE models applied to a CFRP component.

Mixed numerical-experimental technique (MNET) applied to laminated composites

As it is mentioned in the introduction, several MNETs have been developed for identification of stiffness parameters in composites [13]- [48]. The MNET is based on the application of inverse methods combining experimental global results with computed FEM results. Many stiffness properties of multilayered rectangular plates have been investigated using experimental modal tests carried out using an impulse hammer, a loudspeaker, a scanner laser Doppler vibrometer

(SLDV), different shell theories and FEM by Sol [13], 1986; De Wilde [14] , 1987; Pedersen [15], 1989; De Wilde [16], 1991; Frederiksen, [18], 1992; Mota Soares *et al.* [22], 1993; Sol *et al.* [26] , 1993; Grediac and Vautrin [24], 1993; Link and Zou [27], 1994; Araujo, [29], 1996; Frederiksen, [19], 1997; Rikards [39], 2000; Araujo, [31], 2001; Cugnoni, [43], 2004; Cugnoni, [44], 2007; Matter [45], 2007; Van den Abeele *et al.* [46], 2010; Badshah, [47], 2013; and Gahnmi, [48], 2013.

Relatively accurate results have been obtained for the elasticity and in-plane moduli with the classical laminate theory (CLT) [13]-[15], but a lack of precision is accomplished on the in-plane Poisson's ratio. A number of improvements of the previous approaches are performed by [16]-[31] in order to identify the elastic properties in composite plates. De Wilde [16] has presented a work using Bayesians estimation instead of optimization techniques for symmetric single material laminates. Frederiksen [18] used for thick plates a higher-order theory associated to the numerical model based on the Rayleigh-Ritz approach for symmetrical layups and specimens made of a single material. Mota *et al.* [22] have obtained accurate identification results for the tensile and in-plane modulus. However, poor estimations are obtained if the plate is relatively thin using the Mindlin plate theory.

Lai and Ip [28] have presented a method using Bayesians and the Kirchhoff plate theory. This method has been validated satisfactorily on symmetric single material laminates. Furthermore, Araujo *et al.* [29] have used the FEM and a high-order displacement field to identify the mechanical properties of specimens made up of several materials and general stacking sequences.

Another method based on response surfaces (regression analysis) was used by Rikards and coworkers [32]-[39]. This technique, called *plannig of experiments*, was used successfully to identify elastic properties in unidirectional laminates based on a design of experiments (DOE) using the PLANEX and RESINT programs. The DOE is highlighted in the industry over other regression analysis because with the DOE can be obtained the best mathematical model even though the form is not known. This iterative process to optimize the results is also known as updating, (see Alsharif *et al.* [40] and Xiaoping *et al.* [41]).

Futhermore, the use of model updating techniques was also presented by Cunha and Piranda [42] applied to sandwich structures for the identification of mechanical properties of laminates. However, the evaluation of in-plane Poisson's ratio in the above studies was still deficient even though more accurate estimations of the composite stiffness parameters were obtained.

More recently, Cugnoni *et al.* [43] have presented an improvement of the stiffness parameters using a MNET based on the the first-order shear deformation theory (FSDT) and the higher-order shear deformation theory (HSDT) evaluating the dynamic response of thick and thin multilayered composite laminated shells. These theories belonged to the hierarchy of equivalent single-layer (ESL) models. The results shown that can be identified the in-plane Young's modulus and shear modulus as well as the in-plane Poisson's ratio with a high precision using the FSDT and HSDT element formulations for thin shells. Both theories highlighted the application of the global sensitive response and accuracy. However, a deterioration in the global response is presented using the FSDT when it increases the shell thickness-to-span ratio.

Furthermore, Cugnoni *et al.* in [44] have developed a MNET for characterizing the constitutive properties of thick and thin composite plates based on the extracted mode shapes and the corresponding natural frequencies of the structure. The author has estimated the elastic properties with a nonlinear-least-squares algorithm based on the MAC. This approach of combining frequency and mode based error norms, allows an accurate identification of Young's modulus, shear modulus and Poisson's ratio using a AS4/PEKK homogenized orthotropic plate element on moderated thick and thin plates.

Matter *et al.* [45] have presented an improvement and extension to modal analysis of an existing multilayered composite shell finite element using a non-contact experimental device, a p-order shear deformation theory (PSDT) and the MAC. Contrary to early MNET optimization procedures, *the proposed MNET by Matters takes into account not only the subset of lowest natural frequencies as optimization criterion, but also the corresponding mode shapes and the nodal lines of these modes* [45]. This MNET emphasized the accuracy of the elastic parameters into two stages instead of one stage compared to the traditional MNET identification methods to show the high sensitivity on the mode shapes and weak sensitivity in the natural frequencies. The improvement of the accuracy is done refining the estimation of the elastic parameters (firstly Young's modulus and shear modulus and secondly Poisson's ratio) and performing a multi-degree-of-freedom curve-fitting strategy in order to extract the modal parameters in the composite component.

Van den Abeele *et al.* [46] have presented an optimization method using the Kirchhoff-Love equations based on in-plane orthotropic elastic constants in sandwich structures with steel skins. Whereas Badshah [47] has presented a MNET to identify elastic behaviour of Aluminum Foam based on the MAC using ANSYS Parametric Design Language APDL. Gahnmi *et al.* [48] have focused on the identification of the stiffness parameters using solid elements in a thin

multilayer composite plate based on a new response surface method procedure using an analysis of variance (ANOVA) and a DOE.

Therefore, the best achievements, identifying the material properties of composite plates based on the MNET literature, were obtained when:

- The experimental measurements possess a good quality to predict the dynamic behaviour in composite components [13]- [48], [130], [139], [142] regarding the accelerometers due to the non-contacting nature [140] with their advantages and disadvantages [141].
- The achievements in mechanical structures to validate their dynamic behaviour were carried out with highly accurate theoretical models using FEM [80], [83], [92].
- The best MNET achievements have shown that the in-plane Young's modulus and shear modulus as well as the in-plane Poisson's ratio can be identified with high precision using the FSDT and HSDT for thin and thick shells, applying MAC and curve-fitting algorithms by [43], [44] and [45].
- Different layer-wise models (LWM) including shear effects were used to improve the response of the global deflections and natural frequencies [77], [76], [84], [94], [96] in composite materials; however, the computer cost is prohibitive.
- Although the FSDT element formulation is quite acceptable to study the global response of high shear deformable thin and thick composite structures, they were not adequate for forecasting local stress-strain characteristics [93]-[96].
- A design of experiments (DOE) was used as a regression analysis to obtain a simple mathematical model for structural optimization problems. The DOE has played an important role in new product designs, manufacturing process development and process improvement in the last 25 years [145].

Taking into consideration the above improvement of achievements using MNET to identify the stiffness parameters of composite components, the proposal of the new MNET will be based on:

1. Triangle elements: Most of the shell structures can be discretized as quadrilateral or triangle elements (plane or curve). The triangle elements are generally preferred due to its advantage in modeling shell geometries [76], [79], [84], [104] beside the accuracy,

reliability and efficiency studied by many researchers in the last 40 years [80], [83], and [92].

2. FSDT: In major commercial codes, the FSDT is implemented in element formulations using the FEM, such as the CTRIA3 element in MSC/NASTRAN to include the transverse shear effects in a laminated composite shell ply-by-ply (PCOMP entry) by setting up the thickness, the orthotropic (MAT8 entry) or anisotropic (MAT2) material properties and the relative orientation of each individual lamina [90], [103], [148], [150].

3. Curve-fitting algorithms: The application of *identification de rèsidus complexes (IDRC)* and *identification de rèsidus multiples (IDRM)* pole/residues curve-fitting algorithms developed by Balmès [152] is proposed for the new MNET for its efficiency in the identification of the modal parameters [154]-[155]. These algorithms are implemented in [106] and will generate a parametric model as approximations of unconstrained pole/residues to identify stiffnes parameters in the composite component. The use of these algorithms should give an enhancement of the robustness of the new MNET identification process applied to a CFRP assembly. Furthermore, the IDRM and IDRC curve-fitting algorithms will be used to perform the correlation of the reduced order model applying the CBMOR method and different MSE techniques to a composite component after updating the elastic parameters in the full model versus the experimental measurements. The application of these algorithms is a fundamental difference compared with other MNET developments.

4. DOE: The accuracy and reliability of the DOE are characterized by a minimum of standard deviation based on the numbers of terms in the regression equation. The reliability of the regression equation means that the standard deviations for the reference points and any other points are approximately the same. Most of the existing methods of regression analysis are based on the principle that the form of the equation is known and the problem is to find the coefficients of the equations [32]. The differences between the DOE applied by Rikards in [32] using the PLANEX program respect to the DOE proposed in this thesis consist of the methodology to identify the main effects per stiffness parameters, an interaction matrix between stiffness parameters, estimated effects and coefficients per stiffness parameter and the transfer function/surface response using the MINITAB 15 program. The DOE methodology implemented in MINITAB 15 will help to identify efficiently the effects and interactions of the stiffness parameters in the CFRP and the transfer funtion using the ANOVA.

Lastly, but no less important point, is the Poisson ratio during the phase transformations in polymer gels, see [97], such as the RTM6 used for the elaboration of CFRP. The phase transformations in polymer gels usually entail a change in structure [156]. This physical characteristic typically occurs if the polymer gel versus temperature associated with a volume phase transition is close to a critical point [157]. Similar behaviour is reported for different polymer gel concentrations when the phase transition temperatures changed [158]. Some authors have achieved low Poisson's ratio values [159] or even negative [31], [160] and [161] in CFRP. Some rather surprising Poisson's ratio results obtained by Herakovich in [98] using two-dimensional lamination theory combined with the appropriate three-dimensional anisotropic constitutive equation: lateral Poisson's ratio obtained were greater than one and negative through-the-thickness. The negative Poisson's ratio for angle-ply laminates with fiber orientations between 15° and 40° was due to the high degree of normal-shear coupling and the constraining influence of adjacent layers. Such Poisson's ratio values have provided a distinctive signature for phase transitions, whatever the type of material. It is proposed to analize the Poisson's ratio value as part of the MNET analysis using the DOE, beside the conventional Poisson's ratio.

Approach of the new MNET to apply CBMOR method with Ritz vector basis

The new MNET framework approach is proposed in the flowchart, (see Fig. 2), to apply and validate a CBMOR method for a CFRP component. A brief description of each step is given below.

1. **Creation of finite element (FE) Model**: The elaboration of the full FE model is the first step. Two full FE models are created in ABAQUS 6.9 using an orthotropic triangular S3 elements: one FE model with coarse mesh and another with fine mesh. The full FE model with the coarse mesh is used to obtain the coordinates of the nodes in order to perform the experimental measurement analysis (EMA) using the SLDV. The full FE model with the fine mesh is used to perform the correlation. The FE models are exported into MATLAB-SDTools.

2. **Export the FE model and perform of experimental measurements**: Once the FE model is generated with coarse mesh, it is exported to perform the experimental measurements using a SLDV and it obtains a UFF58 file format. The UFF58 file is exported into

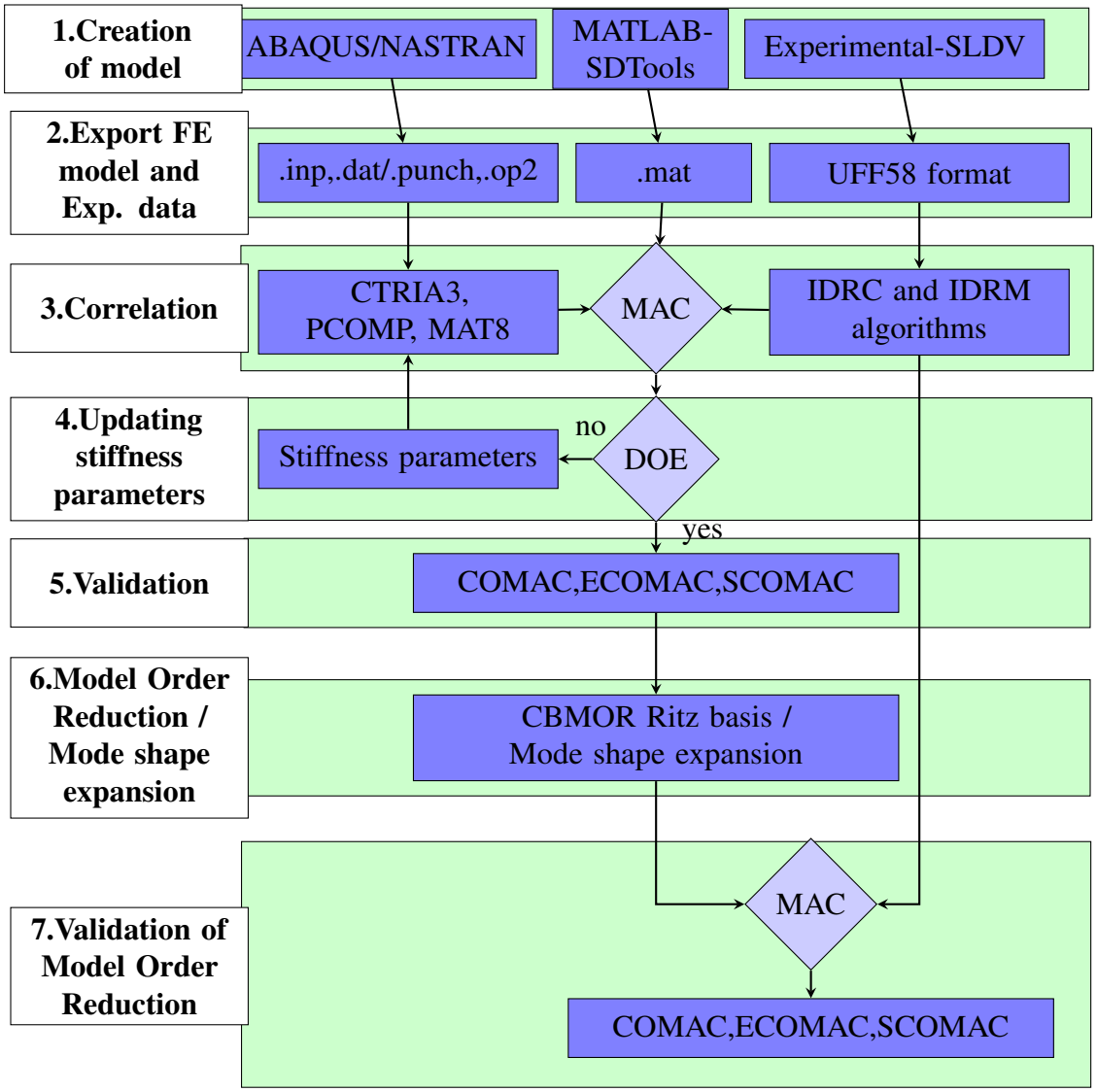

Fig. 2 MNET and Craig-Bampton model order reduction method flowchart

MATLAB using the SDTool-box [106] to perform a curve-fitting. The FE model with fine mesh is also exported into SDTools, using FEMLINK [106].

3. **Correlation of the FE model**: The IDRC and IDRM algorithms are used to perfom the curve-fitting. The correlation of the experimental measurements and the full FE model is performed using the MAC implemented in [106]. The modal analysis of the FE model is performed using the fe_eig command implemented in SDTools.

4. **Updating stiffness parameters**: The updating of the stiffness parameters in the full FE model is performed using the DOE based on the MAC values. A transfer function and surface response are obtained based on a number of stiffness parameters.

5. **Validation of the FE model**: The verification of the full FE model quality is done using different MAC, MACco, COMAC, eCOMAC, COMAC-S and MSE techniques implemented in the SDTools-box [106]. For comparative purposes the FE model with fine mesh is exported to MSC/NASTRAN [148] with PCOMP and MAT8 cards.

6. **Model Order Reduction/Mode shape expansion**: Once the stiffness parameters of the full FE model are updated then the model order reduction is performed based on the CBMOR and AMLS methods using Ritz basis in terms of substructures/super-element technique implemented in [106]. Several MSE techniques are also perfomed based on the updated stiffness parameters and experimental measurements to validate the results.

7. **Validation of Model Order Reduction**: The quality of the ROM is also verified applying different modal assurance criteria used in the validation of the full FE model.

Goal of the thesis

The aim of this thesis is to evaluate the dynamic behaviour applying a MOR method in a composite component divided into two specific parts: a multidisciplinary MNET methodology to obtain accurate stiffness parameters and the application of the CBMOR and AMLS methods based on the Ritz vector basis in terms of substructure/super element technique. On one hand the main difference of this research respect to the state-of-the-art consists to document that the principal properties and limitations, using condensation algorithms, are basically caused by reduction in the number of DOF's or the modal range included and on the other hand those

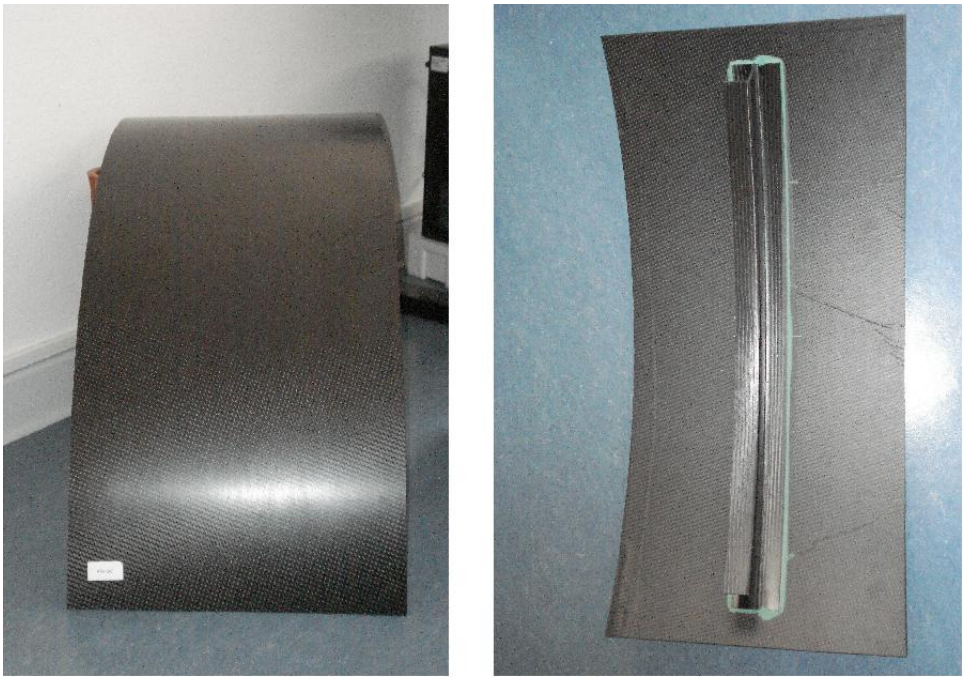

Fig. 3 RTM Composite component assembly

numbers depends strongly of the stiffness parameters of the composite structure using FRF's such as in the FBS method to represent the physical behaviour of the structure whereas cannot be described by CMS approaches. The Author of this thesis could not find a similar approach or report in the literature based on the stiffness parameters obtained with a new MNET and then to apply MOR method to a composite component assembly. Moreover, a regression analysis using a DOE as part of the MNET is performed based on the MAC values to update the stiffness parameters in a full FE model including transverse shear effects with enough accuracy. The correlation of the full FE and reduced models versus the experimental measurements is performed using MAC, different coordinate modal assurance criteria (MACco, COMAC, eCOMAC, COMAC-S), and the IDRC and IDRM curve-fitting algorithms. Furthermore, the MSE techniques based on MOR methods are performed to validate the impact of the updated stiffness parameters obtained with the new MNET using the K-MAC and M-MAC for comparative purposes applying different condensation algorithms. The MSE techniques are well established for more conventional materials and structures based on STATIC or Guyan condensation, MODAL transformations, SEREP, DYNAMIC, CMS and FBS or hybrid methods. The MNET should be applicable to problems of engineering interest in German industry that

requiere MOR method in terms of substructure/super-element technique for composite as well as conventional components. This research will concentrate on a composite component provided by the DLR Braunschweig, (see Figs. 3 and 4). The composite structure is made up of three parts. The first component is made of Huntsman Ly 564 + Hexcel Gewebe G0926 (High Tenacity-Faser, HTA) with dimensions of 0.390m×0.810m×0.007m, (see Fig. 3). The second shell that connects the two principal parts, (see Fig. 4), has dimensions of 0.710m×0.030m×0.0035m. Finally, there is the C-section Hexcel resin transfer moulding (RTM6) + Saertex Multi-Axial-Gelege (MAG) with a intermediate modulus (IM7-Faser) with dimensions of 0.710m×0.030m×0.0035m. All the parts have symmetric layer distribution $[45/-45/45/-45/]_S$.

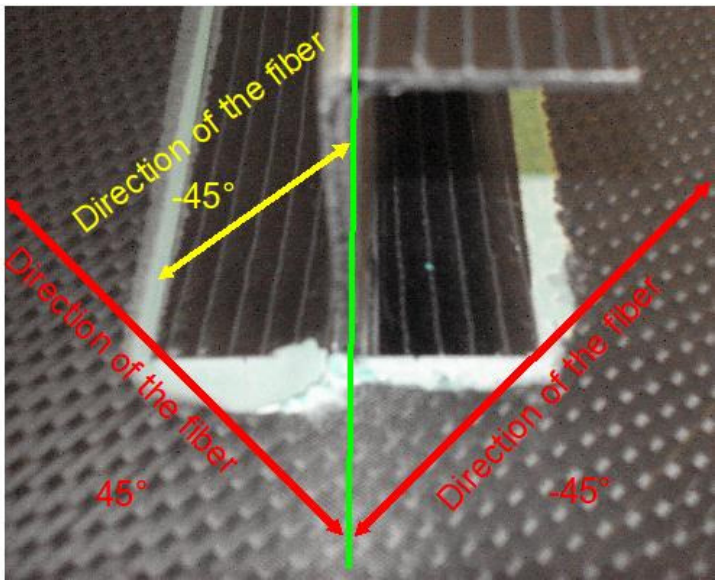

Fig. 4 Composite component assembly detail.

Thesis outline

The work presented in this thesis is divided into three parts. Part I deals with the theory behind the numerical-experimental techniques, 2D FE model with orthotropic proporties, curve-fitting algorithms, design of experiments, the different well established modal assurance criteria, the CMS based on the Ritz vectors basis, the AMLS and MSE techniques. In Part II the

techniques and methods from Part I are applied to the composite component. In Part III there are recommendations and conclusions for further work. Each part consists of several chapters.

Part I - Introduction to mixed numerical-experimental technique (MNET) and component mode synthesis (CMS)

Chapter 1 gives a general framework of the mixed numerical-experimental techniques. Subsection 2.1 addresses the type of CFRP used with MNET, subsection 1.1.1 gives a general theory framework of the modal analysis theory, frequency response function method 1.1.2, the fast Fourier transform 1.1.3, parametric identification using pole/residues based on the IDRC and IDRM curve-fitting algorithms 1.1.4. The subsection 1.2 introduces the numerical simulation of CFRP using the finite element method based on the first-order shear deformation theory (FSDT) [83]. Subsection 1.4 gives a general framework of the design of experiments implemented in MINITAB 15.

Chapter 2 introduces different quality modal assurance methods employed with a full FE model or ROM such as: MAC, MACco, COMAC, eCOMAC and COMAC-S.

Chapter 3 gives a general framework about model order reduction (MOR) with Ritz vectors, the classical CMS bases as approximation of the frequency response, automatic generation of interfaces known in literature as AMLS and MSE techniques.

Part II - Application of the Craig-Bampton model order reduction to a CFRP component using a MNET

Chapter 4 gives a description of the MNET to obtain the stiffness parameters of the composite component provided by the DLR Braunschweig. Firstly, an experimental modal analysis is performed based on a SLDV. Secondly, the curve-fitting is obtained using the IDRC and IDRM algorithms implemented in SDTools. Thirdly, numerical modal analysis is performed based on the pshell element formulation with PCOMP and MAT8 card definition implemented in SDTools. Fourthly, the full FE model is updated applying the DOE using the MAC. The best stiffness parameters are obtained with the MNET for the established parameters $E_1, E_2, G_{12}, G_{23}, G_{13}$ and ν_{12}.

Chapter 5 shows how the stiffness parameters obtained in Chapter 4 of the full FE are validated applying the MAC and different COMACs. For comparison purposes the full FEM

model in SDTools is exported using FEMLINK and solved in MSC/NASTRAN SOL 103 and ABAQUS 6.9. The validation of the exported FE models is performed also with the same MAC, COMAC, eCOMAC, COMAC-S and MACco criteria.

In Chapter 6 the modeling of the substructures is established based on the Craig-Bampton model order reduction and AMLS methodology using the Rayleigh-Ritz vector basis using single value decomposition established in the structural dynamic toolbox for MATLAB. The updated full FE model, obtained in the Chapter 4, is divided in two super-elements and the CBMOR method is performed according the appropiate $[T]$ matrix used in [106]. The reduced model using the CBMOR method is validated using the same modal assurance criteria and different COMACs applied to the full FE models. Furthermore, the influence of the stiffness parameters obtained with the MNET is analyzed applying several MSE techniques in terms of MOR methods based on the stiffness- and mass-weighted criteria (K-MAC and M-MAC) using the MAC.

Part III - Conclusion and recommendations

Chapter 7 gives a number of recommendations for future work such as: evaluation of Poisson's ratio (ν_{12}, ν_{13}, ν_{23}) of a RTM6 polymer gel versus temperature associated with a volume phase transition close to a critical point used with CFRP, the application of others ESL and LWM models, the analysis of fatigue and fracture of CFRP (for example the Puck criterion) using the MNET, comparison of results using other discrete Mindlin Kirchhoff triangle (DMKT) element including transverse shear effects, comparison of results using the enhanced AMLS method and the application of other curve-fitting algorithms with experimental modal analysis.

Part I

Introduction to mixed numerical-experimental technique (MNET) and component mode synthesis (CMS)

Chapter 1

General concept of MNET

1.1 Introduction

Traditionally, the general concept of numerical methods is usually formulated to identify directly[1] the physical properties (such as Young's modulus, shear modulus and Poisson's ratio) of mechanical parts, (see Fig. 1.1). The application of several numerical methods is used to obtain directly these physical properties and analize the mechanical performance. However, there is an increasing interest to obtain indirectly the physical properties of CFRP using MNETs [13]-[48]. The reason to use a MNET is justified in the literature when it is limited the application of standard testing methods to determine directly the constitutive physical properties. Typical examples applying MNET are found in many industrial processes such as: deep drawing, extrusion, cutting, blanking and forging processes [167]. The MNET can be also used in different fields such as biological materials [168], rocks and soils [169].

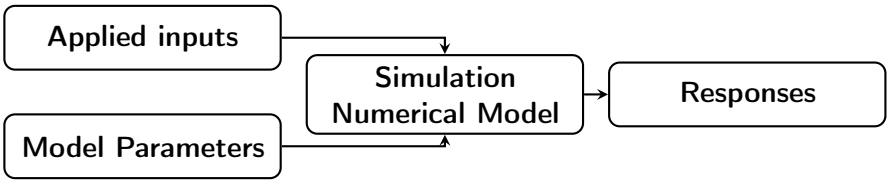

Fig. 1.1 The direct problem [170].

The purpose of using a MNET is not the numerical method that has to be solved to obtain the model parameters. The model parameters are obtained using the responses of an experimental

[1] The numerical method is also called direct problem [170].

system to a particular input in order to find in an interactive way the solution using a numerical method. However, the numerical method used with MNET plays a critical role to identify the model parameters of CFRP, (see Fig. 1.2), with advantages and disadvantages discussed in [168] and [171]. Thus, the MNET approach can be only used when there is a simple relationship between the measured quantities and the physical properties of interest [170]. Due to these characteristics, the MNET is also known as inverse problem [167].

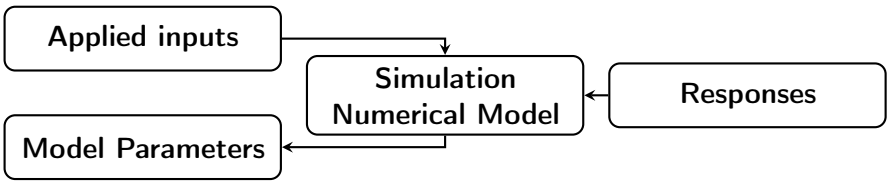

Fig. 1.2 The inverse problem [170].

The general concept of MNET applied to different CFRP plates and shells, (see Fig. 1.3), is divided mainly into five stages, based on the improvements archived in the literature, see [32]-[39], [43], [44], [45] and [48]. These stages are:

1. Type of CFRP.
2. Experimental modal analysis (EMA).
3. Curve-fitting approximation of the resulting responses using algorithms.
4. Simulation of a numerical model in order to obtain the stiffness parameters.
5. Updating of the stiffness parameters applying a DOE, genetic algorithms, minimizing the error approach using computational modal predictions and corresponding experimental data using the modal assurance criterion (MAC).

Firstly, the CFRP component described in the Introduction generally consists of two parts: textile reinforcements and polymer matrix. The textile reinforcements includes woven fabric[2] produced by the interlacing of warp (0°) and weft (90°) fibres in a regular pattern or wave style, (see Fig. 1.4). Common CFRP woven fabric elaborated with yarns are preferred with minimal or nominally zero twist (tows) in the aerospace industry. The polymer matrices, such as epoxies

[2] *A woven fabric is a planar textile structure produced by interlacing two or more sets of yarns, fibres, rovings or filaments where the elements pass each other usually at right angles and one set of elements is parallel to the fabric axis [173].*

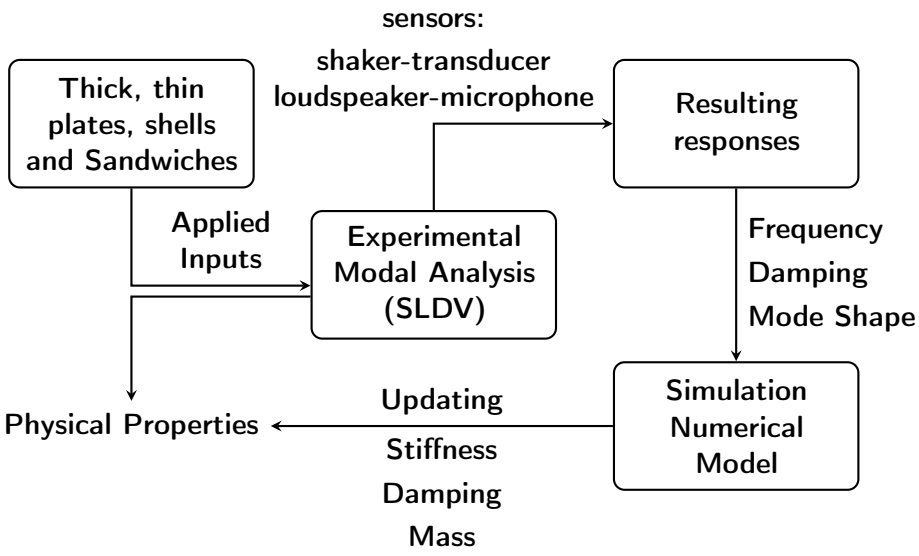

Fig. 1.3 General concept of MNET applied to CFRP [170].

and polyesters, are usually the resin systems. The polymer matrix has desirable properties such as: easily formed into complex shapes as well as transmit the load to the textile reinforcements [173].

Three types of CFRP can be distinguished using MNET: thin, thick and honeycomb (sandwich). A state-of-the-art of different thin composite plates[3], thick composite plates[4] and sandwiches[5] textile reinforcements is discussed by Khan in [173] and by Knipprath in [172], Balvers [176] and Tochukwu [177] respectively.

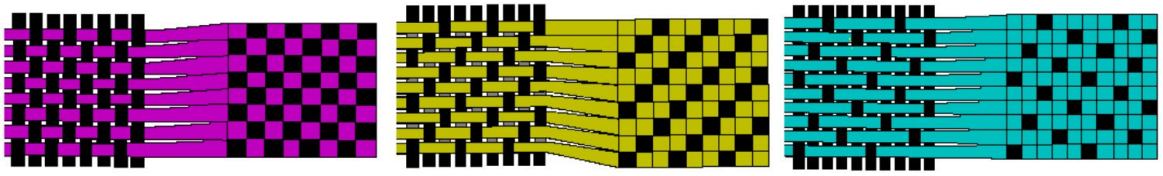

(a) Plain weave fabric. (b) Twill weave fabric (c) Satin weave fabric

Fig. 1.4 Woven Fabrics [173]

[3]Thin-plate formulation is defined as plane structural elements with small thickness compared to the planar dimension elaborated with woven fabrics, plane wave, twill weave, satin weave, non-crimp fabrics (NCF) [173].

[4]Thick-plate formulation is defined as plane structural elements with bigger thickness compared to the planar dimension. Balvers [176] provided a state-of-the-art study of the importance of 'thick' advanced composite structures.

[5]Sandwich panels consisting of pairs of light, stiff, strong faces separated by low density cores are introduced by Tochukwu, see [177]. The sandwich materials offer exceptional structural load support, especially in bending.

Secondly, the EMA is a process of determining the modal parameters (natural frequencies, damping factors and modal vectors), based on the modal analysis theory [143], illustrated in section 1.1.1. A common reason to use EMA data is to verify the results of an analytical or a FEM numerical approach interpolating frequency response functions (FRF)[6]. The use of FRFs is introduced in section 1.1.2 as an input for the estimation of the modal parameters. The use of fast Fourier transform (FFT) and digital signal analizer (DSA) are fundamental steps to acquiere and record the FRF that isolates the inherent dynamic properties of a mechanical structure introduced in section 1.1.3. Traditionally these procedures are divided into three steps: the excitation of the structure, measuring the response motion and post-process of the FRF.

Thirdly, the goal of using the curve-fitting algorithms, illustrated in section 1.1.4, is to produce an accurate estimation of the modal parameters of a CFRP component obtained with FRF. The FRFs obtained are used to provide a way to compare the test and the FE model (during the experimental approach and during the model updating process) [178].

Fourthly, the simulation of numerical methods using FEM to obtain the mechanical behaviour of CFRP flat or doubly curved laminate shells components is described normally using different equivalent single-layer (ESL) laminate theory. One of the relevant ESL laminate theories based on the accuracy, computational cost and simplicity is the first-order shear deformation theory (FSDT). An extense research using the FSDT is documented in bibliography for the possibility of including transverse shear effects [76], [83], [84], [99], [104]. In essence, the FSDT approach introduced in section 1.2 of this work can be applied using a discrete shear triangle (DST) elements formulation developed by Lardeur [84] and Batoz [104] for CFRP also known as discrete Mindlin Kirchhoff triangle elements [76] (DMKT) with transverse shear effects included.

Fifthly, several methods can be found in the bibliography [13]-[48] to update the stiffness parameters of CFRP using MNET (genetic algorithms, DOE). The DOE [145] is a senstivity analysis tool widely used in the industry to identify the critical parameters of the mechanical components, illustrated in section 1.4. These critical parameters can be used to control the target of FE models using experimental measurements. The MAC is a well-established modal correlation criteria (MCC) to verify FE models versus experimental measurements. There are other MCC such as different coordinate modal assurance criteria to verify the identified parameters of the FE model.

[6]The acquisition and interpolation of the FRF play an important role into the MNET to validate the application of CMS using a CFRP assembly.

Finally, once the MNET is established to control the stiffness parameters of a CFRP, part of the objetive of this work will be to verify the application of a MOR using super-elements to a CFRP. The super-elements can be created from CMS in MOR literature. A super-element is a reduced model that is included in another global model as an element. The approximation of reduced models using super-elements is evaluated in further sections and chapters using the same experimental measurements.

1.1.1 Modal Analysis Theory

The single DOF system can be used as a basic model in time and frequency domains to estimate modal parameters summarised by Giorelli in [178] and reworked in this section. Cases with multiple DOF can be viewed simply as a linear superposition of a single DOF system in [131], [182] and [183]. *The general mathematical representation of a single DOF system, represented schematically, (see Fig. 1.5), is given by equation* (1.1) *where* $[M],[C]$ *and* $[K]$ *are the mass, damping and stiffness matrices* $\ddot{x}(t),\dot{x}(t),x(t)$ *are the acceleration, velocity and displacement vectors respectively. The* $F(t)$ *is the function that respresents the excitation applied to the*

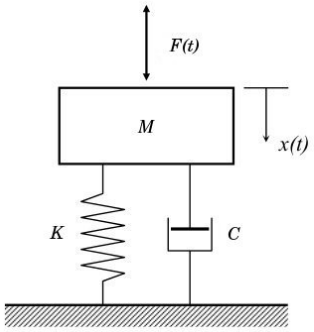

Fig. 1.5 Single Degree of Freedom (SDOF) System [178].

system [178]:

$$[M]\{\ddot{x}(t)\}+[C]\{\dot{x}(t)\}+[K]\{x(t)\}=\{F(t)\} \tag{1.1}$$

Setting $F(t)$ equal to zero, the general solution of the Eq. (1.1) is

$$x(t)=Ae^{\lambda_1 t}+Be^{\lambda_2 t} \tag{1.2}$$

where A and B are constant and the values of λ_1 and λ_2, for an underdamped system, are given by

$$\lambda_r = \sigma_r + j\omega_r \tag{1.3}$$

where σ_r is the damping factor and ω_r is the damped natural frequency[7]*. The fraction of critical damping for most real structures is rarely greater than 10%, if there is not presented active damping systems. In such an underdamped system, λ_1 and λ_2 roots are always complex conjugates. The roots are referred to as the poles of the system. The two coefficients, A and B, are also complex conjugates of one another. Equation* (1.1) *is the time-domain representation of the system, see Fig. 1.5. An equivalent equation can be determined for the frequency domain. The frequency representation has the advantage of converting a differential into an algebraic equation. This is accomplished by taking the Fourier transform*[8] *of Eq.* (1.1)*. Thus, it becomes* [178]:

$$[-\omega^2[M] + j[C]\omega + [K]]X(\omega) = F(\omega) \tag{1.4}$$

then if

$$B(\omega) = -\omega[M] + j[C]\omega + [K] \tag{1.5}$$

and substituting the Eq. (1.5) into (1.4), it is transformed into

$$B(\omega)X(\omega) = F(\omega). \tag{1.6}$$

Eq. (1.6) *is an equivalent representation of Eq.* (1.1) *in the Fourier domain. The system response $X(\omega)$ is directly related to the system forcing function $F(\omega)$ through the quantity $B(\omega)$. If the system forcing $F(\omega)$ and its response $X(\omega)$ are known, $B(\omega)$ can be obtained by* [178]:

$$B(\omega) = \frac{F(\omega)}{X(\omega)} \tag{1.7}$$

[7] The units of both factors are specified in radians per time-unit.

[8] The Fourier transform of a function $x(t)$ is denoted by $X(\omega)$ which transform the variable $x(t)$ from a function of time into a function of frequency ω [178].

Reordering this equation is obtained

$$X(\omega) = \frac{F(\omega)}{B(\omega)} \tag{1.8}$$

and establishing $H(\omega) = \frac{1}{B(\omega)}$ Eq. (1.8) is transformed into

$$X(\omega) = H(\omega)F(\omega). \tag{1.9}$$

The $H(\omega)$ is known as the FRF of the system. The FRFs, $H(\omega)$, are defined as the ratio of the transformed excitation [131]:

$$H(\omega) = \frac{X(\omega)}{F(\omega)}. \tag{1.10}$$

where $H(\omega)$ is the identified (predicted) FRF transfer function matrix, $H(\omega)$ the measured FRF transfer function matrix, $X(\omega)$ the Fourier spectrum of response and $F(\omega)$ is the Fourier spectrum of excitation force. The FRF in Eq. (1.10) is the inverse of the dynamic stiffness matrix

$$H(\omega) = \left[-\omega^2[M] + [C]\omega + [K]\right]^{-1} \tag{1.11}$$

where the mass $[M]$, damping $[C]$ and stiffness $[K]$ matrices in Eq. (1.11) are dependent on physical parameters such as material's density, Young's modulus and shear modulus and Poisson's ratio. Experimentally, the values of the transfer function are measured only along the $j\omega$-axis in the $s-plane$, that is $(s = j\omega)$. Thus, $H(\omega)$ can be rewritten as a function of the complex poles;

$$H(\omega) = \frac{1}{(j\omega - \lambda_1)(j\omega - \lambda_2^*)} \tag{1.12}$$

where $\lambda_1 = \sigma_1 + j\omega_1$ is the complex pole and λ_2 its complex conjugate. The FRFs, $H(\omega)$, are complex-valued functions of a real-valued independent variable (ω) that can be identified by a pair of curves (real and imaginary parts) [178], (see Fig. 1.6).

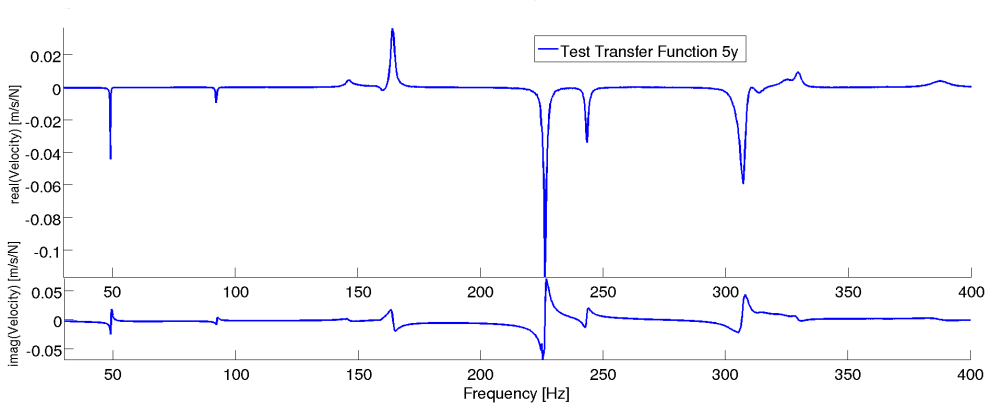

Fig. 1.6 FRF real and imaginary parts.

1.1.2 Frequency Response Function (FRF) Method

The interpolation between the experimental measurements uses FRF. The FRFs allow the comparison of the experimental modal data and it is a common approach to estimate modal parameters (frequency, damping, and mode shape), see [182], [183] and [184]. The FRFs were defined as the quotient between the input and output Fourier transforms, see Eq. (1.10), and it can be used as an input to interpolate the estimation of modal parameters of the FEM or experimental data [185], (see Fig. 1.7). Furthermore, it is also possible to use FRFs comparing experimental modal parameters and FE model to update the stiffness parameters of a FE model [152]. The FRFs are measured throughout the structure using an excitation sensor at a single or at multiple points. This excitation can be narrowband or broadband. Multiple independent modal vectors can be obtained using FRFs. These modal vectors are estimated from multiple rows or columns of the FRF matrix. A complete set of frequency response measurements would form a square matrix of size n, where the rows correspond to response points and the column to excitation points, see Eq. (1.13). The frequency response matrix of a linear system has an additional important property. If the system behaves linear, the frequency response matrix is always symmetric due to the Maxwell's Reciprocity Theorem [186]. For example, referring to the matrix in Eq. (1.13):

$$\begin{Bmatrix} X_1(j\omega) \\ X_2(j\omega) \\ \vdots \\ X_n(j\omega) \end{Bmatrix} = \begin{bmatrix} H_{1,1}(j\omega) & H_{1,2}(j\omega) & \dots & H_{1,n}(j\omega) \\ H_{2,1}(j\omega) & H_{2,2}(j\omega) & \dots & H_{2,n}(j\omega) \\ \vdots & \vdots & \ddots & \vdots \\ H_{n,1}(j\omega) & H_{n,2}(j\omega) & \dots & H_{n,n}(j\omega) \end{bmatrix} \begin{Bmatrix} F_1(j\omega) \\ F_2(j\omega) \\ \vdots \\ F_n(j\omega) \end{Bmatrix}, \tag{1.13}$$

if $H_{1,2}(j\omega) = H_{2,1}(j\omega)$, this property is helpful to provide the linearity assumption. By comparing two reciprocal measurements at various pairs of points and observing the differences between them, the degree of linearity of the system can be estimated [178].

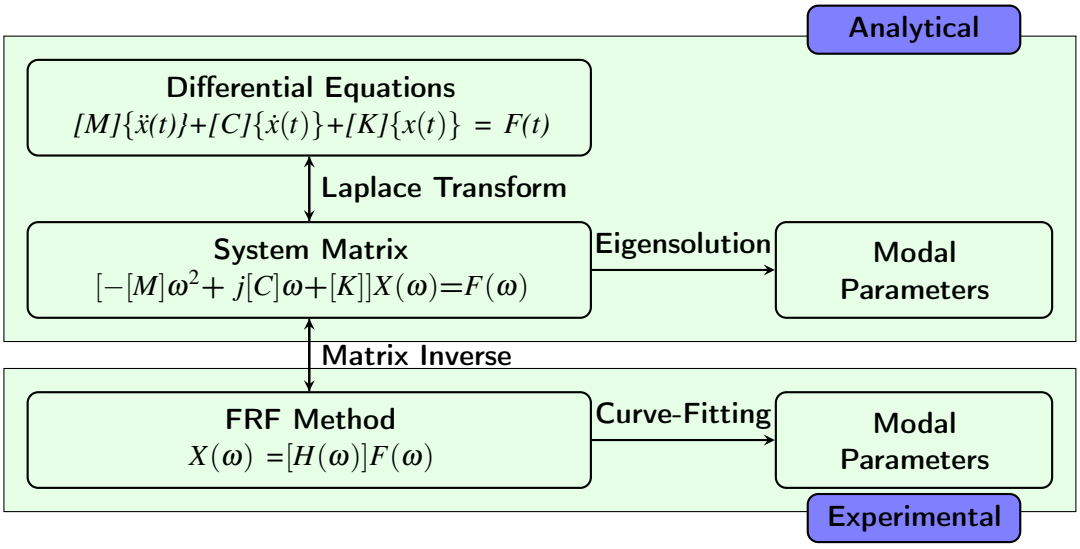

Fig. 1.7 Sources of modal parameters [185].

The frequency response matrix is the classical format to store non-parametric FRF [106]. Moreover, the FRFs corresponding to parametric representations of sets of transfer functions can be generated in the form of a ratio of polynomials [106]. Thus, the characterization of properties of parametric representations to check the quality of FRF measurements is obtained applying the Fast Fourier Transform (FFT) algorithm to accomplish a comprehensive modal analysis. The FFT is a fundamental procedure that isolates the inherent dynamic properties of a mechanical structures [131] introduced in the next subsection.

1.1.3 The Fast Fourier Transform (FFT) algorithm and Dynamic Signal Analyzer (DSA)

The acquisition of FRFs for the formulation of a modal model involves the use of a spectrum analyser signal processor that allows recording a signal in time and frequency domains. Modern Dynamic Signal Analyzer (DSA) or Frequency Spectrum Analyzer (FSA) are digital signal processors, which transform the signal data using of very efficient algorithm, the FFT algorithm published by J.W. Cooley and J.W. Tuckey [189]. The FFT algorithm is the basis of the

formulation of any frequency-domain function in modern acquisition systems based on the Fourier analysis theory [190], [191]. In terms of an integral Fourier transform, a function must exist always, at any time, in a continuous sense in order to be evaluated, or "transformed". *In a real measurement situation, data are available in a discrete sense over a limited time period. Therefore, the FFT is based on a set of assumptions concerning this discrete sequence of values. Those assumptions can be reduced down to one or two situations that must be met by every signal processed by the FFT algorithm:*

1. *The transient signal must be captured completely within the time record.*

2. *The signal must be composed only of harmonics of time record (i.e., it must be an exact periodic record in the time record).*

If one of these assumptions is not met by any experimental measurements processed by the FFT algorithm, then the resulting spectrum will contain bias errors accordingly. The accurate measurement of FRFs depends significantly on the errors involved with the digital signal processing. In order to take full advantage of experimental data in the correlation of experimental procedures with numerical approaches, the errors in measurement, generally designated as noise, must be reduced to acceptable levels. The acceptable levels of noise in FFT analyzers requieres a careful selection of the measurement settings for the averaging, triggering und window parameters[9], see Chapter 4.2.

Furthermore, the measurement capability of the DSA is built around a tri-spectrum average loop. This loop assumes that two or more time domain signals are simultaneously digitized and recorded. A variety of FRF measurements are calculated from these loops using the tri-spectrum estimates [185]. *One of the advantages using the loop averaging is to remove random noise and randomly excited non-linealilty's from the XPS of each signal pair. This low noise measurement of the effective linear vibration of the structure is useful for the EMA* [185].

The tri-spectrum average loop is calculated using an auto Power Spectrum (APS) for each channel and the Cross Power Spectrum (XPS) between the two channels[10]. The APS and XPS spectrum responses are formed by taking the product of the response spectrum matrix $[G_{x,x}(j\omega)] = [X(j\omega)][X(j\omega)]^T$ and the force spectrum matrix. $[G_{f,f}(j\omega)] = [F(j\omega)][F(j\omega)]^T$,

[9] Each of these measurements settings is merely a convenient grouping of many individual errors that cause a specific kind of inaccuracy in the frequency response function estimate [178].

[10] The diagonal elements of the response and force spectrum matrices are called APS and the non-diagonal elements are called XPS [187].

where $[F(j\omega)]$ and $[X(j\omega)]$ were defined in the previous section. The response spectrum matrix is formed by taking the product of Eq. (1.14):

$$[G_{x,x}(j\omega)] = [H(j\omega)][G_{f,f}(j\omega)][H(j\omega)]^T. \tag{1.14}$$

Every row and column of the response spectrum matrix contains the spectrum of each measured response multiplied by the conjugate spectrum of a reference response. A row or column of the response spectrum matrix can be curve-fitted to estimate modal parameters, if the excitation force spectrum matrix can be assumed to be "relatively flat" over the frequency range of the modes of interest [185]. Thus, once the acquisition of FRFs is performed, a curve-fitting method applying Pole/Residue parametrization can be used to estimate the modal parameters introduced in the next section.

1.1.4 Curve Fitting of Modal Parameters using Pole/Residue Parametrization

The goal of using the curve-fitting algorithms is to produce an accurate estimation of the modal parameters of the CFRP component using the FRF according the materials and manufacturing process selected . The majority of modern EMA using DSA relies upon the application of curve-fitting technique (algorithms) to estimate the modal parameters to a set of FRF measurements with enough accuracy, (see Fig. 1.7). As it was pointed in the Introduction, the accuracy of the FRF measurements is a crucial factor when judging the estimation of a modal parameter applying the curve-fitting process. There are several methods that can be used to estimate the modal parameters highly influenced by the experimental data based on one mode at a time (SDOF) or more modes at a time (MDOF, global and multi-reference) [185]. The global curve-fitting expression called the rational fraction polynomial (RFP) or partial fraction expansion (PFE) is received with great interest and attention for its simplicity and easy implemention in personal computers (PC) [192] for the last 20 years [193], [194]. The RFP expression not only can be used to estimate the modal parameters, but also yields the numerators and denominator polynomial coefficients as well the poles and zeros. The RFP form of poles and residues, illustrated in Eq. (1.15), offers advantages over other forms [185]:

$$H(s) = \sum_{k=1}^{modes} \left(\frac{[R_k]}{s-\lambda_1} + \frac{[R_k^*]}{s-\lambda_2^*} \right). \tag{1.15}$$

The residue matrix[11] $[R_k]$ is defined as the constant numerators of the transfer function matrix, "*modes*" is the number of modes of vibration, and λ_r is the pole location. The first advantage using the RFP form is related that it can be applied directly to an FRF measurement over any frequency range. The second advantage is related to the possibility to identify the pole in the vicinity of a resonance peak. The third advantage is related to the identification of repeated roots for the nature of the CFRP assembly component. The last advantage is related into the application of CMS methods. *Hundreds of studies related to CMS methods have shown, that for analytical models the representation of the residual flexibility is generally necessary and sufficient to obtain a good representation of the low frequency dynamics* [152].

The RFP form in Eq. (1.15) is typically used when the modal data is obtained from experimental transfer function measurements (introduced as FRF). Traditionally the relationship between residues and mode shapes are expressed in terms of FRFs. Thus, the identification of experimental measurements is determined obtaining modes whose poles are located in the test frequency range selected using transfer functions. A characteristic of the transfer functions IDRC and IDRM used in this work are the residual terms $[E(s)]$ and $[F(s)]$ defined in [152]. The contributions of the residual terms $[E(s)]$ and $[F(s)]$ in the transfer functions are used to evaluate the high and low frequency mode terms respectively. The residual terms are known also as residual modes or residual vectors [152] and it is documented in literature the advantages of the application of the residual terms in the accuracy [153]. Thus, the estimation of the poles depends linearly on the residual terms $[R_j(\lambda_r), E(s), F(s)]$ solving the linear least squares problem associated with the frequency domain output error illustrated in Eq. (1.16).

$$\begin{aligned}[R_k(\lambda_r), E(s), F(s)] &= arg\ min\ |[H(s)]_{test} - H(s)|^2 \\ &= arg\ min\ \left| [H(s)]_{test} - \sum_{k=1}^{modes} \left(\frac{[R_k]}{s-\lambda_1} + \frac{[R_k^*]}{s-\lambda_2^*} \right) + [E(s)] + \frac{[F(s)]}{s^2} \right|^2 \end{aligned} \tag{1.16}$$

where the residue matrix $[R_k] = \{c\phi_j\}\{\phi_j^T b\}$ is given by the product of a column observability $\{c\phi_j\}$ and row controllability $\{\phi_j^T b\}$. The residue matrix $[R_k]$ is often expressed as $[A_j] = \{\phi_j\}\{L_j\}$ in the structural dynamics community, where $[A_j]$ is commonly called *modal participation factor*, $\{\phi_j\}$ is the modeshape and $\{L_j\}$ is the controllability [126]. Assuming

[11] The residue matrix is formed by an outer product of the mode shape multiply by itself and a scale constant A_k, $[R_k] = A_k\{u_k\}\{u_k\}^T$. *Estimation of the residues for a specific response means calculating the amplitude and phase of the roots estimated. All parameters are included in the calculation of residues* [178].

that the complex poles come in conjugate pairs and the residue matrices too, the normal mode residue with symmetric pole structure can be defined as a rational fraction expression (to determine the damping ratios that are different for each pole using the normal mode model format proposed by Balmès in [106]) of the form:

$$H(s) = \sum_{j=1}^{N} \frac{\{[c]\phi_j\}\{\phi_j^T[b]\}}{s^2 + 2\zeta_j\omega_j s + \omega_j^2} = \sum_{j=1}^{N} \frac{[T_j]}{s^2 + 2\zeta_j\omega_j s + \omega_j^2} \tag{1.17}$$

where the contribution of each mode is characterized by the pole frequency ω_j, damping ratio ζ_j, and the residue matrix $[T_j]$. The matrix $[T_j]$ is equal to the product of the normal mode output shape matrix $\{[c]\phi_j\}$ by the normal mode input shape matrix $\{\phi_j^T[b]\}$. The matrix $[b]$ is called the input shape matrix and the matrix $[c]$ is called the output shape matrix. The use of normal modes[12] defined by the spectral decomposition of elastic structures is fundamental in modal analysis. The representation of models using the normal mode format is established using several assumptions[13], illustrated in Eq. (1.18) in modal coordinates $\{p(s)\} = [\phi]^{-1}\{q(s)\}$

$$\begin{aligned} \left[[I]s^2 + [\Gamma]s + [\Omega^2]\right]\{p(s)\} &= \{\phi_j^T[b]\}\{u(s)\} \\ \{y(s)\} &= \{[c]\phi_j\}\{p(s)\} \end{aligned} \tag{1.18}$$

where the mass matrix $[M]$ is a unity matrix $[I]$, the modal damping $[\Gamma]$ is non-diagonal and the modal stiffness matrix and $[\Omega^2]$ (normal mode frequency squared) is diagonal, (s) is the Laplace variable, $\{u(s)\}$ are the inputs describing the time/frequency dependence, $\{y(s)\}$ is the physical outputs, $\{[c]\phi_j\}$ is the modal output shape matrix, and $\{\phi_j^T[b]\}$ the modal input shape matrix [180], [181]. For lightly damped structures, imposing diagonal modal damping assumption, may simplify the identification [106]. Most accurate viscous damping models are obtained with a full damping matrix $[\Gamma]$. If $[\Gamma]$ is assumed diagonal for a modally damped model, the normal mode model can be rewritten in the RFP form and it is sufficient to represent dissipation effects at the system level. Traditionally, the modal damping was associated to the *proportional damping model* introduced by Lord Rayleigh. This association assumed the usefulness of a

[12] The associated modes are called complex modes by opposition to normal modes which are associated with elastic models of structures and are always real value [106].

[13] It is assumed that there is a viscously damped model of the form described by second order models, see Eq. (3.2), where the normal modes are defined as solutions of the associated undamped eigenvalue problem verifying two orthogonality conditions [106][152].

global damped model with a *dynamic stiffness* of the form

$$[Z(s)] = \left[[M](s)^2 + (\alpha[M] + \beta[K])(s) + [K]\right] \tag{1.19}$$

This leads to a modally damped normal mode model where the mass α and stiffness β coefficients are adjusted to represent physical damping mechanisms over narrow frequency bands [106]. The modal damping matrix proposed by Balmes is defined as

$$\Gamma = \begin{bmatrix} \ddots & & \\ & \alpha + \beta\omega_j^2 & \\ & & \ddots \end{bmatrix} \tag{1.20}$$

which leads to damping ratios

$$2\zeta_j = \frac{\alpha}{\omega_j} + \beta\omega_j \tag{1.21}$$

where, mass coefficient α leads to high damping ratios in the low frequency range and stiffness coefficients β leads to a damping ratio linearly increasing with the frequency. Normally the non-zero tems of the matrix $[\Gamma]$ are expressed in terms of damping ratios $[\Gamma] = 2\zeta_j\omega_j$. Thus, the proportional model using damping ratio is defined as a scalar uniform damping ratio for each of the pole frequencies ω_j [106].

1.2 Fundamentals of numerical simulation of CFRP using finite element method (FEM)

The increasing use of anisotropic materials and multilayer CFRP components with a large ratio between bending and shear rigidities has encouraged many researchers and developers to adopt and implement the numerical simulations using FEM for the development of powerful MNET routines. There are hundreds of papers and theses documenting different numerical simulation approaches based on the plane state of stresses, accuracy, computational cost and simplicity using the FEM. The FEM is a commonly used technique in the analysis of CFRP, particularly useful to compute the dynamic behaviour. Most of CFRP are typically stacking of several thin layers and experience a plane state of stresses. It is well known that the stacking of several orthotropic layers in CFRP leads to inhomogeneous stiffness properties through thickness [98].

The fundamentals of the numerical simulation of CFRP used in this work are presented in this section and it is divided in three parts: the theory of linear elasticity, the first-order shear deformation laminated plate theory (FSDT) and the fundamentals of the FEM.

1.2.1 Governing equations of linear elasticity

The main objetive of the theory of elasticity is to find the unknown deformation field and the corresponding strains and stresses [83]. The deformation problem can be described using a solid body applying kinematic equations and static boundary conditions, (see Fig. 1.8). It is

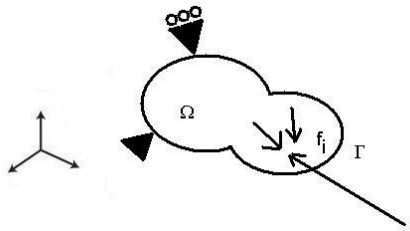

Fig. 1.8 Solid body, kinematic and static boundary conditions(improve Fig).

assumed that the relation between strains and stresses is linear and the displacements are small. Thus, the governing equations of the linear elasticity are described using the constitutive laws, the equilibrium and kinematic equations. Traditionally, the equlibrium equation is expressed in Cartesian coordinates and formulated with the second Newton's law on an infinitesimal volume in the three dimensions, x_1, x_2, x_3, (see Fig. 1.9). The equilibrium equations can be written

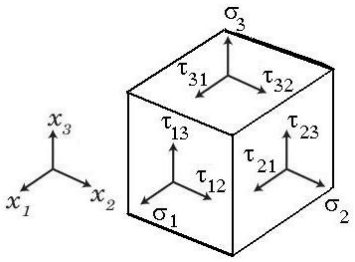

Fig. 1.9 Stress components on an infinitesimal volume element.

using a tensor notation $i, j = 1,2,3$ in the reference system as

$$\sigma_{ij} + f_i = \rho \ddot{u}_i \tag{1.22}$$

Where σ_{ij},f_i, ρ and $\ddot{u}_i$ denotes the Cauchy stress tensor, body forces, the material density and the displacements respectively (the dots denote the time derivative traditionally expressed as acceleration). The kinematic equations relate the displacements with the strains, see Eqs. (1.23) and (1.24). The strains ε_{kl} can be expressed as a function of the displacements $k,l = 1,2,3$ as.

$$\varepsilon_{kl} = \frac{1}{2}(u_{k,l} + u_{l,k}) \tag{1.23}$$

The stress-strain relation of a material is given by the generalised Hooke's law (when a linear elastic behaviour is assumed) and it can be expressed with a 4^{th}-order tensor $C_{i,j,k,l}$ described by 81 coefficients

$$\sigma_{ij} = C_{i,j,k,l}\varepsilon_{kl} \text{ where } i,j,k,l = 1,2,3 \tag{1.24}$$

where $\{\sigma\}$ and $\{\varepsilon\}$ are the the stress and strain vector components respectively. The equilibrium and the kinematic equations as well as the constitutive law can be integrated into the equation of motion in order to solve it for the unknown displacements u_i

$$\frac{1}{2}C_{ijkl}(u_{k,l} + u_{l,k}) + f_i = \rho\ddot{u}_i \tag{1.25}$$

Considering a static problem, the time dependent term $\rho\ddot{u}_i$ is equal to zero. The governing equations can be expressed into matrix notation where the stresses σ, strains ε and displacements u can be formulated as arrays and the Hooke's law as a stiffness matrix $[C]$, see Eq. (1.26). The general expression in matrix notation within the framework of the linear elasticity of an anisotropic material which has no planes of symmetry is given by Eq. (1.26)

$$\begin{Bmatrix} \sigma_1 \\ \sigma_2 \\ \sigma_3 \\ \tau_{23} \\ \tau_{31} \\ \tau_{12} \end{Bmatrix} = \begin{bmatrix} C_{11} & C_{12} & C_{13} & C_{14} & C_{15} & C_{16} \\ C_{12} & C_{22} & C_{23} & C_{24} & C_{25} & C_{26} \\ C_{13} & C_{23} & C_{33} & C_{34} & C_{35} & C_{36} \\ C_{14} & C_{24} & C_{34} & C_{44} & C_{45} & C_{46} \\ C_{15} & C_{25} & C_{35} & C_{45} & C_{55} & C_{56} \\ C_{16} & C_{26} & C_{36} & C_{46} & C_{56} & C_{66} \end{bmatrix} \begin{Bmatrix} \varepsilon_1 \\ \varepsilon_2 \\ \varepsilon_3 \\ \gamma_{23} \\ \gamma_{31} \\ \gamma_{12} \end{Bmatrix}. \tag{1.26}$$

If any material symmetry exists, the number of independent properties decreases. This is done taking advantage of the stress tensor symmetry, the strain tensor symmetry and the deformation energy U [83]. These symmetry assumptions reduce the original 81 coefficients of the Hooke's law to 21 and is the most general framework of the linear elasticity. Thus, the stresses, strains

Table 1.1 Indexing of tensors and matrix formulations

Stresses		Strains	
matrix	tensor	matrix	tensor
σ_1	σ_{11}	ε_1	ε_{11}
σ_2	σ_{22}	ε_2	ε_{22}
σ_3	σ_{33}	ε_3	ε_{33}
σ_4	τ_{23}	ε_4	$\gamma_{23} = 2\varepsilon_{23}$
σ_5	τ_{13}	ε_5	$\gamma_{13} = 2\varepsilon_{13}$
σ_6	τ_{12}	ε_5	$\gamma_{12} = 2\varepsilon_{12}$

and the $[C]$ arrays in Eq. (1.26) can be expressed using the Hooke's law $\{\sigma_i\} = [C]\{\varepsilon_i\}$, where $\{\sigma_i\}$ $\{\varepsilon_i\}$ are the normal stress and strain components in the i-direction while $\{\tau_{ij}\}$ and $\{\gamma_{ij}\}$ are the shear stress and shear strain in the ij-plane.

$$C_{ortho} = \begin{bmatrix} C_{11} & C_{12} & C_{13} & 0 & 0 & 0 \\ C_{12} & C_{22} & C_{23} & 0 & 0 & 0 \\ C_{13} & C_{23} & C_{33} & 0 & 0 & 0 \\ 0 & 0 & 0 & C_{44} & 0 & 0 \\ 0 & 0 & 0 & 0 & C_{55} & 0 \\ 0 & 0 & 0 & 0 & 0 & C_{66} \end{bmatrix} \tag{1.27}$$

The material constants in an orthotropic material are reduced to nine coefficients. The constitute matrix of an orthotropic material notes that there is not a coupling between the shear and normal components within the principal coordinates, see Eq. (1.27). The existence of two orthogonal symmetry planes in a orthotropic material automatically implies the presence of a third symmetry plane, orthogonal to the first two. A special orthotropic material with three orthogonal symmetry planes is called orthotropic elasticity in plane stress [83], see ABAQUS v13 analysis user guide section 22.2.1. It is important to mention that the relationship between the indexing of the tensor and the matrix formulation is different. Considering the symmetry of material properties using the Hooke's law, the tensor shear strains have to be multiplied with a factor of two in order to fulfill the equivalence of more common engineering shear strains $\{\gamma_{ij}\}$. This relationship is given in Table 1.1.

Moreover, the displacement vector $\{u\} = \{u, v, w\}^T$ contains the entries of the displacement $\{u_i\}$ in the Cartesian coordinate directions (x_1, x_2, x_3). These coordinates can alternatively be

expressed with (x, y, z). The kinematic equations can be expressed in a matrix notation defining a differential matrix operator L. This differential operator L is used to map the displacements $\{u\}$ on the strains $\{\varepsilon\}$ with a simple matrix multiplication $\{\varepsilon\} = [L]\{u\}$. The matrix notations of this multiplication are expressed in Eq. (1.28).

$$\begin{Bmatrix} \varepsilon_1 \\ \varepsilon_2 \\ \varepsilon_3 \\ \gamma_{23} \\ \gamma_{31} \\ \gamma_{12} \end{Bmatrix} = \begin{bmatrix} \frac{\partial}{\partial x} & 0 & 0 \\ 0 & \frac{\partial}{\partial y} & 0 \\ 0 & 0 & \frac{\partial}{\partial z} \\ 0 & \frac{\partial}{\partial z} & \frac{\partial}{\partial y} \\ \frac{\partial}{\partial z} & 0 & \frac{\partial}{\partial x} \\ \frac{\partial}{\partial y} & \frac{\partial}{\partial x} & 0 \end{bmatrix} \begin{Bmatrix} u \\ v \\ w \end{Bmatrix} = [L]\{u\} \tag{1.28}$$

where $\{u\}$, $\{v\}$, and $\{w\}$ contain the entries for the displacement components expressed in the coordinate directions (x, y), and (z), respectively. The differential operator $[L]$ can be also used in the equilibrium Eq. (1.22)

$$[L]^T \sigma + f_i = \rho \ddot{u}_i \tag{1.29}$$

The combination of the equilibrium Eq. (1.29), the kinematic Eq. (1.28) and the constitutive law Eq. (1.26) for the static problem leads to a simplified partial differential equation for the unknown displacements $\{u\}$

$$[L]^T [C][L]\{u\} + f_i = 0 \tag{1.30}$$

The aim of the linear elasticity is to find the displacement solution $\{u\}$ of the static problem considering stress and displacement boundary conditions. For simple geometries, a displacement solution $\{u\}$ can be found analytically. However, in general, non closed-form solutions using the FEM are available for problems with complex domain geometries and inhomogeneous material distributions. The evaluation of complex domain geometries using the FEM is straightforward using the theory of thin plates relating the force, moments and shear resultants to the strain of a laminate through a lamina-wise thickness integration.

1.2.2 First-order shear deformation laminated plate theory (FSDT)

In the classical laminated shell theory, which forms the simplest ESL approach, problems are based on the *Kirchhoff hypothesis*, which amounts to neglecting both transverse shear deformation and transverse normal effects. In the first-order shear deformation laminated plate

theory (FSDT), the *Kirchhoff hypothesis* is relaxed considering that the transverse normals do not remain perpendicular to the midsurface after the deformation [83]. The FSDT thin plate theory is needed in this work to evaluate the correlation accuracy of modal experimental measurements and the advantageous effect of curvature utilized in a composite shell structure since the longitudinal elastic modulus is much higher than the shear and the transversal moduli, hence the use of a shear deformation laminate theory is recommended. To quantify a stress state distribution of the laminate, the components have to be evaluated layer by layer, assuming that each layer is orthotropic with respect to its material symmetry lines and obeys Hooke's law. The stiffness homogenization using the FSDT follow precisely the assumption of Reissner-Mindlin [60]-[62] and Kirchhoff-Love plate theories [86], based on:

1. The laminate is assumed to be thin compared to the other dimensions and its thickness is constant.

2. The transverse normals do not experience elongation.

3. A plane stress state is assumed $\{\sigma_3\} = 0$.

4. Rotation of the transverse normals of the undeformed middle plane remains straight but not necessarily orthogonal to the middle plane after deformation.

5. The single layers are linear elastic and bonded perfectly.

6. Deformations are small.

The 1, 2, 5 and 6 assumptions allow the displacement field to be defined over the whole plate. Assumtions 3 and 4 affect the stress-strain relationship. The rotation of the normal in each of the two vertical planes xz and yz is obtained as the sum of two terms: 1) the adequate slope of the plate middle plane, and 2) an additional rotation ϕ (introduced in the next sections) resulting from the lack of orthogonality of the normal with the middle plane after deformation. This is a substantial difference between Reissner–Mindlin and Kirchhoff plate theories [99].

1.2.3 Plane-stress state and stiffness transformation

The stiffness matrix of an orthotropic layer is defined with the expression Eq. (1.27). This stiffness matrix $[C_{ij}]$ of an orthotropic material can be also written in terms of compliances

relating strains and stresses as function of the engineering constants defined by

$$\left\{\begin{array}{c}\varepsilon_1\\ \varepsilon_2\\ \varepsilon_3\\ \gamma_{23}\\ \gamma_{31}\\ \gamma_{12}\end{array}\right\} = \left[\begin{array}{cccccc} S_{11} & S_{12} & S_{13} & 0 & 0 & 0\\ S_{12} & S_{22} & S_{23} & 0 & 0 & 0\\ S_{13} & S_{23} & S_{33} & 0 & 0 & 0\\ 0 & 0 & 0 & S_{44} & 0 & 0\\ 0 & 0 & 0 & 0 & S_{55} & 0\\ 0 & 0 & 0 & 0 & 0 & S_{66}\end{array}\right] \left\{\begin{array}{c}\sigma_1\\ \sigma_2\\ \sigma_3\\ \tau_{23}\\ \tau_{31}\\ \tau_{12}\end{array}\right\} \tag{1.31}$$

where $[S_{ij}]$ are the material compliance parameters $[C_{ij}] = [S_{ij}]^{-1}$ given in terms of the engineering constants as

$$\begin{array}{c} S_{11} = \dfrac{1}{E_1},\ S_{12} = -\dfrac{\nu_{12}}{E_1},\ S_{13} = -\dfrac{\nu_{31}}{E_1}\\ S_{22} = \dfrac{1}{E_2},\ S_{23} = -\dfrac{\nu_{23}}{E_2},\ S_{33} = \dfrac{1}{E_3}\\ S_{44} = \dfrac{1}{G_{23}},\ S_{55} = \dfrac{1}{G_{31}}\ S_{66} = \dfrac{1}{G_{12}}\end{array} \tag{1.32}$$

The measured engineering constants can be directly used in Eq. (1.31) as function of nine engineering independent constants such as the Young's modulus, Poisson's ratio and the shear modulus. Assumming a plane where the material properties are the equal in all directions, the number of coefficients can be reduced to five (transversely isotropic case) introducing the plane stress state assumption $\{\sigma_3\} = 0$. It is possible to reduce the $[S]$ matrix of an orthotropic material with orthotropic axis (x, y, z) satisfying the condition of plane anisotropy in a relationship between the non–zero stresses and strains into a 3×3 an 2×2 matrices. Thus the stiffness matrix $[C_{ij}]$ can be reduced to the so-called reduced matrix $[Q_{ij}]^{(k)}$ as:

$$\left\{\begin{array}{c}\sigma_1\\ \sigma_2\\ \tau_{12}\end{array}\right\}^{(k)} = \left[\begin{array}{ccc} Q_{11} & Q_{12} & 0\\ Q_{21} & Q_{22} & 0\\ 0 & 0 & Q_{66}\end{array}\right]^{(k)} \left\{\begin{array}{c}\varepsilon_1\\ \varepsilon_2\\ \gamma_{12}\end{array}\right\}^{(k)} = [Q_b]^{(k)} \left\{\begin{array}{c}\varepsilon_1\\ \varepsilon_2\\ \gamma_{12}\end{array}\right\}^{(k)} \tag{1.33}$$

and another for the transverse shear stresses (off-plane).

$$\left\{\begin{array}{c}\tau_{23}\\ \tau_{31}\end{array}\right\}^{(k)} = \left[\begin{array}{cc} Q_{44} & 0\\ 0 & Q_{55}\end{array}\right]^{(k)} \left\{\begin{array}{c}\gamma_{23}\\ \gamma_{31}\end{array}\right\}^{(k)} = [Q_s]^{(k)} \left\{\begin{array}{c}\gamma_{23}\\ \gamma_{31}\end{array}\right\}^{(k)} \tag{1.34}$$

where $[Q_{ij}]^{(k)}$ is called the plane stress-reduced stiffness and it is related to the engineering constanst as follows.

$$Q_{11}^{(k)} = \frac{E_1^{(k)}}{1-\nu_{12}^{(k)}\nu_{21}^{(k)}},\ Q_{12}^{(k)} = \frac{\nu_{12}^{(k)}E_2^{(k)}}{1-\nu_{12}^{(k)}\nu_{21}^{(k)}},\ Q_{22}^{(k)} = \frac{E_2^{(k)}}{1-\nu_{12}^{(k)}\nu_{21}^{(k)}} \qquad (1.35)$$
$$Q_{44}^{(k)} = G_{23},\ Q_{55}^{(k)} = G_{31}^{(k)},\ Q_{66}^{(k)} = G_{12}^{(k)}$$

Note that the CFRP, see Fig. 4, is a stack-up made of several plain wave layers[14], see Figs. 1.13, with their material axes oriented arbitrarily with respect to the laminate coordinates, the constitutive equations of each layer must be transformed to the laminate coordinates (x, y, z) [83]. A relation that transforms the stresses and strains from the material coordinate system to the global coordinate system is needed. This is achieved by applying a rotation matrices $[T_b]$ for the in-plane components (bending) and a rotation matrix $[T_s]$ for the off-plane (transverse shear) , see Eq. (1.36). Fig. 1.10 illustrates the laminate transformation of the coordinates (1, 2) to

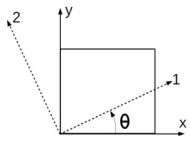

Fig. 1.10 Material principal and global coordinate system [31].

the global coordinates (x, y) by a given angle θ. Note that the reduced stiffnesses involve six independent engineering constants E_1, E_2, ν_{12}, G_{12}, G_{23}, G_{13} [76], [84], [104].

$$[T_b] = \begin{bmatrix} \cos^2\theta & \sin^2\theta & 2\sin\theta\cos\theta \\ \sin^2\theta & \cos^2\theta & -2\sin\theta\cos\theta \\ -\sin\theta\cos\theta & \sin\theta\cos\theta & \cos^2\theta-\sin^2\theta \end{bmatrix}, [T_s] = \begin{bmatrix} \cos\theta & -\sin\theta \\ \sin\theta & \cos\theta \end{bmatrix} \qquad (1.36)$$

The materials stresses and strains are mapped directly using the matrices $[T_i]$ for the in- and off-plane respectively, illustrated in Eq. (1.37)

$$\begin{Bmatrix} \sigma_1 \\ \sigma_2 \\ \tau_{12} \end{Bmatrix}^{(k)} = [T_b] \begin{Bmatrix} \sigma_x \\ \sigma_y \\ \tau_{xy} \end{Bmatrix}^{(k)}, \begin{Bmatrix} \tau_{23} \\ \tau_{13} \end{Bmatrix}^{(k)} = [T_s] \begin{Bmatrix} \tau_{yz} \\ \tau_{xz} \end{Bmatrix}^{(k)} \qquad (1.37)$$

[14] Stack-up of layers is modeled and evaluated in this work based the CLT and FSDT by assigning a composite (e.g. PCOMP) and orthotropic material , (e.g. MAT8-NASTRAN) properties to it, see Appendixes D, E and F.

According the Table 1.1, the enginnering shear strains $\{\gamma_{ij}\}$ are 2 times the tensorial shear strains, where results the following relation

$$\left\{ \begin{array}{c} \varepsilon_1 \\ \varepsilon_2 \\ \frac{1}{2}\gamma_{12} \end{array} \right\}^{(k)} = [T_b] \left\{ \begin{array}{c} \varepsilon_x \\ \varepsilon_y \\ \frac{1}{2}\gamma_{xy} \end{array} \right\}^{(k)} , \left\{ \begin{array}{c} \frac{1}{2}\gamma_{23} \\ \frac{1}{2}\gamma_{13} \end{array} \right\}^{(k)} = [T_s] \left\{ \begin{array}{c} \frac{1}{2}\gamma_{yz} \\ \frac{1}{2}\gamma_{xz} \end{array} \right\}^{(k)} \tag{1.38}$$

In order to work directly with the engineering strains without a pre-factor, Reuter [82] introduced a simple matrix, that reduces to a minimum the potential of mistakes. The Reuter matrix can be divided into two parts (in- and off-planes), introducing the stress plane assumption $\{\sigma_3\} = 0$, the engineering strains can be transformed using the Reuter matrix, see Eq. (1.39)

$$R_b = \left[\begin{array}{ccc} 1 & 0 & 0 \\ 0 & 1 & 0 \\ 0 & 0 & 2 \end{array} \right] \text{ in-plane }, R_s = \left[\begin{array}{cc} 2 & 0 \\ 0 & 2 \end{array} \right] \text{ off-plane.} \tag{1.39}$$

The in-plane part can be expressed as

$$\left\{ \begin{array}{c} \varepsilon_x \\ \varepsilon_y \\ \gamma_{xy} \end{array} \right\}^{(k)} = [R_b]^{-1} [T_b] [R_b] \left\{ \begin{array}{c} \varepsilon_1 \\ \varepsilon_2 \\ \gamma_{12} \end{array} \right\}^{(k)} . \tag{1.40}$$

A similar assumption can be done for using the off-plane part of the Reuter matrix, the engineering strains can be transformed, illustrated in Eq. (1.41).

$$\left\{ \begin{array}{c} \gamma_{yz} \\ \gamma_{xz} \end{array} \right\}^{(k)} = [R_s]^{-1} [T_s] [R_s] \left\{ \begin{array}{c} \gamma_{23} \\ \gamma_{13} \end{array} \right\}^{(k)} \tag{1.41}$$

The global stresses and strains can be mapped to the material principal stresses and strains performing a multiplication with the inverse rotation of matrix $[T_b]^{-1}$ and $[T_s]^{-1}$. The inverse of these matrices must be used if it is desired to transform from $(1-2)$ coordinate system to the $(x-y)$ coordinate system. The conection between the strains and stresses in global coordinates is defined on the new matrix called the lamina stiffness (sometimes called reduced stiffness

matrix $[\bar{Q}_{ij}]$. The $[\bar{Q}_{ij}]$ matrix is therefore a function of $[Q_i]$, $[R_i]$ and $[T_i]$

$$\left\{ \begin{array}{c} \sigma_x \\ \sigma_y \\ \tau_{xy} \end{array} \right\}^{(k)} = \left[\begin{array}{ccc} \bar{Q}_{11} & \bar{Q}_{12} & 0 \\ \bar{Q}_{21} & \bar{Q}_{22} & 0 \\ 0 & 0 & \bar{Q}_{66} \end{array} \right]^{(k)} \left\{ \begin{array}{c} \varepsilon_x \\ \varepsilon_y \\ \gamma_{xy} \end{array} \right\}^{(k)} = \left[\bar{Q}_b\right] \left\{ \begin{array}{c} \varepsilon_x \\ \varepsilon_y \\ \gamma_{xy} \end{array} \right\}^{(k)} \tag{1.42}$$

$$\left\{ \begin{array}{c} \tau_{yz} \\ \tau_{xz} \end{array} \right\}^{(k)} = \left[\begin{array}{cc} \bar{Q}_{44} & 0 \\ 0 & \bar{Q}_{55} \end{array} \right]^{(k)} \left\{ \begin{array}{c} \gamma_{yz} \\ \gamma_{xz} \end{array} \right\}^{(k)} = \left[\bar{Q}_s\right] \left\{ \begin{array}{c} \gamma_{yz} \\ \gamma_{xz} \end{array} \right\}^{(k)} \tag{1.43}$$

The transformed $[\bar{Q}_{ij}]$ can be derived using the equations (1.33), (1.38) and (1.40)

$$\bar{Q}_{11} = Q_{11}\cos^4\ \theta + 2(Q_{12}+2Q_{66})\sin^2\theta\ \cos^2\theta + Q_{22}\sin^4\theta \tag{1.44}$$

$$\bar{Q}_{12} = (Q_{11}+Q_{22}-4Q_{66})\sin^2\ \theta\cos^2\theta + Q_{12}(\sin^4\ \theta+\cos^4\ \theta) \tag{1.45}$$

$$\bar{Q}_{22} = Q_{11}\sin^4\ \theta + 2(Q_{12}+4Q_{66})\ \sin^2\theta\cos^2\ \theta + Q_{22}\cos^4\ \theta \tag{1.46}$$

$$\bar{Q}_{66} = (Q_{11}+Q_{22}-2Q_{66})\sin^2\ \theta\ \cos^2\ \theta + Q_{66}(\sin^4\ \theta+\cos^4\ \theta) \tag{1.47}$$

$$\bar{Q}_{44} = Q_{44}\cos^2\ \theta + Q_{55}\sin^2\ \theta \tag{1.48}$$

$$\bar{Q}_{55} = Q_{55}\cos^2\ \theta + Q_{44}\ \sin^2\ \theta \tag{1.49}$$

The reduced stiffness matrix $[\bar{Q}_{ij}]$ has to be evaluated for every laminate layer in order to homogenize the material data of the entire staking of the CFRP.

1.2.4 Stiffness homogenization

The displacement field of the FSDT theory is of the form

$$\begin{aligned} u(x,y,z) &= u_0(x,y) + z\phi_x(x,y) \\ v(x,y,z) &= v_0(x,y) + z\phi_y(x,y) \\ w(x,y,z) &= w_0(x,y) \end{aligned} \tag{1.50}$$

where u_0, v_0 and w_0 denotes the displacements of the middle plane and the transverse displacement, $\phi_x = -\frac{\partial w_0}{\partial x}$ and $\phi_y = -\frac{\partial w_0}{\partial y}$ are the rotations of the normal to the undeformed middle surface, (see Fig. 1.11). The strain vector is obtained from the expressions of 3D elasticity theory assuming the plane stress assumption $\{\sigma_3\} = 0$. Using the kinematic relation Eq. (1.23),

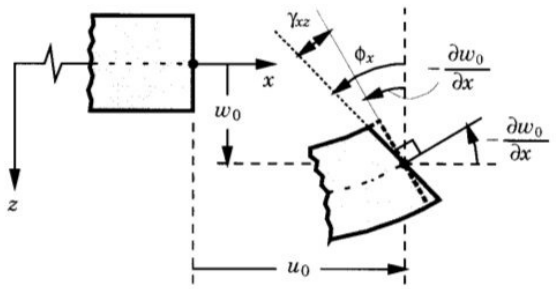

Fig. 1.11 Undeformed and deformed kinematics of a FSDT [83].

the strain expressions of 3D elasticity derives into

$$\left\{\begin{array}{c}\varepsilon_x\\ \varepsilon_y\\ \gamma_{xy}\\ --\\ \gamma_{yz}\\ \gamma_{xz}\end{array}\right\}=\left\{\begin{array}{c}\frac{\partial u_0}{\partial x}+\frac{1}{2}\left(\frac{\partial w_o}{\partial x}\right)^2\\ \frac{\partial v_0}{\partial y}+\frac{1}{2}\left(\frac{\partial w_o}{\partial y}\right)^2\\ \frac{\partial u_0}{\partial y}+\frac{\partial v}{\partial x}+\frac{\partial w_0}{\partial x}\frac{\partial w_0}{\partial y}\\ ---------\\ \frac{\partial w_0}{\partial y}+\phi_y\\ \frac{\partial w_0}{\partial x}+\phi_x\end{array}\right\}+z\left\{\begin{array}{c}\frac{\partial \phi_x}{\partial x}\\ \frac{\partial \phi_y}{\partial y}\\ \frac{\partial \phi_x}{\partial y}+\frac{\partial \phi_y}{\partial x}\\ ----\\ 0\\ 0\end{array}\right\}=\left\{\begin{array}{c}\varepsilon^0\\ --\\ \gamma^0\end{array}\right\}+z\left\{\begin{array}{c}\kappa\\ --\\ \gamma^1\end{array}\right\} \tag{1.51}$$

where

$$\varepsilon^0=\left\{\begin{array}{c}\varepsilon_x^0\\ \varepsilon_y^0\\ \gamma_{xy}^0\end{array}\right\},\kappa=\left\{\begin{array}{c}\kappa_x\\ \kappa_y\\ \kappa_{xy}\end{array}\right\},\text{ and }\gamma^0=\left\{\begin{array}{c}\gamma_{yz}\\ \gamma_{xz}\end{array}\right\} \tag{1.52}$$

$\{\varepsilon^0\},\{\kappa\}$ and $\{\gamma^0\},\{\gamma^1\}$ are the generalised (resultant) strain vectors due to membrane, bending or curvature and transverse shear deformation effects, respectively. Note that the strains $\{\varepsilon_x\},\{\varepsilon_y\},\{\gamma_{xy}\}$ are linear through the laminate thickness while the transverse shear strains $\{\gamma_{yz}\},\{\gamma_{xz}\}$ are constant through the thickness of the laminate in the FSDT. It is well known that the stiffness distribution thought the thickness (layer-wise configuration) is discontinuous, which results in a discontinuous stress distribution [83]. For that reason, the components needed to be evaluated for each layer to quantify a stress state in the laminate. The quantification is performed with a line load units that includes all layers classified in three groups: the force per unit length $\{N_i\}$ that integrates the stress components over the thickness, the moment per unit length $\{M_i\}$ that integrates the stress components multiplied by the stacking position z and the transverse shear stresses $\{S_{ij}\}$ over the thickness, (see Fig. 1.12).

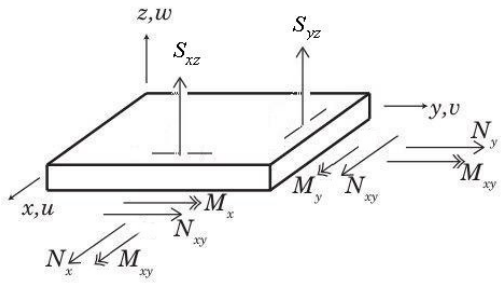

Fig. 1.12 Loads of a FSDT.

$$\begin{Bmatrix} N_x \\ N_y \\ N_{xy} \end{Bmatrix} = \int_{-\frac{h}{2}}^{\frac{h}{2}} \begin{Bmatrix} \sigma_x \\ \sigma_y \\ \gamma_{xy} \end{Bmatrix} dz = \sum_{K=1}^{N} [\bar{Q}_{ij}]^{(k)} \int_{z_k}^{z_{k+1}} (\varepsilon_0 + z\kappa) dz \tag{1.53}$$

$$\begin{Bmatrix} M_x \\ M_y \\ M_{xy} \end{Bmatrix} = \int_{-\frac{h}{2}}^{\frac{h}{2}} \begin{Bmatrix} \sigma_x \\ \sigma_y \\ \gamma_{xy} \end{Bmatrix} z\, dz = \sum_{K=1}^{N} [\bar{Q}_{ij}]^{(k)} \int_{z_k}^{z_{k+1}} (\varepsilon_0 + z\kappa) z dz \tag{1.54}$$

$$\begin{Bmatrix} S_{yz} \\ S_{xz} \end{Bmatrix} = \int_{-\frac{h}{2}}^{\frac{h}{2}} \begin{Bmatrix} \gamma_{yz} \\ \gamma_{xz} \end{Bmatrix} dz = K \sum_{K=1}^{N} [\bar{Q}_{ij}]^{(k)} \int_{z_k}^{z_{k+1}} (\gamma^0) dz \tag{1.55}$$

Due to the stiffness it is constant along the laminate, (see Fig.1.13), the integration can be

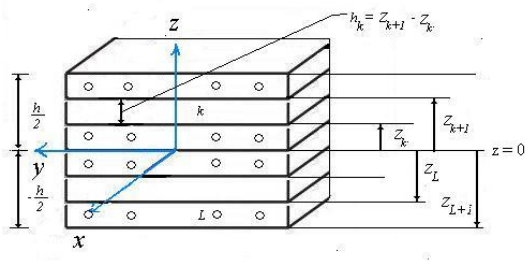

Fig. 1.13 General layup of a laminated composite material.

replaced with a summation of the integrals of each layer using the transform reduced matrix $[\bar{Q}_{ij}]$. Taking advantage of the transformed reduced stiffness matrix $[\bar{Q}_{ij}]$, the forces and the moments per unit length can be expressed as a function of the membrane strains $\{\varepsilon_0\}$, curvatures $\{\kappa\}$ and transverse strains $\{\gamma^0\}$. Matrices $[A_{ij}], [B_{ij}], [D_{ij}]$ and $[\bar{S}_{ij}]$ can be obtained. The $[A_{ij}]$ matrix connects the membrane strains $\{\varepsilon_0\}$ with the force per unit length $\{N_i\}$ and it is called

extensional stiffness, the $[D_{ij}]$ matrix connects the plate curvature $\{\kappa\}$ with the moments per unit length $\{M_i\}$ and it is called the bending stiffness, the $[B_{ij}]$ matrix couple the membrane and bending component and it is called the bending extensional coupling stiffness, describing a coupling between bending and extensional stiffness. Finally the $[\bar{S}_{ij}]$ matrix connects the transverse shear strains $\{\gamma^0\}$ over the thickness and K is the shear correction factor[15], usually taken as $\frac{5}{6}$.

$$\begin{aligned}
[A_{ij}] &= \sum_{K=1}^{N} [\bar{Q}_{ij}]^{(k)}(z_{k+1}-z_k), \quad i,j=1,2,6 \\
[B_{ij}] &= \frac{1}{2}\sum_{K=1}^{N} [\bar{Q}_{ij}]^{(k)}(z_{k+1}^2-z_k^2), \quad i,j=1,2,6 \\
[D_{ij}] &= \frac{1}{3}\sum_{K=1}^{N} [\bar{Q}_{ij}]^{(k)}(z_{k+1}^3-z_k^3), \quad i,j=1,2,6 \\
[\bar{S}_{ij}] &= K\sum_{K=1}^{N} [\bar{Q}_{ij}]^{(k)}(z_{k+1}-z_k), \quad i,j=4,5
\end{aligned} \tag{1.56}$$

In case of a symmetric laminate problem, there is no coupling between bending and membrane effects and the $[B_{ij}]$ matrix vanishes. These matrices are known as the $[ABD-\bar{S}]$ matrix and they are the main achievement of the homogenization process. Thus, the stress, moment and shear resultans can be written in matrix form as

$$\begin{Bmatrix} N_i \\ M_i \\ S_{ij} \end{Bmatrix} = \begin{bmatrix} A & B & 0 \\ B & D & 0 \\ 0 & 0 & \tilde{S} \end{bmatrix} \begin{Bmatrix} \varepsilon^0 \\ \kappa \\ \gamma^0 \end{Bmatrix} \tag{1.57}$$

where the reduced stiffness matrices $[\bar{Q}_{ij}]$ is represented in the $[ABD-\bar{S}]$ matrix and it is possible to map the global strains taking advantage of its inverse needed for the strengh analysis.

1.3 The finite element method (FEM)

A short overview of the FEM is given based on the textbook of Reddy [83]. The FEM is a numerical method for solving differential equations widely used to solve physical problems. Three key steps are needed using FEM applicable to any continuum mechanical problem:

[15] The use of the K factor tries to overcome the physical incorrect assumption of the FSDT, that the shear distribution across the the thickness is constant. In composite laminated beams and plates, the transverse shear stresses vary at least quadratically through the layer thickness [83].

idealization, discretization and solution (post-processing) , (see Fig. 1.14), introduced in the next subsections.

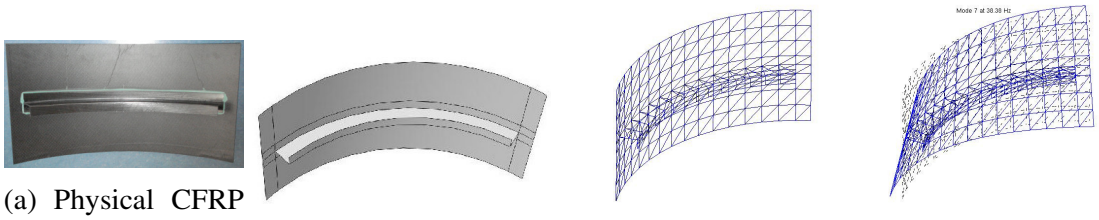

(a) Physical CFRP component (b) Idealization (c) Discrete model (d) Discrete solution

Fig. 1.14 Solving a physical problem with the finite element method.

1.3.1 Idealization

The idealization consists of transforming the physical model into a mathematical model. This "transformation" is done assuming a certain amount of simplifications in the mathematical model. The mathematical representation of the CFRP component will be contructed making assumptions such as:

1. Linear behaviour.
2. Orthotropically elastic material behaviour.
3. Homogeneous layers.
4. A perfect bounding of the layers.
5. The three components are considered coupled (no contacts) but divided in groups of elements to specified the geometric characteristics of the CFRP.

The mathematical model can be obtained by expressing the equilibrium using the principle of virtual displacements [83] based on the equation of motion of Lagrangian mechanics[16]. Applying this principle, for any small virtual displacement imposed to the body, the Lagrangian L is defined as:

$$L = T - \Pi = T - (U - W) \tag{1.58}$$

[16]The Lagrangian equation is defined as $\frac{d}{dt}\left(\frac{\partial L}{\partial \dot{x}}\right) - \frac{\partial L}{\partial x} = 0$, where L is the Lagrangian and x the generalised coordinates.

where T represents the kinetic energy and Π the potential energy. Hamilton's principle is used as a formalism to represent an elastic body with the equation[17]:

$$\delta \int_{h_1}^{h_2} [T - (U - W)]\, dt = \delta \int_{h_1}^{h_2} L dt = 0 \tag{1.59}$$

where the potential energy Π is the sum of the deformation energy U and the potential of the external forces W. The Lagrangian mechanics tranform the equation of motion to its weak form needed for the finite element formulation, see Eq. (1.59). It is a requirement of the linear elasticity problem that the displacements u are small. Thus, the kinetic energy can be formulated as the integral over the domain Ω of the density ρ and the scalar product of the velocities[18] $\dot{u}$.

$$T = \frac{1}{2} \int_{\Omega} \rho \dot{u}^T \dot{u} d\Omega \tag{1.60}$$

The domain integral of the scalar product of stresses σ and strains ε is defined as the deformation energy U.

$$U = \frac{1}{2} \int_{\Omega} \varepsilon^T \sigma d\Omega \tag{1.61}$$

Finally, the potential of the external forces W is the sum of the body forces f_i and the surface stresses $\hat{\sigma}$. The surface stresses need to be integrated over the surface Γ.

$$W = \int_{\Omega} f_i^T u d\Omega + \int_{\Gamma} \hat{\sigma}^T u d\Gamma \tag{1.62}$$

The Lagrangian L is calculated for the entire domain Ω.

1.3.2 Discretization

The domain must be discretized into smaller sub-domains Ω_e in order to get the FEM triangle formulation namely the finite elements, see [84], [76], [104]. The integrations are substituted with a summation of the integrals over the sub-domains Ω_e. Furthermore, it is needed to define local approximations functions $[N_e]$, called also shape functions. These functions map the finite element nodal displacements $\tilde{q}$ and represent the DOF of the continuous displacements u. The

[17] The calculus of variation shows that solving the Lagrange equations is equivalent to finding the solution of the Hamilton's principle.

[18] The velocities can be approximated with displacement time derivatives $\dot{u}$.

nodal velocities $\dot{\tilde{q}}$ and the accelerations $\ddot{\tilde{q}}$ can be obtained similarly.

$$u \approx [N_e]^T \tilde{q},\ \dot{u} \approx [N_e]^T \dot{\tilde{q}},\ \ddot{u} \approx [N_e]^T \ddot{\tilde{q}} \tag{1.63}$$

Using the kinematic Eq. (1.28), the strains ε can be expressed as a function for the nodal point displacements $\tilde{q}$.

$$\varepsilon = [L]\, u = [L]\, [N_e]^T \tilde{q} = [B]\, \tilde{q} \tag{1.64}$$

The strain-displacement matrix $[B]$ is built using the differential operator $[L]$ and the shape functions $[N_e]$. The discrete form of the total Lagrangian for the discretized system is expressed as

$$\begin{aligned} L = \sum_{n_{elem}} \frac{1}{2} \int_{\Omega_e} \rho \dot{\tilde{q}}^T [N_e]\, [N_e]^T \dot{\tilde{q}} d\Omega_e \Big] - \sum_{n_{elem}} \frac{1}{2} \int_{\Omega_e} \tilde{q}^T [B]^T [C][B] \tilde{q} d\Omega_e \Big] \\ + \sum_{n_{elem}} \int_{\Omega_e} f^T [N_e]^T \tilde{q} d\Omega_e \Big] + \sum_{n_{elem}} \int_{\Gamma_e} \sigma^T [N_e]^T \tilde{q} d\Gamma_e \Big] \end{aligned} \tag{1.65}$$

The evaluation of discrete form leads to the equation of motion, where the unknown nodal displacements $\tilde{q}$ are expressed as generalised coordinates.

$$\begin{aligned} \sum_{n_{elem}} \left[\int_{\Omega_e} \rho\, [N_e]\, [N_e]^T \ddot{\tilde{q}} d\Omega_e \right] + \sum_{n_{elem}} \left[\int_{\Omega_e} [B]^T [C][B] \tilde{q} d\Omega_e \right] \\ - \sum_{n_{elem}} \left[\int_{\Omega_e} f\, [N_e]\, d\Omega_e \right] - \sum_{n_{elem}} \left[\int_{\Gamma_e} \hat{\sigma}\, [N_e]\, d\Gamma_e \right] = 0 \end{aligned} \tag{1.66}$$

Rearranging the terms, the terms without dependence on the nodal displacements $\tilde{q}$ are moved to the right hand side

$$\begin{aligned} \sum_{n_{elem}} \left[\int_{\Omega_e} \rho\, [N_e]\, [N_e]^T d\Omega_e \right] \ddot{\tilde{q}} + \sum_{n_{elem}} \left[\int_{\Omega_e} [B]^T [C][B] d\Omega_e \right] \tilde{q} \\ = \sum_{n_{elem}} \left[\int_{\Omega_e} f\, [N_e]\, d\Omega_e \right] - \sum_{n_{elem}} \left[\int_{\Gamma_e} \hat{\sigma}\, [N_e]\, d\Gamma_e \right] \end{aligned} \tag{1.67}$$

The terms in the left side represent the global stiffness matrix $[K]$ and the global mass matrix $[M]$. The terms in the right side represent the load vector $\{r\}$. With these terms, the basic problem of the FEM for the linear elastic case can be written as

$$[M]\, \ddot{\tilde{q}} + [K]\, \tilde{q} = \{r\} \tag{1.68}$$

Assuming a static problem the accelerations $\ddot{\tilde{q}}$ vanish so

$$[K]\,\tilde{q} = \{r\} \tag{1.69}$$

The equation of motion (1.68) can be used for the determination of the harmonic eigenfrequencies of the structural system if it is assumed that the load vector $\{r\}$ is zero taking advantage of the harmonic solution approach.

1.3.3 Solution

Assuming that the load vector $\{r\}$ is zero, the equation can be transformed into an eigenvalue problem with the unknown eigenvalues λ and eigenvectors ϕ (λ is equal to the squared of the angular frequency ω and ϕ represents the modeshapes).

$$\begin{aligned} \tilde{q} &= \phi sin(\omega t) \\ \ddot{\tilde{q}} &= -\omega^2 \phi sin(\omega t) \end{aligned} \tag{1.70}$$

The combination of the equation of motion (1.69) and the harmonic approach (1.70) leads to the eigenvalue problem for the harmonic vibration (without damping).

$$\left([K] - \omega^2\,[M]\right)\phi = 0 \tag{1.71}$$

By defining a diagonal matrix that group all the eigenvalues and combine all the eigen vectors in one mode shape matrix is called normal modes analysis in FEM terminology. The normal modes are defined as solutions of associated undamped eigenvalue problem represented by Eq. (1.71). The normal modes are based on the inertial properties represented by the mass matrix $[M]$ and the elastic properties represented by the stiffness matrix $[K]$. In the above matrices, there are N independent eigenvectors ϕ forming a matrix noted as $[\phi]$ and eigenvalues ω^2 forming a diagonal matrix noted as $[\omega^2]$. The solution of the eigenvalue problem of Eq. (1.71), is a full set of N normal modes $[\phi]$ that verify two orthogonality conditions with respect to the mass and stiffness matrices

$$[\phi]^T\,[M]\,[\phi] = \begin{bmatrix} \ddots & & \\ & \mu & \\ & & \ddots \end{bmatrix} \text{ and } [\phi]^T\,[K]\,[\phi] = \begin{bmatrix} \ddots & & \\ & \mu\,\omega^2 & \\ & & \ddots \end{bmatrix}, \tag{1.72}$$

where $[\mu]$ is a diagonal matix of modal masses, and $[\phi]$ indicates the mode shapes associated with unity mass ($[\mu] = [I]$) [106]. In this work the normal mode shapes are assumed to be mass normalized.

1.4 Design of Experiments (DOE)

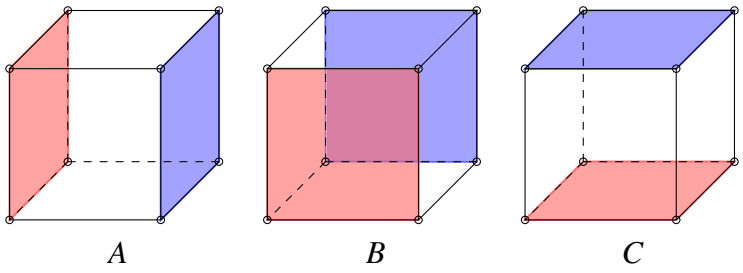

(a) Main effects

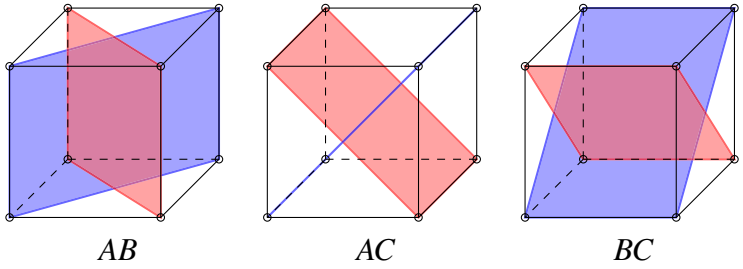

(b) Two-factor interactions

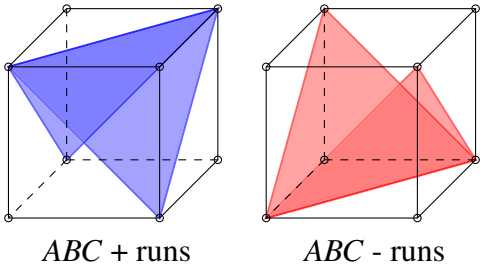

(c) Three-factor interactions

Fig. 1.15 DOE geometric representation. In each case, high levels are highlighted in blue, low levels in red [145].

The design of experiments [145] (DOE) (also called factorial designs) is a regression analysis widely used in the industry (experimental research) to find which are the critical

parameters and control them to improve the quality of the products. Experimental research is generally expensive, time consuming, and it involves studying the effects of two or more factors. It is possible applying a factorial design to investigate all possible combinations of the levels of the factors defined, (see Fig. 1.15). However, one needs to pay attention to the selection of factors due to the cost and time of the experiments[19]. Thus, one of the most important reasons in the literature to apply a DOE is to reduced the number of experimental tests and obtained a transfer function. Another reason for using the DOE is an easy integration of experimental measurements and the FEM. There are other factors involved in the elaboration of CFRP beyond of the analysis of this work [172], [173], that can be also studied using a DOE [174], [175].

The integration of the experimental measurements and the FEM with the DOE is used in the literature to simulate the changes of physical parameters (factors). Exhaustive MNET literature reviewed about identification of mechanical properties of CFRP revealed that physical parameters, such as Poisson's ratio (ν_{ij}), Young's modulus (E_i) and shear modulus (G_{ij}), depend on manufacturing process and the material selected (carbon, glass, epoxy) [13]- [48], [97]. Most of the literature reported the use different FE models and methodologies to update the physical parameters. For example, Rikards in [33] has applied the DOE using FEM to obtain physical parameters in different CFRP types, see [32], [34]-[39].

A full factorial design is constituted combining all possible number of "levels" and a number of "factors". These levels are called "low" (in red) and "high" (in blue) and denotes them "-" and "+" . The effect of the factor is defined as the change in response produced by a change in the level of the factor. This is frequently called *main effect*[20] because it refers to the primary factors of interest in the experiment. Furthermore, in some experiments, one may find that the difference in response between levels of one factor is not the same at all levels of the other factors. When this occurs, there is an *interaction* between the factors [145]. It is possible to analyze the main effects and the interactions between factors of the experimental results to achive one or more of the following objetives [146]:

- Estimation of the optimum condition for a defined interval.
- Estimation of the contribution of individual parameters and interactions.
- Estimate the response under optimum condition.

[19] The total number of experiments requiered for a full factorial design will increase exponentially as more possible updating parameters are taking into account.

[20] The main effect of a factor can be thought as the difference between the average response at the low level minus the average response of the high level.

Thus, the estimation of the contribution of individual parameters and interactions for a defined interval in this thesis is established to obtain a response function ($\hat{y}$) defined by the individual parameters or factors ($x's$), coefficients b_i and the error ε_{error}, see Eq. (1.73)

$$\hat{y} = b_0 + \sum_{i=0}^{k} b_1 x_1 + \sum_{i=0}^{k} b_2 x_2 + + \sum_{i=0}^{k} b_{12} x_1 x_2 + \cdots + \varepsilon_{error} \tag{1.73}$$

Eq. (1.73) can be written in matrix notation substituting x_i by the parameters identified in the FSDT as the factors of the function, see Eq. (1.74).

$$Y = Xb + \varepsilon \tag{1.74}$$

where

$$Y = \begin{bmatrix} y_1 \\ y_2 \\ \vdots \\ y_3 \end{bmatrix}, X = \begin{bmatrix} 1 & x_{11} & x_{12} & \dots & x_{1k} \\ 1 & x_{21} & x_{22} & \dots & x_{2k} \\ \vdots & \vdots & & \vdots & \vdots \\ 1 & x_{11} & x_{12} & \dots & x_{1k} \end{bmatrix} b = \begin{bmatrix} b_1 \\ b_2 \\ \vdots \\ b_3 \end{bmatrix}, \text{ and } \varepsilon = \begin{bmatrix} \varepsilon_{error_1} \\ \varepsilon_{error_2} \\ \vdots \\ \varepsilon_{error_3} \end{bmatrix}, \tag{1.75}$$

$[Y]$ will be defined as the MAC response, $[X]$ is a $n \times p$ matrix of independent variables (defined as A, B, C, D, E, F in Table 1.2), b is the vector of regression coefficients and ε_{error} is a vector of random errors. The MAC is introduced in the next Chapter addressed as the modal correlation of experimental and simulation FE models based on defined parameters x.

Moreover, once the parameters are defined, the DOE is analyzed mainly into three phases, which encompasses all the experimental and FEM work. These phases are:

- Planning phase
- Analysis phase
- Results phase

The planning phase is the most important part of the DOE. It is needed to create an orthogonal array to accomodate the effects of several factors that affect the MAC response of the CFRP. In the literature, these factors are related to physical parameters of the CFRP that needed to be verified quantitative and qualitative using FE models.

Table 1.2 Levels per factors used with different MNET

Factor	Name	Level		Units
		Low	High	
A	E_1	-	+	GPa
B	E_2	-	+	GPa
C	G_{12}	-	+	GPa
D	G_{23}	-	+	GPa
E	G_{13}	-	+	GPa
F	ν_{12}	-	+	—

Thus, six parameters with two levels (low and high levels) are proposed as a factors, (see Table 1.2), to perform a 2^6 full factorial in this phase. The Table 1.3 presents the array to follow based on the levels per factors proposed in Table 1.2. The interaction signs are obtained multiplying the signs of each interaction displayed in Table 1.3 until the third interaction for reasons of size of the array. Thus, the first value of the AB column is equal to $+$ and it is obtained multiplying the A^- and the B^- signs. The rest of the signs are obtained in the same way and so on for the higher interactions. The MAC averages (low and high values) values are calculated using interaction signs and the MAC response to obtain the coefficients, see bottom part of the table. These coefficients values are calculated using MINITAB and they are used to elaborate the main interaction effects plots. It is a requierement that the low and high levels are orthogonal respect to each other keeping the same proportion between the factors. These values will depend on the nominal values selected to perform the DOE. For example, if the nominal value is 5, the low and high limits will be 2.5 and 7.5.

The analysis phase is basically constituted into several statistical decision approaches: the distribution significance, the analysis of varianza (ANOVA) and the coefficient R-Sq (ratio of the variation of each variable). Based on these approaches can be distinguished the coefficients to construct the transfer function in two steps.

Firstly, the distribution significance analysis of the MAC is evaluated for a confidence level of 95%, that is for significance level of α=0.05 for a single population proportion. Alpha α is the maximum acceptable probability of being wrong if the alternative hypothesis is selected [147]. The MAC results Y are analysed based on analysis of averages[21] ($\mu = \sum_{i=1}^{N} \frac{Y_i}{N}$) , the

[21] The μ is a measure of central tendency. It is the mean or average of all values in the population [147].

standard deviation[22] $s = \sum_{i=1}^{N} \frac{(Y_i - \mu)^2}{N}$, Sum-of-Squares of the squared Deviations (SST)=$\sum s^2$ and the variance $s^2 = \frac{SST}{DF}$ of the factors that influence the MAC, where N is the number of "runs" and "DF" = the degree of freedom =$n-1$ [145].

Secondly, the ANOVA test compares the averages (it is also called misleading) that influence the MAC. A P-value $\leq$0.05 will highlight in the ANOVA the significance of the main parameters and it's interactions. It is possible with the ANOVA to identify the variance between factors and it's interactions. The coefficients and the errors are obtained based on statistical-decision approaches checking the distribution significance (normality) of data using the Anderson-Darling test using MINITAB 15. The ANOVA will be performed using the the MAC response obtained based on the orthogonal array, see Table 1.3. Different graphs are used to analyze the factors and interaction that influence the MAC (main effects plots, interaction effects, contour and surface plots).

Finally, the results phase consists of assemblying the transfer function and it is achived using the coefficients obtained by the determination of R-Sq. The coefficient of determination R-Sq is defined as the ratio of the variation of each variable to the total variation (variation of the Mean Sum of Squares (MSS)). The coefficient R-Sq is also known as a measure of the degree of fit. If the R-Sq approaches 100 %, a better total variation of the MAC response is obtained, see Chapter 4, Table 4.9.

[22]The σ is a measure of dispersion or variability, see Table B.1. With smaller values of σ, all values in the population lie closer to the mean [147].

Table 1.3 Design of experiments 2^6- Orthogonal array

Run (n)	Factor A	B	C	D	E	F	AB	AC	BC	ABC	Response MAC
1	-	-	-	-	-	-	+	+	+	-	
2	+	-	-	-	-	-	-	-	+	+	
3	-	+	-	-	-	-	-	+	-	+	
4	+	+	-	-	-	-	+	-	-	-	
5	-	-	+	-	-	-	+	-	-	+	
6	+	-	+	-	-	-	-	+	-	-	
7	-	+	+	-	-	-	-	-	+	-	
8	+	+	+	-	-	-	+	+	+	+	
9	-	-	-	+	-	-	+	+	+	-	
10	+	-	-	+	-	-	-	-	+	+	
11	-	+	-	+	-	-	-	+	-	+	
12	+	+	-	+	-	-	+	-	-	-	
13	-	-	+	+	-	-	+	-	-	+	
14	+	-	+	+	-	-	-	+	-	-	
15	-	+	+	+	-	-	-	-	+	-	
16	+	+	+	+	-	-	+	+	+	+	
17	-	-	-	-	+	-	+	+	+	-	
18	+	-	-	-	+	-	-	-	+	+	
19	-	+	-	-	+	-	-	+	-	+	
20	+	+	-	-	+	-	+	-	-	-	
21	-	-	+	-	+	-	+	-	-	+	
22	+	-	+	-	+	-	-	+	-	-	
23	-	+	+	-	+	-	-	-	+	-	
24	+	+	+	-	+	-	+	+	+	+	
25	-	-	-	+	+	-	+	+	+	-	
26	+	-	-	+	+	-	-	-	+	+	
27	-	+	-	+	+	-	-	+	-	+	
28	+	+	-	+	+	-	+	-	-	-	
29	-	-	+	+	+	-	+	-	-	+	
30	+	-	+	+	+	-	-	+	-	-	
31	-	+	+	+	+	-	-	-	+	-	
32	+	+	+	+	+	-	+	+	+	+	
33	-	-	-	-	-	+	+	+	+	-	
34	+	-	-	-	-	+	-	-	+	+	
35	-	+	-	-	-	+	-	+	-	+	
36	+	+	-	-	-	+	+	-	-	-	
37	-	-	+	-	-	+	+	-	-	+	
38	+	-	+	-	-	+	-	+	-	-	
39	-	+	+	-	-	+	-	-	+	-	
40	+	+	+	-	-	+	+	+	+	+	
41	-	-	-	+	-	+	+	+	+	-	
42	+	-	-	+	-	+	-	-	+	+	
43	-	+	-	+	-	+	-	+	-	+	
44	+	+	-	+	-	+	+	-	-	-	-
45	-	-	+	+	-	+	+	-	-	+	
46	+	-	+	+	-	+	-	+	-	-	
47	-	+	+	+	-	+	-	-	+	-	
48	+	+	+	+	-	+	+	+	+	+	
49	-	-	-	-	+	+	+	+	+	-	
50	+	-	-	-	+	+	-	-	+	+	
51	-	+	-	-	+	+	-	+	-	+	
52	+	+	-	-	+	+	+	-	-	-	
53	-	-	+	-	+	+	+	-	-	+	
54	+	-	+	-	+	+	-	+	-	-	
55	-	+	+	-	+	+	-	-	+	-	
56	+	+	+	-	+	+	+	+	+	+	
57	-	-	-	+	+	+	+	+	+	-	
58	+	-	-	+	+	+	-	-	+	+	
59	-	+	-	+	+	+	-	+	-	+	
60	+	+	-	+	+	+	+	-	-	-	
61	-	-	+	+	+	+	+	-	-	+	
62	+	-	+	+	+	+	-	+	-	-	
63	-	+	+	+	+	+	-	-	+	-	
64	+	+	+	+	+	+	+	+	+	+	
$MAC_{Ave}at\,factor_{high} = \sum factor_{A+}/nfactor_{A+}$											
$MAC_{Ave}at\,factor_{low} = \sum factor_{A-}/nfactor_{A-}$											
Effects = $MAC_{Ave}at\,factor_{high} - MAC_{Ave}at\,factor_{low}$											
Coefficients = $Effects/2$											

Chapter 2

Modal correlation criteria (MCC)

2.1 Modal Assurance Criterion (MAC)

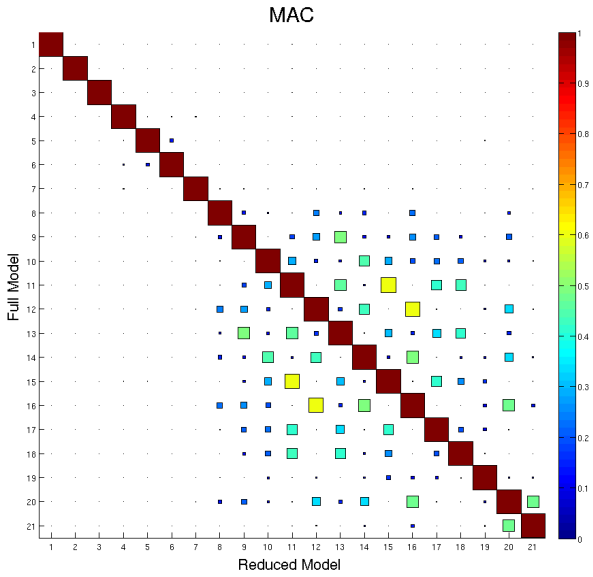

Fig. 2.1 Modal assurance criterion.

There are two general categories of modal correlation criterion (MCC), eigenfrequencies and eigenvectors. The modal assurance criterion [125] (MAC) is one of the most useful comparison methods, which relies on the eigenvector information.

The MAC is a known vector correlation criterion between the experimental and the FE model or between two FE models. In the case of experimental-FE model correlation, the measurements can be approximated through a polynomial function[1].

The MAC quantifies how well two vectors correspond, where $\{c_j\phi_{id}\}$ is the j^{th} mode shape at sensors and $\{c_j\phi_k\}$ is the j^{th} analytical mode shape, see Eq. (2.1), provided that the observability law for the selection of DOF's is not violated. A scalar value from 0 to 1 is obtained per pair, (see Fig. 2.1). When the values are 1 (or 100), there is a correlation and when the computation yields are 0, there is no correlation at all.

There are two explanations for high MAC values, a mathematical and a physical explanation. Matematically seen, both vectors have the same direction in a N-dimensional space, irrespective of their amplitudes [106]. Looked at physically, both vectors describe the same mode shape. The MAC can be computed for any set of (complex or real) vectors. It is often used to perform a corrrelation to identify the accuracy (eigengrequencies and mode shapes) of a experimental modal analysis versus a finite element simulation. The application of the MAC can be also used to peform orthogonality (XOR) and cross-orthogonality matrices verification. The XOR matrix indicates the goodness of the mass distribution of the FE model. The cross-orthogonality MAC matrix identifies the accuracy of the reduced mode shapes using experimental measurements.

$$MAC = \frac{|\sum_{j=1}^{l}\{c_j\phi_{id}\}^H\{c_j\phi_k\}|^2}{|\sum_{j=1}^{l}\{c_j\phi_{id}\}^H\{c_j\phi_{id}\}||\sum_{j=1}^{l}\{c_j\phi_k\}^H\{c_j\phi_k\}|} \tag{2.1}$$

2.1.1 Modal Assurance Criterion per pair-sensor (MACco)

The MAC per pair-sensor (MACco) criterion consists in the sequential order of sensors per paired mode (It is defined 153 Y-sensors perperdicular to the experimental measurements in this work) that contribute most to the poor correlation. This MCC is known with different names: the MAC coordinate criterion [106] or the MAC validation technique [127]. It is an iterative algorithm that takes modes in $\{c_j\phi_{id}\}$, $\{c_j\phi_k\}$ and computes the paired MAC with one sensor "removed" that contributed to low MAC values [126]. *The MACco algorithm's is leading to the best mean MAC for the paired modes and is a direct indication of where the poorest correlation is located* [106]. The MACco is interpreted in the same way as the MAC, where 1 indicates a good correlation and 0 indicates null correlation. However, it is possible to observe the main difference between the traditional MAC and the MACco in the number of pair modes by the

[1]The polynomial function or FFT, was introduced in Chapter 1.

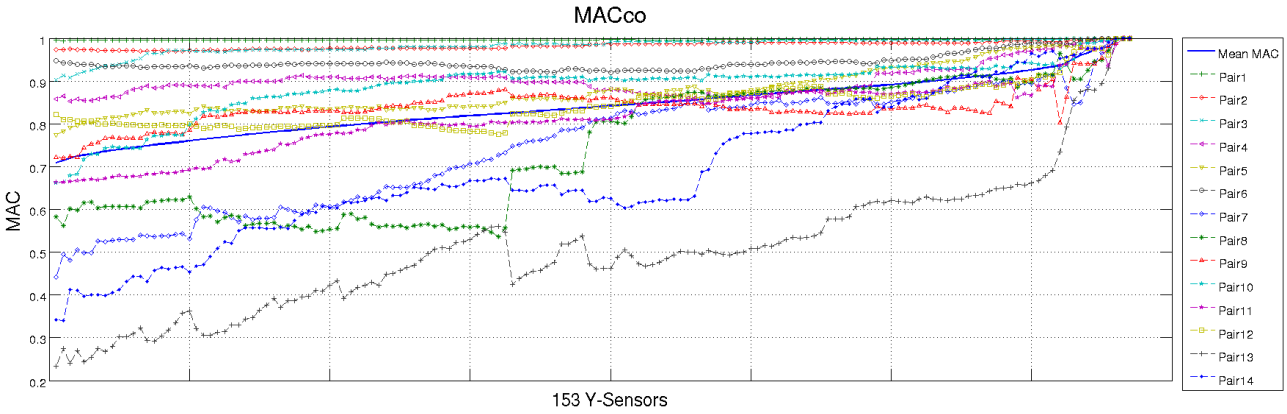

Fig. 2.2 Modal assurance criterion validation technique [106] plot.

number of sensors used, (see "x" axis of Fig. 2.1), respect to the pairing criterion, (see "x" axis of the Fig. 2.2). The "mean MAC" displayed in Fig. 2.2 is obtained calculating the mean of the MAC per pair mode-sensor requested in the analysis. Tables with the data can be obtained and will be provided. A block diagram of the algorithm implemented in [106] is illustrated in Fig. 2.3.

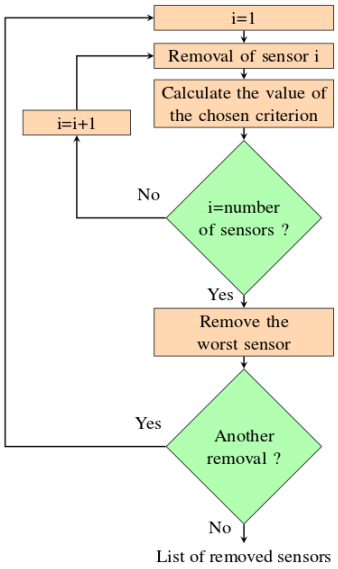

Fig. 2.3 Modal assurance criterion per pair mode [126] algorithm.

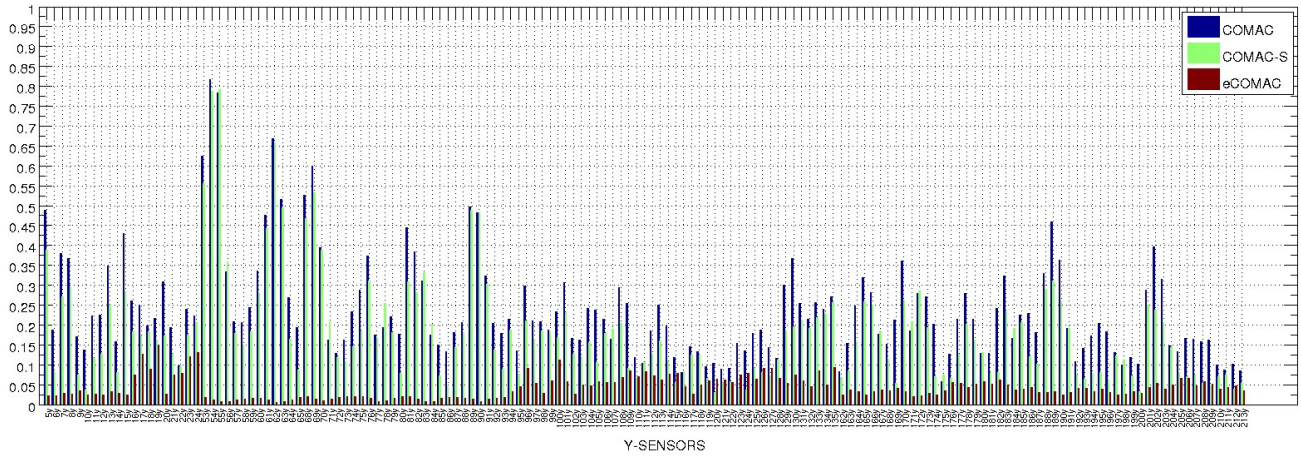

Fig. 2.4 Different COMAC's criterion: COMAC (blue), eCOMAC(brown), COMAC-S(green).

2.1.2 Coordinate Modal Assurance Criterion (COMAC)

The coordinate modal assurance criterion (COMAC) is an extension of the MAC developed by Lieven and Ewins [128]. *The implementation of the COMAC technique requires two stages of calculation. In the first stage, the modes from the two sets are matched using a MAC. After constructing the set NM of mode pairs to be correlated, the second stage of COMAC is the calculation of correlation values at each coordinate, over all the correlated mode pairs* [132], see Eq. (2.2):

$$COMAC_l = 1 - \frac{\sum_j^{NM} |\{c_l\phi_{jA}\}\{c_l\phi_{jB}\}|^2}{\sum_j^{NM} |\{c_l\phi_{jA}\}|^2 \sum_j^{NM} |\{c_l\phi_{jB}\}|^2}, \tag{2.2}$$

where $\{c_l\phi_{jA}\}$ is the j^{th} at sensors and $\{c_l\phi_{jB}\}$ is the j^{th} in the analytical mode shape selected. It is important to note that the modes have to be normalized as this gives equal weighting to all modes. *Unfortunately, the standard COMAC, as developed by Lieven and Ewins* [128], *cannot identify differences which occur due to fairly common problems appearing during modal testing. These problems include incorrect orientation of accelerometers and transducer scale factor errors* [129]. Additionally, the COMAC is equally sensitive to large motion DOF and small motion DOF, which can make COMAC results more difficult to interpret. COMAC values closer to zero per DOF will have a higher agreement, (see Fig. 2.4).

2.1.3 Scale Coordinate Modal Assurance Criterion (COMAC-S)

The definition of COMAC is applied assuming that the modes are similarly scaled. *The scale COMAC is computed with shapes in set B scaled using the Modal Scale Factor*[2] [106] (MSF), see Eq. (2.3). The MSF provides a qualitative way of comparing two modal vector sets (entries). The vector entries are the coefficients of the two sets of matched modal vectors at a defined location. Using the MSF is also possible for providing an indication of the type of error vector superimposed on the modal vector. This criterion has been perfomed by Balmés [106], Ewins [131], Catbas [132], Allemang [133] and Schwarz [187] for a variety of different analysis for comparison with experimental data, including structural modifications using FRFs, CMS and MSE techniques [187].

$$\begin{aligned} COMAC - S_l &= 1 - \frac{\sum_j^{NM} |\left\{c_l\phi_{jA}\right\}\left\{c_l\tilde{\phi}_{jB}\right\}|^2}{\sum_j^{NM} |\left\{c_l\phi_{jA}\right\}|^2 \sum_j^{NM} |\left\{c_l\tilde{\phi}_{jB}\right\}|^2} \\ \left\{c_l\tilde{\phi}_{jB}\right\} &= \left\{c_l\phi_{jB}\right\} MSF = \left\{c_l\phi_{jB}\right\} \frac{\left\{c_l\phi_{jB}\right\}^T \left\{c_l\phi_{jA}\right\}}{\left\{c_l\phi_{jB}\right\}^T \left\{c_l\phi_{jB}\right\}} \end{aligned} \tag{2.3}$$

The COMAC-S criterion sets the scaling of vectors in set B to minimize the quadratic norm of the difference between $\{c_l\phi_{jA}\}$ and $\{c_l\tilde{\phi}_{jB}\}$ [106]. *Scaling assumes that each experimental mode shape is already correlated with an analytical shape. When two modal vectors are scaled similarly, elements of each vector can be averaged, differentiated or sorted to provide a best estimate of the modal vector* [133]. Thus, the lower values of the COMAC-S obtained also represent a higher agreement per DOF.

2.1.4 Enhanced Coordinate Modal Assurance Criterion (eCOMAC)

The formulation of an enhanced COMAC, introduced by Hunt [129], overcome some of the limitations of the standard COMAC expressed as:

$$eCOMAC_l = \frac{\sum_j^{NM} ||\left\{c_l\hat{\phi}_{jA}\right\} - \left\{c_l\tilde{\phi}_{jB}\right\}||}{2NM} \tag{2.4}$$

[2]The function of the MSF is to provide a means of normalizing all estimates of the same model vector, taking into account magnitude and phase differences [133].

The comparison is done using mode shapes that are vector nomalized to 1 and there must be phase correlation between pair modes, see Eq. (2.5)

$$\left\{c_l \hat{\phi}_{jA}\right\} = \frac{\left\{c\phi_{jA}\right\}}{||c\phi_{jA}||} \tag{2.5}$$

This can be accomplished by examining the high coefficient DOF in the mode pairs or by using the MSF to determine if the normalization mode should be multiplied by -1. The use of the eCOMAC requieres this extra step in mode shape nomalization, namely a check for phase consistency between each mode pair using the MSF [129]. This unit normalization and correct phasing, are being interpreted in the same way as the COMAC. The eCOMAC values are obtained from 0 to 1 similarly as the COMAC, where a value closer to zero per DOF will have a higher correlation agreement, (see Fig. 2.4). Furthermore, Hunt reported in [129] that *the eCOMAC can sucessfully identify measurement errors such as scaling and polarity. This is because the eCOMAC is less sensitive to errors at small motion of degrees of freedom and it is considered more robust than the standard COMAC* [129]. Thus, the lower COMAC, eCOMAC and COMAC-S values are obtained, a higher agreement per DOF is represented according to each formulation.

Chapter 3

Component model synthesis theory with Rayleigh-Ritz vectors

3.1 Introduction

Many techniques have been proposed to obtain reduced order finite element models (known as model order reduction (MOR) methods) by reducing the order of mass and stiffness matrices of structures made of conventional materials [8], [9], [112]-[127], [134]-[138], [217]-[223]. The substitution of conventional materials by composite materials in the aeronautic, space and automotive industry is becoming increasingly important today for the production of industrial high-performance components [1]- [2]. The state-of-the-art MOR techniques are classified in four groups [116]: direct reduction, modal methods, reduction with Rayleigh-Ritz vectors, and the component mode synthesis (CMS). According to this classification, the last two groups yield the best results. The Rayleigh-Ritz vectors improve the accuracy-cost ratio and the CMS combines the first three classes of methods.

The Rayleigh-Ritz reduction approach is applied as a basis $[T_R]_{N\times n}$ in [118] by Balmès, so that finite element DOF $\{q\}_{N\times 1}$ are written as a combination $\{q_R\}_{n\times 1}$ of the basis n Rayleigh-Ritz vectors as

$$\{q\}_{N\times 1} = [T_R]_{N\times n}\{q_R\}_{n\times 1} \tag{3.1}$$

where the DOFs of a reduced model cannot be expressed as displacement of a particular mesh point, but rather in the contribution of the global shape responses. The DOFs of a reduced model can be defined as a classical denomination of generalised DOFs [121].

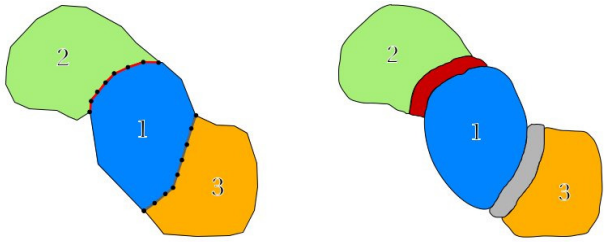

(a) Displacement coupling (b) Energy coupling

Fig. 3.1 Interface representation, coupling strategies [203].

Furthermore, an extensive bibliography can be found about the research of CMS, see [113], [114], [116], [217]-[223], or substructuring [8]-[12], [199] studied since the 1970s. The CMS method belongs to the category of sub-structuring techniques introduced in Chapter 1: the model is split up into sub-structures and for each sub-structure the reduction approach is applied. Two conditions must be satified using assembling sub-structures:

- Interface displacements of the substructures must be the same and zero work of interfaces forces.
- The forces connecting the substructures' interfaces DOF must be in equilibrium using elements to compute the energy.

Figure 3.1 shows the two main strategies used to account for the component coupling: displacement or energy.

The displacement strategy, represented in Figure 3.1a, assumes the continuity of displacement and zero work of interfaces forces. Both substructures must share the same set of interface DOF as well as compatibility and equilibrium needed to be satisfied. This strategy is commonly labeled as a *primal*[1] method and is the classical framework of CMS [203].

The energy strategy, commonly labeld *dual*[2] methods represented in Figure 3.1b, uses elements to compute the energy associated with relative displacement of disjoint components.

[1]By choosing a unique set of DOF, one set of interface DOF is eliminated. Both substructures thus share the same set of interface DOF and compatibility and equilibrium are both a priori satisfied [198].

[2]The connection forces on both sides of the interface must be in equilibrium. One way of enforcing this is by choosing an unique set of interface forces, which will a *priori* satisfy the equilibrium condition [198].

Other energy strategy method used loads to couple components discussed in [199], that does not correspond to dual methods [203].

Hence the MOR method based on the Rayleigh-Ritz approach is used to improve the accuracy-time ratio in civil and aeronautical engineering applications in many areas of structural dynamics [9], [116], [120], [121], [123]. A number of articles and theses published by Balmès *et al.* regarding CMS, the optimization of reduction bases and MSE techniques using the Rayleigh-Ritz vectors constitute the theoretical basis and design advanced methods implemented in MATLAB-SDTools, see [117], [118]-[123], [137], [152]-[155], [180], [203]-[214]. Thus, it is necessary to study the feasibility and efficiency of using the CMS with the Rayleigh-Ritz reduction basis in order to describe the dynamic behavior of a composite structure.

3.2 Model order reduction with Rayleigh-Ritz vectors

It is typical for coupled problems with model substructuring [117], [118], [120] and [121] to have an accurate second order representation expressed in the form:

$$\begin{aligned} \left[[M]s^2+[C]s+[K]\right]\{q(s)\} &= [b]\{u(s)\} \\ \{y(s)\} &= [c]\{q(s)\} \end{aligned} \tag{3.2}$$

where (s) is the Laplace variable, $[M],[C],[K]$ are mass, damping and stiffness matrices respectively, $\{q(s)\}$ are generalised degrees of freedom (DOFs), $[b]$ and $[c]$ are input and output matrices, respectively, $\{u(s)\}$ are the inputs describing the time/frequency dependence and $\{y(s)\}$ are the physical outputs. Notice that the representation form between Eq. (1.68) expressed in Chapter 2 and Eq. (3.2) is different. *The general form description in Eq. (3.2) is commonly in the control theory (state-space models are composed of two set of equations) but rarely used in mechanical applications* [106]. With this description, two - not very classical and yet important - assumptions are made [118]:

1. The descomposition of discretized loads $F(s)$ as the product of the fixed input shape matrix specifying the spatial localization of loads $[b]$ and inputs $\{u(s)\}$

2. The definition of physical outputs $\{y(s)\}$ is a linear combination of DOF's $\{q(s)\}$:

The Ritz-Galerkin displacement methods seek approximations of the response within a subspace characterized by matrix $[T]$ associated with generalised DOF's $\{q_R\}$, see [117]

$$\{q(s)\} = [T]\{q_R\} \tag{3.3}$$

where $\{q(s)\}$ is the original set of DOF and $\{q_R\}$ is the reduced set of DOF, susbtituting Eq. (3.3) into Eq. (3.2) leading to an overdetermined set of equations. The Rayleigh-Ritz approximation assumes that the virtual work of displacements in the dual space generated by $[T]^T$ is also zero, thus leading to a reduced model:

$$\begin{aligned} \left([T]^T[M][T]s^2 + [T]^T[C][T]s + [T]^T[K][T]\right)\{q_R(s)\} &= [T]^T[b]\{u(s)\} \\ \{y(s)\} &= [c][T]\{q_R(s)\} \end{aligned} \tag{3.4}$$

3.3 Component Mode Syntesis concepts

3.3.1 Classical Component Mode Synthesis (CMS) bases as approximation of the frequency response

The method was first developed by Walter Hurty in 1964 [8] and later expanded by Roy Craig and Mervyn Bampton [9] in 1968. Component Mode Synthesis (CMS) and model order reduction methods provide for the means for building appropiate $[T]$ bases (the subspace spanned rectangular matrix). There are many ways of providing classical bases [10]. Their validity is associated with two assumptions [118]: the model needs to be valid over a restricted frequency band and the number of inputs is limited. One needs to translate this hypothesis into the requirement to include mode shapes and static responses into $[T]$ basis. Most of the literature on CMS implies the fundamental assumption for coupling, which states that the displacement is continuous at the interfaces. Considering the response of an elastic structure to applied loads $F(s) = [b]\{u(s)\}$ without damping $[C]$, the exact response at a given frequency $[H(s)]$ is given by:

$$[H(s)] = [c]\left([M]s^2 + [K]\right)^{-1}[b] = [c]\,[Z(s)]^{-1}\,[b] \tag{3.5}$$

where $[Z(s)]$ is the dynamic stiffness. If there is no external excitation:

$$\left[Z(\lambda_j)\right]^{-1}\left\{\phi_j\right\} = \{0\} \tag{3.6}$$

and the solutions are known as free modes of the structure, where λ_j is j^{th} eigenvalue of the matrix and $\{\phi_j\}$ is j^{th} eigenvector. A reduction model should include these shapes to allow for an accurate representation of the resonances, which are associated with the singularities of the dynamic stiffness. A point of particular interest is the static response at $(s=0)$. The associated deformation is:

$$\{q(s=0)\} = [Z(0)]^{-1}[b]\{u(0)\} = [T_s]\{u(0)\} \tag{3.7}$$

The columns of $[T_s]$ are also called attachment modes [10]. In the case of free floating structures (structures with rigid modes), $[Z(0)]$ is singular and one defines attachment modes as responses of all except for the rigid modes. The bases combining free modes and attachment modes are valid over a certain frequency range (truncation of the series of free modes) and certain inputs characterized by $[b]$. One, thus, considers the response of the structure with enforced displacements on a subset of DOFs. Division of the DOFs in two groups - active or interface DOFs denoted by *i* in the subscript, and complementary, denoted by *c* in the subscript, leads to:

$$\begin{bmatrix} [Z_{ii}(s)] & [Z_{ic}(s)] \\ [Z_{ci}(s)] & [Z_{cc}(s)] \end{bmatrix} \begin{Bmatrix} < \{q_i(s)\} > \\ q_c(s) \end{Bmatrix} = \begin{Bmatrix} R_i(s) \\ < \{0\} > \end{Bmatrix} \tag{3.8}$$

where $< \{q_i(s)\} >$ and $< \{0\} >$ denotes a defined quantity. The exact solution to this problem is:

$$\{q\} = [T(s)]\{q_i\} = \begin{bmatrix} [I] \\ -[Z_{cc}]^{-1}[Z_{ci}] \end{bmatrix} \{q_i\}. \tag{3.9}$$

The subspace found here is frequency dependent and can only be used in very restricted applications [123]. A classical approximation is to evaluate the static $(s=0)$ value in this subspace for the active or interface DOFs denoted by *ci* in the subscript, and complementar, *cc* in the subscript:

$$[T] = \begin{bmatrix} [I] \\ [-K_{cc}(s)]^{-1}[K_{ci}] \end{bmatrix}. \tag{3.10}$$

Reduction on this basis is known as static or Guyan condensation [108]. The columns of $[T]$ are called constraint modes [10]. They correspond to unit displacements of the DOF of the interface. Significant deviations can be expected when $[Z_{cc}(s)]^{-1}$ differs from $[Z_{cc}(0)]^{-1} = [K_{cc}]^{-1}$. Such

difference is significant for singularities of $[Z_{cc}(s)]^{-1}$ which are computed by the eigenvalue problem

$$\begin{bmatrix} [0] & [0] \\ [0] & [Z_{cc}(\omega_j)] \end{bmatrix} \begin{Bmatrix} \{0\} \\ \phi_{j,c} \end{Bmatrix} = 0 \tag{3.11}$$

The use of a basis combining constraint, Eq. (3.10) and fixed attachment modes, Eq. (3.11), is proposed in [9]. It yields the Craig-Bampton method:

$$[T] = \begin{bmatrix} [I] & [0] \\ [-K_{cc}]^{-1}[K_{ci}] & [\phi_{NM,c}] \end{bmatrix}, \tag{3.12}$$

where $[\phi_{NM,c}]$ is the interior part of the matrix of kept fixed-interfaces modes. There are many results reported by Balmès *et al.* [117], [118]-[123] obtained by the Craig-Bampton model order reduction (CBMOR) and the Rayleigh-Ritz vectors approach in order to solve coupled problems related to model sub-structuring (also known as CMS). One should be aware of the fact that the use of Rayleigh-Ritz vectors leads to dense matrices, as opposed to not reduced FE models characterized by a sparse form of the matrices.

3.3.2 Application of substructures (super-elements) to a CFRP

Substructuring is a procedure that condenses a group of finite elements into one element. It implies that the whole structure is divided into smaller structures and the resulting elements are referred to as super-elements. In the considered case (see Fig. 3.2), the CFRP is divided into

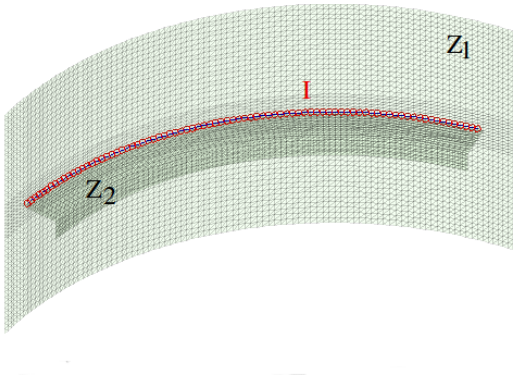

Fig. 3.2 CMS applied to our composite component assembly divided in two sub-structures. (I) Interface, Z_i for complementary DOF of structures 1 and 2

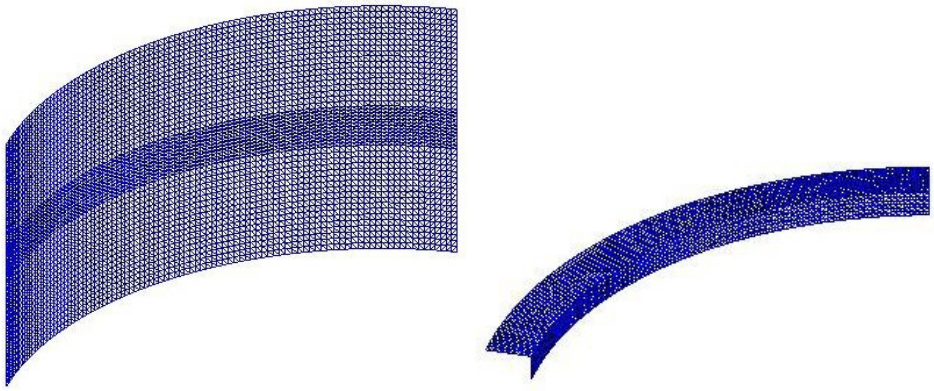

(a) Sub-structure 1 (b) Sub-structure 2

Fig. 3.3 Sub-structuring.

two sub-structures, namely 1 and 2, (see Fig. 3.3). Each sub-structure is considered to have two separate types of DOF, *interface* DOF, denominated by the subscript i, representing the structure DOF interface, and *complementary* DOF, denominated by the subscript c, representing the structure DOF outside the interface. The displacement vector of component 1, q_1, can be described considering splitting DOF in two groups, the DOF interface $\{q_{i1}\}_{N_{1i}\times 1}$ and the complementary DOF $\{q_{c1}\}_{N_{1c}\times 1}$. The sub-structure 2 can be handled in the same way splitting q_2 into $\{q_{i2}\}_{N_{2i}\times 1}$ and $\{q_{c2}\}_{N_{2c}\times 1}$. The principle of the method is to consider disjoint components and seek a reduction that reproduces full system modes exactly, see [212]. Reduction bases defined by a block are then written as [203]:

$$\{q\}_{N_{1c}+N_{2c}\times 1} = [T]\{q_R\}_{n_{1c}+n_{2c}\times 1} = \begin{bmatrix} [T_{c1}] & 0 \\ 0 & [T_{c2}] \end{bmatrix} \begin{Bmatrix} q_{R1} \\ q_{R2} \end{Bmatrix} \tag{3.13}$$

and the dynamic stiffness can be separated as the sum of independent component contributions Z_i and an interface coupling matrix Z_I [203]

$$[Z]_{(N_{1c}+N_{2c})\times(N_{1c}+N_{2c})} = [Z_{el}] + [Z_I] = \begin{bmatrix} [Z_1] & 0 \\ 0 & [Z_2] \end{bmatrix} + \begin{bmatrix} [Z_{I_{11}}] & [Z_{I_{12}}] \\ [Z_{I_{21}}] & [Z_{I_{22}}] \end{bmatrix}. \tag{3.14}$$

The physical coupling of the CFRP assembly is based on the super-element strategy dividing the full FE model by element groups established in [106]. *The continuity is obviously always verified in this formulation since Eq.* (3.13) *expresses motion using the full FE model coordinates. The*

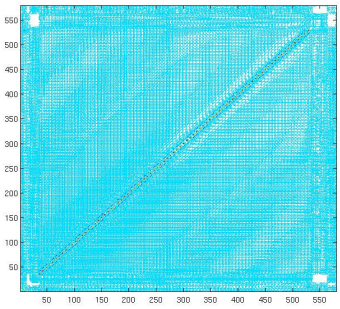

(a) Stiffness Matrix

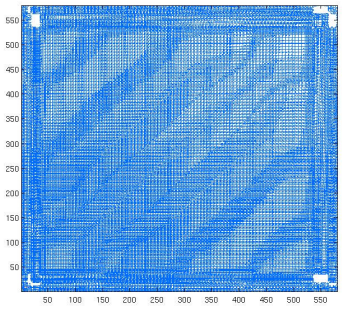

(b) Mass Matrix

Fig. 3.4 Reduced matrix topologies of a CFRP using Rayleigh-Ritz vectors.

reduced dynamic stiffness matrix $[Z_R]$ *is written as*

$$[Z_R]_{(n_{1c}+n_{2c})\times(n_{1c}+n_{2c})} = \begin{bmatrix} [T_{c1}]^T [Z_1] [T_{c1}] & 0 \\ 0 & [T_{c2}]^T [Z_2] [T_{c2}] \end{bmatrix} + \begin{bmatrix} [T_{c1}]^T [Z_{I11}] [T_{c1}] & [T_{c1}]^T [Z_{I12}] [T_{c2}] \\ [T_{c2}]^T [Z_{I21}] [T_{c1}] & [T_{c2}]^T [Z_{I22}] [T_{c2}] \end{bmatrix} \tag{3.15}$$

where the elastic dynamic stiffness considers each component independently and contains the dynamic stiffness of each component. The topology of the interaction matrix (block diagonal) represents the component coupling associated to each interface DOF [203]. The block diagonal (see Fig. 3.4) can be well illustrated using the defined substructures of FE model. *In constrast with the Craig-Bampton*[3]*, the method established by Balmes [117] in SDTools only needs to focus on selecting retained shapes. Reduction bases* $[T_{ci}]_{N_i\times n_i}$ *can be generated using the restriction of the system modes on each component,* $[\Phi_{ci}]$*. In that case the reduced system will give the exact result. The subspaces generated by each component are effectively coherent with the assembled system subspace and all interface motion is well described since all the desired motion is retained in the basis* [203].

3.3.3 Using component modes as DOF

A richer component description can be obtained using the modes of the components [121] with

$$[T_{ci}]_{N_i\times n_i} = \left[\phi_{|ci}\right] \tag{3.16}$$

[3]The Craig-Bampton needed complete interface description to enforce continuity.

one has

$$\begin{cases} [T_{c1}]^T [Z_1] [T_{c1}] = [\phi_{j1}]^T [Z_1] [\phi_{j1}] = \begin{bmatrix} \ddots \omega_{j1}^2 & \\ & \ddots \end{bmatrix} \\ [T_{c2}]^T [Z_2] [T_{c2}] = [\phi_{j2}]^T [Z_2] [\phi_{j2}] = \begin{bmatrix} \ddots \omega_{j2}^2 & \\ & \ddots \end{bmatrix} \end{cases} \tag{3.17}$$

and the coupled system equations

$$[Z_R]_{(n_{1c}+n_{2c})\times(n_{1c}+n_{2c})} = \begin{bmatrix} \begin{bmatrix} \ddots \omega_{j1}^2 & \\ & \ddots \end{bmatrix} & 0 \\ 0 & \begin{bmatrix} \ddots \omega_{j2}^2 & \\ & \ddots \end{bmatrix} \end{bmatrix} + \begin{bmatrix} [T_{c1}]^T [Z_{I11}] [T_{c1}] & [T_{c1}]^T [Z_{I12}] [T_{c2}] \\ [T_{c2}]^T [Z_{I21}] [T_{c1}] & [T_{c2}]^T [Z_{I22}] [T_{c2}] \end{bmatrix} \tag{3.18}$$

The space of the full system real modes $[\Phi]$ *provides a subspace containing all relevant information for the interface movements. From a single component point of view, the basis of real free/free is complemented by the trace of the real system modes on the component, noted* $\Phi_{|ci}$, see Eq. (3.16). *Computing the full modes of the assembled system at a nominal state is deemed accesible, using Automated-multi level solvers*[4] *(AMLS) developed by Kaplan [201] and Bennighof et al. [208]. The additional information introduced mainly concerns that the component interaction with others and thus provide and adequate subspace containing the component free/free modes and all the relevant interface movements. For component i, the reduction basis is written as*

$$[T_{ci}]_{N_i \times n_i} = \left[\phi_{ci}\ \Phi_{|ci}\right]_{Orth.} \tag{3.19}$$

To avoid redundant data, Eq. (3.19) *specifies an orthogonalization at the component level with respect to mass and stiffness, so that*

$$\begin{cases} [T_{ci}]^T [K_i] [T_{ci}] = \begin{bmatrix} \ddots \omega_{i,j}^2 & \\ & \ddots \end{bmatrix} \\ [T_{ci}]^T [M_i] [T_{ci}] = \begin{bmatrix} \ddots \mathscr{I} & \\ & \ddots \end{bmatrix} \end{cases} \tag{3.20}$$

[4]The AMLS method is based on domain decomposition and parallel resolution and allow computation of systems of over a few million DOF on workstations in a reasonable time [203].

Since the orthogonalization is performed at the component scale, the component free/free modes verify Eq. (3.20) *by definition. Only the contribution of the enrichment modes is made orthogonal to the component modes. The topology of the assembly matrices is then optimal with the system mass matrix being the identity* $[\mathscr{I}]$ *and the elastic stiffness being diagonal with the square of free/free component* $[\omega_{i,j}^2]$*. The interaction matrix only shows a full block for interacting components, (see Fig. 3.4). The first remarkable feature of the reduced system is that it produces features with exactly the same modes as the full one - to numerical precision. Indeed, the assembled real modes information have been used explicitly and can therefore be recovered. The second interesting feature is that modified components, than can be well represented by the nominal components modes, can be well predicted by the same reduced model but the problem here is much smaller than with the Craig-Bampton approach since the interface sizes are associated with the number of system and component modes and thus unrelated to the number of DOF in the interface topology.*

The main drawback is that while the interaction matrix still features a block topology, non-null reduced blocks are somehow full. The generation of full blocks is inevitable using Rayleigh-Ritz vectors [203].

3.3.4 Automatic generation of interfaces

The principal idea of the CMS is to partition the problem in simply entities that is much less costly combined with the coupling problem that need to be controlled at the same time[5]. The automatic generation of interfaces involving computational efficiency and recursive partition matrix has become popular in the application of reduced-order models using CMS (such as CBMOR) applying the automated multi-level substructuring (AMLS) method initiated by the research of Kaplan *et al.* [201] and Bennighof *et al.* [208]. In the original CBMOR and AMLS methods a transformation matrix is constructed retaining the dominant substructure modes. Using the transformation matrix original FE modes can be transformed into reduced FE models obtaining residual substructure modes. If the residual mode effect is considered the accuracy of the reduced model can be improved that means the original global modes can be more precisely approximated [118], [209], [213]. The AMLS algorithm implemented in [106] is integrated with an error estimation of the discrete model (substructures) using error residual associated with the full FE model solution developed by Bobillot [213] and a singular value decomposition

[5]Traditionally the solution of linear system methods require the computation of an LDU decomposition [203].

(SVD) [117] method developed by Balmès[6]. Its application is presented by Vermot in [203], see Appendix A and B, and it is therefore not reproduced here in details. The CBMOR and AMLS methods are implemented in the major commercial codes (NASTRAN, ABAQUS, ANSYS) applied to high performance computing (HPC) with few associated publications [202]. The accuracy approximation of the reduced models using the original CBMOR and AMLS methods has encourage a Kim *et al.* [209] to develop an enhanced AMLS method.

Thus, the main idea using CMS and AMLS methods is then to partition the problem in a series of smaller and much less costly uncoupled problems, combined with a coupling problem whose cost needs to be controlled. Partitioning is thus the generation of interfaces between subdomains [203].

Partitions of the FE model are controlled though the generation of interfaces between the components. *The partition of the FE model can be achived in two ways: working in the finite element mesh or in the system stiffness matrix. The second way is preferable as the target application for automatic partitioning concerns applications like the AMLS. The system partition is performed thanks to a front elimination tree*[7]*. Front elimination trees are based on a graph theory. Several techniques exist, see [204] and [205]. They are based on graphs associated with the stiffness matrix for which vertices are the DOF and the edges correspond to non-zero coupling terms between two* DOF[s]. *The procedure then seeks a way of minimizing connections and finding a single root. Three canonical ways of graph partitioning exist, briefly detailed in [204]. The first way is based on level set order techniques (Cuthill-McKee algorithm), which basically ranges partitions as a leveled neighborhood from an initial vertex. Moreover, the improvement of computer performance helped the emergence of other techniques based on graph dissection, and in particular bisection. These techniques are the base of the minimum degreee algorithm which was widely used in the last decade* [203]. The second way is based on spectral bisection. This procedure can be computed iteratively on the subparts, yielding the recursive spectral bisection method and it is known for producing high quality partitions [206]. The third one is a bisection method based on graph transversing. The bisection method used a coarsened graph to compute and refine in subgraphs afterwards. *It proved to be very efficient and it is the based technique of the METIS library [206]. The SPOOLES library [207] is linked in a*

[6]The residual interaction method have been shown to be very efficient for computation of normal and complex modes [213]. The SVD is a classical mathematical tool used to select important directions in a given subspace [118].

[7]Front elimination method is classically used to factor matrices since it optimizes storage space, operations and subsequent fill in patterns [203]

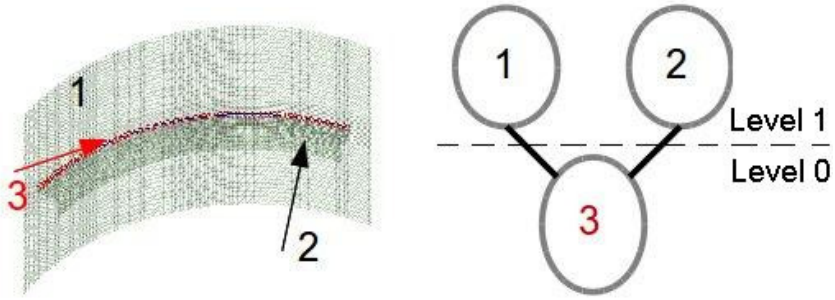

Fig. 3.5 Composite component partition, corresponding elimination tree and reorder matrix

robust manner to SDTools and provides similar methods. Its most interesting implementation is the use of a hybrid approach exploiting either nested dissection or multisection. Multisection is a generalization of bisection, which will either start with an initial multisector as the root, or perform local multisections from a bisected graph [203]. Partitioning can be well illustrated in application of the full FE model divided by groups. Figure 3.5 shows the CFRP component mesh divided into two parts (red nodes represent the interface). The model matrices can then be reordered by blocks to follow the tree ordering, yielding specific matrix topologies. *The result of matrix partitioning can be represented in the form of an elimination tree* [203]. Each of the two vertices stands for a substructure, i.e. a subset of DOFs of the original model. The vertice can be sorted in two categories: *leaf vertices* and *separator vertices*. The two leaves displayed in Figure 3.5 are substructures without any child and can be compared to usual CMS substructures (1 and 2 in the example, level 1). The root (3) (top level 0, no parent vertices) is a separator, and play a role of the leaves interfaces. The separators are considered as actual substructures with proper DOF sets [203].

3.3.5 Formulation of an iterative CMS

A short overview corresponding of the iterative CMS formulation nomenclature in the classical SDT notation is given. The content in italics in this section is mainly based on the textbook of Vermot [203] and the rest of it is reworked. *The goal is to find a basis in which the stiffness matrix* $[K]$ *is block diagonal, using a classical* $[LDL^T]$ *decomposition. All coupling terms then go to the mass matrix* $[M]$ *which is used for the eigenvalue solution.* The $[K]$ and $[M]$ matrices needed to be block partitioned, by one of the methods introduced in section 3.3.4, expressed as:

$$[K] = \left[K_{ij}\right]_{1\leq i,j\leq N} \tag{3.21}$$

A LU decomposition of $[K]$ is needed to obtain a block diagonal stiffness matrix $[D]$, (see [204]), such as

$$[K] = \left[LDL^T\right] \tag{3.22}$$

where $[L]$ *is a lower block triangular matrix and* $[D]$ *is block diagonal.* $[L]$ *can be used to project the mass matrix into* $[\hat{M}]$*. The* $[L]$ *and* $[D]$ *terms can be identified as part of the product* $[LDL^T]$*, writing*

$$\left[K_{ij}\right] = \left[LDL^T\right]_{ij} = \sum_{0<k\leq min(i,j)} L_{ik} D_{kk} L^T_{jk} \tag{3.23}$$

and

$$\left[M_{ij}\right] = \left[L\hat{M}L^T\right]_{ij} = \sum_{k\leq i} L_{ik} \sum_{p\leq j} \hat{M}_{kp} L^T_{jp} \tag{3.24}$$

Many terms can be simplified in Eqs. (3.23) *and* (3.24)*. The conditions on intermediary indices can be written as functions of Parent and Children groups, respectively written for node* i*,* $\mathscr{P}_i$ *and* $\mathscr{C}_i$*. These notations follow the tree representations from Figure 3.5.* An iterative identification per block from leaf to root is then possible from $[L]$ and $[D]$, yielding

$$L_{ij} = \begin{cases} \left[\hat{K}_{ji}\right][D_{ii}]^{-1} & \text{if} \quad j \in \mathscr{P}_i; \\ \mathscr{I} & \text{if} \quad i = j; \\ 0 & \text{otherwise.} \end{cases} \tag{3.25}$$

for $i \neq j$ and thanks to the base matrices topology

$$\left[\hat{K}_{ij}\right] = \left[K_{ij}\right] - \sum_{k\in\mathscr{C}_i} \hat{K}_{ik} L^T_{jk} \tag{3.26}$$

and

$$[D_{ii}] = [K_{ii}] - \sum_{k\in\mathscr{C}_i} L_{ij} D_{jj} L^T_{ij} \tag{3.27}$$

It can be noticed that intermediate stiffness coupling elements $\hat{K}$ *appear in the process, although simplified in the resulting* $[D]$ *matrix. Mass matrix terms can eventually be obtained by projection or also iteratively identified as*

$$\left[\hat{M}_{ij}\right] = \left[M_{ij}\right] - \sum_{k\in\mathscr{C}_i} \sum_{p\in\mathscr{C}_j\cup\{j\}} L_{ik} \hat{M}_{kp} L^T_{jp} - \sum_{k\in\mathscr{C}_j} L_{ii} \hat{M}_{ik} L^T_{jk} \tag{3.28}$$

Equations (3.25)- (3.28) allow the computation of all terms of the projected matrices. *In the classical SDTools notations corresponding to the CMS nomenclature, one identifies the matrix* $[\tilde{T}_{ij}]$ *as a recursive projection of* $[L]$

$$\left[\tilde{T}_{ij}\right] = \begin{cases} -\left[D_{ii}\right]^{-1}\left[\hat{K}_{ij}\right] & \text{if } j \in \mathscr{P}_i; \\ \mathscr{I} & \text{if } i = j; \\ 0 & \text{otherwise.} \end{cases} \tag{3.29}$$

In the following, matrices and vectors superscripted with a tilde indicate recursively written bases. The recursive notion is kept for the presentation as it is the base of the algorithms classically presented in the literature. The composite example given in the Figure 3.5, shows in particular that each leaf is connected to its parent by one side and the root by the other side. The restitution is then formulated in a recursive way, which can be written as

$$q_i = \tilde{q}_i + \sum_{j \in \mathscr{P}_i} \left[\tilde{T}_{ij}\right] q_j \tag{3.30}$$

A recursive definition of the restituted projection basis can be expressed as

$$\left[T_{ij}\right] = \left[\tilde{T}_{ij}\right] + \sum_{k \in \mathscr{P}_j} \tilde{T}_{ik} T_{kj} \tag{3.31}$$

Fig. 3 of the composite component provided in Chapter 1 helps as an illustration. To recover the full displacement on leaf vertex #1, the restitution must already been proceeded for the root vertex #3. The leaf displacement depends on the displacement on the separator#3. Recursively, the displacement of #2 depends on #3 as well, which generates cross coupling terms.

$$\begin{cases} q_3 = & \tilde{q}_3 \\ q_1 = \tilde{q}_1 + \tilde{T}_{13} & q_3 \end{cases} \tag{3.32}$$

As a result the full restitution on q_1 is

$$q_1 = \tilde{q}_1 + \tilde{T}_{13}\tilde{q}_3 \tag{3.33}$$

At this stage, an iterative Guyan condensation has been performed for a structure decomposed into sub-domains. One seeks then a reduction basis diagonalizing the stiffness matrix, whose topology follows the initial stiffness topology.

$$[T] = \left[T_{ij}\right]_{1\leq i,j\leq N} \tag{3.34}$$

where $[T_{ij}] \neq [0]$ *if* $j \in \mathscr{P}_i$ *and* $j > i$. *Using equation* (3.31) *to represent the full condesation basis, the system reduction can be represented as*

$$[T_R] = [T]\,[\Phi] \tag{3.35}$$

where $[\Phi]$ *represents the modes* ϕ_i *of each vertex on which all lower level condensations have been performed, which can be represented as*

$$[T_R] = \begin{bmatrix} \mathscr{I} & \dots & T_{1i} & \dots & T_{1N} \\ \vdots & \ddots & \vdots & \ddots & \vdots \\ 0 & \dots & \mathscr{I} & \dots & T_{iN} \\ \vdots & \ddots & \vdots & \ddots & \vdots \\ 0 & \dots & 0 & \dots & \mathscr{I} \end{bmatrix} \begin{bmatrix} \phi_1 & \dots & 0 & \dots & 0 \\ \vdots & \ddots & \vdots & \ddots & \vdots \\ 0 & \dots & \phi_i & \dots & 0 \\ \vdots & \ddots & \vdots & \ddots & \vdots \\ 0 & \dots & 0 & \dots & \phi_N \end{bmatrix} \tag{3.36}$$

The matrices obtained by the reduction phase are much smaller in size than the initial ones. Thus, the reduced stiffness matrix $[\mathscr{K}]$ *obtained is diagonal, with*

$$\begin{cases} [\mathscr{K}_{ii}] & = [\phi_i]^T [D_{ii}] [\phi_i] = \begin{bmatrix} \ddots & & \\ & \omega_i^2 & \\ & & \ddots \end{bmatrix} \\ \left[\mathscr{K}_{ij}\right] & = 0 \qquad\qquad i \neq j \end{cases} \tag{3.37}$$

The mass matrix diagonal blocks $[\mathscr{M}]$ *are diagonal thanks to a reduction basis normalization per substructure. Coupling blocks are usually full and are not simplified for the projection. The final system size is directly the sum of each reduction basis size,*

$$\begin{cases} [\mathscr{M}_{ii}] & = [\phi_i]^T \left[\hat{M}_{ii}\right] [\phi_i] = [\mathscr{I}] \\ \left[\mathscr{M}_{ij}\right] & = [\phi_i]^T \left[\hat{M}_{ij}\right] [\phi_i] \quad \text{full if j} \in \mathscr{P}_i \end{cases} \tag{3.38}$$

The only solution to reduce coupling computation times is to perform substructure reduction before coupling. An information loss thus occurs, whose control is not as easy as seemed in the first developments of Kaplan [201], and still as an open reseach field. A practical implementation of sequencing the operations leads to several algorithm philosophies classically Lazy ones or Greedy ones [201]. Thus, the global procedure used in this section is split in 7 phases. The implementation is described in the Appendix A, from step 16 to 20 as following :

1. Input: M, K, DOF
2. Graph partitioning and matrix reordering
3. Multi-level static condensation
4. Matrices projection
5. Resolution
6. Restitution
7. Output: $SE_i, [\mathscr{M}], [\mathscr{K}], [\phi_j], [\omega_j], [T]$

The graph partitioning is performed by groups of elements. The recursive projection basis of $[T] = [\tilde{T}]^{-1}$ is applied and it is the base of all AMLS variants. The matrix projection is critical as the mass projection cost is very sensitive to the implementation. The reduction bases are eventually computed in this step. The resolution in step 5 is performed using a standard Lanczos algorithm. The solution is then restituted and the outputs are obtained [213].

3.4 Introduction to mode shape expansion technique using MOR methods

The concept of model reduction and MSE techniques play a significant role, especially when comparing a large analytical set of DOF with relatively small experimental measurements[8]. Techniques of model reduction that are well established for more conventional materials and structures as MODAL transformations [111], [112], STATIC or Guyan condensation [108], CMS [9] and FBS [200] methods have been used extensively in the past, and are still very popular in engineering in order to reduce the complexity and the size of computational models.

[8]The experimental measurements are critical for the success of any structural dynamic analysis and contain characteristics that cannot be obtained analytically [137].

Traditionally, interface model reductions [118] are used to estimate the motion at interfaces DOFs by the motion of sensors using EMA, where the EMA plays a significant role in the correlation and updating of analytical models in terms of FRFs. Many approaches to correlate analytical modeling require the measurements of FRFs to be available at the full set of finite element DOF. Likewise, model updating at the set of tested DOF requires the large model to be reduced to a much smaller size but without distortion of the reduced model.

Coupled or paired predictions can also be estimated using MSE techniques. They can basically be distinguished by two groups to characterise paired predictions in structures: unmodified structures, see [215] for more details, and modified structures illustrated in [137]. The difference between the two groups is basically that the first group needs to impose some of the measurement points on the interface and in the second it is not needed.

The methodology presented by Balmès, Corus in [138] and by Billet [137] combines techniques offering the advantages of the second group of paired predictions consisting of: a local FE model, classical theory of structural modification by pairing it with mode shape expansion and CMS with interface model reduction method (subspace selection). The use of different mode shape interpolations is distinguished by *using or not using modifications as an indicator for the validity of coupled predictions* in [118], [138], [137], [211]. This combination of experimental measurements and theoretical results were referred to in the introduction as hybrid analysis, and it will be evaluated in this work using different condensation algorithms established in [106] to estimate the responses of all DOF of the interface of the CFRP component defined by the motion of sensors applying MSE methods. The mode shape interpolation algorithms are based on: STATIC [108], SEREP [111], MODAL [112], DYNAMIC [134], MDRE [135] and MDRE-WE [136] detailed in [118], [121]-[124], [137], [138], [154] and [213]. Thus, these advance interpolation methods can be performed to determine the paired predictions in the CFRP component for unmeasured DOFs in a CFRP component based on the experimental measurements (FRF), the curve-fitting performed with the IDRC and IDRM algorithms, and the updated stiffness parameters of the full FE model obtained with the MNET for comparative purposes versus the CBMOR.

3.4.1 Theoretical background

Initially, the theoretical background of the MSE methodologies combining different techniques was established as a close loop prediction problem for structural modifications. The knowledge

of the close loop prediction problem between the physical and the analytical model is used in the industry applying experimental measurements, and the finite element method (FEM) to reduce the cost of prototypes components [137]. A number of steps are described in [137] such as: experimental measurements, form of the lineal differential equation, dealing with continuous interfaces and the evaluation of the error. Some of these steps were introduced in Chapters 1 and 3 and they are adapted from [137] for the objective of this work. A brief description is introduced in the following subsections.

3.4.2 Experimental measurements

The experimental measurements described by the FRF, $H(\omega)$ were defined as the ratio of the transformed excitation in Eq. (1.10). Thus, the FRF of Eq. (1.10) is the receptance matrix obtained in Eq. (1.11), where the mass $[M]$, damping $[C]$ and stiffness $[K]$ matrices are dependent on physical parameters such as material's density, Young's and shear moduli and Poisson ratio. Moreover, the IDRC and IDRM algorithms were established to perform the curve-fitting to obtain the modal parameters in Chapter 1.

3.4.3 Form of the linear differential equation

It is considered only second order models of the form, (previously introduced in section 3.2 and reintroduced in this section to perform MSE)

$$\begin{aligned} \left[[M]s^2+[C]s+[K]\right]_B\{q_B(s)\} &= [b_{IB}]\{u_{IB}(s)\} \\ \{y_{IB}(s)\} &= [c_{IB}]\{q_B(s)\} \end{aligned} \tag{3.39}$$

where (s) is the Laplace variable, $[M],[C],[K]$ are the mass, damping and stiffness matrices, respectively, $\{q_B(s)\}$ are the generalised degrees of freedom (DOFs) of the base, $[b_{IB}]$ and $[c_{IB}]$ are the input and output matrices of the base interface, respectively, $\{u_{IB}(s)\}$ are the inputs describing the time/frequency dependence, and $\{y_{IB}(s)\}$ are the physical outputs of the base interface defined in [118], [121]-[124], [137], [138], [154] and [213]. Note that the input/output shape matrix formalism decouples the choice of DOF $\{q_B(s)\}$ from the choice of $\{u_{IB}(s)\}$ and $\{y_{IB}(s)\}$ [137]. The $[b_{IB}]$ and $[c_{IB}]$ are Boolean matrices of the base interface of the full FE models with compatible interface meshes. Considering the response of an elastic structure to

applied loads $F(s) = [b_{IB}]\{u_{IB}(s)\}$, the exact response at a given frequency $[H(s)]$ is given by:

$$[H(s)] = [c_{IB}]\left[[M]s^2 + [C]s + [K]\right]_B^{-1}[b_{IB}] = [c_{IB}]\,[Z_B(s)]^{-1}\,[b_{IB}], \tag{3.40}$$

where $[Z(s)]$ is the dynamic stiffness. The interest of writing the transformation of the DOFs in this way, per Balmès, Corus and Billet, is the easy translation of $[b_{IB}]$ and $[c_{IB}]$ denoted by *IB* in the subscript. For the coupled prediction in the CFRP component one assumes that the modification of the stiffness parameters can be modeled with the FE model in the base interface (denoted as *IM* subscript and *M* superscript). Thus, one can write the modification of the model in the form

$$\begin{bmatrix} [Z^M_{II}(s)] & [Z^M_{IC}(s)] \\ [Z^M_{CI}(s)] & [Z^M_{CC}(s)] \end{bmatrix} \begin{Bmatrix} \{y_{IM}(s)\} \\ q_C(s) \end{Bmatrix} = \begin{Bmatrix} \{u_{IM}(s)\} \\ \{0\} \end{Bmatrix}, \tag{3.41}$$

where the interface of DOFs explicitly appears as DOFs of the model, see [121]. The Division of the DOFs is divided into two groups.– active or interface DOFs denoted by *I* in the subscript, complementary, denoted by *C* in the subscript – observed in Eqs. (3.41) and (3.42). *Using the framework of Ritz methods, the coupled prediction is obtained by imposing displacement continuity on the base interface* ($\{y_{IB}(s)\} = \{y_{IM}(s)\}$)*, and projecting the associated model on loads dual to the displacement subspace admissible under the continuity constrain. The projection thus combines continuity and dynamic equilibrium loads* ($\{u_{IB}(s)\} = \{u_{IM}(s)\}$)*. The base model given by Eq.* (3.39) *and a modification described by Eq.* (3.41) *in [137] leads to*

$$\begin{aligned} &\begin{bmatrix} [Z_B(s)] & 0 \\ 0 & [Z^M_{CC}(s)] \end{bmatrix} + \begin{bmatrix} b_{IB}(s) \\ 0 \end{bmatrix} [Z^M_{II}(s)] \begin{bmatrix} c_{IB} & 0 \end{bmatrix} + \begin{bmatrix} b_{IB}(s) \\ 0 \end{bmatrix} \begin{bmatrix} 0 & Z^M_{IC}(s) \end{bmatrix} \\ &\qquad + \begin{bmatrix} 0 \\ Z^M_{IC}(s) \end{bmatrix} \begin{bmatrix} c_{IB} & 0 \end{bmatrix} \begin{Bmatrix} q_B(s) \\ q_C(s) \end{Bmatrix} = F(s) \end{aligned} \tag{3.42}$$

For $\{q_B(s)\}$ and $\{q_C(s)\}$ corresponding to FEM DOFs, $[b_{IB}]$ and $[c_{IB}]$ are the input and output Boolean matrices of the base interface respectively. Equation (3.42) corresponds to the standard assembly process established in [137]. For the applications considered in [106], the $\{q_B(s)\}$ are defined in modal coordinates and $\{q_C(s)\}$ corresponds to fixed interface modes of a Craig-Bampton model [137].

Table 3.1 Operator $[T_G]$ using different model order reduction methods applied to mode shape expansion methods.

MODAL/SEREP	$\{q_I(s)\}=[c_{IT}][T_G]_{MODAL/SEREP}\{y_T(s)\}$
STATIC	$\{q_I(s)\}=[c_{IT}][T_G]_{GUYAN}\{y_T(s)\}$
DYNAMIC	$\{q_I(s)\}=[c_{IT}][T_G]_{DYNAMIC}\{y_T(s)\}$
MDRE	$\{q_I(s)\}=[c_{IT}][T_G]_{MDRE}\{y_T(s)\}$
MDRE-WE	$\{q_I(s)\}=[c_{IT}][T_G]_{MDRE-WE}\{y_T(s)\}$

3.4.4 Dealing with continuous interfaces

The incompatibiliy between the discretisation of the FE model $\{y_I(s)\}$ and the experimental measurements $\{y_T(s)\}$ is documented in [137]. A highlight of this methodology assumes that exists a constant coefficient linear combination $[c_{IT}]$ relating the interface $\{y_I(s)\}$ and the test displacements $\{y_T(s)\}$ for the coupled response.

$$\{y_I(s)\} \approx [c_{IT}]\{y_T(s)\}. \tag{3.43}$$

This relation imposes a strong constraint on the interface kinematics since $\{y_I(s)\}$ must be approximated by a subspace of basis $[T_G]$ that dimension is smaller than the number of sensors used. The choice of this subspace $[T_G]$, and the justification of its ability to represent the coupled response, is a key aspect proposed in [137]. The construction of a reduced interface model ($[T_G]$ subspace) is a classical extension of CMS addressed in the literature [117], [118]-[123] using a Craig-Bampton type reduction of the modification where the constraint modes are replaced by the low order modes of the model statically condensed on its interface [137], as originally proposed in [9].

For this study, the updated FE model elaborated with triangle elements [76], [84], [104] [149] is used to deal with the incompatibility of the interface between the FE model and the experimental measurements. The main purpose of using this updated FE model is to allow the interpolation of test motion at an arbitrary number of DOF of the interface to analyze the influence of the subspace-basis $[T_G]$ based on MOR methods in the CFRP component, (see Table 3.1). The subspace $[T_G]$ is defined on the DOFs of a local part of the updated FE model $[c_{IL}]$ including or not the modification, (see Fig. 3.6).

The extraction of the interface of motion $\{y_I(s)\}$ using the updated FE model is thus written as

$$\{y_I(s)\} = [c_{IT}][T_G]\{y_G(s)\}. \tag{3.44}$$

An observation matrix $[T_G]$ can be constructed relating the $\{q_L(s)\}$ (DOFs of the updated FE model) with measurements $\{y_T(s)\} = [c_{TL}]\{q_L(s)\} = [c_{TG}]\{y_G(s)\} = [c_{TL}][T_G]\{y_G(s)\}$, (see [122] for possible methods). The estimation of the generalised motion of the interface $\{y_G(s)\}$, denoted by G in the subscript, can be established as

$$\{y_G(s)\} = [c_{GB}]\{q_B(s)\}. \tag{3.45}$$

The standard approach to estimate the full response using different subspace-based expansion methods in [123] and [137] is then obtained by minimising test error (distance between the test data and the associated response for the expanded shape). The minimum is generally obtained by solving the least squares problem as

$$\{y_G(s)\} = \underbrace{Arg\ min}_{\{y_G\}} || [c_{TG}]\{y_G(s)\} - [c_{TB}]\{q_B(s)\} ||^2 \tag{3.46}$$

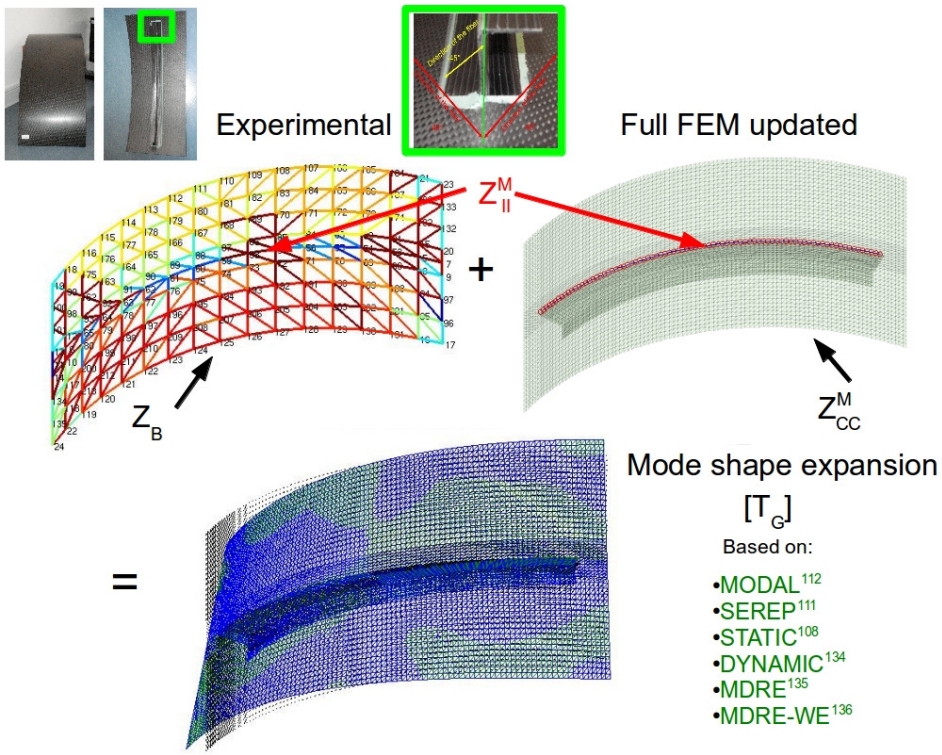

Fig. 3.6 MSE process.

whose solution is given by

$$[c_{GB}] = [c_{TG}^T c_{TG}]^{-1} [c_{TG}^T c_{TB}] \tag{3.47}$$

which leads to the observation Eq. (3.43) *with* $[c_{IT}] = [c_{IL}][T_G][c_{GB}]$.

The given assumption (3.44)*, the second block row of Eq.* (3.41)*, describes the motion of the modification*

$$[Z_{CC}]\{q_C(s)\} = -[Z_{CI}^M(s)][T_G]\{y_G(s)\}. \tag{3.48}$$

For the first block row it is assumed that the generalised loads are defined by projection on the subspace $[T_G]$ *of the form in*

$$\{u_{GM}\} = [c_{IG}]^T [Z_{IC}^M(s)]\{q_C(s)\} + [c_{IG}]^T [Z_{II}^M(s)][c_{IG}]\{y_G(s)\}. \tag{3.49}$$

The coupled response is obtained assuming dynamic equilibrium of generalised loads $\{u_{GB}\} = \{u_{GM}\}$ *established in* [137].

3.4.5 Evaluation of the error

It is necessary one way to evaluate the predictions based on many assumptions by introducing error evaluation tools [137]. The evaluation of the error in the correlation in this study is analyzed applying a modal assurance criteria (MAC) based on the eigenfrequencies and eigenvectors divided into four parts. In the first part, the MAC of experimental measurements versus the updated stiffness parameters of the full FE model is analyzed. The MAC is one of the most useful comparison methods that relies on the eigenvector information, see Eq. (2.1).

In the second part, the MSE methods are calculated to estimate the interface motion $\{y_I(s)\}$ using the experimental measurements, curve-fitting performed with the IDRC and IDRM algorithms, set-up of sensors, and full FE model results.

In the third part, once $\{c_j\phi_{id}\}$ and $\{c_j\phi_k\}$ are defined at sensors, it is proposed to obtain the stiffness and mass-weighted criterias, K-MAC and M-MAC, (see Eqs. (3.50) and (3.51) respectively), also called cross-generalised mass (CGM) and the less used cross-generalised stiffness (CGK) to observe the influence of the MOR using MSE methods. The K-MAC and

M-MAC values closer to 1 or 100 represent a higher agreement, and these values are being interpreted in the same way as the MAC [106].

$$MAC-K=\frac{|\sum_{j=1}^{l}\left\{c_j\phi_{id}\right\}^H[K]\left\{c_j\phi_k\right\}|^2}{|\sum_{j=1}^{l}\left\{c_j\phi_{id}\right\}^H[K]\left\{c_j\phi_{id}\right\}||\sum_{j=1}^{l}\left\{c_j\phi_k\right\}^H[K]\left\{c_j\phi_k\right\}|} \tag{3.50}$$

$$MAC-M=\frac{|\sum_{j=1}^{l}\left\{c_j\phi_{id}\right\}^H[M]\left\{c_j\phi_k\right\}|^2}{|\sum_{j=1}^{l}\left\{c_j\phi_{id}\right\}^H[M]\left\{c_j\phi_{id}\right\}||\sum_{j=1}^{l}\left\{c_j\phi_k\right\}^H[M]\left\{c_j\phi_k\right\}|} \tag{3.51}$$

The implementation of these criteria supports the original methods for reducing the mass on the sensor set that used vectors defined at DOFs implemented in [106] based on the mass and stiffness matrices of the full FE model.

The fourth part is evaluated once the stiffness parameters are updated with the MNET to observe the impact of the stiffness and mass matrices in the interface motion applying subspace-based expansion methods using the K-MAC and M- MAC criteria.

Part II

Application of the Craig-Bampton model order reduction method to a CFRP component using the MNET

Chapter 4

Application of a MNET to a CFRP component

4.1 Introduction

Five ideas were illustrated in this work to verify the feasibility to use the CMS applied to CFRP establishing a MNET.

Firstly, the CFRP component is analyzed and tested in its free/free configuration using a SLDV. The accuracy of the FRFs generated with EMA are critical to understand the behaviour between the properties of the CFRP component illustrated in this Chapter, (see section 4.2), and the forthcoming full and reduced FE models.

Secondly, in section 4.3, the curve-fitting or parameter estimation of the experimental CFRP component is performed using the pole/residue parametrization [152] through the IDRC and IDRM algorithms. This step is particularly critical if one wants to compare the full FE and reduced models with the experimental results using the natural frequencies and normal mode shapes. The curve-fitting of the experimental results, introduced in section 1.1.4, enables a quantitative comparison between the experimental measurements and the FEM models denoted as normal modes analysis in FEM terminology.

Thirdly, the idea of the MNET approach is divided in two parts. In the first part is analyzed the stiffness parameters obtained with different MNET methodologies to use as a initial stiffness parameters including Poisson's ratio values during phase transformation in polymer gels, see section 4.4. The evaluation of these initial stiffness parameters versus the curve-fitting

performed is needed to assess the level of correlation between the experimental model and a numerical FEM result. A normal mode analysis is performed using the FEM to obtain the natural frequencies and normal mode shapes of these initial parameters. The application of the FEM allows to obtain an accurate result of the stiffness parameters that affect the dynamic behaviour of the CFRP. A convergency analysis is performed to select the FE model. The pshell, CTRIA3, and S3 element formulations [106], [148], and [151] are used for comparative purposes.

The second part consists of performing a DOE with the best MAC results of the initial stiffness parameters evaluated to improve the MAC results updating the stiffness parameters, see section 4.5. In this part is analyzed how the stiffness parameters affect the MAC response (main effects and interaction of the stiffness parameters). A convenient correlation (also called normalization) is deemed adequeate if the orthogonallity (XOR) and cross-orthogonallity using the MAC of the diagonal term matrices meet > 0.90 and the off-diagonal terms < 0.10. The XOR and the MAC provide similar information about the experimental accuracy. The XOR matrix indicates the goodness of the mass distribution in the full and reduced FE models [178]. The MAC can also be used to indicate the accuracy of the mode shapes of reduced FE model using the CBMOR method or a mode shape expansion technique based on Ritz vectors. Moreover, different modal correlation criteria (COMAC, COMAC-S, eCOMAC, MACco) are used to validate the MAC correlation.

Fourthly, once is obtained and validated the stiffness parameters of the full FE model with the established MNET, (see Chapter 5), the idea is to perform a model reduction in terms of CBMOR of a full FE component model on the basis of the exact system modes using Ritz vectors[1]. The Ritz vectors improve the accuracy-cost ratio and the CBMOR method based on the Rayleigh-Ritz approach is used to improve the accuracy-time ratio. This CBMOR was previously used in [203] and [212] to generate extremely compact models that have similar modes, illustrated in Chapter 6. Thus, the components and interface models are then generated into SDTools [106] using super-element utilities to manage further computations [118], [154]. Extensions of CMS to reduce the error in the reduced model proposed by Kaplan [201] and Bennighof [208] are implemented in [106] applying the automatic multi-level substructuring

[1] Application of the Craig-Bampton model order reduction and AMLS methods based on the Rayleigh-Ritz vector approach [106], [117], [118].

(AMLS) for frequency response analysis of structures implemented in MATLAB[2] based on the updated stiffness parameters of the CFRP.

The final idea is associated with the ability to use the different modal assurance criteria and modeshape expansion [122], [123], [124], [137], [138] and [211] to estimate the quality of the updated stiffness parameters in the full and reduced FE models based on the observation of particular measurements at sensors. A number of mode shape expansion techniques are applied based on the basis of reduction methods introduced in [118], [122], [123] and [137] to validate the updated material properties obtained with the MNET consisting of: experimental measurements, a local FE model, classical theory of structural modification by coupling it with mode shape expansion and CMS with interface model reduction method (subspace selection).

4.2 Experimental measurements of a CFRP component

All the experimental measurements are performed with the scanning Laser Doppler Vibrometer (SLDV) constituted by: Polytec controller OFV-5000 with junction box, LASER head scanhead PSV400, shaker LDS V406, power-amplifier LDS PA100, Stinger with length of 65mm and a force transducer Dytran 1051V3 (Sensitivity: 81.32N/V) for both the signal generation and data acquisition, as shown in Fig. 4.1. The SLDV offers unique advantages compared to using traditional surface mounted accelerometers [140] [141], such as high-precision definition of the measurement points [142] [143]. It is a complete and compact system including a sensor head, a PC with DSP boards and Windows NT-based application software packages [139]. The SLDV employs a laser to sweep over the structure continuously while measuring, capturing the response of the structure from a moving measurement point. Various methods have been devised to determine mode shapes of the structure everywhere along the scan path measurement [139]. The SLDV and shaker-transducer can be used to estimate the modal parameters of a structure (defined by the natural frequency, the modal damping and the mode shape for each mode) [140]. Moreover, the hammer-microphone [31], and the loudspeaker- microphone [43], [44], [45] can be also used with the SLDV to estimate modal parameters. Several studies are achieved with very close results to theoretical predictions using a SLDV with conventional as well as non-conventional materials [29], [131] and [215] .

[2]The implementation of AMLS in MATLAB is included in the SDTools license adquired for the TU-Berlin. In Appendix 3 is archived an example in ABAQUS using substructures without AMLS as part of the research for comparative purposes.

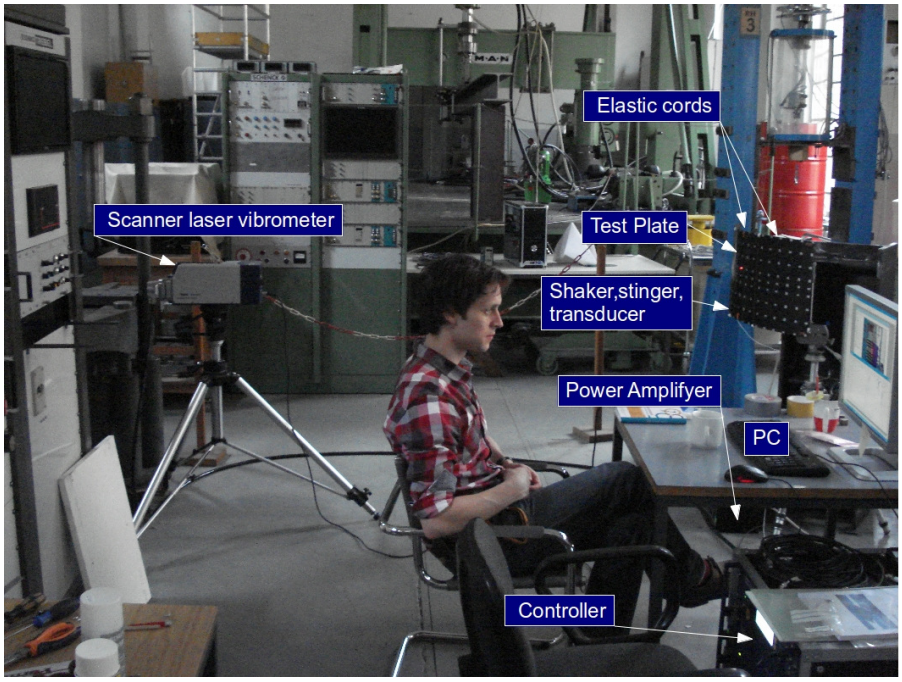

Fig. 4.1 Experimental set up.

Generally, the estimation of the modal parameters using an SLDV can be established in three steps: structure excitation, measuring the response motion in the response points and post processing the vibration data [178]. These three steps are introduced in the next sections.

Step 1: Structure excitation

Three basic assumptions are established to *excite the structure*: the excitation must be *linear, time-invariant* and *observable* [178]. For a structure being *linear*[3] means, that the response of the structure to any combination of forces, simultaneously applied, is the sum of the individual responses to each of the forces acting alone [178].

The *time-invariant* assumption is related to the modal parameters. These modal parameters are constants[4] to be determined. Assuming a structure to be *observable* means, that the input-

[3]The linear assumption has three implications for FRF. Firstly, the FRFs are not dependent on the type of excitation waveform used to excite the structure. Secondly, measured FRFs are independent of the excitation level. The last implication of linearity on FRFs is related to the reciprocity. This implies that the FRFs measured between two DOFs are independent of the ones that are used for excitation or response [178].

[4]A system that is not time-invariant has components whose mass, stiffness or damping depends on factors that may vary with time [178].

output measurements have to contain enough information to generate an adequate behaviour model of the structure [178]. Furthermore, another assumption that might have to be made, concerns *repeated roots*[5]. *The experimental set up and parameter estimation algorithm chosen may allow the determination of* ***repeated roots*** *upon a limited ability to gather and process data respectively* [178]. Another key test configuration factor is the type of support of the CFRP structure to be tested: *"free"* or *"grounded"* conditions. *Free boundary condition*[6] is particularly important in this study to validate the stiffness matrix of a CFRP component. *Free boundary condition* means that the structure is not attached to the ground and is freely suspended in space. The CFRP component should not contain any grounding effects over all the structure. The reason for this is that it is very difficult to provide a sufficient enough rigid base or fixturing mechanism in order to attach the object to be tested. In other words, it is difficult to approximate the grounded condition without taking the extraordinary precautions that make this condition impractical to implement in a variety of applications. Whereas the grounded condition is difficult to approximate, it is feasible to provide a test article with a suspension system that closely approximates the free condition. This can be archived by suspending the structures from very soft elastic cords [178].

Measurements in modal testing are usually made under controlled conditions. A shaker LDS V406 and a stinger with length of 65mm and a force transducer Dytran 1051V3 are used to *excite the structure* that produce a *sinusoidal vibration velocity*[7] signal on the line of sight of the SLDV (out-of-plane), (see Fig. 4.1). The input (excitation) force is measured using a force transducer with a stinger in combination with a charge to CCLD converter in order to record the excitation in the transverse direction. The shaker can be found at node 17, (see Figs. 4.2a and 4.2b) that is located in the left bottom corner. The reason to use a stinger is to ensure that the shaker will only impart force to the structure along the axis of the stinger [178].

[5] *Repeated roots refer to the situation where one complex root or eigenvalue occurs more than once in the characteristic equation. Each root with the same value has an independent modal vector or eigenvector. This situation, which is critical in developing a truly complete modal model, can only be detected by the use of multiple inputs or references. However, sometimes the occurrence of repeated roots is in theory easily predictable and it can be assumed, even if it is not being measured and included in the modal parameters estimation process* [178].

[6] In this condition the structure will exhibit rigid body modes, which are merely determined by its mass and inertia properties and where there is not bending or torsion at all. Theoretically, any structure will disclose six rigid modes and each of these modes has a natural frequency of zero Hz [178].

[7] The sinusoidal vibration velocity is defined on the SLDV as $v_z(s,t) = V_a(s)\cos\omega t + V_b(s)\sin\omega t$ where v_z is the vibration velocity of a point in direction z, perpendicular to the surface nominally in the plane $x-y$, at frequency ω, s is the distance of the point along a scan line and V_a and V_b are in-phase and quadrature coefficients relative usually an input force signal [143].

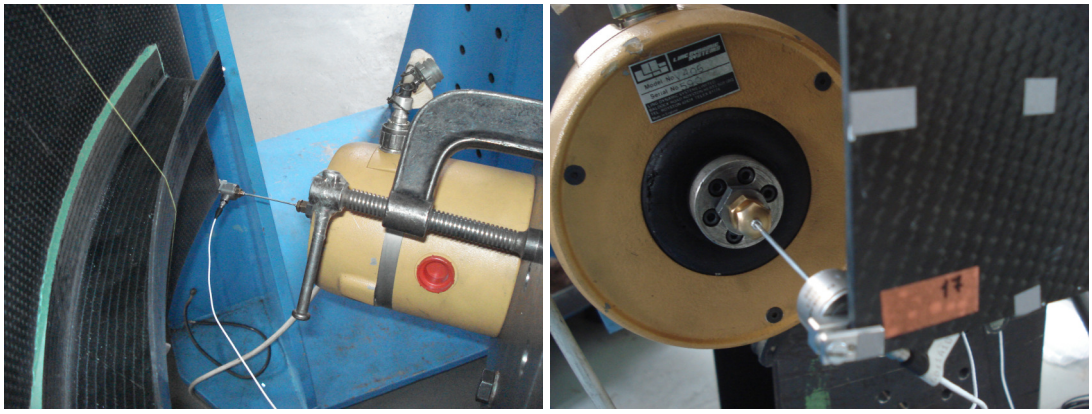

(a) Shaker-transducer view 1 (b) Shaker-transducer view 2

Fig. 4.2 Single-point excitation technique

The excitation signal selected is a periodic chirp averaged[8]. A number of excitation signals exists for making shaker measurements with fast Fourier transform analyzers (FFT). Reflective foil is used to acquire the response measurement location, including the *driving point measurement*[9] introduced in measuring the response motion, (see Figs. 4.3 and 4.4, respectively).

Step 2: Measuring the response motion

Once the structure is excited with the shaker, input and output quantities need to be measured with the transducer[10]. The maximum vibration level expected during the test should not exceed one third of the transducer shock limit [178]. The quality of the FRF responses is a crucial factor for the final outcome in this study. The response motion of the EMA is defined on the whole surface forming a geometric grid[11] constituted of 153 sensor points along the surface

[8]Periodic chirp average is calculated by squaring all the values, adding the squares together, dividing by the number of measurements (ten, in this case), and taking the square root of the results.

[9]If the response and direction of the measurement point coincided with the excitation point and direction, it is often called a *driving point measurement* [178].

[10]The force induced by the shaker is measured by a force transducer. The transducers needed to be selected to record force and motion. The piezoelectric type is the most widely in modal testing. Piezoelectric transducers are electromechanical sensors that generate an electrical output when are subjeted to vibration, in general, they have wide and dynamic operational ranges and good linearity. Sensitivity is measured in terms of voltage/force in force transducers, typically, with units of (V/lbf) or (mV/N), and it is measured in terms of voltage/acceleration (mV/g) in accelerometers [178].

[11]The grid of points is also known as test-analysis model (TAM).

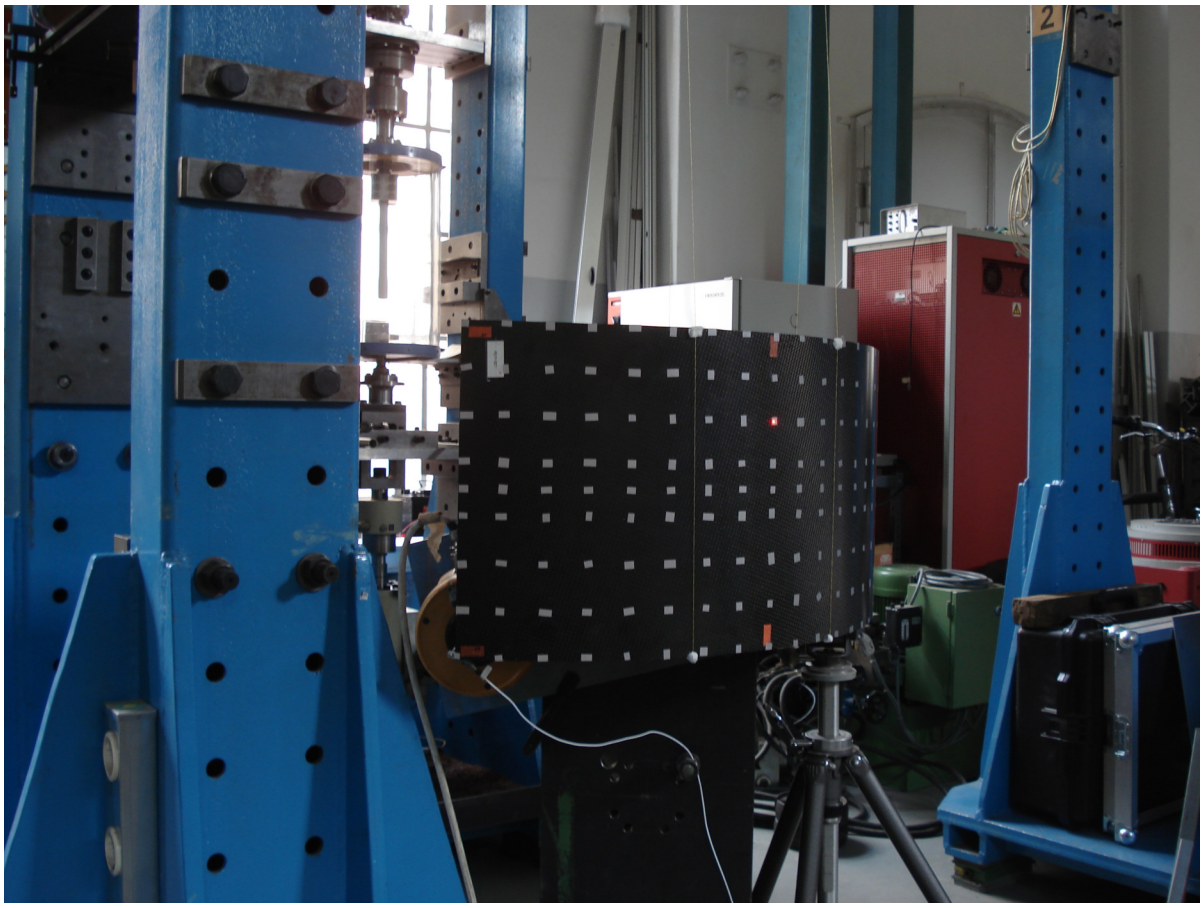

(a) Foil over the CFRP and cords set up

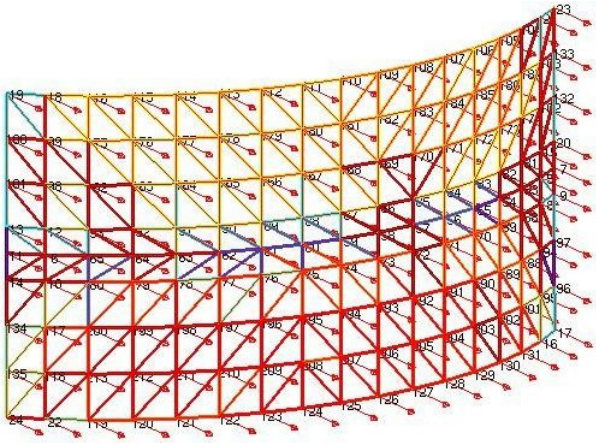

(b) Test-analysis Model
(TAM) 153 Y-Sensors

Fig. 4.3 Test set up

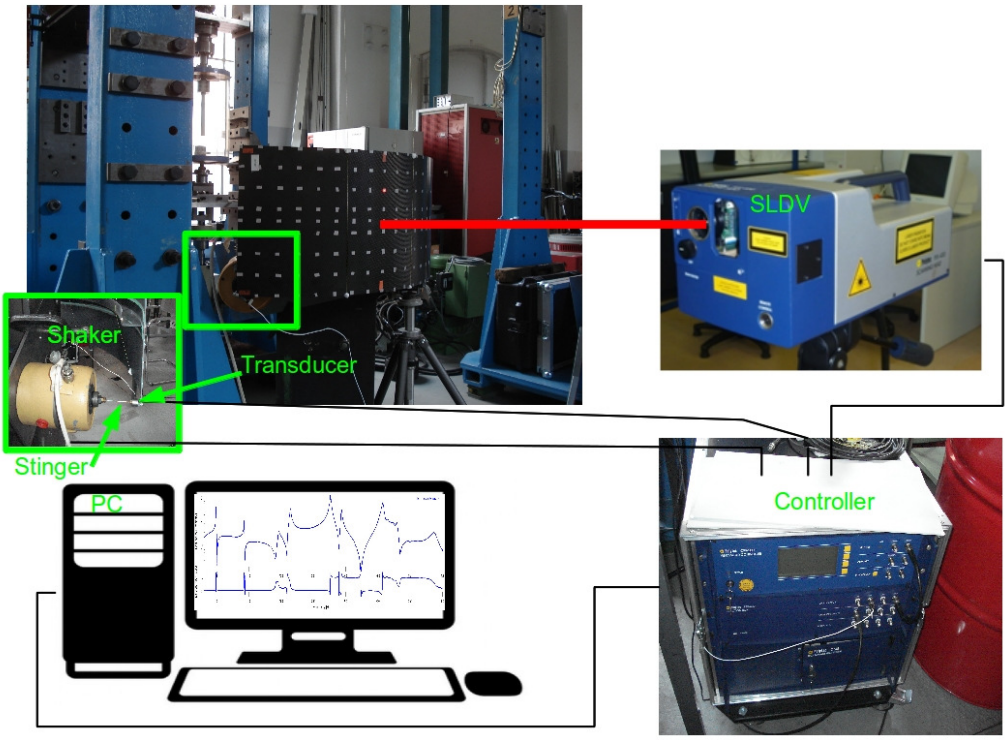

Fig. 4.4 SLDV and Driving point measurement set up (green square).

displayed in Figs. (4.3a) and (4.3b), respectively. The measured points consist of a series of vibration measurement data responses [143], generally measured FRF, that can be scanned at each single point, (see Fig. 4.4). *Even when the system has been proven to behave linearly and the excitation applied and supporting system selected are appropiate to avoid the measurement error, still some noise will be present in the measurement process. Noise is a general designation describing the difference between the true value and the estimated value of the response. A more exact designation is to view noise as the total error comprised of two terms,* variance[12] *and* bias[13]. *Each of these classifications is merely a convenient grouping of many individual errors that cause a specific kind of inaccuracy in the frequency response function estimate* [178].

Step 3: Post-processing the vibration data

The post-processing of the modal parameters throughout this work is performed from a set of FRF measurements obtained with the SLDV, (see Fig. 4.5). The FRFs describe the input-output relationship between two single response DOFs on the structure as a function of frequency [179]. Commonly, modal parameters are identified by curve-fitting using a set of FRFs. In general, curve-fitting is a process of matching a mathematical expression to a set of empirical data points. This is usually done in two steps where the system poles, damping and modal participation factors are estimated in the first step and the mode shapes in the second using a DSA. *The DSA based on FFT analysis often have limitations of inadequate frequency resolution. This is especially true if multiple resonances occur at natural frequencies that are very close to each other. This problem arises because of the constrains imposed by the limited number of discrete points available, the maximum frequency range to be covered, and/or the length of time sample necessary to gather the data. To improve frequency resolution, the time length of the data record must be increased until the desired Fourier series frequency is achieved. Since most FFT analyzers calculate a fixed number of Fourier series frequencies, the only means by which higher resolution can be attained is to reduce the number of closely spaced set of Fourier series frequencies in the interval of interest* [178].

[12]The variance portion of the error essentially is Gaussian distributed and can be reduced by any form of synchronization in the measurement process. In the presence variance or random errors, the average response value in the limit, approaches the expected response value [178].

[13]The bias or distortion portion of the error causes the expected value of the estimated function to be different from the true value. In the presence of bias error, the average response value, in the limit, does not approach the expected respose value. Many bias errors can be removed or reduced in magnitude because their form and source

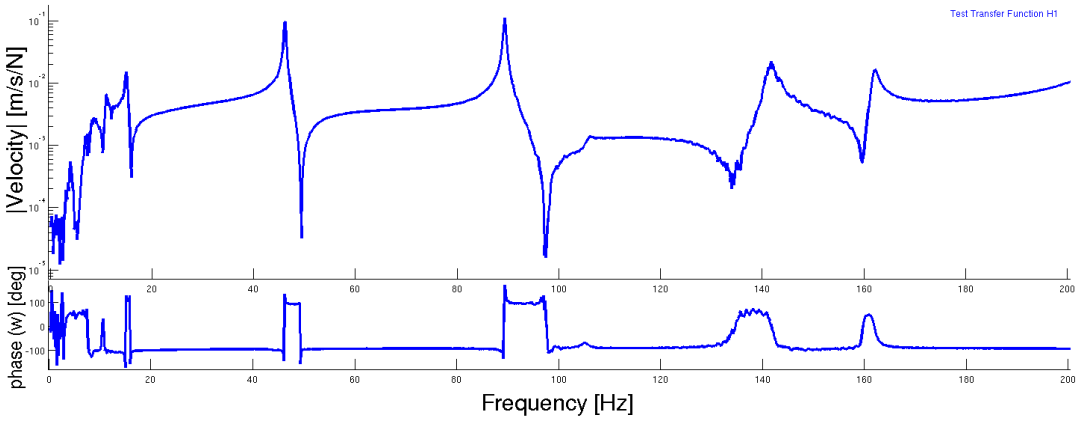

Fig. 4.5 Rigid Body Modes in the Composite Component Assembly are close to zero Hz

In other words, the common solution for finer frequency resolution is to "zoom in" on the frequency range of interest and to concentrate all the spectral lines into a narrow band. When using zoom to measure FRF in a narrow frequency range, it is important to ensure that there is as little vibration energy as possible outside the frequency range of interest [178].

The first step in determining if zooming is needed is to collect broadband FRF measurements that cover the entire frequency range of interest [178]. Subsequently and depending on the natural frequency density observed, zoomed FRF measurements are collected with the SLDV, (see Table 4.1). The post processing of FRFs obtained by curve-fitting is evaluated into two parts: firstly evaluating the correlation between the full FEM model versus the EMA and then evaluating the correlation between a reduced model applying the Craig-Bampton model order reduction[14](MOR) method versus the EMA.

4.2.1 Rigid Body Modes

In section 4.2 the experimental measurement set up was illustrated and discussed the way of selecting the support system for the composite component assembly. The free condition was preferred over the grounded condition. *It was stated that a very soft system of suspension will limit the structure rigid body modes to occur at very low frequencies relative to those at*

are predictable. Several approaches are available to reduce the error involved in frequency response functions measurements in FFT analyzer [178].

[14]The concept of reduced model using the Craig-Bampton model order reduction method was introduced in Chapter 3.

Table 4.1 Modal data acquisition parameters with a SLVD.

	Frequency Span (Hz)			
	0-1000	0-1600	30-400	30-800
DOF Measured (TAM DOF)	152	152	153	153
Frequency Span Length (Hz)	1000	1600	370	770
Lines of resolution	6400	6400	6400	6400
Window Function Type	Rectangular	Rectangular	Rectangular	Rectangular
Average Type	Complex	Complex	Complex	Complex
Number of Average per FRF	10	10	10	10

the first bending modes. "Very low" in this context means that the highest rigid body mode frequency must be 15% less than the lowest bending mode [178]. The composite component was suspended on very soft elastic cords in order to closely approximate the free condition. The assumption of linearity for the composite component was confirmed and the structure was also assumed to be observable and time-invariant. Fig. 4.5 shows the FRF in which the natural frequency of the first bending mode was detected. This measured response indicates that this bending mode occurs at approximately 49 Hz. Fig. 4.5, also reveals that the FRF peaks before 20 Hertz correspond to rigid body modes. *Therefore, it can be certained that the soft elastic cords selected do not interfere with the overall test article structural characteristics* [178].

4.2.2 Narrowband and Broadband Measurements

Broadband measurements of different frequency spans (fourth spans) were performed using the SLDV. The acquisition parameters of each frequency span performed in this study are displayed in Table 4.1. The response of the data points for each measurement was measured and acquired at 153 different locations (17×9), including the input location itself or reference distributed over the composite component curve surface, (see Fig. 4.3). A total of 1481 responses per sensor were taken of the composite structure standing in front of SLDV obtained a total of 226,593 data points.

Each recorded response for a particular location and direction was the product of an average of the response measurements for the same location and direction. The responses were measured by the direct reflection of the LASER beam using a reflective tape stick to the surface of the

specimen, showing evidence of some noise (describing by variance[15] and bias[16]) in certain nodes, such as the 5*y* sensor around 400Hz and 700 Hz in the frequency range until 1000 Hz, (see Fig. 4.6a), but the results were quite satisfactory in a narrowband from 30 Hz to 400 Hz, (see Fig. 4.6b). The FRF of the sensor 5*y* is presented in Figs. 4.6a and 4.6b, respectively, for comparative purposes between frequencies spans. The division of the frequency range into two narrower spans, one from 30 Hz to 400Hz and the other from 400 Hz to 800 Hz, was performed in order to capture all the target modes with sufficient resolution (reduced errors). The narrowband measurements revealed that a lower frequency resolution is desirable particularly in the 30-400 Hz frequency range illustrated in Fig. 4.6b. The identified poles and mode shapes are illustrated in Fig. 4.7 measuring velocity responses. The mesh covered the whole composite's surface.

The number of spectral lines for the measurements collected in each narrower spans (6,400 FRF) among other data adquisition parameters such as the type of average, number of average per FRF type and window function type, see Table 4.1. Each of the 6,400 FRF measured was obtained averaging the response estimated. The type of average used was complex. *Signal averaging can significantly reduce errors of variance and it is probably the most general technique in the reduction of errors in FRF measurements. By averaging several frequency-domain records together, statistical reliability can be increased and spurious random noise can be removed or reduced from the signals* [178]. There are a number of different window functions available. The rectangular window (used for windowing) gives the best approximation to the desired frequency response in a least square sense. The rectangular window gives the minimum integrated squared error from the ideal response [178]. Thus, the frequency response functions collected in the format UFF58[17] based on the modal data adquisition parameters established can then be used as an input for a modal paramenter estimation process applying curve-fitting algorithms in the next section.

[15] In the presence of variance or random errors, the averaged response value, in the limit, approaches the expected value [178].

[16] The bias or distortion portion of the error causes the expected value of the estimated function to be different from the true value [178].

[17] UFF is the industry standart format for storage geometry, DOF information and measurements, supporting both, ASCII and binary formats. Originally developed by the Structural Dynamic Research Corporation in the late 1960s, they facilitate the data transfer between test measurements and dedicate engineering software programs [144].

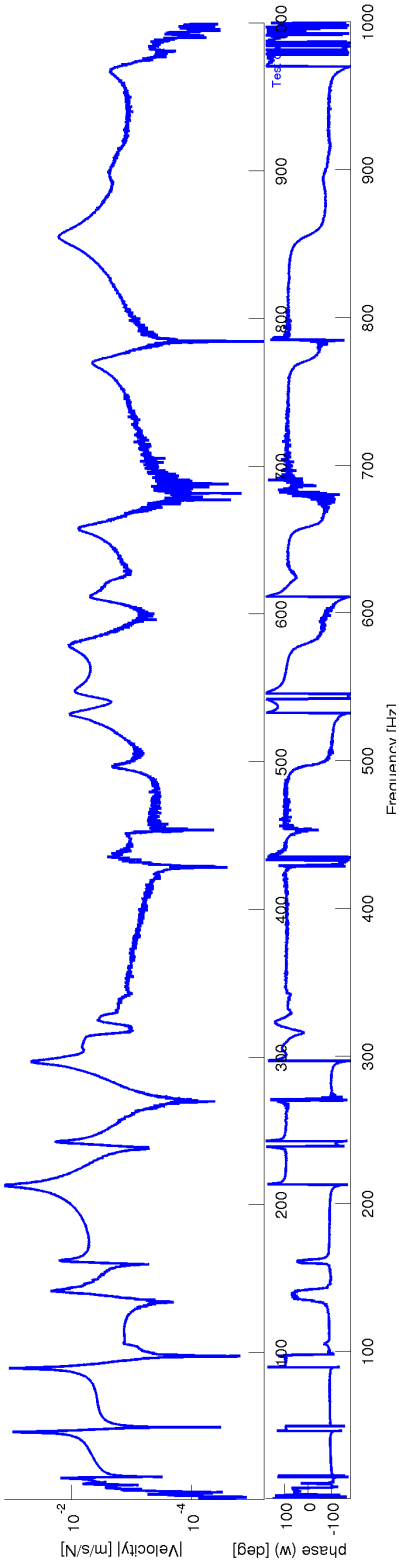

(a) Broadband from 0 Hz to 1000 Hz at sensor 5y.

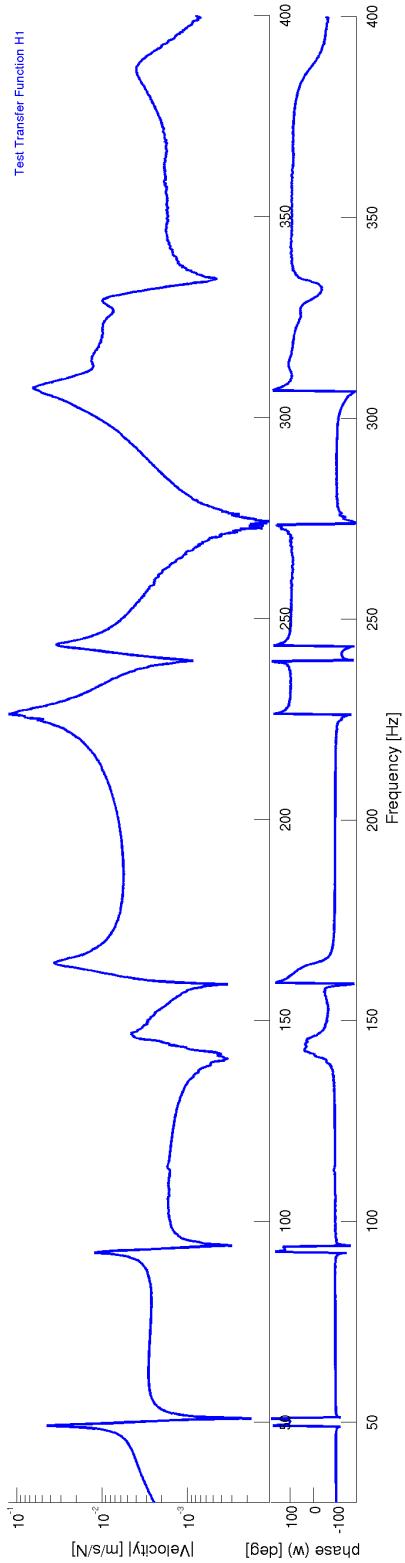

(b) Narrowband from 30 Hz to 400 Hz at sensor 5y .

Fig. 4.6 Comparison of Fast Fourier Transforms spans

Table 4.2 Experimental modes - frequency span from 30-400 Hz.

# Mode	Frequency (Hz) (Hz)	ζ %	# Mode	Frequency (Hz) (Hz)	ζ %
1	49.2	0.308	1	49.24257	0.257
2	92.3	0.510	2	92.26513	0.254
3	93.3	0.327	3	93.75552	0.425
4	146.0	1.000	4	145.28942	0.643
5	160.1	0.831	5	160.05492	0.989
6	164.1	0.525	6	164.17756	0.563
7	226.4	0.362	7	226.35654	0.292
8	243.3	0.277	8	243.39876	0.278
9	307.1	0.337	9	307.32632	0.364
10	313.0	0.500	10	314.17947	0.489
11	324.3	0.600	11	324.83236	0.488
12	329.6	0.900	12	329.66575	0.430

Notes: Comparison of curve-fitting left) Vibrolaser VL Win 3.2.56 software, right) IDRC and IDRM algorithms.

4.3 Identification of a pole/residue form with IDRC and IDRM algorithms

Once all the FRFs of the frequency span were obtained, the next step is to perform the curve-fitting. The FRFs were first observed with the Vibrolaser version VL Win 3.2.56 software. The identified poles were directly obtained from the measured FRFs as well as the damping values for each mode. The comparison of frequencies values and damping ratios can be observed in Table 4.2 using the Vibrolaser VL Win 3.2.56 software and the IDRC and IDRM algorithms. The EMA results generated with the SLDV were saved in UFF58 format and imported into MATLAB-SDTools, see Appendix A, step 3. Furthermore, a curve-fitting using the IDRC and IDRM algorithms is performed to extract the modal parameters of the measured FRF data.

The creation of an initial model is the first step using the IDRC algorithm. A first approximation of the poles is provided with the frequency values obtained with the Vibrolaser VL Win 3.2.56 software. The objective of the identification of an "optimal" pole/residue model (second step) is to obtain all physical modes in the bandwith, and only those (no computational modes). Generally, identification algorithms can be used to generate the initial pole, but it leads to the necessity to eliminate computational poles.

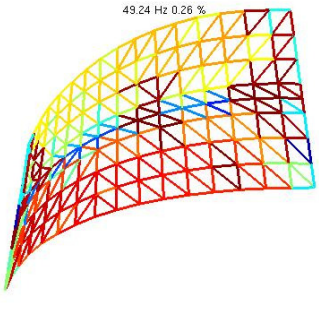

(a) Mode 1=49.24 Hz.

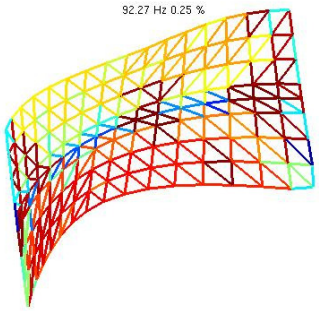

(b) Mode 2=92.27 Hz.

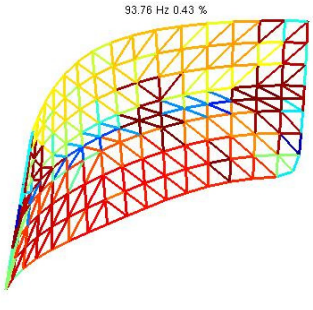

(c) Mode 3=93.76 Hz.

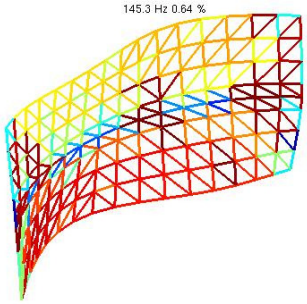

(d) Mode 4 = 145.3 Hz.

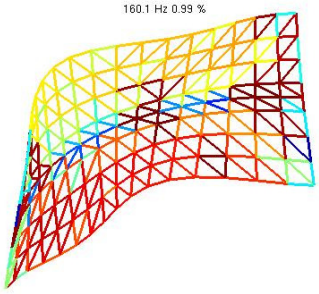

(e) Mode 5=160.1 Hz.

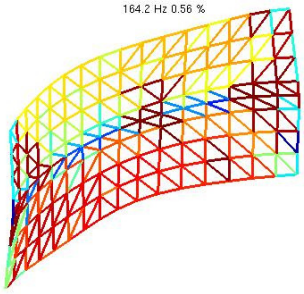

(f) Mode 6=164.2 Hz.

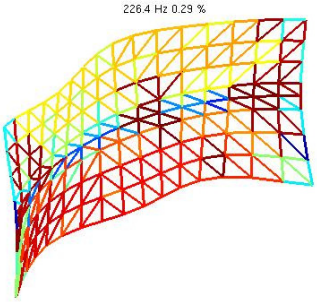

(g) Mode 7=226.4 Hz.

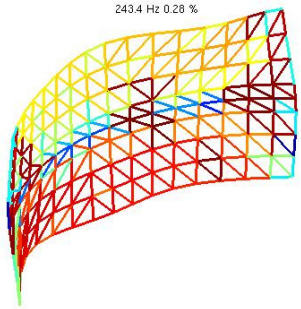

(h) Mode 8=243.4 Hz.

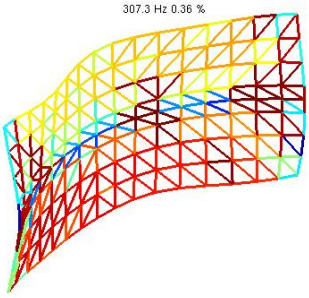

(i) Mode 9=307.3 Hz.

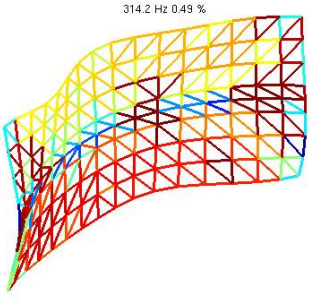

(j) Mode 10=314.2 Hz.

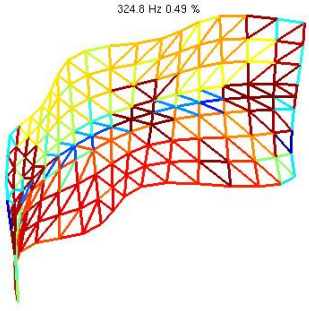

(k) Mode 11=324.8 Hz.

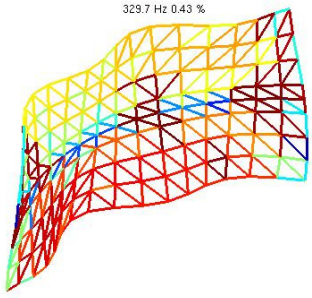

(l) Mode 12=329.7 Hz.

Fig. 4.7 CFRP component assembly experimental measurements free-free.

Once the "optimal" pole/residual of the form Eq. (1.16) has been identified, the systems can be considered linear and diagonalizable (third step) and the residue flexibility $[E(s)]$ gives a sufficient representation of the poles (IDRM approach).

The first 12^{th} mode shapes are obtained and illustrated in Fig. 4.7 associated to the frequencies and damping in Table 4.2. Some differences can be also appreciated in the pole and damping results applying each curve-fiting algorithm tool in the Table 4.2. A bandwidth of 2% is used in order to localize the eigenfrequencies. Traditional single pole methods[18] generally give very satisfactory results, but often leave out some modes (local modes or closely space model). Furthermore, a Nyquist analysis plot is performed to check the quality of the results obtained applying the algorithms, (see Fig. 4.8). The Nyquist is a vector response plot used to gain insight into the variance of a measurement (Repeatability check). If the circle appears very distorted for a measurement with few averages per FRF in the broadband span (10 in each span), see Figs. 4.8b,d,f,h, it is necessary to decrease the frequency range until get a satisfactory smooth out results in most of the results, see Figs. 4.8a,c,e,g. These distortions (deficiencies) to estimate the modal parameters of the CFRP is a trade-off of time that needs to be considered in this research associated to the modal data adquisition parameters that will impact the final stiffness parameters of the CFRP assemblied with epoxy resin.

These distortions with 10 averages per FRF between the experimental measurements versus the curve-fitting in some sensors (such as in sensor $5y$, see Fig. 4.8a) in the narrowband span might be associated to the anisotropy of the stiffness parameters by the difference in temperature along the CFRP during the manufacturing process in the autoclave or by some inconsistencies in the assembly by the epoxy resin between the three componenets that can not be captured with the curve-fitting with 10 averages. Furthermore, bigger distortions may also indicate that the current measured data are not adecuate or exhaustive to properly construct the analytical function involved in the calculation of residues. In other words, the dissimilarities obtained from $5y$ to $97y$ sensors between 30 Hz and 150 Hz in the narrowband span may be sufficient to consistently characterize a CFRP structure in order to obtain the final stiffness parameters based on the set of modal data acquisition parameters. Thus, the Nyquist of the sensors $6y, 12y$ and $23y$ is illustrated in Fig. 4.8 showing the resolution and evidence the quite satisfactory measurement results (blue line) as well the curve-fitting approximation (green line) in the fequency span from 30 Hz to 400 Hz. However, the results obtained on sensor $5y$ for the same frequency span indicates deficiencies observed in the broadband from 0 Hz to 1000 Hz. The

[18] Circle fitting (Nyquist) and narrow band-single model SIMO models

Nyquist, FRFs (blue line) and the curve-fitting (green line) of sensors $5y, 6y, 12y$ and $23y$ are illustrated in Figs. 4.8, 4.9 and 4.10 respectively to visualize graphically the quality of the approximation of the sensors.

Thus, the Nyquist comparision of the illustrated sensors indicates differences in the residue calculations in some sensors in the central part of the assembly (from $5y$ to $98y$) according the poles and damping obtained based on the IDRC and IDRM algorithms displayed in Table 4.2. The difference or distortions obtained with each curve-fitting approximation is essential to improve the approximation of the poles and phase of the measured FRFs in the next sections, (see Fig. 4.9). It is worth nothing that the accuracy of the parameters obtained by curve-fitting the experimental data is only as good as the data used in the procedure [178]. Once the frequencies and damping portions of the roots have been computed, the residues for a function with a particular response and reference set can be calculated. Estimation of residues for a specific response and reference means calculating the amplitud and the phase of the roots estimated previously. All the modal data adqusition parameters are included in the calculation of the residues.

The curve-fitting performed using the IDRC and IDRM algorithms on sensors $12y$ and $23y$ presents sufficient accuracy in the frequency span from 30 Hz to 400 Hz in the amplitud and phase as well as in the rest of the sensons (from $99y$ to $213y$) applying the pole/residue form, (see Figs. 4.9 and 4.10). However, deficiencies are observed from sensor $5y$ to $98y$ between 30 Hz and 150 Hz, (see Fig. 4.9). It is not observed deficiencies in the accuracy on sensors (from $99y$ to $213y$) in the amplitud and phase based on the poles and damping according the modal data adquisition parameters defined in Table 4.2. The results obtained applying the parametric[19] IDRC and IDRM algorithms display that the eigenfrequencies (or poles) are close to those obtained with the Vibrolaser software. Thus, the curve-fitting algorithms implemented in [106] can be used to find the poles and identify the modal parameter problems up to three steps: creation of an initial model, the identification of an "optimal" pole/residue model of the form Eq. (1.16) by tuning the initial estimate, and the consideration of lineality to determine the approximation of the identified model that verifies other desired properties [152].

[19]The identified parametric model of the form Eq. (1.16) is obtained verifying constrains of minimality, reciprocity, properness or proportional damping. The minimality corresponds to the constraint of the rank of the residue matrix found for the single poles. For reciprocal models, the residue matrix must be symmetric. An approximation is thus found by taking the symmetric part of the identified matrix and using a singular value decomposition to simultaneously enforce minimality and reciprocity. Properness allows the separation of mass, damping and stiffness properties [106].

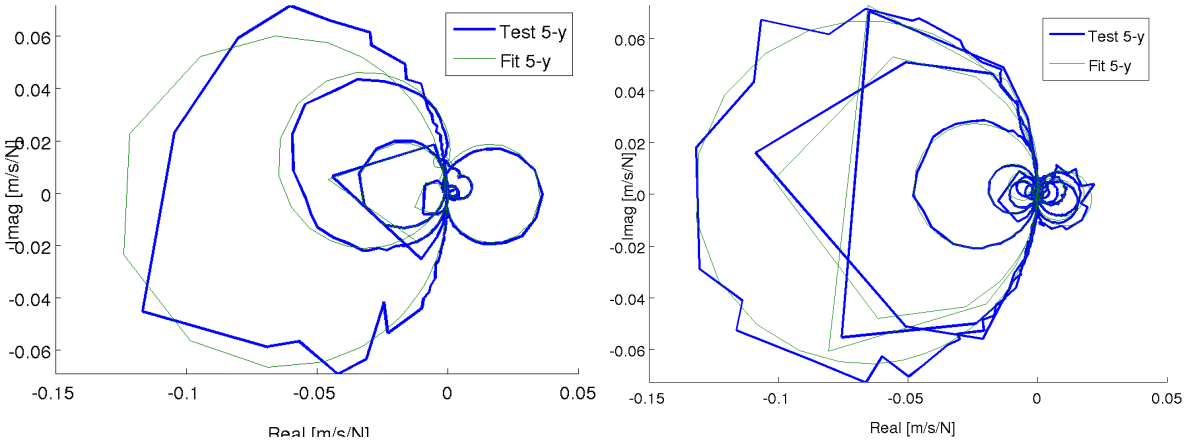

(a) Nyquist 5-y sensor

(b) Nyquist 5-y sensor

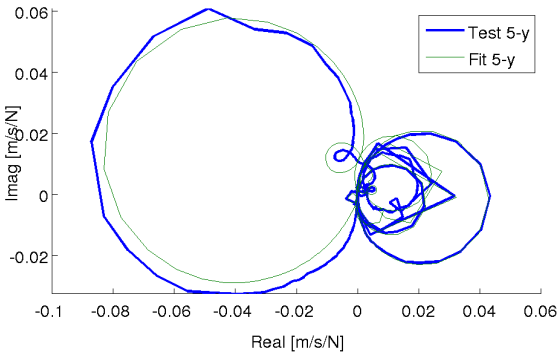

(c) Nyquist 6-y sensor

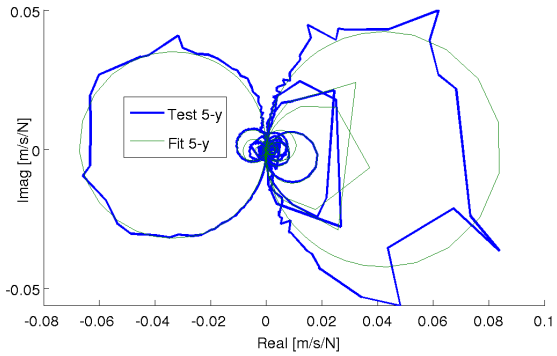

(d) Nyquist 6-y sensor

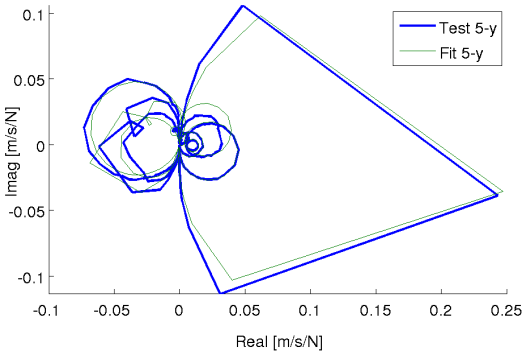

(e) Nyquist 12-y sensor

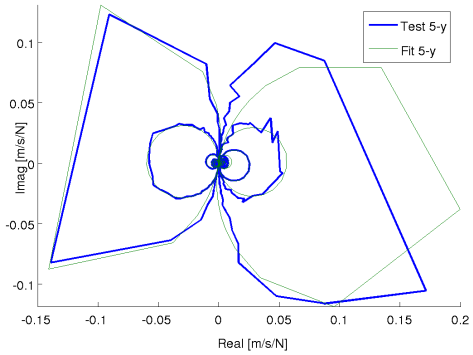

(f) Nyquist 12-y sensor

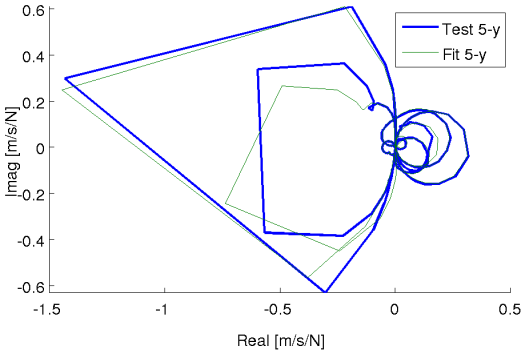

(g) Nyquist 23-y sensor

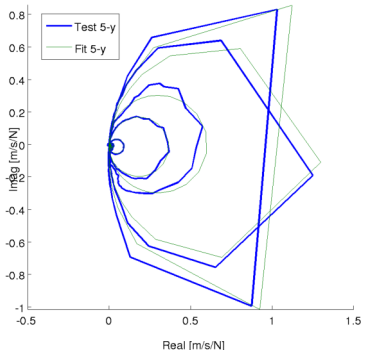

(h) Nyquist 23-y sensor

Fig. 4.8 Nyquist of frequency span 30-400 Hz. (a,c,e,g) frequency span 0-1000 Hz. (b,d,f,h) at different sensors.

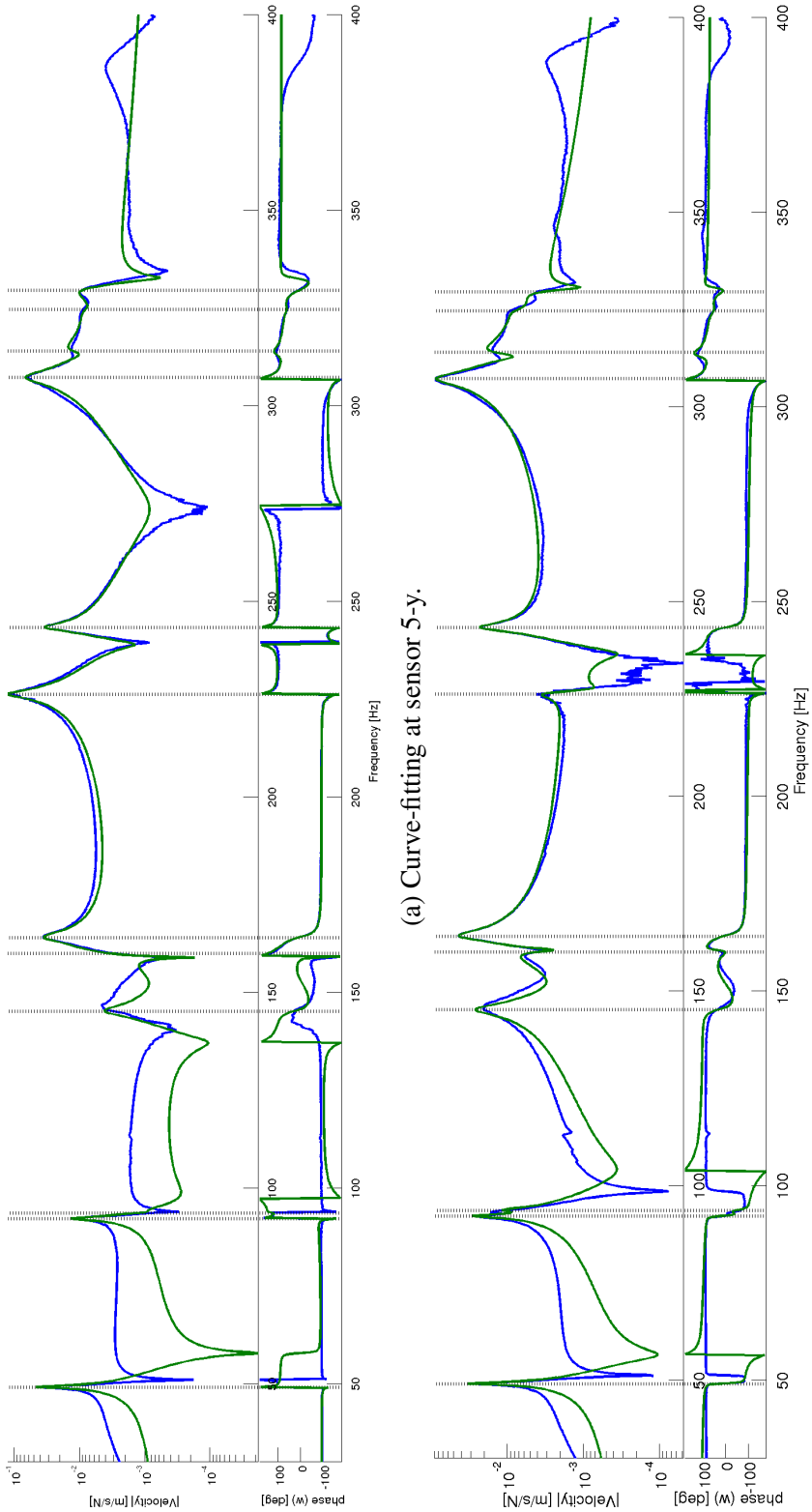

(a) Curve-fitting at sensor 5-y.

(b) Curve-fitting at sensor 6-y.

Fig. 4.9 FRF (blue) curve-fitting (green) at different sensors 30-400 Hz.

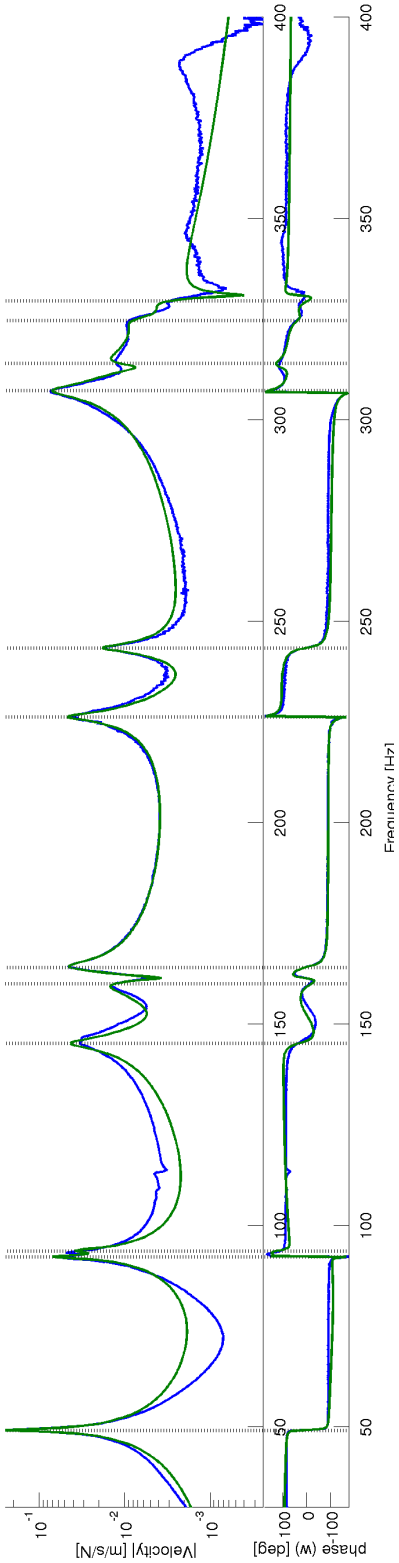

(a) Curve-fitting at sensor 12-y.

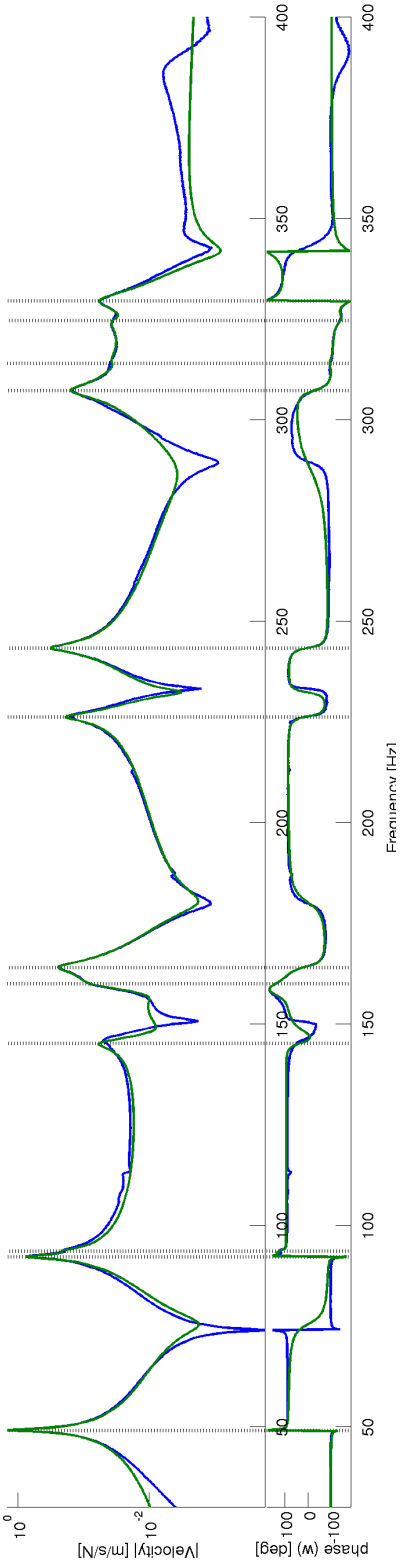

(b) Curve-fitting at sensor 23-y.

Fig. 4.10 FRF (blue) curve-fitting (green) at different sensors from 30-400 Hz.

4.4 Initial material properties of the CFRP component to perform a MAC

One of the characteristics of the MNET is to establish the initial stiffness parameters to perform the MAC. These initial stiffness parameters will provide MAC results that will be useful to establish an analysis range in the DOE. The reasons not to use the raw material test specimen as initial stiffness parameters or the CLT are ilustrated on the correlation results obtained, see Appendix E. Thus, it is needed to organize and analyze some potential stiffness parameters that influenced the MAC of the CFRP. The organization part of the potential causes can be performed using a fishbone, (see Fig. 4.11). Based on this diagram can be elaborated a Table that classified these potential causes that affect the MAC (MNET, stiffness parameters, experimental measurements, types of CFRP, carbon/epoxy and glass/epoxy, by author, method, experimental method used). The Table 4.3 is elaborated with some of the state-of-the-art stiffness parameters found in the literature using MNETs in order to analyze these initial parameters in the proposed MNET methodology. A high anisotropy can be observed in some CFRP in the Young's modulus and shear modulus, see [29] and [43]. It is also observed that most of the methods obtained six stiffness parameters $E_1, E_2, G_{12}, G_{13}, G_{23}, \nu_{12}$. The evaluation of these six parameters will be performed using orthotropic shell element based on the FSDT in order to improve the accuracy in the results, as was introduced in Chapter 1. Note that Poisson's ratio reported in [31], [45], [43] are not the typical values found in the literature (for example, low and negative values). The consideration of low and negative Poisson's ratio values for the evaluation of the stiffness parameters is nowadays an open field [97], [166]. Some studies can be found about Poisson's ratio values during phase transformation in a polymer gels [156]. This concept is introduced in the next subsection to be taken into consideration in the analysis of the stiffness parameters. Thus, using the number of stiffness parameters defined in the Table 4.3 and the curve-fitting obtained can be perfomed a MAC to establish the initial stiffness parameters in a FE model.

4.4.1 Poisson's ratio during phase transformation in a polymers gel

Traditional Poisson's ratio values of 0.3-0.5 are reported in the literature to correlate CFRP with EMA. Recently, studies have been associated to unusual or extreme behaviour in material properties of anisotropic materials with low and negative Poisson's ratio values, including polymer gels, like the Hunstman Ly 564, used to elaborate CFRP, see [97], [156], [160].

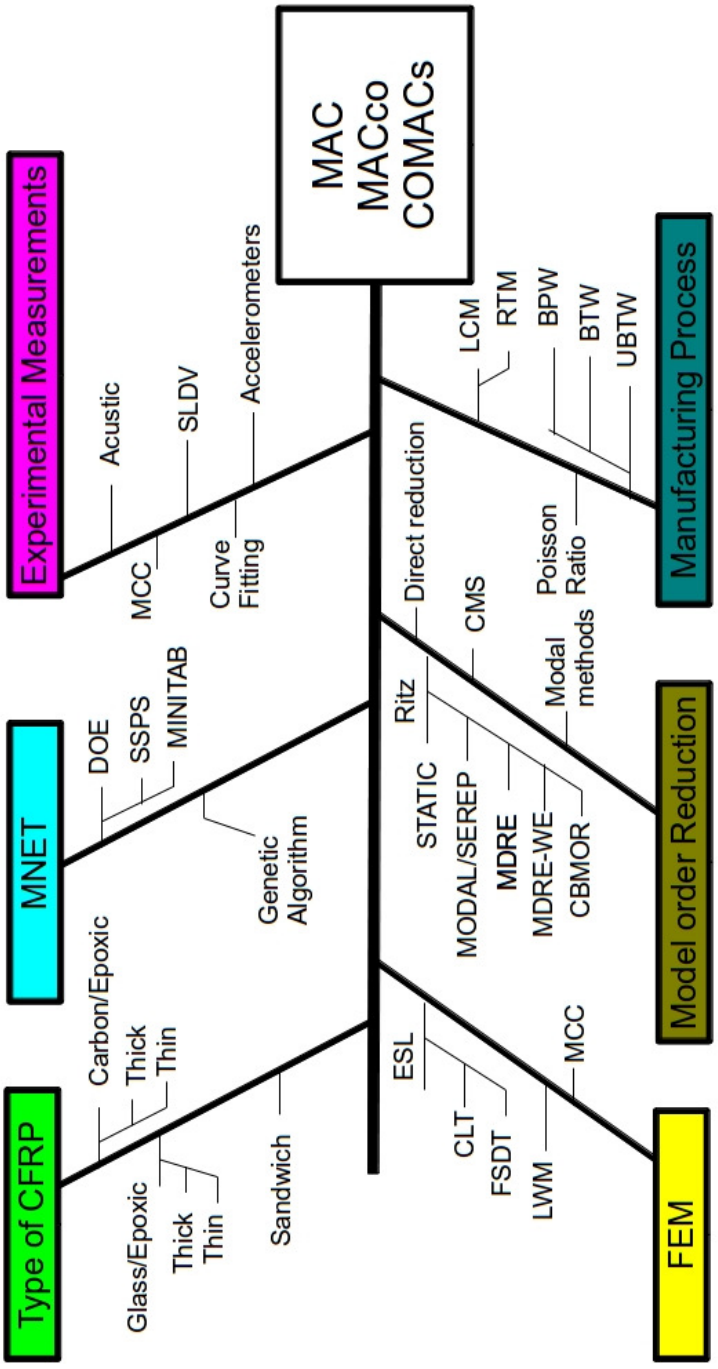

Fig. 4.11 Fishbone diagram to identify the MAC cause-effect to apply model order reduction in CFRP.

Table 4.3 Summary of MNET Methods applied to CFRP and GFRP

	ESL Theory	Exp	Method	E_1	E_2	G_{12}	G_{23}	G_{13}	ν_{12}
Carbon/epoxy (thick)	CLT	Acustic	Araujo [31]	161.1	9.3	6.8	3.2	3.1	0.166
				162.3	8.9	6.0	2.4	2.4	0.249
				164.8	9.6	6.8	1.4	2.6	-0.036
				159.6	9.8	6.2	4.4	3.0	0.264
			Maletta [197]	126.3	10.5	6.1	–	–	0.238
			Pedersen [15]	127.0	10.6	6.06	–	–	0.29
			Mota Soares [22]	126.3	10.5	6.1	6.5	–	0.24
Carbon/epoxy (thin)	FSDT, HSDT	SLDV	Cugnoni [43]	114	8.0	3.1	2.9	3.1	0.29
	PSDT, FSDT		Cugnoni [44]	92.5	7.27	3.87	2.55	3.46	0.37
		SLDV	Matter [45]	91.9	7.23	3.74	2.11	3.33	0.38
Glass/epoxy (thin)			Rikards [32]	71.3	68.8	24.5	–	–	0.32
			Mota Soares [22]	68.7	68.1	24.6	26.9	–	0.34
			Pedersen [15]	69.5	67.8	24.5	–	–	0.34
			Maletta [197]	61.0	20.5	10.1	–	–	0.283
Glass/epoxy (thick)			Sol [13]	45.6	16.9	6.9	–	–	0.22
			Frederiksen [17]	45.4	17.3	7.3	–	–	0.225
			Frederiksen [18]	42.4	11.6	4.68	4.55	–	0.305

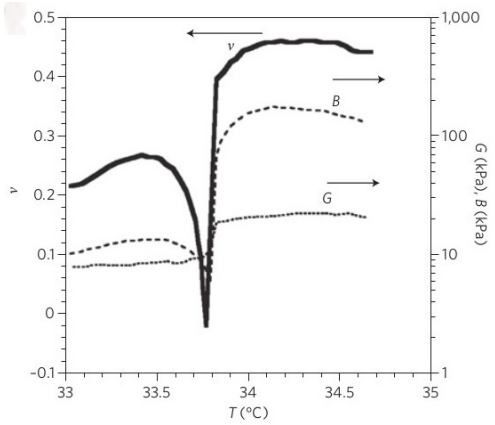

Fig. 4.12 Bulk modulus (B), shear modulus (G) and Poisson's ratio (ν) of a polymer gel versus temperature associated with a volume phase transition close to a critical point measured optically [97].

Reviewing in general the MNET bibliography applied to CFRP, Araujo *et al.* in [31] and Cugnoni *et al.* in [43] reported also negative (-0.036) and low (0.08) Poisson ratio values respectively. The atypical Poisson's ratio obtained in [31], [43] and the low and negative Poisson's ratio values of polymer gels are documented in [97], [156] and [158]. The low and negative Poisson ratio values of polymer gels during the phase transformation documented by Hirotsu in [156] might be one of the reasons that influence the final stiffness parameters of CFRP documented in [31], [43], [45], [97], [98], [159]-[165] also related as a sensitive indicator of (fatigue) damage in fibre-reinforced plastics [166]. Similar behaviour is reported for different gel concentrations [156], [158], [160]. The Poisson ratio is related to the Young's modulus and shear modulus, which describes the change in size and shape respectively in CFRP. Poisson's ratio behaviour during phase transformation in a polymer gel is related also to the temperature associated with a volume phase transition [97], (see Fig. 4.12).

Thus, the Huntsman (Araldyte) Ly 564, see Appendix D, is a polymer gel for liquid moulding applications and it is used in this work for the elaboration of the CFRP component. A typical process temperature profile can be applied to a Huntsman (Araldyte) Ly 564 using RTM6 illustrated in Fig. 4.13 for cure cycle design. There are different temperature profiles documented in the literature that can be applied for cure cycle designs, that might affect the Poisson ratio during the manufacturing process.

Furthermore, it is documented in the literature that the characterization of Poisson's ratio can be controlled by the appropriate selection of the substrate parameters such as fiber orientation,

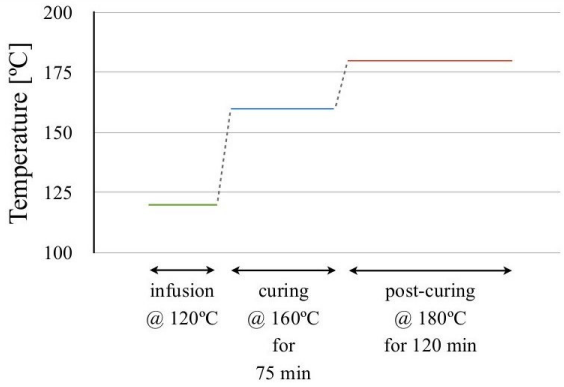

Fig. 4.13 Cure cycle for RTM6 as provided by the manufacturer [172].

volume fraction, fiber spacing, layer sequence and the type of conventional cure cycle that contribute to process-induced reduced residual strains[20] [100].

For example, the cure cycle with an intermediate dwell the infusion tool should be heated up to 120°C. After the infusion is completed, the tool is heated up further and held at 160°C for 75 minute to cure the resin. This process is followed by a post-cure cycle where the CFRP component is removed from the mould and held at 180°C for 120 minute [172].

Moreover, an analysis presented by Herakovich in [98] using two-dimensional lamination theory combined with the appropriate three-dimensional anisotropic constitutive equation reported some rather surprising results for range of values through-the-thickness of the effective Poisson's ratio (ν_{xz}) versus angle-ply laminates. Results for graphite-epoxy show that the effective Poisson's ratio through-the-thickness can be ranged from a high of 0.49 for a laminate layer distribution of [90] to a minimum negative value of -0.21 for a laminate layer distribution of $[\pm 25]$. Based on the different temperature profiles used to elaborate CFRP and variables involved in the manufacturing can be suggested to evaluate low or negative Poisson's ratio values because of the phase transformation in gels used in the elaboration of composite components, (see Fig. 4.12). The evaluation of the initial stiffness parameters reported will establish the range of the analysis and the accuracy. These initial values are selected from the Table 4.3 and then are evaluated in the next section using the MAC applying FEM. In the next section is established the preparation of a FE model.

[20]Traditional analyses of process-induced strains in thin laminates are based on the mismatch in coefficient of thermal expansions (CTEs) between adjacent plies, homogeneous temperature difference between ambient and cure temperature, and no stress development prior to the end of the cure [176].

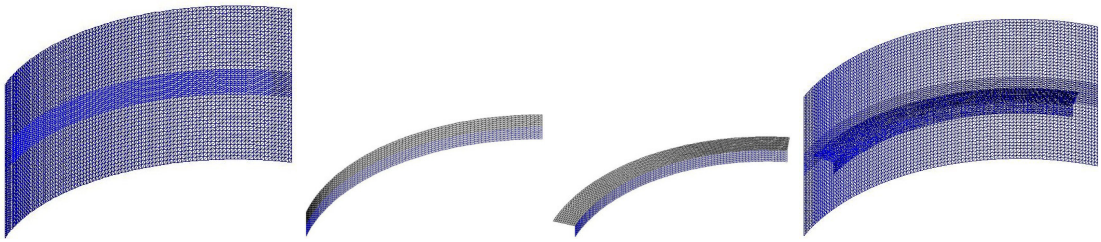

(a) Part 1. (b) Part 2. (c) Part 3. (d) CFRP Assembly.

Fig. 4.14 FE model groups.

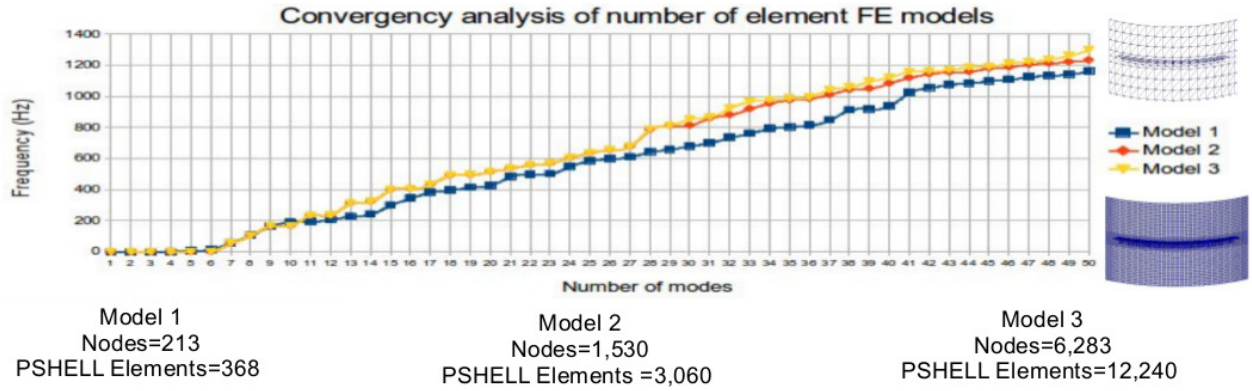

Fig. 4.15 Convergency analysis

4.4.2 Finite element model preparation and normal mode solution

Firstly, the CFRP was measured and then a FE model was elaborated in ABAQUS using primarily S3 triangle shell elements in the mesh, (see Fig. 4.14). The triangle elements defined (discretization introduced in Chapter 1) in SDTools are called 'pshell' and in MSC/NASTRAN CTRIA3 [148]. All the elements according the help documentation have similar properties [76], [84], [104], [149].

An appropiate assessment was perfomed to evaluate the mesh density (lineal) of the FE model using the pshell elements, (see Fig. 4.15).

Normal modes are computed using the FE model to obtain the natural frequencies and normal mode shapes of a CFRP structure. It verifies the orthogonality condition.

The model 3 is selected based on the frequency difference lower than 2.5 % in respect to the model 2 until 800 Hz (mode 29th) displayed in Table B.2. The model is divided in three parts, (see Fig. 4.14), for convienience to modify the physical parameters per group of elements.

Table 4.4 Test article and FE model weight comparison

Component	Test Article (Kg)	FE model (Kg)	Difference	
			Kg	%
CFRP	2.1	2.2	0.1	4.7619%

The model illustrated in Fig. 4.14, is composed by triangle shell elements with a fairly regular shape and pattern. Traditionaly in modal analysis using FE model assemblies, the components are coupled using *rigid body elements* (RBE) or couplings as a boundary conditions to perform a modal analysis in the assembly. In this work, the FE model is prepared as a continuous body between the three components for convienience to simplify the FE model. After the FE model is developed, a number of validity checks were performed on the model prior to conduct the modal analysis [178]. These checks are listed below.

1. Units
2. Mass comparison
3. Layer Stack-up
4. Material and element properties
5. Input and output coodinate systems

Table 4.4 reports the mass comparison between the complete model and the test article. The validation of the weight in the FE model is calculated comparing the weight of the real weight of the CFRP using a scale.

The small difference of the weight (4.7619 %) between the CFRP component versus the analytical FE model might be related to the small difference in the density values considered in each FE component respect to the technical data, see Appendix D. The characteristics of the FE model, number of nodes, elements and DOF per part, are displayed in Table 4.5 and in Fig. 4.14.

The layer stack-up is established and verified the thickness of each group defined according each element formulation. The density of each part is defined in Table 4.7.

Table 4.5 FE model element, node and DOF, see Fig. 4.14

Component	Element Type	Number of Elements	Number of Nodes
Part 1	pshell	7,200	3,840
Part 2	pshell	2,016	1,105
Part 3	pshell	3,024	1,615
Assembly		12,240	6,283
Total DOF			37,698

4.4.3 Application of MAC and other correlation criteria using the initial material properties

The MAC is perfomed using the curve-fitting results obtained in section 4.3 and the *normal modes analysis* of the FE model. The curve-fitting results are saved in UFF58 format and are imported into MATLAB-SDTools to perfom the MAC correlation. The results of the FE model are obtained in MATLAB format (.m). The MAC evaluation of the initial material properties (stiffness parameters) is divided in four proposals due to the non-uniformity of the material properties summarized in Table 4.3.

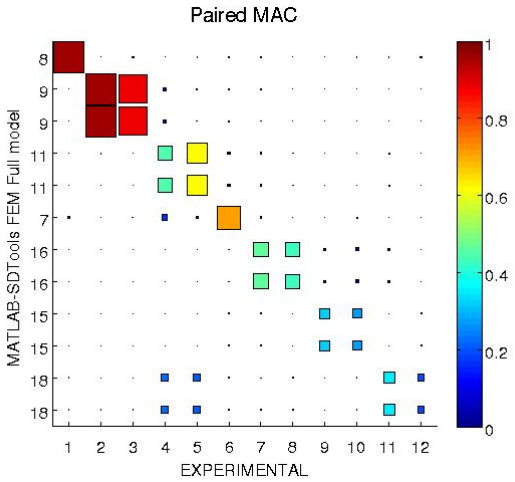

(a) Proposal 1, material properties of part 1, $E_1 = E_2$ =114. GPa and $G_{12} = G_{13} = G_{23}$ =25. GPa, $\nu = 0.3$, $\rho = 2600Kg/m^{-3}$ and for Part 2 and Part 3 see Table 4.7.

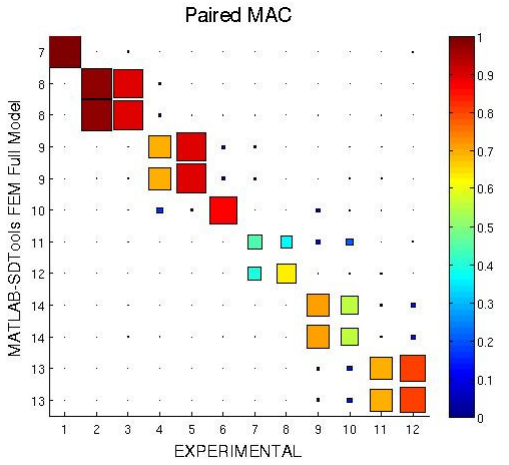

(b) Proposal 2, material properties of part 1, $E_1 = E_2$ =91.9. GPa and $G_{12} = G_{13}$ =3.5 GPa, G_{23} =2.5GPa, $\nu = 0.3$, $\rho = 2600Kg/m^{-3}$ and for Part 2 and Part 3 see Table 4.7.

Fig. 4.16 Initial material properties Proposals 1 and 2.

The first Proposal is observed in Fig. 4.16a and it shows the MAC results using the material properties obtained by Cugnoni [43]. The first two mode pairs showed a good agreement while the rest of the pairs showed a poor correlation.

The second Proposal used the material properties obtained by Matter [45], (see Fig. 4.16b), showing an improvement in most of the pair modes with respect to the previous. At this point, the decrease of E_i as well as the G_{ij} showed an improvement of the MAC correlation. After several iteractions, Proposal 3 is a combination of values based on the results of E_i obtained by Rikards [32], the G_{ij} used in the Proposal 2 and the low Poisson's ratio obtained by Araujo [31].

The MAC results of Proposal 3 are displayed in Fig. 4.17a. It is clear that the results of Proposal 3 displayed a significant improvement in the correlation using the values proposed respect to the previous proposals. Proposal 4, (see Fig. 4.17b), is evaluated keeping the values of the Fig. 4.17a and just changing the Poisson's ratio to negative. For visualization purposes using Fig. 4.12, it is observed the different MAC results associated to each stiffness parameter considering different (low and negative) Poisson's ratio values during the phase transformation in Fig. 4.18 .

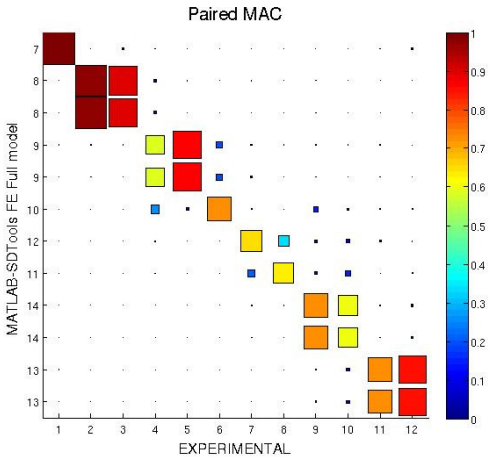

(a) Proposal 3, material properties of part 1, E_1 =35.65 GPa E_2 =48.65 GPa and G_{12} = G_{13} =3.5GPa, G_{23} =2.5GPa, $\nu = 0.015$, ρ = $2600Kg/m^{-3}$ and for the Part 2 and Part 3 see Table 4.7.

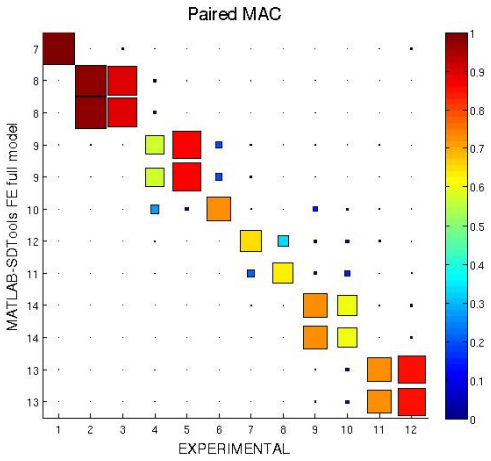

(b) Proposal 4, material properties of part 1, E_1 =35.65 GPa E_2 =48.65 GPa and G_{12} = G_{13} =3.5GPa, G_{23} =2.5GPa, $\nu = -0.015$,ρ = $2600Kg/m^{-3}$ and for the Part 2 and Part 3 see Table 4.7.

Fig. 4.17 Initial material properties Proposals 3 and 4.

Thus, to establish the DOE one needs to define an interval per factor. These intervals are defined in Table 4.6 for Part 1 based on the initial approximations (Proposal 3) multiplying all the values by itself to obtain the upper limit. The group of material properties in Proposal 3 defined in Table 4.7 were selected based on the MAC results obtained to perform the DOE. The initial material properties of Part 2 and Part 3 are also displayed in the Table 4.7. The experimental measurements of the Part 2 and 3 are suggested to be performed in a future research.

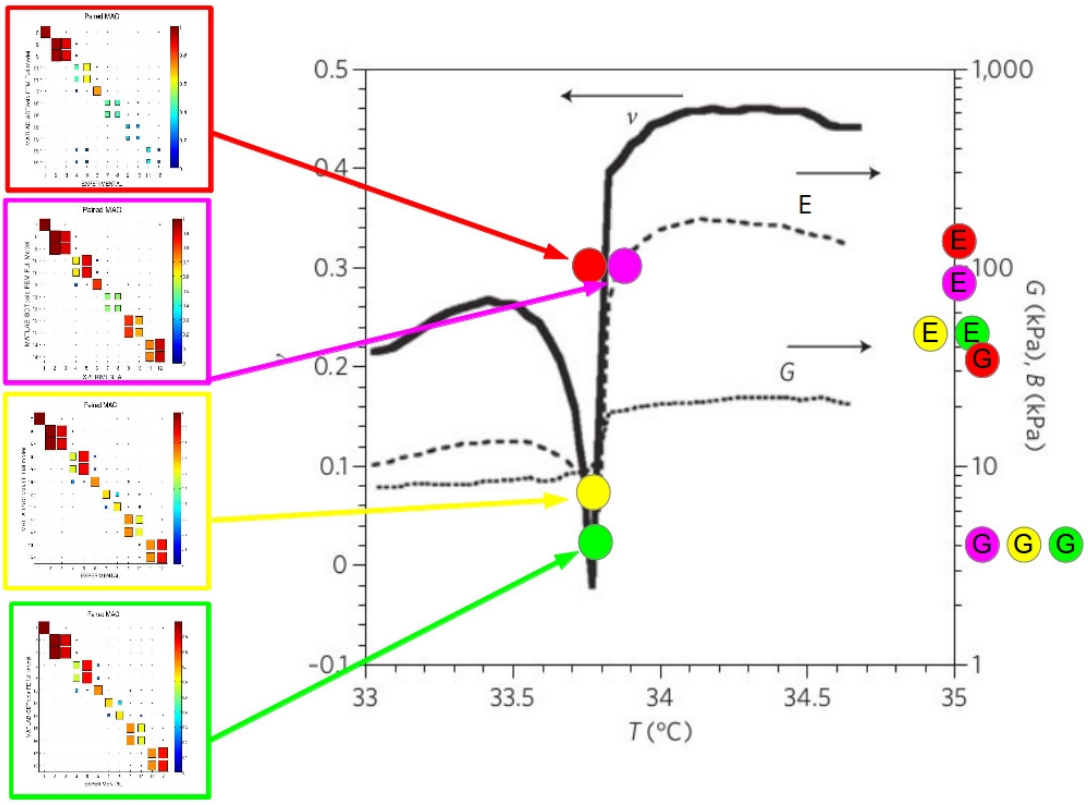

Fig. 4.18 Comparison of MAC results using different proposals of material values.

Notes: : a)Proposal 1(red), b)Proposal 2(magenta), c)Proposal 3(yellow), d)Proposal 4(green), E = Young's Modulus, G=Shear Modulus.

The orthogonal array of Part 1 is presented in Table 4.8 according the limits established in Table 4.6. If the results at the end of the DOE are not satisfactory, a new DOE can be performed using material properties evaluated in Fig. 4.17b.

Table 4.6 Levels and intervals per factors used in the DOE for the first component- Part 1

Factor	Name	Level		Units
		Low	High	
A	E_1	35.65	71.3	GPa
B	E_2	48.65	97.3	GPa
C	G_{12}	3.5	7	GPa
D	G_{23}	2.5	5	GPa
E	G_{13}	3.5	7	GPa
F	ν_{12}	0.015	0.03	—

Other criteria can also be used to perform the DOE, such as MACco and COMAC. For comparative purposes, the MACco and different COMACs are performed using the stiffness parameters of Table 4.7 versus number of Y-sensors (x-axis) to emphasise the improvement in the results after updating the stiffness parameters in forthcoming chapters, (see Figs. 4.19 and 4.20).

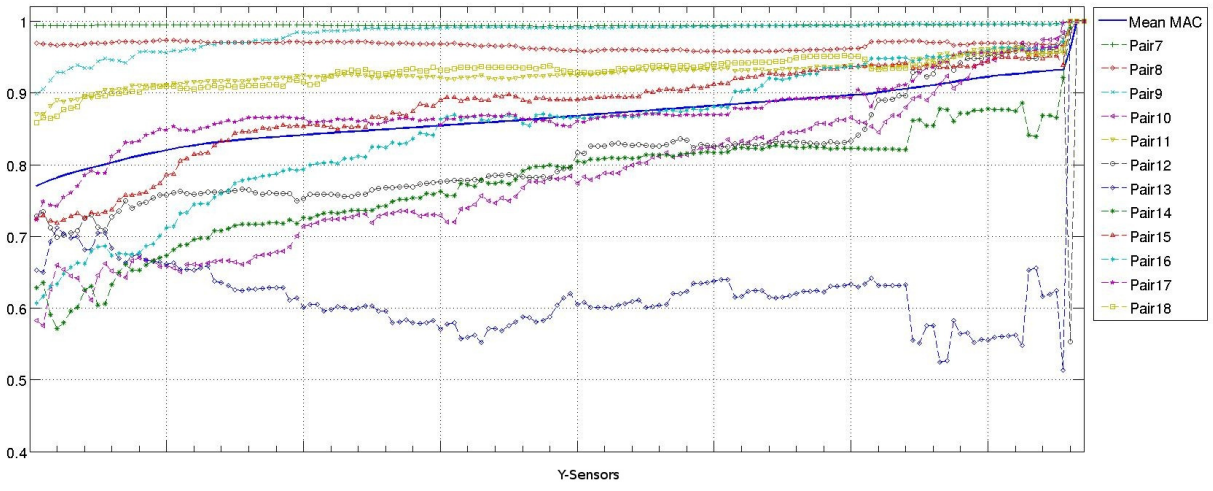

Fig. 4.19 MACco with material properties of Table 4.7 versus Y-sensors.

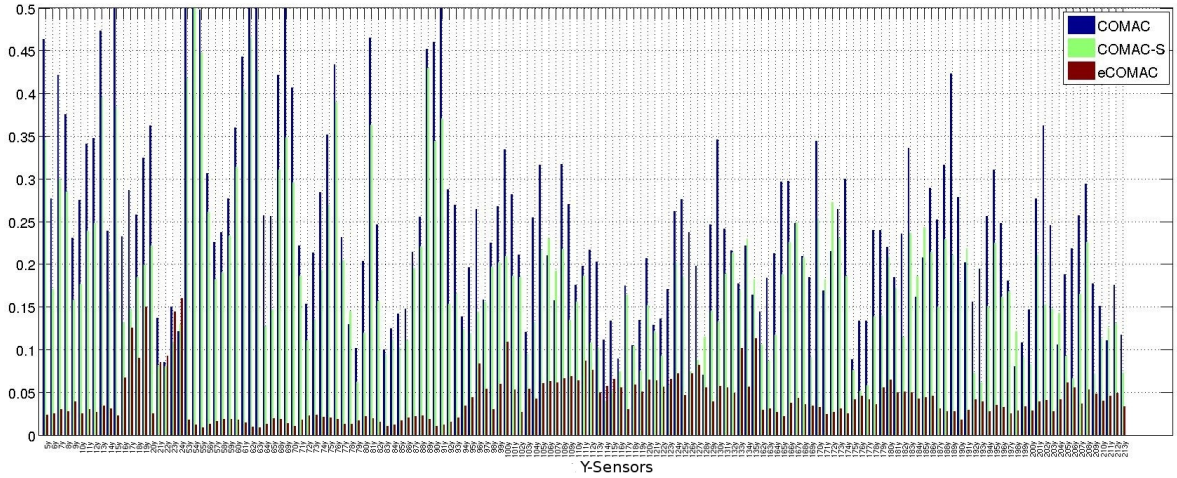

Fig. 4.20 COMACs with material properties of Table 4.7 versus Y-sensors.

4.5 MNET using a Design of Experiments (DOE) - Full Factorial Analysis

Different methodologies were introduced in previous chapters that constituted the stages of the MNET to obtain the stiffness parameters. Two methodologies were identified (genetic algorithms and DOE) to achieve the stiffness parameters using MNET, (see Fig. 4.11).

The DOE is selected to achieve an improvement in the MAC response. The initial stiffness parameters in the Proposal 3 will be used to perform a correlation analysis based on the MAC responses using the curve-fitting with the FE model. The stiffness parameters displayed in Table 4.6 will define the range to analyze. Furthermore, one can observe the stiffness parameters per part of the CFRP in Table 4.7. It is important to mention that the stiffness parameters of the Part 2 and Part 3 are obtained in a similar way as it is obtained in the Part 1 using the initial stiffness parameters proposals. The DOE of Parts 2 and 3 is not included in this study, however, an additional DOE can be performed for Part 2 and Part 3 using the stiffness parameters in Table 4.7 once the experimental measurements of the respective parts are acquired. Using these initial values, the DOE can be established in three steps:

1. Set up of the orthogonal array 2^6 in order to obtain the MAC.
2. Pearson analysis: Main effects, interactions, cube, contour and surface analysis.
3. ANOVA analysis and transfer function of the MAC.

Table 4.7 Initial elastic mechanical properties.(*th=thickness)

Part 1(m)	***Modulus***	***E(GPa)***	***ν* (-)**	**Shear**	***G(GPa)***	***ρ*** (Kgm^{-3})
**th=0.0035*	E_1	35.65	0.015	G_{12}	3.5	2600
	E_2	48.65	0.015	G_{23}	2.5	
				G_{13}	3.5	
Part 2(m)	***Modulus***	***E(GPa)***	***ν* (-)**	**Shear**	***G(GPa)***	***ρ*** (Kgm^{-3})
**th=0.007*	E_1	71.3	0.02	G_{12}	6	1500
	E_2	68.3	0.02	G_{23}	5	
				G_{13}	6	
Part 3(m)	***Modulus***	***E(GPa)***	***ν*(-)**	**Shear**	***G(GPa)***	***ρ*** (Kgm^{-3})
**th=0.0035*	E_1	71.3	0.02	G_{12}	6	1500
	E_2	68.3	0.02	G_{23}	5	
				G_{13}	6	

4.5.1 Set up of the orthogonal array

The full factorial design or DOE is established as an array of combinations or runs based on the number of parameters. Table 4.8 shows the array of a $2^6 = 64$ runs and the MAC obtained for each combination.

The order of the runs is randomized in order to avoid alias[21]. A MAC response value is calculated based on each combination "low" and "high" values of the parameters established in the Table 4.8.

The DOE is performed using each combination based on the array of $2^6 = 64$ runs to obtain the MAC response and the next step is to analyze the main effects and interaction of the stiffness parameters that influence the MAC.

4.5.2 Main effects analysis.

Once are obtained the MAC values based on the array combination established in Table 4.8, a main effects analysis can be peformed to indentify the critical parameters and interactions using a Pearson correlation[22]. The Pearson correlation provides a measure of the linear relation between the defined variables for a defined significance level (in this case of α=0.05). These

[21]The alias structure describes the confounding effects that occur in the design. It can also be defined as the effects that cannot be estimated separately from each other [147].

[22]The Pearson correlation provides a range of values from -1 to +1, whereas a value of 0 is indicative of no linear relationship between the variables. A correlation of -1 indicates a perfect negative linear relationship and a +1 indicates a perfect positive linear relationship [147].

Table 4.8 Design of experiments 2^6

		Factor		A	B	C	D	E	F	Response
Run order	N	center point	Blocks							MAC
64	1	1	1	71.30	97.30	7.0	5.0	7.0	0.030	87
30	2	1	1	71.30	48.65	7.0	5.0	7.0	0.015	83
41	3	1	1	35.65	48.65	3.5	5.0	3.5	0.030	77
5	4	1	1	35.65	48.65	7.0	2.5	3.5	0.015	82
15	5	1	1	35.65	97.30	7.0	5.0	3.5	0.015	80
25	6	1	1	35.65	48.65	3.5	5.0	7.0	0.015	77
35	7	1	1	35.65	97.30	3.5	2.5	3.5	0.030	83
48	8	1	1	71.30	97.30	7.0	5.0	3.5	0.030	80
51	9	1	1	35.65	97.30	3.5	2.5	7.0	0.030	83
55	10	1	1	35.65	97.30	7.0	2.5	7.0	0.030	80
16	11	1	1	71.30	97.30	7.0	5.0	3.5	0.015	87
36	12	1	1	71.30	97.30	3.5	2.5	3.5	0.030	80
53	13	1	1	35.65	48.65	7.0	2.5	7.0	0.030	82
6	14	1	1	71.30	48.65	7.0	2.5	3.5	0.015	83
29	15	1	1	35.65	48.65	7.0	5.0	7.0	0.015	82
7	16	1	1	35.65	97.30	7.0	2.5	3.5	0.015	80
20	17	1	1	71.30	97.30	3.5	2.5	7.0	0.015	80
61	18	1	1	35.65	48.65	7.0	5.0	7.0	0.030	82
18	19	1	1	71.30	48.65	3.5	2.5	7.0	0.015	76
58	20	1	1	71.30	48.65	3.5	5.0	7.0	0.030	77
22	21	1	1	71.30	48.65	7.0	2.5	7.0	0.015	83
42	22	1	1	71.30	48.65	3.5	5.0	3.5	0.030	77
3	23	1	1	35.65	97.30	3.5	2.5	3.5	0.015	84
59	24	1	1	35.65	97.30	3.5	5.0	7.0	0.030	83
46	25	1	1	71.30	48.65	7.0	5.0	3.5	0.030	83
11	26	1	1	35.65	97.30	3.5	5.0	3.5	0.015	84
10	27	1	1	71.30	48.65	3.5	5.0	3.5	0.015	76
27	28	1	1	35.65	97.30	3.5	5.0	7.0	0.015	84
1	29	1	1	35.65	48.65	3.5	2.5	3.5	0.015	77
62	30	1	1	71.30	48.65	7.0	5.0	7.0	0.030	83
47	31	1	1	35.65	97.30	7.0	5.0	3.5	0.030	80
24	32	1	1	71.30	97.30	7.0	2.5	7.0	0.015	87
23	33	1	1	35.65	97.30	7.0	2.5	7.0	0.015	80
19	34	1	1	35.65	97.30	3.5	2.5	7.0	0.015	84
37	35	1	1	35.65	48.65	7.0	2.5	3.5	0.030	82
33	36	1	1	35.65	48.65	3.5	2.5	3.5	0.030	77
28	37	1	1	71.30	97.30	3.5	5.0	7.0	0.015	80
50	38	1	1	71.30	48.65	3.5	2.5	7.0	0.030	77
60	39	1	1	71.30	97.30	3.5	5.0	7.0	0.030	80
40	40	1	1	71.30	97.30	7.0	2.5	3.5	0.030	87
56	41	1	1	71.30	97.30	7.0	2.5	7.0	0.030	87
34	42	1	1	71.30	48.65	3.5	2.5	3.5	0.030	77
21	43	1	1	35.65	48.65	7.0	2.5	7.0	0.015	82
14	44	1	1	71.30	48.65	7.0	5.0	3.5	0.015	83
39	45	1	1	35.65	97.30	7.0	2.5	3.5	0.030	80
17	46	1	1	35.65	48.65	3.5	2.5	7.0	0.015	77
43	47	1	1	35.65	97.30	3.5	5.0	3.5	0.030	83
12	48	1	1	71.30	97.30	3.5	5.0	3.5	0.015	80
45	49	1	1	35.65	48.65	7.0	5.0	3.5	0.030	82
8	50	1	1	71.30	97.30	7.0	2.5	3.5	0.015	87
2	51	1	1	71.30	48.65	3.5	2.5	3.5	0.015	76
26	52	1	1	71.30	48.65	3.5	5.0	7.0	0.015	76
4	53	1	1	71.30	97.30	3.5	2.5	3.5	0.015	80
31	54	1	1	35.65	97.30	7.0	5.0	7.0	0.015	80
52	55	1	1	71.30	97.30	3.5	2.5	7.0	0.030	80
44	56	1	1	71.30	97.30	3.5	5.0	3.5	0.030	80
63	57	1	1	35.65	97.30	7.0	5.0	7.0	0.030	80
38	58	1	1	71.30	48.65	7.0	2.5	3.5	0.030	83
32	59	1	1	71.30	97.30	7.0	5.0	7.0	0.015	87
54	60	1	1	71.30	48.65	7.0	2.5	7.0	0.030	83
13	61	1	1	35.65	48.65	7.0	5.0	3.5	0.015	82
49	62	1	1	35.65	48.65	3.5	2.5	7.0	0.030	77
9	63	1	1	35.65	48.65	3.5	5.0	3.5	0.015	77
57	64	1	1	35.65	48.65	3.5	5.0	7.0	0.030	77

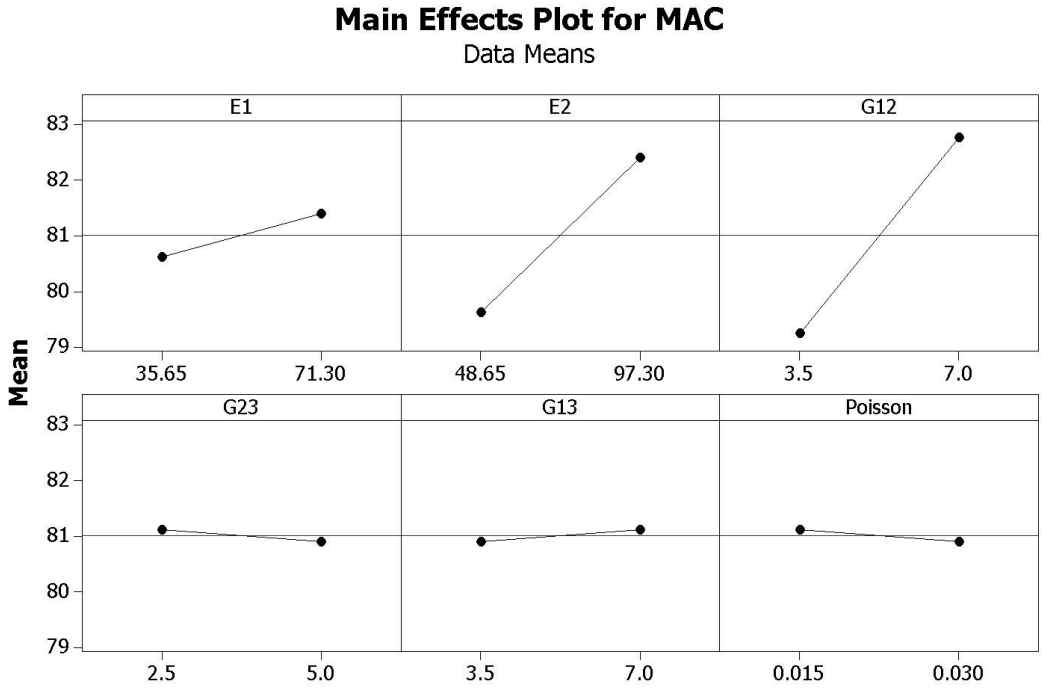

Fig. 4.21 Main Effects Mean MAC.

range of values (low and high) were established per parameter in the Table 4.6. Furthermore, the interactions between the parameters can also be analyzed. One must notice that the range of values was defined multiplying each of the parameters of Table 4.6 by 2. The multiplication of parameters by 2 is known as orthogonality in the full factorial to keep the "balance" of the design.

The effects of each parameter in the composite structure can be observed in Fig. 4.21. The main effects are identified through the slope generated as a consequence of the MAC values between the limits defined for each parameter – a bigger slope means a stronger parameter effect. The Young's modulus E_1, E_2 and the shear modulus G_{12} parameters have a strong influence reflected in the slope.

The G_{13}, G_{23} and Poisson's ratio ν_{12} have a medium influence on the MAC. Furthermore, Fig. 4.22 shows the interactions between the parameters. The interactions can be also identified through the slope generated between the specified limits. The columns of the interaction plot represent the response for a given factor (- or +) interaction. The rows represent the mean MAC response for a given setting (- or +) of a given factor interaction. Parallel lines in an interaction plot indicate no interaction. The greater the difference in slope between the lines,

the higher the degree of interaction. Thus, the "high" values of the interval defined show a positive impact in the MAC results in comparison with the "low" values. The interactions $E_1 - E_2, E_1 - G_{12}, E_2 - G_{12}$ are indentified with the strongest influence according to the slope between them and between all of the parameters, (see Fig. 4.22). Thus, the E_1, E_2 and G_{12} present a positive impact using the upper limit value improving the mean MAC value. However, the interaction plot doesn't alert the reader if the interaction is statistically significant. This point will be overcome using the ANOVA analysis. Furthermore, a cube, contour and surface analysis will provide a map with the trend for each interaction using the interval established.

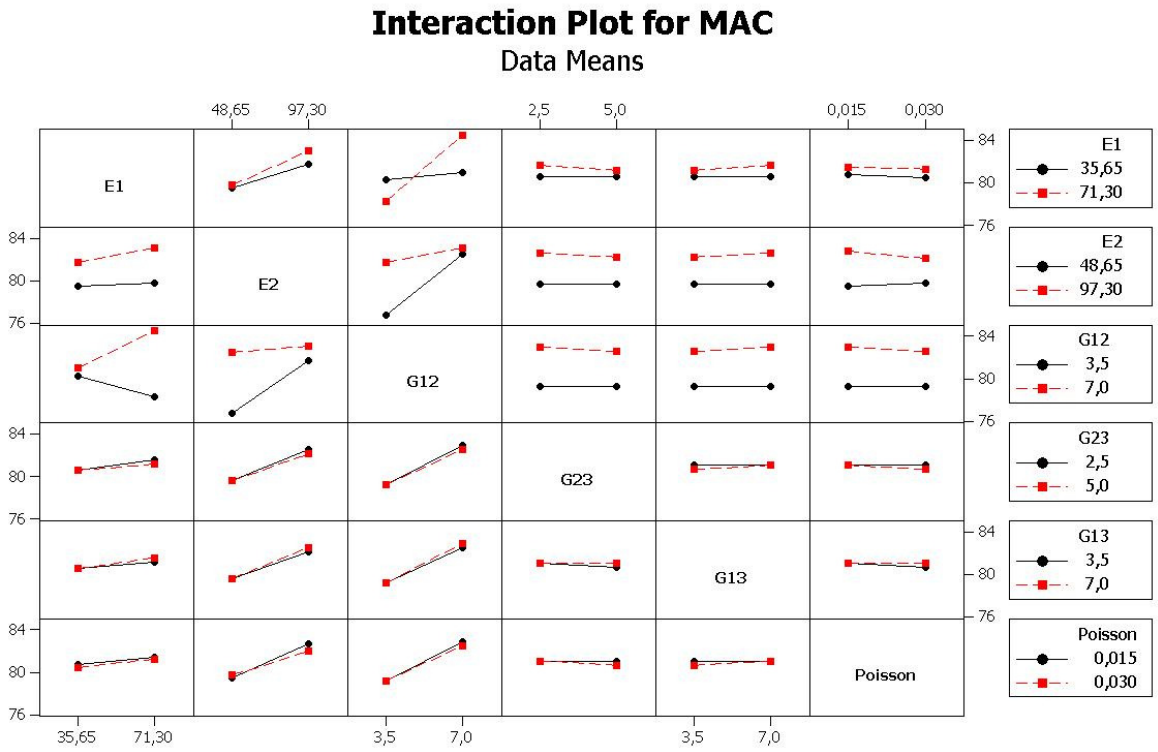

Fig. 4.22 Full Interaction Mean MAC plot matrix.

4.5.3 Cube, Contour and Surface MAC analysis.

A cube plot, (see Fig. 4.23), can be used to show the relationships between the six factors with a MAC response measure for 2-level factorial designs or Plackett-Burman designs. The factors with the MAC response displayed in the cube plot represents what a factorial design looks like. Viewing the factors with the MAC response one can observed the impact of the MAC values

according to the factors. The contour, (see Figs. 4.24 and 4.25), and the surface plots, (see Figs. 4.26 and 4.27), are used to visualize and explore the potential interaction of all the parameters versus the MAC response. The contour figures provide a 2-dimensional contour plot for the lower and higher limits. These values are plotted on the $x-$ and $y-$ scales respectively and the MAC response values represented by the contours. A contour plot is like a topographical map in which $x-, y-$, and $z-$ values are plotted instead of longitude, latitude, and elevation and are connected by contour lines of constant MAC responses. One can observe an interchange of the MAC response (minimum and maximum pattern) between Fig. 4.24, interaction $G_{12} - E_1$ and Fig. 4.25, interaction $G_{12} - E_1$ for the specified low and high limits. Most of the contour plots of MAC (lower an upper limits) show a rising ridge pattern.

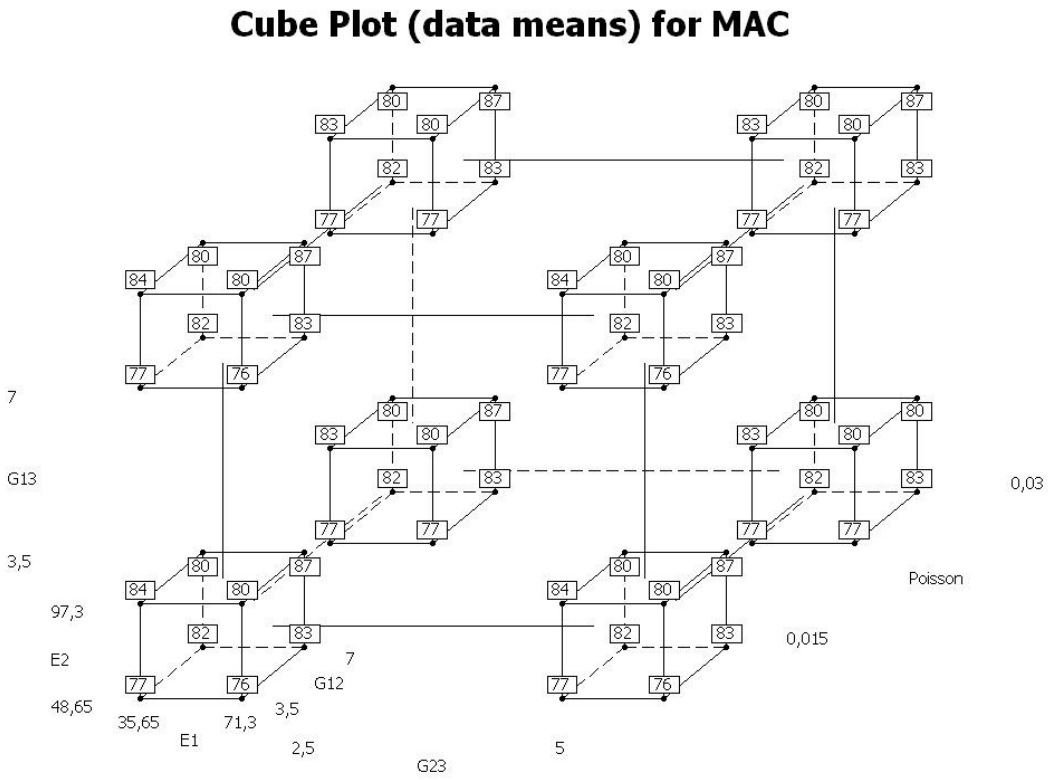

Fig. 4.23 Cube MAC plot.

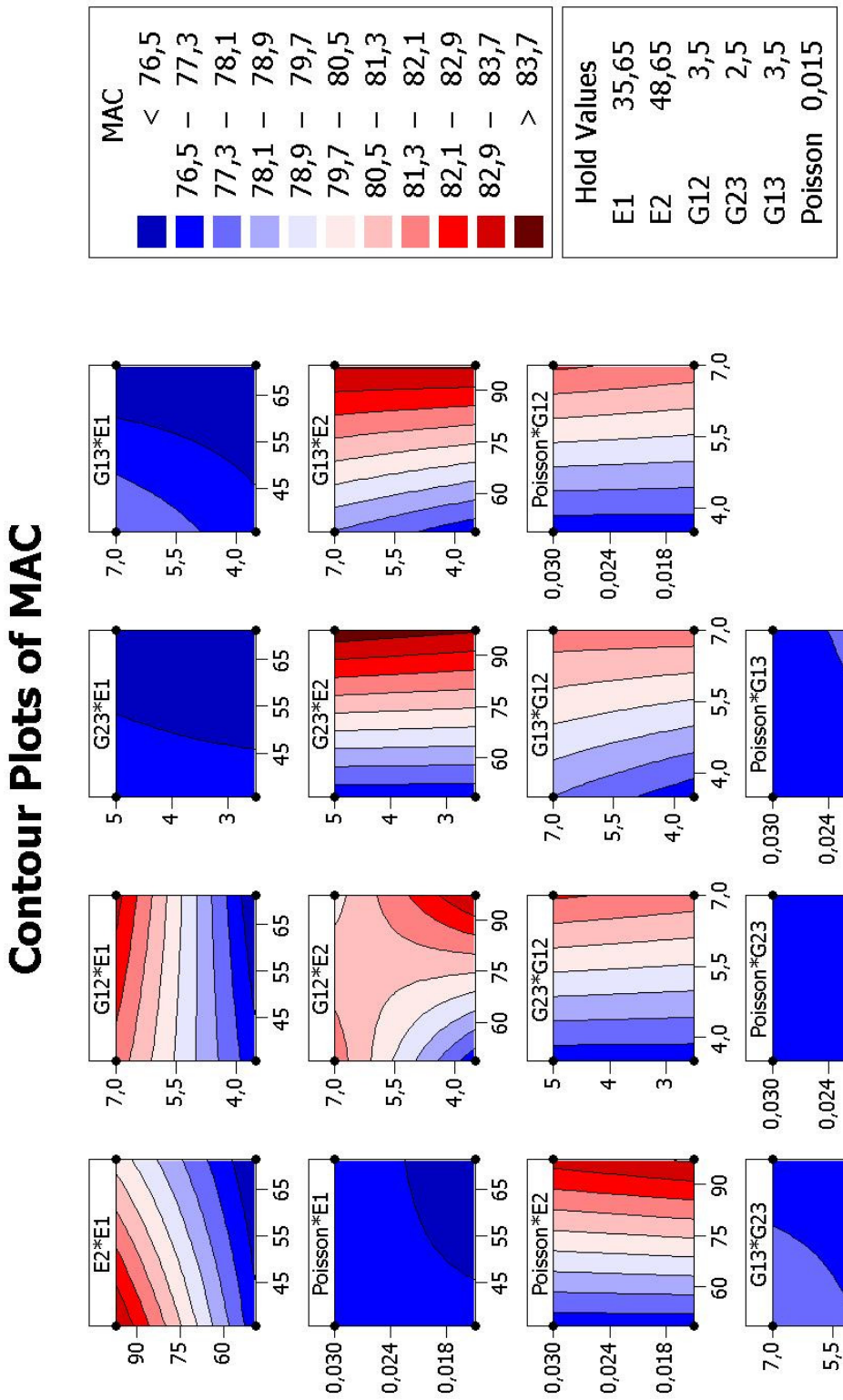

Fig. 4.24 Contour MAC for all pairs lower limit.

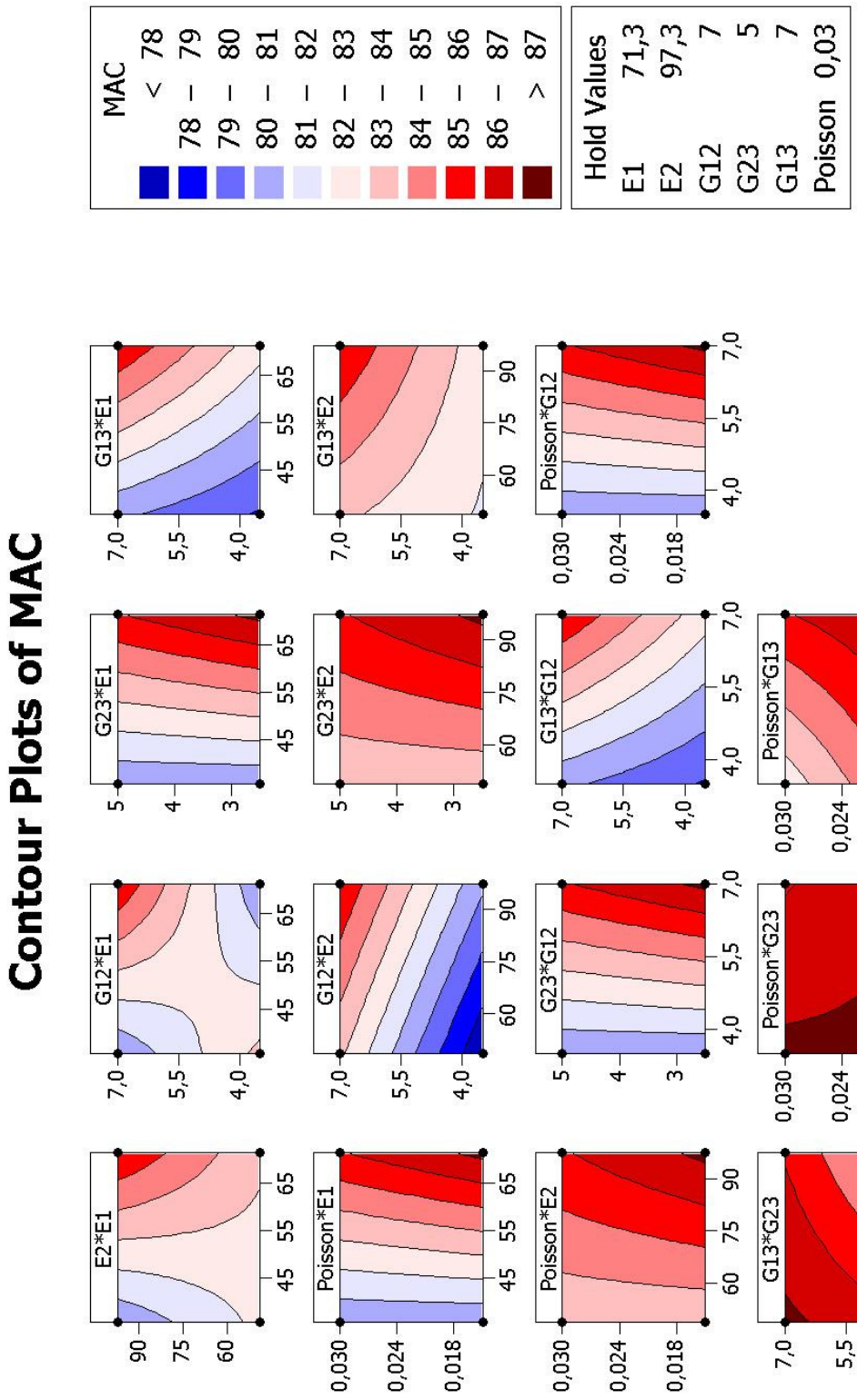

Fig. 4.25 Contour MAC for all pairs upper limmit.

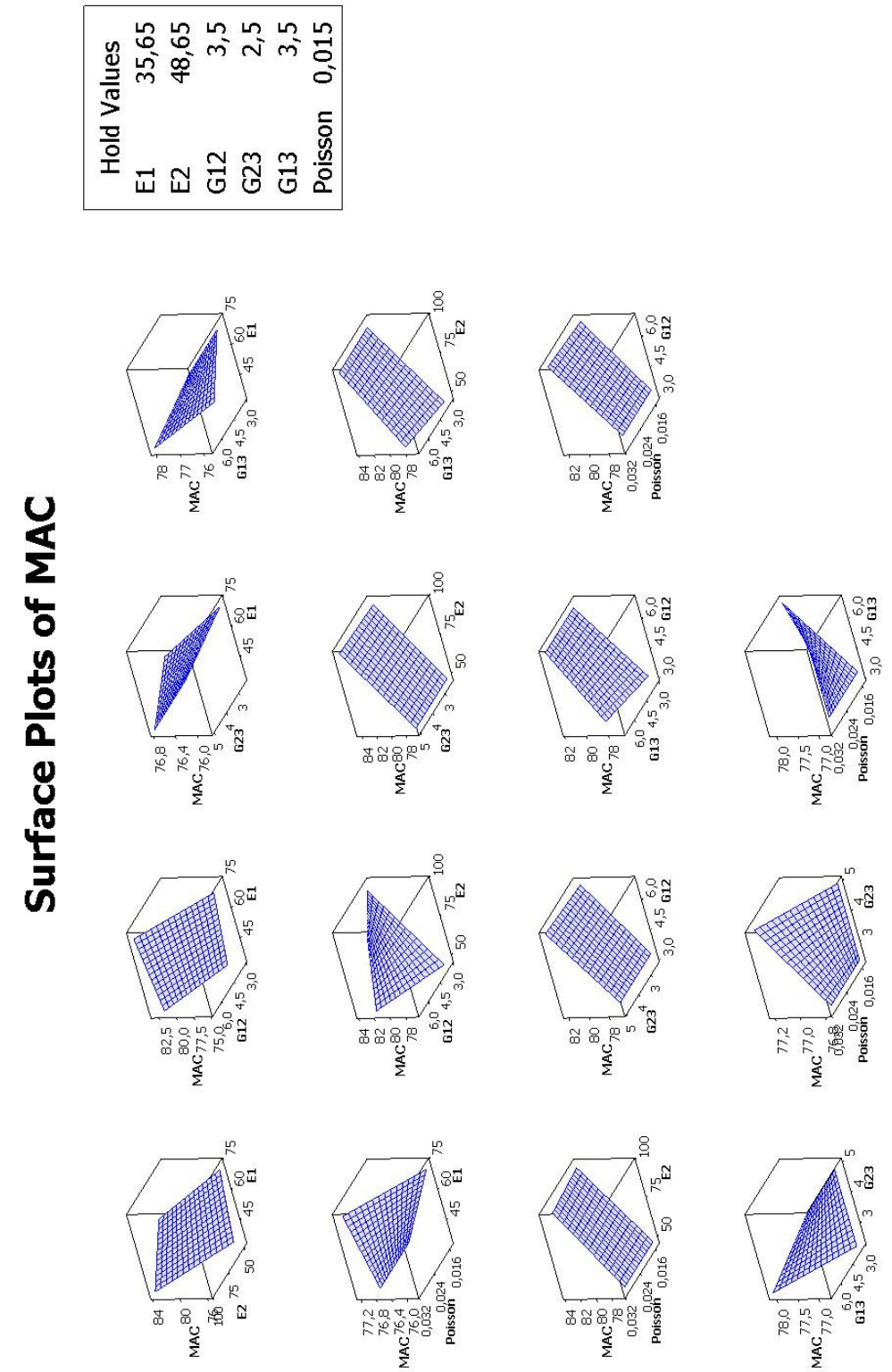

Fig. 4.26 Surface MAC for all pairs lower limit.

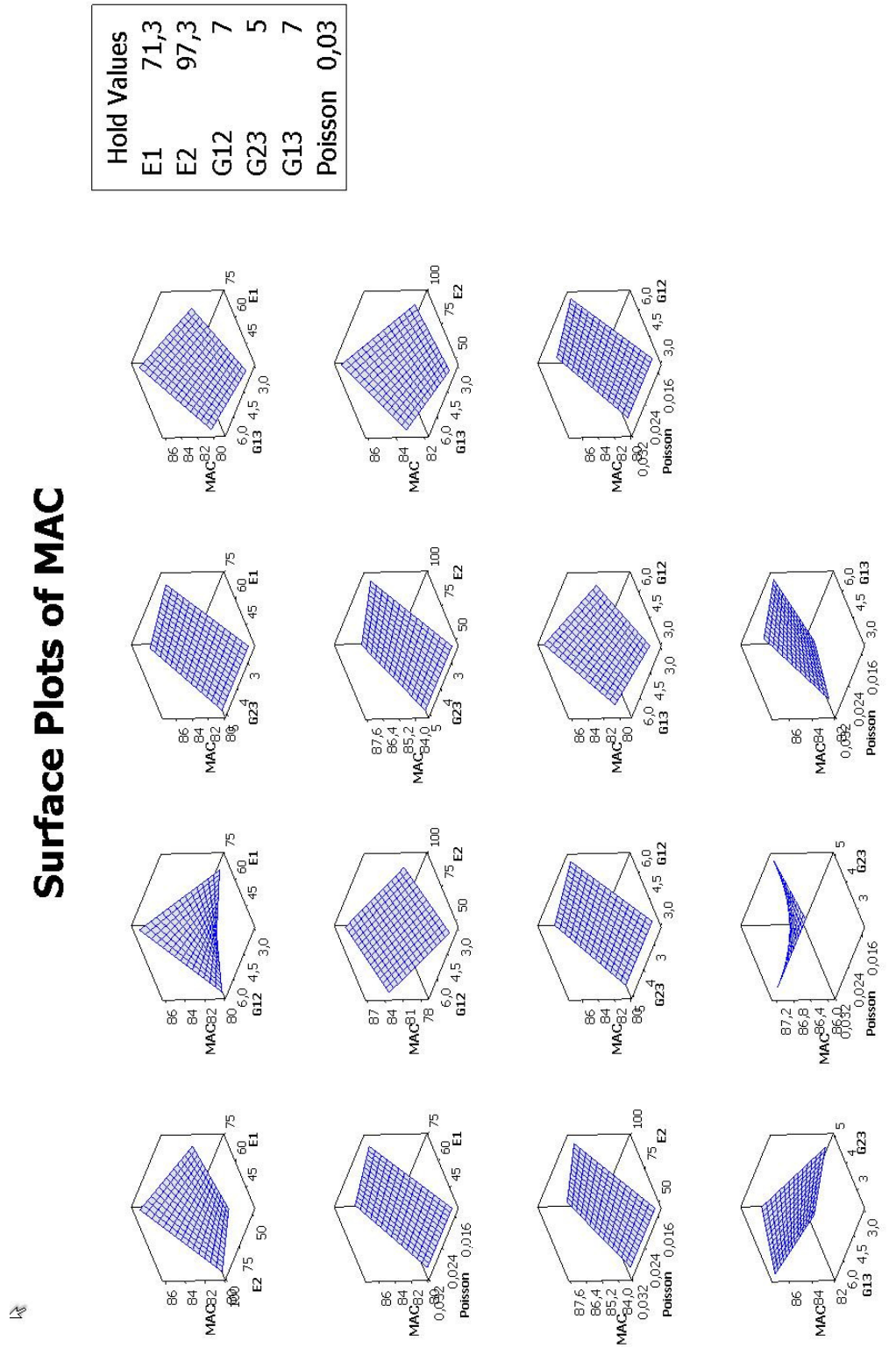

Fig. 4.27 Surface MAC for all pairs upper limit.

Table 4.9 ANOVA results for MAC - Part 1

Source	DF	Seq-SS	Adj-SS	Adj-MS	F	P
Main Effects	6	335.34	335.34	55.8906	73.00	0.000
2-Way Interactions	15	218.23	218.23	14.5490	19.00	0.000
3-Way Interactions	20	82.56	82.56	4.1281	5.39	0.000
Residual Error	22	16.84	16.84	0.7656		
Total	63	652.98				

Notes: DF, degree of freedom, Seq SS, Sequential Sum of squares, Adj SS, Adjust sum of squares, Adj MS, Adjust mean of squares, F=F-value, P=P-value.

S = 0.875 , R-Sq=97.42%, R-Sq(Adj)=92.61%

The contour plots are also useful to see the trend of the MAC for a particular factor between lower and upper limits. The quasi-lineal behavior of the MAC value between interaction of factors can be appreciated, for example $Poisson * E2$ and $G_{23} * G_{12}$. MAC surface plots, Figs. (4.26) and (4.27), show the variable surface response for the lower and higher limits values respectively. The surface with the contour plots complement the visualization of the results. The figures provide a 3D surface where the points have different responses, in some cases a quadratic surface response, see the Poisson*G_{23} and $E_1 * G_{12}$ for lower and upper limits. If we change the holding values, the MAC response surface changes.

4.5.4 ANOVA analysis

The analysis of variance (ANOVA) is used to determine the significance of the design parameters that influence the MAC. This analysis is evaluated with a confidence level of 95% that is equal to α=0.05. It can be observed from the results obtained in Table 4.9 dividing the sum of squares by main effects or interactions can indentify the influence in the MAC response. The main effects have a significant effect (51.36%) on the MAC response followed by the 2-Way Interactions (33.42%), the 3-Way Interactions (12.64%) and the Residual Error (2.58%), respectively. When the P-value is less than 0.05 then the paramenter or interaction can be considered as statistically significant. With the ANOVA results obtained in Table 4.9, it is demostrated that the parameters, second and third interactions in the model have a significant effect in the MAC response. The influence of the interactions in the MAC response can be illustrated using the coefficient of determination R-Sq defined as the ratio of the variation of the total variation. The approximation

Table 4.10 Uncoded Coefficients for MAC - part 1

Term	Coefficient	P-value
Constant	43.2813	0
E_1	0.134993	0.002
E_2	0.571686	0
G_{12}	5.375	0
G_{23}	-0.875	0.328
G_{13}	4.75	0.328
ν_{12}	-145.833	0.328
$E_1 * E_2$	-0.00565767	0.024
$E_1 * G_{12}$	-0.030555	0
$E_1 * G_{23}$	0.0245442	0.328
$E_1 * G_{13}$	-0.0385694	0.328
$E_1 * \nu_{12}$	7.83076	0.888
$E_2 * G_{12}$	-0.0987373	0
$E_2 * G_{23}$	0.0179856	0.328
$E_2 * G_{13}$	-0.0282631	0.328
$E_2 * \nu_{12}$	0.25694	0.043
$G_{12} * G_{23}$	0.25	0.328
$G_{12} * G_{13}$	-0.392857	0.328
$G_{12} * \nu_{12}$	41.6667	0.328
$G_{23} * G_{13}$	-0.55	0.328
$G_{23} * \nu_{12}$	58.3333	0.328
$G_{13} * \nu_{12}$	-91.6667	0.328
$E_1 * E_2 * G_{12}$	0.00133848	0
$E_1 * E_2 * G_{23}$	-2.02E-004	0.328
$E_1 * E_2 * G_{13}$	0.000144144	0.328
$E_1 * E_2 * \nu_{12}$	-0.0336337	0.328
$E_1 * G_{12} * G_{23}$	-0.00280505	0.328
$E_1 * G_{12} * G_{13}$	0.00200361	0.328
$E_1 * G_{12} * \nu_{12}$	-1.0018	0.043
$E_1 * G_{23} * G_{13}$	0.00280505	0.328
$E_1 * G_{23} * \nu_{12}$	-0.654511	0.328
$E_1 * G_{13} * \nu_{12}$	0.467508	0.328
$E_2 * G_{12} * G_{23}$	-0.0020555	0.328
$E_2 * G_{12} * G_{13}$	0.00146821	0.328
$E_2 * G_{12} * \nu_{12}$	0.04894	0.888
$E_2 * G_{23} * G_{13}$	0.0020555	0.328
$E_2 * G_{23} * \nu_{12}$	-0.479616	0.328
$E_2 * G_{13} * \nu_{12}$	0.342583	0.328
$G_{12} * G_{23} * G_{13}$	0.0285714	0.328
$G_{12} * G_{23} * \nu_{12}$	-6.66667	0.328
$G_{12} * G_{13} * \nu_{12}$	4.7619	0.328
$G_{23} * G_{13} * \nu_{12}$	6.66667	0.328

of R-Sq to the unity means a better response model results and the degree of fits. The value of R-Sq calculated for this model is 97.42%, including up to 3-Way Interactions, is very close to the unit and it shows a good variability in the data based on the factors and their interactions using the MAC values.

4.5.5 Transfer function of the MAC response

Once the ANOVA is perfomed, the transfer function can be obtained using the estimated uncoded coefficients obtained with MINITAB. The uncoded coefficients are displayed in Table 4.10 based on the ANOVA analysis up to 3-Way Interactions, (see Table 4.9). It is important to highlight the number of interactions needed in order to reduce the error in the transfer function. The estimated uncoded coefficients are obtained considering until 3-interactions to reduce the error in the transfer function, (see Table 4.9, R-Sq value[23]).

$$\begin{aligned} Y = MAC = 43.2813 + (E_1 * 0.134993) + (E_2 * 0.571686) + (G_{12} * 5.375) \\ -(E_1 * E_2 * 0.00565767) - (E_1 * G_{12} * 0.030555) - (E_2 * G_{12} * 0.0987373) \\ +(E_2 * \nu_{12} * 0.25694) + (E_1 * E_2 * G_{12} * 0.00133848) = 89.78 \end{aligned} \tag{4.1}$$

As was mentioned, one of the advantages of applying the DOE is to create a transfer function

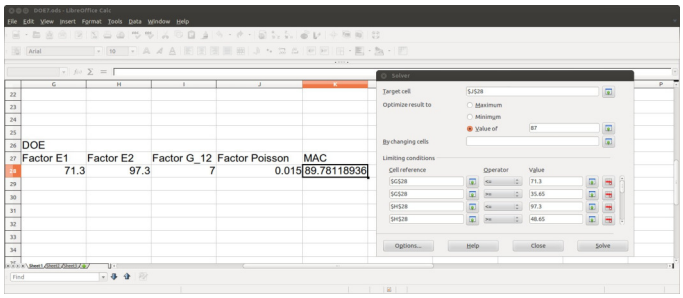

Fig. 4.28 Solver function in Libreoffice

based on the uncoded coefficients obtained with the ANOVA using the MAC response of the

[23]The value of R-Sq decreases to 51.36% if it is only considering the main effects. The R-Sq improved to 84.78% considering the 2-Way Interactions. R-Sq is obtained dividing the Seq-SS of the main effects by the total, see Table B.1.

Table 4.11 Updated elastic mechanical properties.(*th=thickness)

Part 1(m)	***Modulus***	***E(GPa)***	***ν* (-)**	**Shear**	***G(GPa)***	***ρ*** (Kgm^{-3})
**th=0.0035*	E_1	71.3	0.03	G_1	7	2600
	E_2	97.3	0.03	G_2	5	
				G_3	7	
Part 2(m)	***Modulus***	***E(GPa)***	***ν* (-)**	**Shear**	***G(GPa)***	***ρ*** (Kgm^{-3})
**th=0.007*	E_1	71.3	0.02	G_1	6	1500
	E_2	68.3	0.02	G_2	5	
				G_3	6	
Part 3(m)	***Modulus***	***E(GPa)***	***ν*(-)**	**Shear**	***G(GPa)***	***ρ*** (Kgm^{-3})
**th=0.0035*	E_1	71.3	0.02	G_1	6	1500
	E_2	68.3	0.02	G_2	5	
				G_3	6	

elaborated array in Table 4.8. The transfer function in Eq. (4.1) is constructed using these uncoded units[24] obtained and displayed in Table 4.10.

The coefficient with P-value $\leq$ to 0.05 displayed in the Table 4.10 are selected because of the most significant coefficients that affect the MAC response. Thus, the transfer function in Eq. (4.1) contains only the coefficients that are significant including the third interaction $E_1 * E_2 * G_{12}$ obtained with the ANOVA using the stiffness parameters. One can notice that the uncoded coefficient $E_1 * G_{12} * \nu_{12}$ is not included in the transfer function even the P-value is below to 0.05. It was decided not to include this coefficient in the transfer function because the MAC value shows a negative impact versus the best possible MAC values displayed in the DOE cube results, (see Fig. 4.23). Thus, the best MAC value is obtained with the "Solver" function in 'Excel' or 'Libreoffice calc', (see Fig. 4.28) using the transfer function of Eq. (4.1) based on the stiffness parameters E_1, E_2, G_{12} and ν_{12}, the uncoded coefficients and the residual error related in the ANOVA analysis. Moreover, the transfer function obtained shows that the stiffness parameters, G_{13} and G_{23}, are not significant according to the P-values obtained in the Table 4.10. One of the reasons that these parameters are not included in the transfer function could be due to the lineal assumption in the stiffness homogenization using the FSDT.

Thus, the MAC value obtained with the transfer function, (see Fig. 4.28), is used to evaluate the sensibility of the Poisson's ratio in the full FE model changing only the Poisson's ratio. A small difference in the MAC results (paired mode 4^{th}) can be appreciated between the two

[24]The uncode units in a DOE are obtained by transforming the low factor levels to -1 and the high factor levels to $+1$.

models changing only the Poisson ratio (upper and lower limits), (see Fig. 4.29), using the updated material properties displayed in Table 4.11. The evaluation of the sensibility of the Poisson ratio value using the MAC suggests choosing the upper Poisson's ratio value instead of the lower value obtained with the transfer function. The evaluation of the sensitivity of the Poisson's ratio value using a ESL model versus a LWM can be performed in a future project to compare the MAC response and the transfer functions

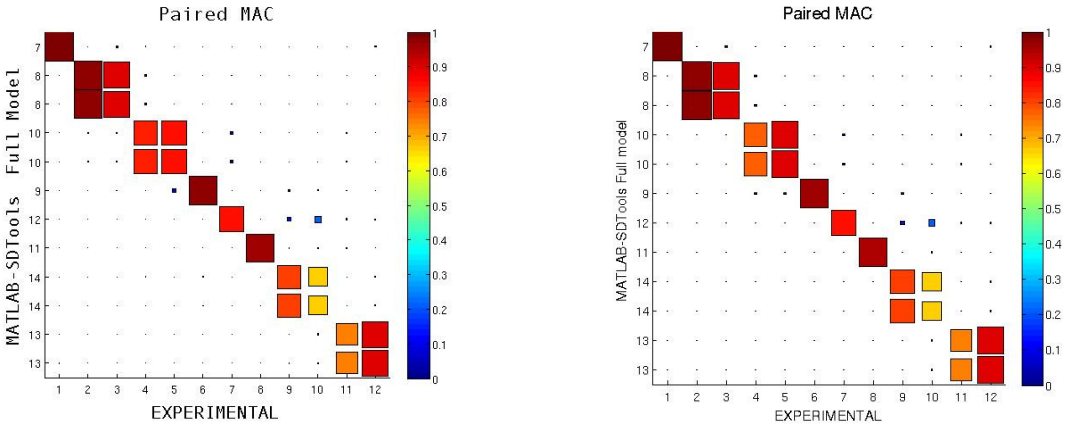

(a) Poisson ratio ν_{12}=0.030.

(b) Poisson ratio ν_{12}=0.015.

Fig. 4.29 The Poisson ratio sensibility evaluation of material properties updated (Table 4.11) using the MAC

Chapter 5

Validation of the CFRP component - FE full model

5.1 Application of the MAC to validate updated stiffness parameters using the MNET

According to the improvement of the MAC results obtained updating the stiffness parameters using the MNET in the previous chapter, the stiffness parameters will be validated using the MAC, XOR, MACco and COMACs criteria as well as other finite elements and solvers.

The MAC and XOR can be used to analyze the accuracy of the mode shapes between the experimental and theoretical models[1]. It is well known that the MAC and XOR provide similar information, illustrated in Figs. 5.1 and 5.2. However, each orthogonality criteria tend to indicate different things. It performs the MAC and XOR criteria to verify the approximation of MATLAB-SDTools, MSC/NASTRAN and ABAQUS full FE models. The same number of modes shapes (19 mode pairs) is calculated in each full FE model.

The MAC analysis with the SDTools full FE model displays the best MAC results computed with the updated stiffness parameters (over 80%) in most of the paired modes with the exception of two paired modes 10^{th}, and 11^{th}. The MAC analysis with the MSC/NASTRAN full FE model shows a similar MAC paired modes behaviour compared with the SDTools model (except the mode pair 4^{th}). The MAC analysis of the full FE performed with ABAQUS presents the lower

[1] Appendix E provides a MAC, MACco and frequencies, see Tables E.2 and E.3 comparison using the technical data of the raw material C-faser-gewebe and the updated stiffness parameters vs experimental measurements.

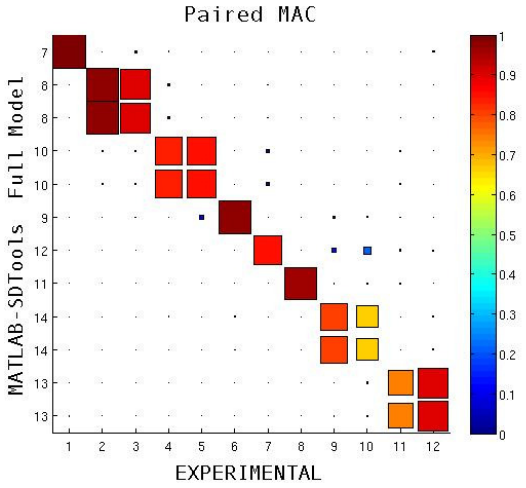

(a) SDTools-Experimental.

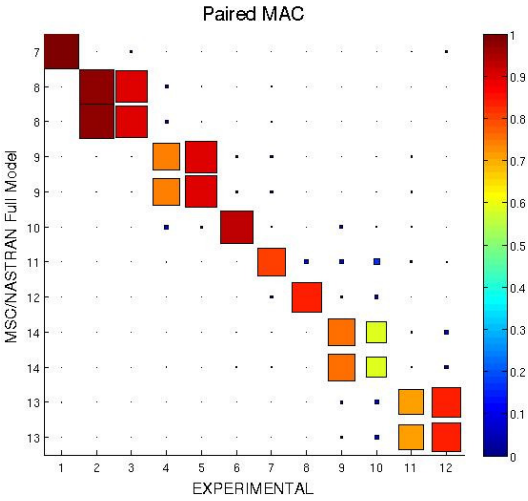

(b) MSC/NASTRAN-Experimental.

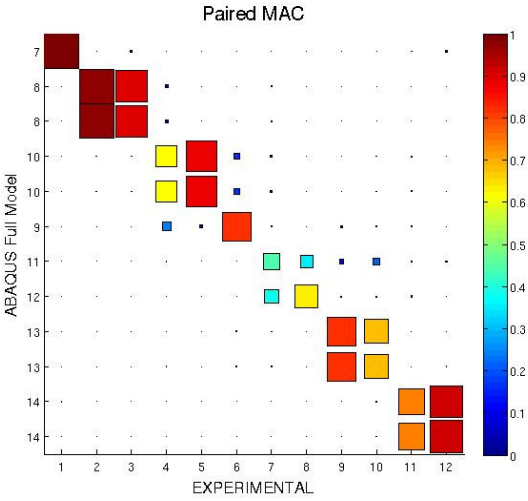

(c) ABAQUS-Experimental

Fig. 5.1 Comparison of MACs using the stiffness parameters of Table 4.11 vs. experimental measurements

correlation in respect to the other full FE models. The MAC analysis shows a high correlation between the experimental measurements and full FE models (performed with SDTools and MSC/NASTRAN) applying the stiffness parameters obtained with the DOE, (see Fig. 5.1). It may be possible to obtain enhanced performance by choosing a thin or thick shell elements[2]. However, the analysis with different types of elements is beyond the objective of this study.

The XOR criterion is performed to display the orthogonality's quality of the experimental and theoretical results in the low frequency range (up to 400 Hz) analyzed in Chapter 4 once it is performed the MAC criterion. Fig. 5.2 shows the XOR of the experimental measurements and the full FE models (MATLAB-SDTools, MSC/NASTRAN and ABAQUS models, respectively). One can observe that the off-diagonal terms in the XOR and MAC of the full FE models versus experimental measurements fulfill the criteria of $\leq$ than 10% with the exception of the XOR of the MATLAB-SDTools FE model. Most of the diagonal values have the value of unity and the off-diagonal terms have the value near zero. Analyzing the XOR and MAC results can be concluded the good mass distribution with the XOR and the good accuracy between the mode shapes with the MAC respectively.

In Fig. 5.3 one can observe some mode shapes of the full FE model. Furthermore, the nearly double correlation in the experimental results identified in Fig. 5.2a suggests the presence of the veering phenomena (bending and torsional mode at the same frequency) in the considered composite component structure. This is reflected in the MAC values for the corresponding experimental modes, (see Table 5.1). Noticed that in the XOR plots of the full FE models are not identified the nearly double correlation for the coupling considerations, (see Figs. 5.2b, 5.2c and 5.2d), however, the nearly double veering phenomena can be observed applying the MAC between the full FE models versus the experimental measurements. The Table 5.1 shows the MAC values (correlation) obtained for each case between the full FE models versus the experimental results with the stiffness parameters obtained with the DOE based on the curve-fitting performed in Chapter 4. The best eigenvector results are observed in the MATLAB-SDTools FE model following by the MSC/NASTRAN FE model. Furthermore, the best eigenfrequency values are observed in the MSC/NASTRAN model following by the MATLAB-SDTools.

[2]The library is divided into three categories consisting of general-purpose, thin, and thick shell elements. Thin shell elements provide solutions to shell problems that are adequately described by classical (Kirchhoff) shell theory, thick shell elements yield solutions for structures that are best modeled by shear flexible (Mindlin) shell theory, and general-purpose shell elements can provide solutions to both thin and thick shell problems [151], see ABAQUS theory manual section 3.6.1.

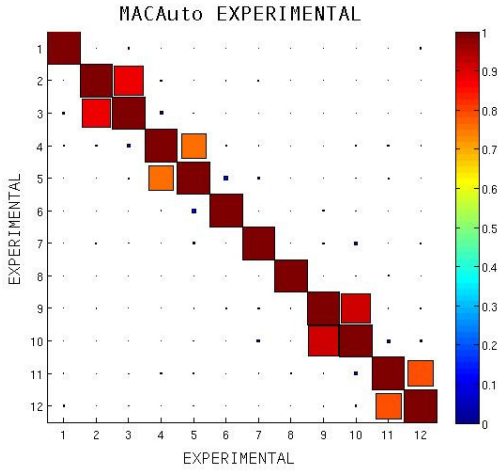

(a) XOR experimental model.

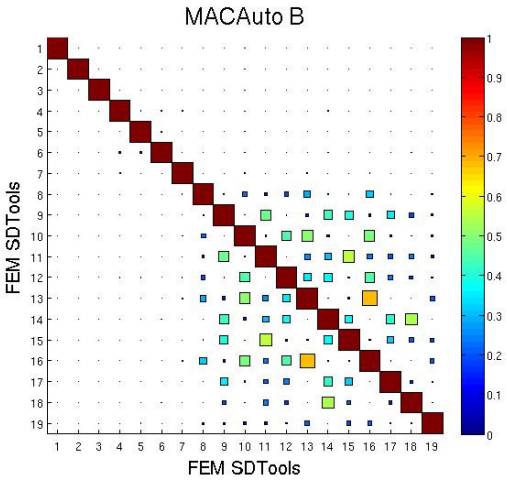

(b) XOR full SDTools model.

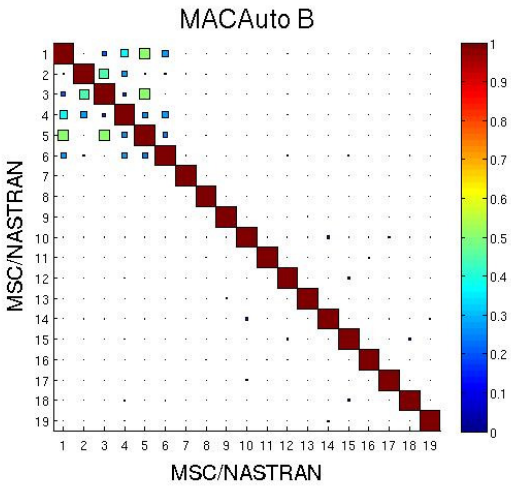

(c) XOR MSC/NASTRAN model

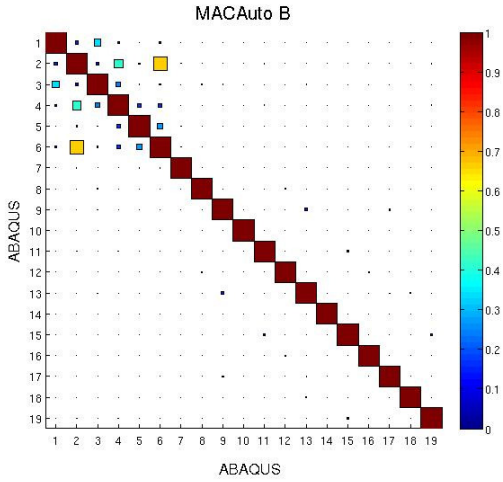

(d) XOR ABAQUS

Fig. 5.2 Comparison of XORs using the stiffness parameters of Table 4.11

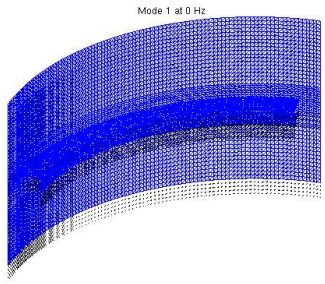

(a) Mode 1=0 Hz.

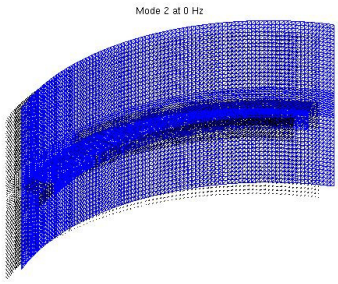

(b) Mode 2=0 Hz.

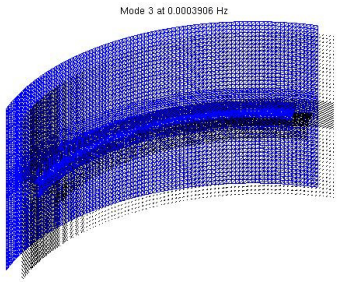

(c) Mode 3=0.0003906Hz.

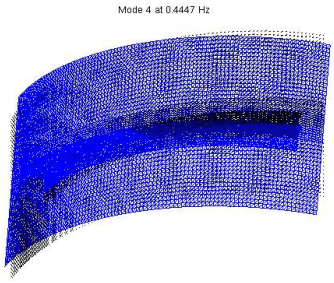

(d) Mode 4 = 0.4447 Hz.

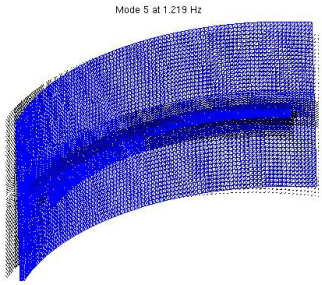

(e) Mode 5=1.2193 Hz.

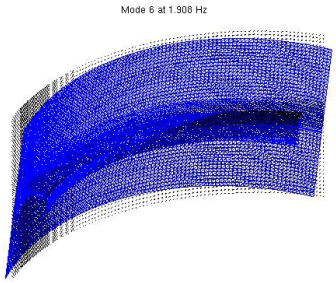

(f) Mode 6=1.9085 Hz.

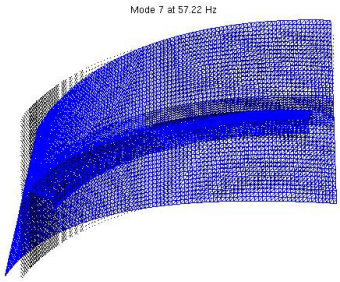

(g) Mode 7=57.2179 Hz.

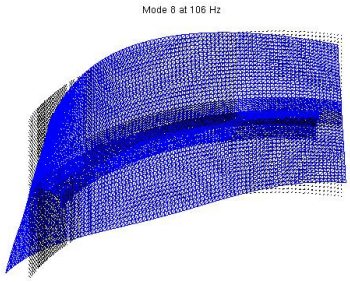

(h) Mode 8=106.0160 Hz.

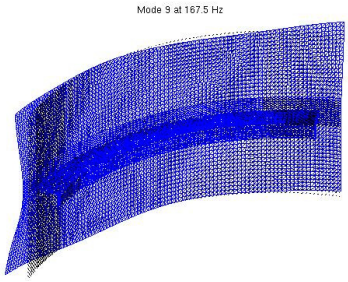

(i) Mode 9=167.4985 Hz.

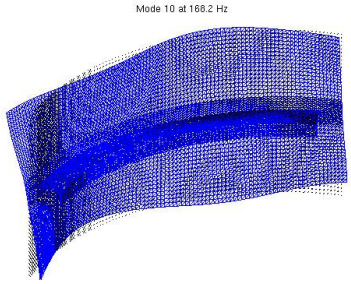

(j) Mode 10=168.1977 Hz.

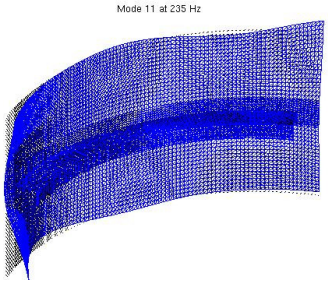

(k) Mode 11=234.9896 Hz.

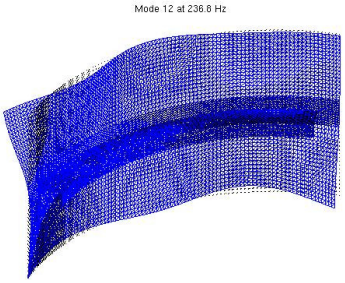

(l) Mode 12=236.8307 Hz.

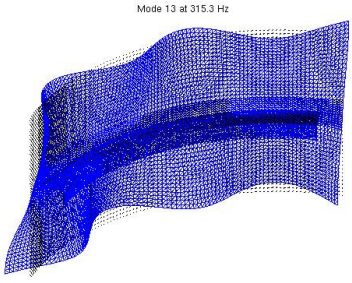

(m) Mode 13=315.2561 Hz.

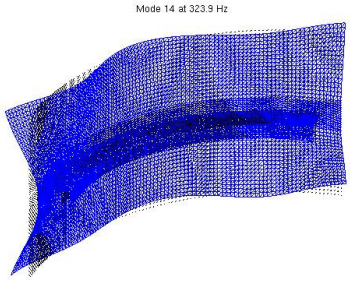

(n) Mode 14=323.9288 Hz.

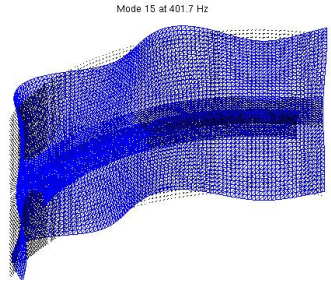

(o) Mode 15=401.7151 Hz.

Fig. 5.3 Mode shapes-SDTools full FE model.

Table 5.1 Comparison of full FEM model results with the material properties obtained with the DOE, see Table 4.11 vs. curve-fitting using experimental measurements.

		FE model				FE model				FE model			
ID	Test (Hz)	ID	SDTools (Hz)	DF/FA %	MAC	ID	MSC/NASTRAN (Hz)	DF/FA %	MAC	ID	ABAQUS (Hz)	DF/FA %	MAC
1	49.243	7	57.218	16.2	100	7	55.954	13.6	100	7	58.653	19.1	100
2	92.265	8	106.02	14.9	97	8	104.14	12.9	97	8	106.58	15.5	97
3	93.756	8	106.02	13.1	90	8	104.14	11.1	90	8	106.58	13.7	90
4	145.29	10	168.2	15.8	83	9	165.51	13.9	74	10	168.14	15.7	90
5	160.05	10	168.2	5.1	86	9	165.51	3.4	90	10	168.14	5.1	89
6	164.18	9	167.5	2.0	98	10	166.55	1.4	93	9	158.32	-3.6	82
7	226.36	12	236.83	4.6	86	11	232.59	2.8	81	11	228.16	0.8	45
8	243.4	11	234.99	-3.5	96	12	233.4	-4.1	84	12	235.31	-3.3	64
9	307.33	14	323.93	5.4	81	14	321.1	4.5	76	13	306.73	-0.2	82
10	314.18	14	323.93	3.1	66	14	321.1	2.2	59	13	306.73	-2.4	68
11	324.83	13	315.26	-2.9	74	13	310.72	-4.3	71	14	313.41	-3.5	75
12	329.67	13	315.26	-4.4	90	13	310.72	-5.7	84	14	313.41	-4.9	91

The ABAQUS FE model presents the worst correlation respet to the other FE models using the curve-fitting perfomed in Chapter 4. The first criterion of selection for the best FE model between the three FE models is the best accuracy of the MAC values obtained (MATLAB-SDTools FE model). The second criterion is the eigenfrequency difference obtained between the FE models and the curve-fitting performed based on the experimental measurements. Furthmore, the bigger eigenfrequency difference in the three FE models might be associated to the anisotropy ratio using the CLT and FSDT illustrated in the Appendix E Tables E.2 and E.3 respectively. Moreover, it is also documented in the literature that the application of the Ritz vectors helps to predict the effect of modifications in structures. The integration interface between the full FE model to perform the MNET is the third criterion. The fourth criterion is application of the CBMOR based on Ritz vectors and the AMLS. Thus, the final criterion is the implementation of this MNET methodolgy with MATLAB-SDTools FE model that offers the best characteristic to apply, calculate, perfom and obtain the CBMOR method with enough accuracy to a CFRP component based on the improvements documented in the literature.

Pierre [227] reported how localization and veering are related to two kinds of "coupling": the physical coupling between the structural components, and the modal coupling set up between the mode shapes through parameter perturbations. His studies show that, in structures with close eigenvalues, such as motions in different dimensions uncouple (could be the case of the CFRP assembly studied) result in both strong localization of modes and abrupt veering away of the loci of the eigevalues when those are plotted against a parameter representing the system disorder. There are only three types of structures made of conservative materials that have been identified to exhibit veering[3]:

1. Symmetric or cyclic structures, where it is allowed through algebraic properties of the group of symmetric properties,

2. Multi-dimensional substructures for which motions in different dimensions uncouple, such as plates having bending and a torsional mode at the same frequency,

3. Structures with fully uncoupled substructures

The considered CFRP structure corresponds to the second type - multi-dimensional plate structures. Du Bois, Adhikari and Lieven [230] presented a detailed experimental and numerical

[3]Multiple modes allowing the eigenvalues to be equal and therefore modal crossing with instantaneous rotation on mode shapes [227].

investigation on veering and crossing phenomena applying model updating and modal correlation algorithms[4]. In this study the MAC index is used before and after updating the material properties. Veering phenomena can be identified using the MAC per paired modes, before and after updating the material properties, (see Figs. 4.16, 4.17, 5.1 and 5.2). The study of the presence of this phenomenon in the CFRP structure is beyond of the scope of this work.

5.1.1 Modal Assurance Criteria per pair-sensor (MACco)

Using the MACco criteria introduced in Chapter 2.1.1, it is possible to analyze the paired modes per sensor that contribute to low MAC values, (see Fig. 5.4).

According to Table 5.2, the indices of the sensors used in the pairing mode show an improvement per sensor followed by an improvement in the "mean MAC" and MAC paired modes associated to each updated FE model. This Table is divided into four sections and displays the ten worse MACco values per paired modes-sensors of each FE full model. The first section of this Table is included and it is calculated using the stiffness parameters of Table 4.7 for comparative purposesis. The next three sections show the MACco results of each full FE model with the updated stiffness parameters obtained with the DOE. The MATLAB-SDTools full FE model presents the best MACco results where worse paired modes are identified at pair numbers 16^{th} and 17^{th} at sensor $16y$ followed by the MSC/NASTRAN full FE model with similar MACco results on the same paired modes-sensors. The ABAQUS full FE model displays the worst MACco results with a decrease of the MACco values on paired modes 10^{th} and 13^{th}. The sensor $16y$ displays the "worst" MACco results in all the full FE models. The differences obtained using different FE models suggest the need to perform an assessment with a different kind of elements.

Better MACco values can be observed in the rest of the sensors applying this criterion once it is updated the stiffness parameters in the full FE models. Before updating the material properties, the sensor $16y$ presents the worst correlation with a MAC correlation of 77%. After, updating the material properties, the MACco displays a significant improvement per paired mode-sensor in the different FE models (mean MAC of 87%, 83%, and 79% respectively). With the exception of the sensor $104y, 97y, 131y, 133y$ in the Table 5.2, the MACco values obtained per paired mode-sensor of each full FE models are interchanged order of mean MAC value. For example, the sensors $129y$ in the Table 5.2 displays a mean MAC of 78%, 90%, 86% and 81%,

[4]The impact of veering on model updating and modal correlation algorithms is highlighted as a discipline concerned with the analysis of closely space modes [229].

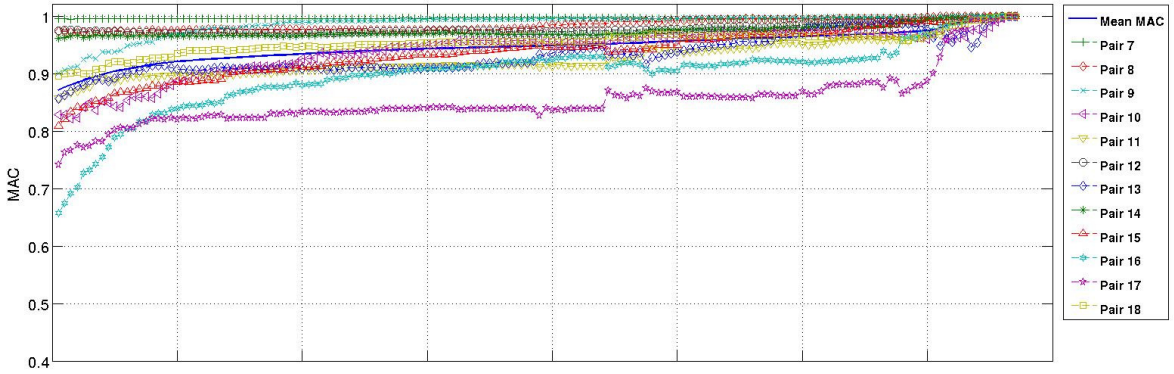

(a) MACco SDTools-Experimental.

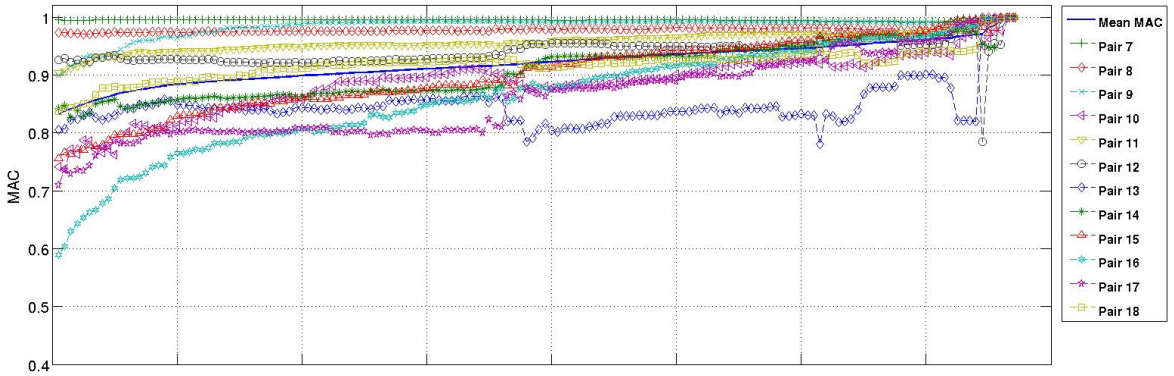

(b) MSC/NASTRAN-Experimental.

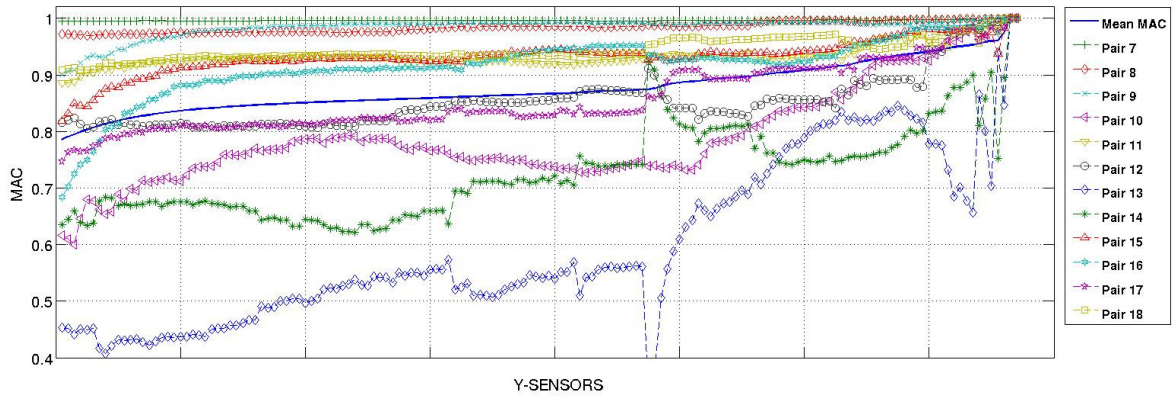

(c) ABAQUS-Experimental

Fig. 5.4 Comparison of MACcos between FE models with material properties of Table 4.11 vs. experimental measurements

Table 5.2 MACco Table Full FE models vs. experimental measurements.

Pair number		7	8	9	10	11	12	13	14	15	16	17	18
EXPERIMENTAL		1	2	3	4	5	6	7	8	9	10	11	12
SDTools FEM (non-updated)		7	8	8	9	9	10	12	11	14	14	13	13
Sensor	Mean MAC												
All	77	99	97	90	58	87	73	65	63	73	61	72	86
16y	77	99	97	91	57	87	73	65	63	73	62	75	87
23y	78	99	97	92	62	88	71	69	59	72	63	74	86
21y	78	99	97	93	66	89	70	71	57	72	63	74	87
129y	78	99	97	93	65	89	70	70	58	72	65	75	88
96y	79	99	97	93	64	89	70	70	60	73	66	76	88
95y	79	99	97	94	64	89	71	70	60	73	66	77	88
17y	79	99	97	94	62	90	72	68	63	73	66	78	90
128y	80	99	97	94	61	89	73	68	63	73	68	79	90
133y	80	99	97	94	64	90	71	70	60	73	69	79	90
104y	80	99	97	95	66	90	71	70	61	74	69	79	90
EXPERIMENTAL		1	2	3	4	5	6	7	8	9	10	11	12
SDTools FEM(updated)		7	8	8	10	10	9	12	11	14	14	13	13
All	87	100	97	90	83	86	98	86	96	81	66	74	90
16y	88	100	97	91	83	86	98	86	96	82	67	76	90
96y	88	99	97	91	82	87	98	87	97	83	69	77	90
95y	88	100	97	91	82	87	98	88	97	84	70	78	90
23y	89	99	97	92	84	87	97	88	96	84	73	77	90
131y	89	100	97	93	85	88	97	89	96	85	73	77	90
17y	89	100	97	93	84	89	97	89	97	85	74	78	91
21y	90	100	97	94	85	89	97	89	97	85	76	78	91
129y	90	100	97	94	85	89	97	89	97	86	77	79	92
128y	90	100	97	94	84	89	97	89	97	86	79	80	92
97y	91	100	97	94	84	89	97	90	97	87	79	81	92
EXPERIMENTAL		1	2	3	4	5	6	7	8	9	10	11	12
MSC/NASTRAN FEM(updated)		7	8	8	9	9	10	11	12	14	14	13	13
All	83	100	97	90	74	90	93	81	84	76	59	71	84
16y	84	99	97	91	74	91	93	81	85	77	60	74	84
23y	84	99	97	92	77	91	92	82	83	76	63	73	84
96y	85	99	97	92	76	92	93	82	84	77	64	74	85
21y	85	99	97	93	79	92	92	83	83	77	65	74	85
95y	85	100	97	93	79	92	92	84	83	78	66	74	85
17y	86	100	97	93	77	93	93	83	85	78	67	76	87
129y	86	100	97	93	77	93	93	82	85	78	68	78	88
131y	86	100	97	94	77	93	93	83	86	79	69	78	88
128y	87	100	97	94	76	93	93	83	86	80	71	79	88
133y	87	100	97	95	79	93	93	84	85	80	72	78	88
EXPERIMENTAL		1	2	3	4	5	6	7	8	9	10	11	12
ABAQUS FEM(updated)		7	8	8	10	10	9	11	12	13	13	14	14
All	79	100	97	90	62	89	82	45	64	82	68	75	91
16y	79	99	97	91	61	89	82	45	64	83	70	76	91
96y	80	99	97	91	60	89	82	44	66	85	73	77	91
23y	80	99	97	92	65	90	81	45	64	85	74	77	91
21y	80	99	97	93	68	90	81	45	63	84	75	77	91
95y	81	99	97	93	68	91	81	45	64	86	76	77	91
17y	81	100	97	93	66	91	82	42	68	87	78	78	91
129y	81	100	97	93	65	91	82	41	68	87	80	79	92
131y	82	100	97	94	66	91	82	42	68	88	81	79	92
133y	82	100	97	95	69	92	81	43	67	88	81	79	92
128y	82	100	97	95	68	91	82	43	67	89	83	79	92

respectively. It is necessary to highlight the updating values observed in the correlation for the paired modes $1^{th}, 2^{th}, 3^{th}, 6^{th}, 8^{th}$ and 12^{th} are almost 1. Before the updating, the paired mode 9^{th} had a value of 60%, (see Fig. 4.17a). The MACco results show an improvement per sensor after updating the material properties in most of the mode pairs (up to 80%) with the exception of the ABAQUS full FE model.

5.1.2 Coordinate Modal Assurance Criteria (COMAC)

After constructing the set of *NM* mode pairs, the next step is the calculation of the COMAC values (in blue), over all the correlated mode pairs as given using the Eq. (2.2). The COMAC values are calculated from zero to one where the value closer to zero per DOF will have the higher agreement. Different COMAC results can be observed in Fig. 5.5 using different updated full FE models (MATLAB, MSC/NASTRAN and ABAQUS respectively) in respect to the number of Y-sensors (x-axis). The COMAC results display an improvement after updating the stiffness parameters with similar pattern and values between FE models, (see Figs. 5.5a, 5.5b, 5.5c). The best COMAC result of the full FE models is obtained at sensors 107y=0.036 and the worst COMAC result at sensor 201y=0.397, (see Fig. 5.5a). The COMAC values in Figs. 5.5b and 5.5c displayed a slightly worse COMAC values in respect to Fig. 5.5a. The COMAC values are consistented according to the MAC results obtained after updating the material properties.

5.1.3 Scale Coordinate Modal Assurance Criteria (COMAC-S)

The COMAC-S results are defined in green in respect to the other COMACs to compare the different full FE models. The COMAC-S results show a similar pattern values between two of the three models. The lowest COMAC-S values can be found in Fig. 5.5 showing an improvement (higher agreement) per DOF according the formulation introduced in Chapter 3. It can be identified that the sensors in Fig. 5.5a and 5.5b display a similar values and pattern (best COMAC-S results). The best COMAC-S results are obtained in the SDTools and MSC/NASTRAN full FE models displayed at sensors 209y=0.019 and the worst on sensor 201y=0.366 respectively. The ABAQUS FE model displays the worse COMAC-S values in respect to the other two FE models.

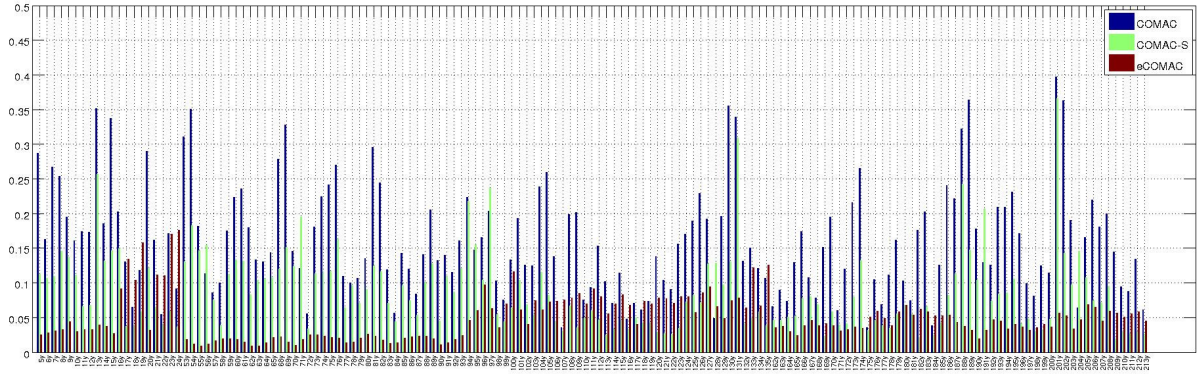

(a) COMAC's SDTools.

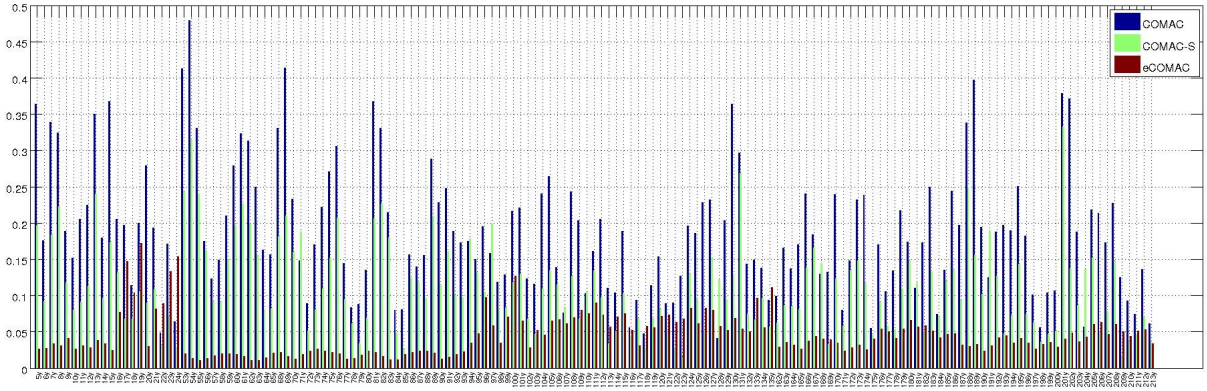

(b) COMAC's MSC/NASTRAN.

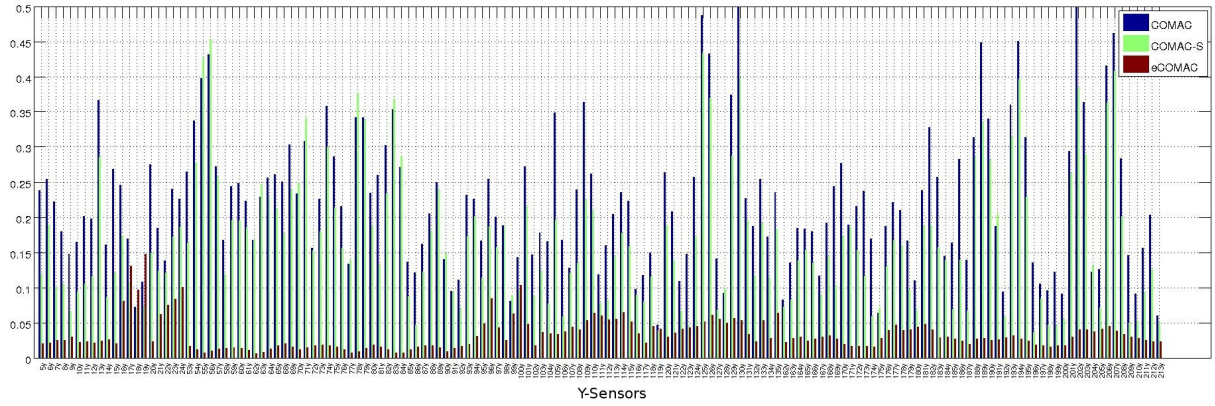

(c) COMAC's ABAQUS.

Fig. 5.5 Comparison of COMACs results between FE models with material properties of Table 4.11 vs. number of sensors.

5.1.4 Enhanced Coordinate Modal Assurance Criteria (eCOMAC)

The eCOMAC results can be observed in brown from zero to one, whereas the value closer to zero per DOF has a higher agreement. The eCOMAC results are interpreted in the same way as the COMAC. The eCOMAC values are the lowest results per DOF of the three full FE models versus the other COMACs with the exception of some sensors ($17y, 19y, 23y, 24y, 100y$), (see Fig. 5.5). The best eCOMAC values are identified at sensors $57y, 58y, 63y$=0.006, (see Fig. 5.5c). Furthermore, the best eCOMAC value in Fig. 5.6a is at sensor $83y$=0.009 for comparative purposes.

In Fig. 5.6 it can be observed clearly that the best eCOMAC results are obtained in the ABAQUS FE model despite that the MAC results obtained are lower. The slightly enhanced eCOMAC results in the ABAQUS model using the S3 elements are beyond of the scope of this work. The lower eCOMAC results suggest an improvement that can be identified in the differences per DOF in the composite component assembly with the updated stiffness parameters.

It can be also appreciated that the eCOMAC is less sensitive to errors at small motion of degrees of freedom for the three FE models and it is more robust than the standard COMAC. The improvement using the COMACs criteria is established in the following order: the eCOMAC results present the better values (the lowest), in second place is the COMAC-S results and in the third position the COMAC using the updated material properties of CFRP.

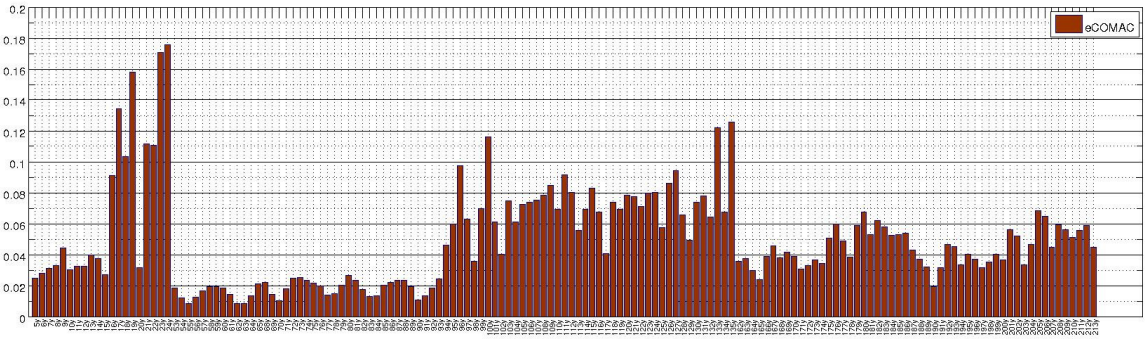

(a) eCOMAC's SDTools.

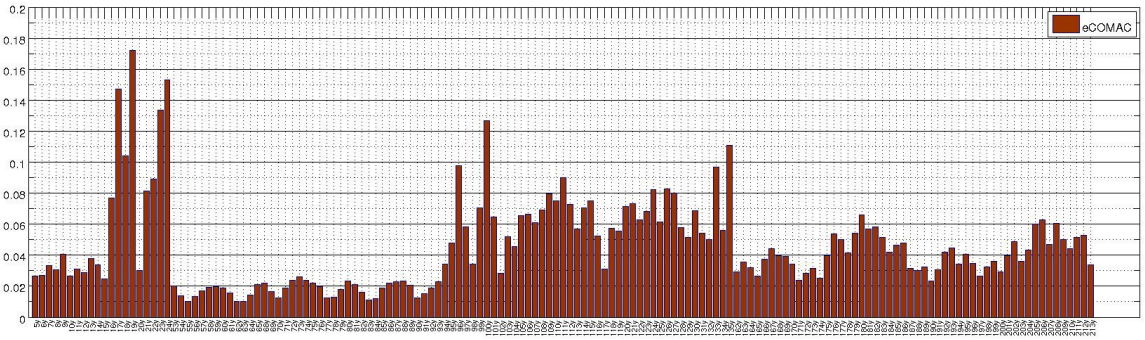

(b) eCOMAC's MSC/NASTRAN.

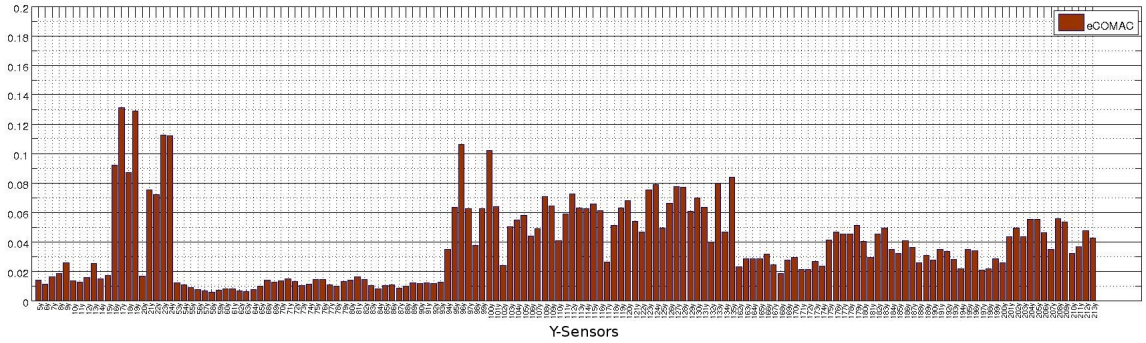

(c) eCOMAC's ABAQUS.

Fig. 5.6 Comparison of eCOMACs results between FE models with material properties of Table 4.11 vs. number of sensors.

Chapter 6

Application of the CBMOR method using Rayleigh-Ritz vector basis to a CFRP

6.1 Introduction

In the first part of this work it was established the feasibility of applying a MNET to obtain the stiffness parameters of a CFRP. The MNET was performed in Chapter 4 to obtain the stiffness parameters in the full FE model using a DOE [145]. Several tools implemented in [106] were also used to validate the correlation in Chapter 5: experimental measurements, curve-fitting algorithms [152], error estimations and residual iterations of substructure modes [213], the subspace classification using singular value decomposition, *and an iterative CMS using Rayleigh-Ritz vectors (Craig-Bampton MOR [117] and the AMLS [201] methods).*

In the second part of this work, once a satisfactory approximation was validated updating the stiffness parameters of the CFRP assembly component using a MNET, the Craig-Bampton MOR method with Rayleigh-Ritz vectors basis is applied using two criteria for the comparison of results: frequency and mode shapes. Different MAC, MACco and COMACs criteria are performed in simliar fashion as was archieved with the full model to know which particular substructure modes are dominant in a certain global mode in Chapter 6. It used the same sensor configuration in both comparisons, illustrated in Chapters 4, 5 and 6.

6.2 Application of the CMS to a CFRP using the updated stiffness parameters obtained applying a MNET

With the stiffness parameters obtained with the MNET, the next step is to apply the CMS to the full FE model. The CMS is applied dividing the full FE model into two independent parts or components using groups[1], illustrated in Fig. 3.3. For each component is computed the same number of retained constrain modes (also known as fixed interface modes). The components are represented in a reduced model that is built up defining two super-elements. The super-element 1 , (see Fig. 3.3a), has 4,753 nodes and 9,219 elements, while super-element 2, (see Fig. 3.3b), has 1,615 nodes and 3,026 elements. The defined super-elements share 123 nodes along the common border with different DOF per node. An appropriate $[T]$ matrix, introduced in Chapter 3, is defined according to the CMS and AMLS methods.

A convergence study of the reduced model shows an increase with different numbers of retained constrain modes (10, 20, 30, 40, 50). The method rapidly archieves accuracy of a few percent in the frequency difference visible in Fig. 6.1a, however, convergence to a higher accuracy requires a fixation of the interface modes with frequencies above the frequency band of interest. The MAC of the full and reduced model is illustrated in Fig. 6.1b until fifty mode pairs. The MAC values of each FE model are displayed in Table 6.1 respectively. The rigid body modes are included in the correlation accuracy.

If the number of interface modes are increased, the number of DOF of the interface will also increase and viceversa. The good initial accuracy using 20 fixed interface modes applying the Craig-Bampton method is sufficient to describe the dynamic behaviour of the CFRP component. Due to the number of mode pairs in the experimental measurements, 19 fixed interface modes are kept. The matrix size is reduced by 98.5% from 37,698 DOF to 579 DOF. Results are good for the stiffness matrix showing a decrease factor of 78.9% from 1,420,413 to 299,544. The mass matrix shows a 78% decrease from 1,349,362 to 299,544. The orthogonallity and cross-orthogonallity using the MAC can be used to analyze the accuracy of the mode shapes using the CBMOR method. The first mode shapes of the reduced model versus the full FE model are illustrated in Fig. 6.2. The mode shapes of the reduced model vs the full FE model per group of super-element can be appreciated in Figs. 6.3 and 6.4. Another MAC is performed changing the number of retained constrain modes per super-element of 7,17, 27, 37 and 47 to compare the accuracy.

[1] Groups of elements can be defined in MSC/NASTRAN, ABAQUS or SDTools.

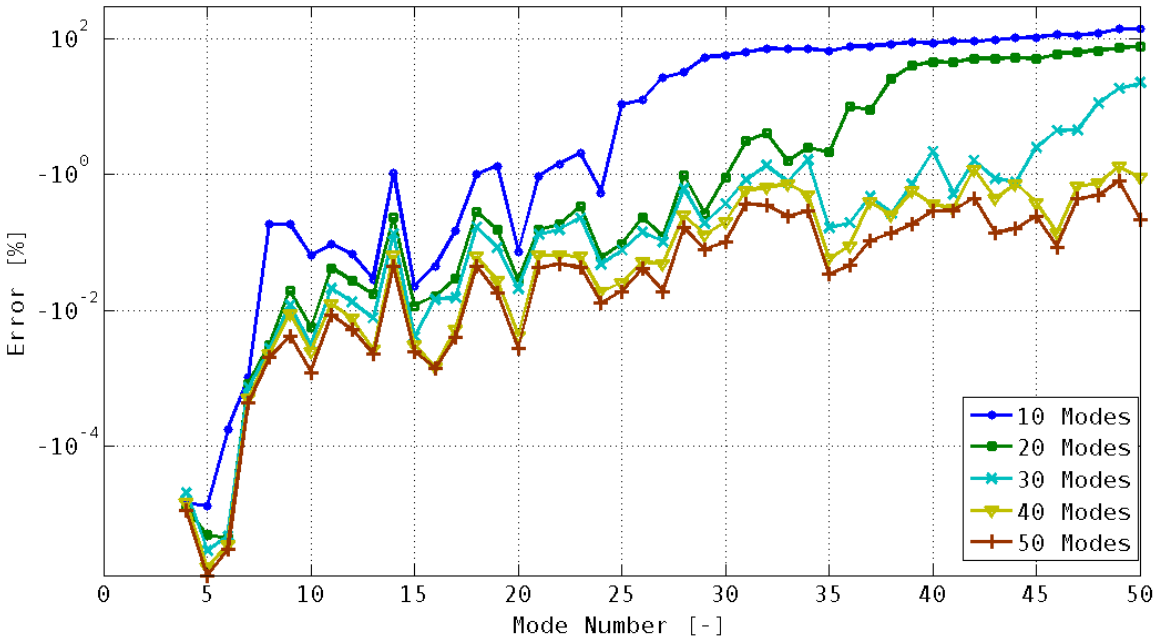

(a)

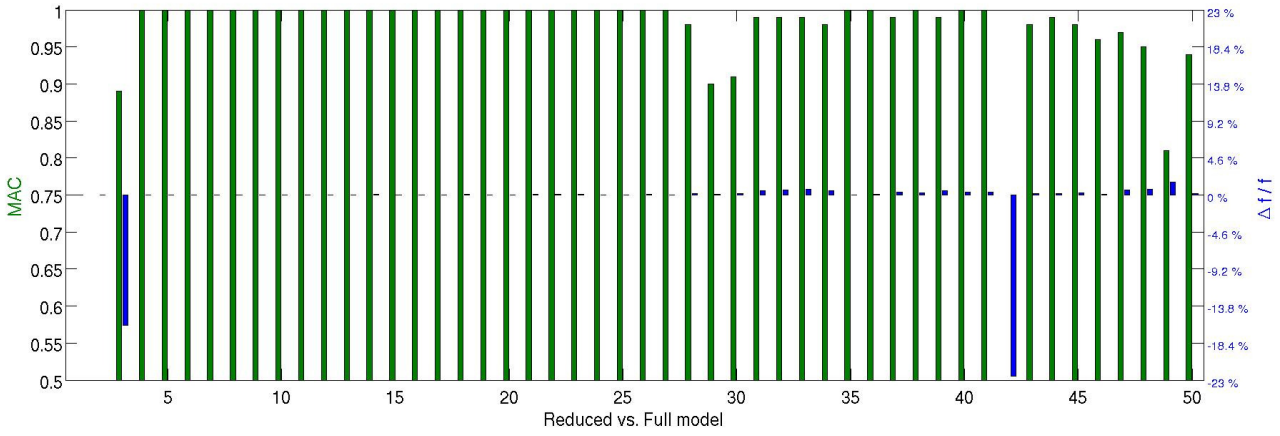

(b)

Fig. 6.1 a) MAC convergence error b) MAC frequency error reduced FE vs. full FE model (green bars MAC, blue bars frequency difference).

Table 6.1 MAC between the full FE model vs. the reduced FE model with 50 modes per super-elements (SE1 and SE2).

# Mode	Full (Hz)	# Mode	Reduced (Hz)	DF/FA %	MAC
1	0	2	9.1826e-05	Inf	88
2	0	1	0	NaN	99
3	4.5127e-4	3	3.7823e-4	-16.2	89
4	0.44472	4	0.44472	0.0	100
5	1.2193	5	1.2193	0.0	100
6	1.9085	6	1.9085	0.0	100
7	57.218	7	57.218	0.0	100
8	106.02	8	106.02	0.0	100
9	167.5	9	167.51	0.0	100
10	168.2	10	168.2	0.0	100
11	234.99	11	235.02	0.0	100
12	236.83	12	236.85	0.0	100
13	315.26	13	315.26	0.0	100
14	323.93	14	324.11	0.1	100
15	401.72	15	401.73	0.0	100
16	408.39	16	408.39	0.0	100
17	432.89	17	432.91	0.0	100
18	494.9	18	495.14	0.0	100
19	497.04	19	497.18	0.0	100
20	516.11	20	516.13	0.0	100
21	538.85	21	539.15	0.1	100
22	559.47	22	559.83	0.1	100
23	571.85	23	572.19	0.1	100
24	607.04	24	607.13	0.0	100
25	637.29	25	637.45	0.0	100
26	657.06	26	657.36	0.0	100
27	678.44	27	678.59	0.0	100
28	787.12	28	788.81	0.2	98
29	812.02	29	812.99	0.1	90
30	814.75	30	816.2	0.2	91
31	861.94	31	866.42	0.5	99
32	882.32	32	887.5	0.6	99
33	921.41	33	927.83	0.7	99
34	956.2	34	961	0.5	98
35	977.96	35	978.36	0.0	100
36	987.49	36	988.3	0.1	100
37	1012.4	37	1016.2	0.4	99
38	1044.4	38	1047	0.2	100
39	1051.5	39	1057.4	0.6	99
40	1085.8	40	1089.6	0.4	100
41	1121.7	41	1125.2	0.3	100
42	1145.6	32	887.5	-22.5	28
43	1157.1	42	1159.3	0.2	98
44	1159.7	43	1162.2	0.2	99
45	1182.8	45	1186.2	0.3	98
46	1190	46	1191.3	0.1	96
47	1206.5	47	1213.9	0.6	97
48	1213.5	48	1221.9	0.7	95
49	1223.2	50	1243	1.6	81
50	1234.2	49	1236.7	0.2	94

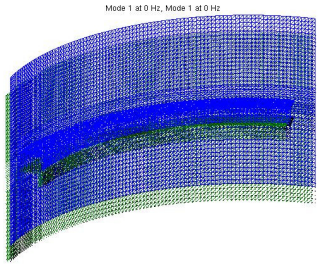

(a) Mode 1 at 0 Hz,
Mode 1 at 0 Hz reduced

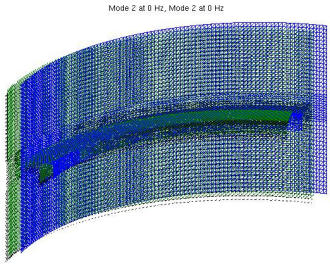

(b) Mode 2 at 0 Hz,
Mode 2 at 0 Hz reduced

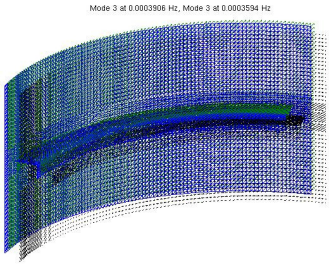

(c) Mode 3 at 3.906e-4 Hz,
Mode 3 at 3.594e-4 Hz reduced

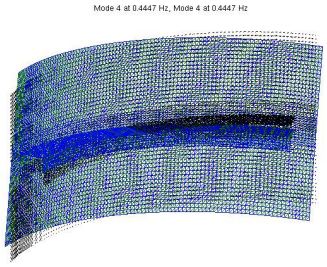

(d) Mode 4 at 0.4447 Hz,
Mode 4 at 0.4447 Hz reduced

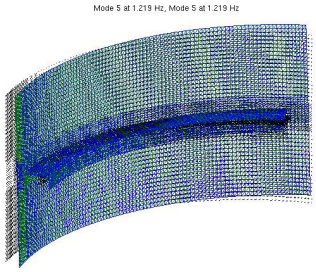

(e) Mode 5 at 1.219 Hz,
Mode 5 at 1.219 Hz reduced

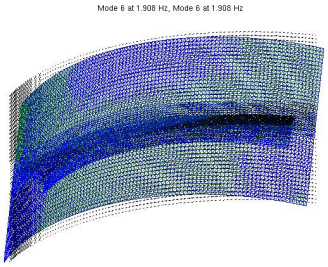

(f) Mode 6 at 1.9085 Hz,
Mode 6 at 1.9085 Hz reduced

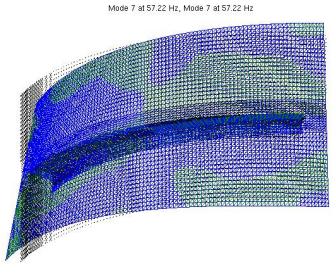

(g) Mode 7 at 57.2179 Hz,
Mode 7 at 57.2183 Hz reduced

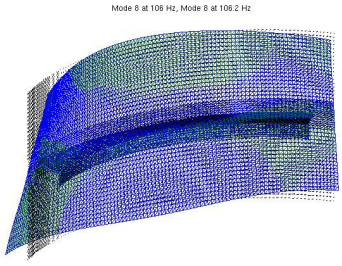

(h) Mode 8 at 106.0160 Hz,
Mode 8 at 106.2092 Hz reduced

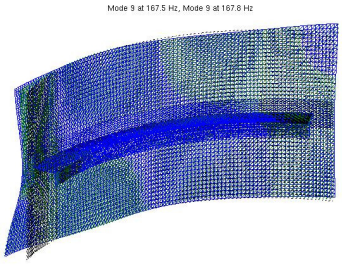

(i) Mode 9 at 167.4985 Hz,
Mode 9 at 167.7910 Hz reduced

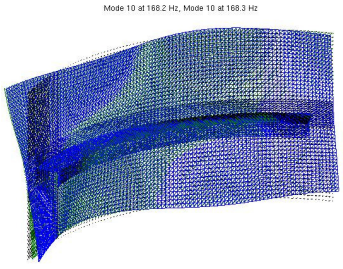

(j) Mode 10 at 168.1977 Hz,
Mode 10 at 168.2881 Hz reduced

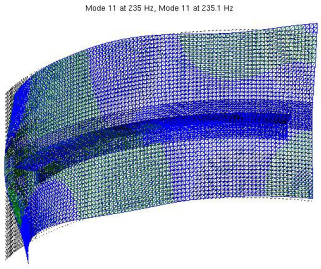

(k) Mode 11 at 234.9896 Hz,
Mode 11 at 235.1202 Hz reduced

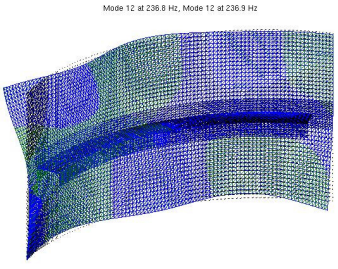

(l) Mode 12 at 236.8307 Hz,
Mode 12 at 236.9254 Hz reduced

Fig. 6.2 CBMOR reduced FE model (in green) vs. full FE model in MATLAB-SDTools (in blue).

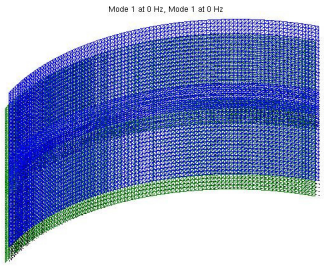

(a) Mode 1 at 0 Hz,
Mode 1 at 0 Hz reduced

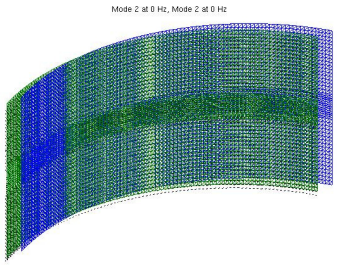

(b) Mode 2 at 0 Hz,
Mode 2 at 0 Hz reduced

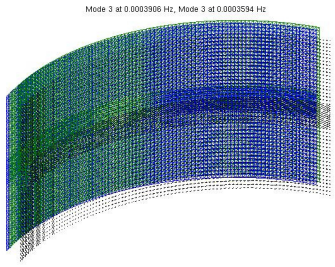

(c) Mode 3 at 3.906e-4 Hz,
Mode 3 at 3.594e-4 Hz reduced

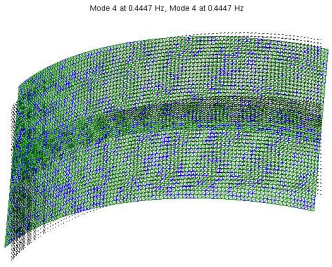

(d) Mode 4 at 0.4447 Hz,
Mode 4 at 0.4447 Hz reduced

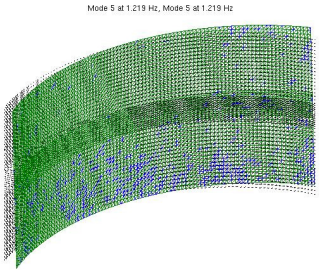

(e) Mode 5 at 1.219 Hz,
Mode 5 at 1.219 Hz reduced

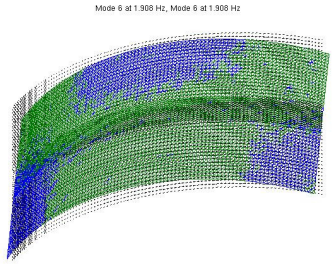

(f) Mode 6 at 1.9085 Hz,
Mode 6 at 1.9085 Hz reduced

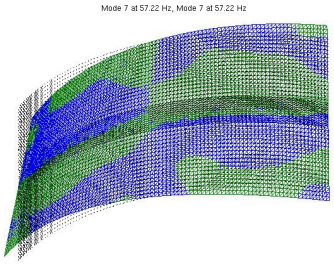

(g) Mode 7 at 57.2179 Hz,
Mode 7 at 57.2183 Hz reduced

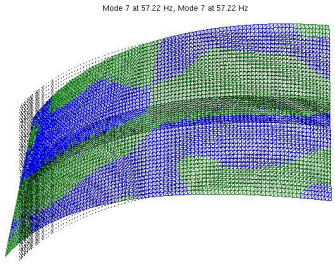

(h) Mode 8 at 106.0160 Hz,
Mode 8 at 106.2092 Hz reduced

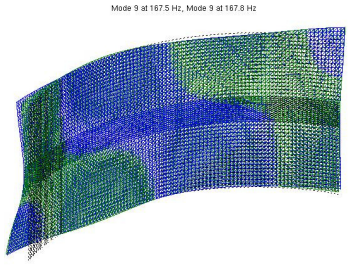

(i) Mode 9 at 167.4985 Hz,
Mode 9 at 167.7910 Hz reduced

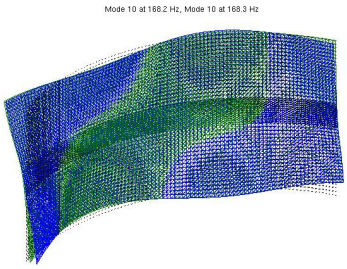

(j) Mode 10 at 168.1977 Hz,
Mode 10 at 168.2881 Hz reduced

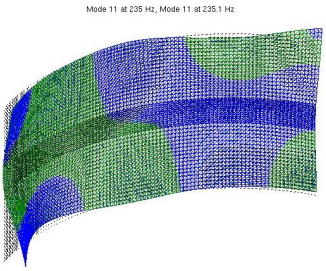

(k) Mode 11 at 234.9896 Hz,
Mode 11 at 235.1202 Hz reduced

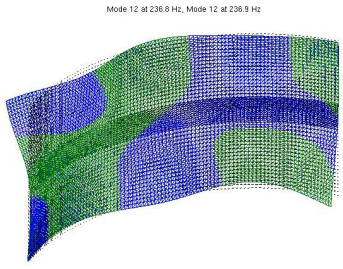

(l) Mode 12 at 236.8307 Hz,
Mode 12 at 236.9254 Hz reduced

Fig. 6.3 Superelement 1 (in green) vs. full FE model in MATLAB-SDTools (in blue).

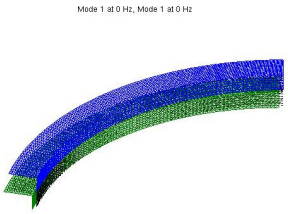

(a) Mode 1 at 0 Hz,
Mode 1 at 0 Hz reduced

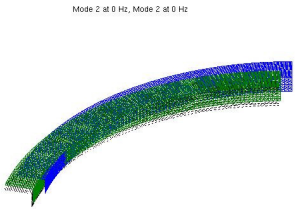

(b) Mode 2 at 0 Hz,
Mode 2 at 0 Hz reduced

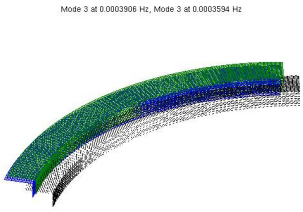

(c) Mode 3 at 3.906e-4 Hz,
Mode 3 at 3.594e-4 Hz reduced

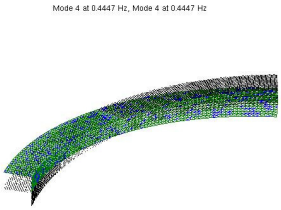

(d) Mode 4 at 0.4447 Hz,
Mode 4 at 0.4447 Hz reduced

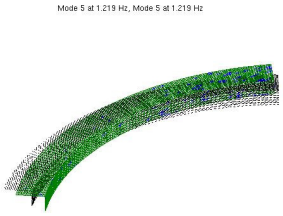

(e) Mode 5 at 1.219 Hz,
Mode 5 at 1.219 Hz reduced

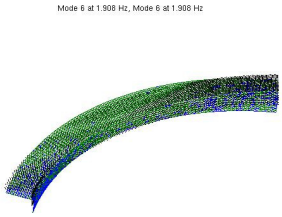

(f) Mode 6 at 1.9085 Hz,
Mode 6 at 1.9085 Hz reduced

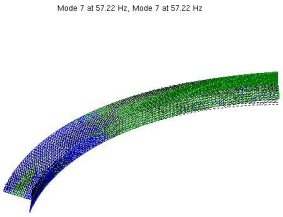

(g) Mode 7 at 57.2179 Hz,
Mode 7 at 57.2183 Hz reduced

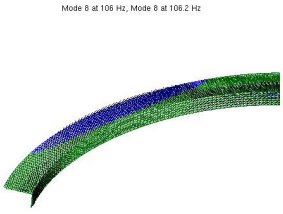

(h) Mode 8 at 106.0160 Hz,
Mode 8 at 106.2092 Hz reduced

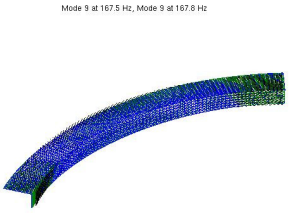

(i) Mode 9 at 167.4985 Hz,
Mode 9 at 167.7910 Hz reduced

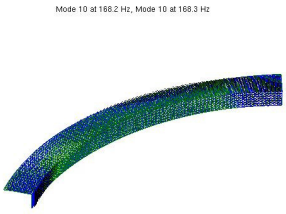

(j) Mode 10 at 168.1977 Hz,
Mode 10 at 168.2881 Hz reduced

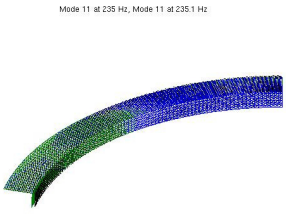

(k) Mode 11 at 234.9896 Hz,
Mode 11 at 235.1202 Hz reduced

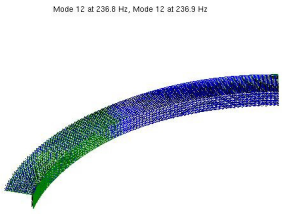

(l) Mode 12 at 236.8307 Hz,
Mode 12 at 236.9254 Hz reduced

Fig. 6.4 Superelement 2 (in green) vs. full FE model in MATLAB-SDTools (in blue).

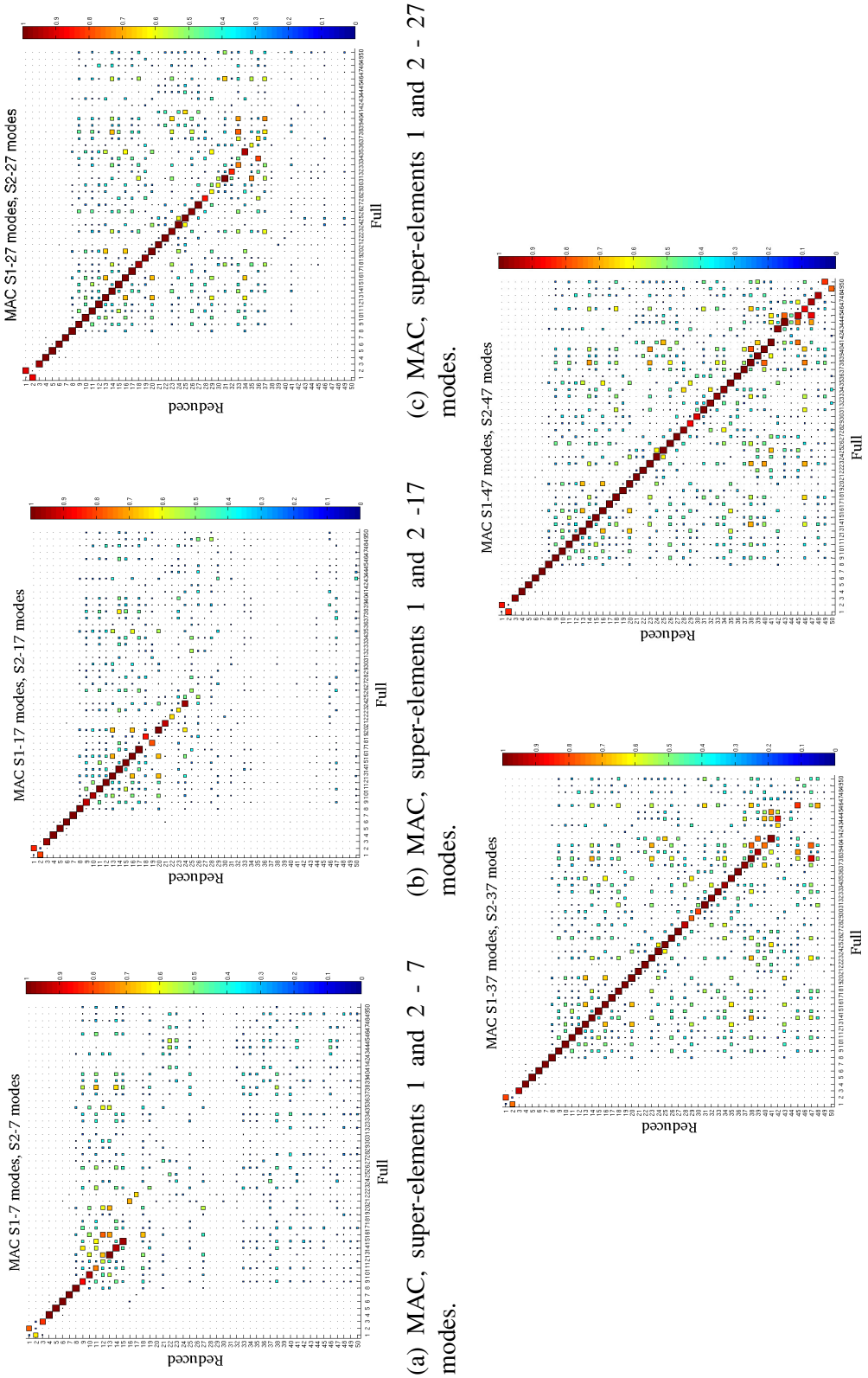

(a) MAC, super-elements 1 and 2 - 7 modes.

(b) MAC, super-elements 1 and 2 -17 modes.

(c) MAC, super-elements 1 and 2 - 27 modes.

(d) MAC, super-elements 1 and 2 - 37 modes.

(e) MAC, super-elements 1 and 2 - 47 modes.

Fig. 6.5 MAC between the full FE model vs. the reduced FE model increasing the same number of retained constrain modes per super-element.

The influence of the mode shapes per superlement is illustrated comparing the MAC results of the reduced model with the full FE model in Fig. 6.5. It is clear the dependence of the correlation accuracy using CMS, based on the retained constrain modes per super-element, (see Figs. 6.5 and 6.6). The rigid body modes of the full and reduced models are included in the correlation accuracy. Table 6.1 can be used for comparison purposes of low and high frequencies and model shapes (for 50 pairs keeping the same number of fixed retained modes per superelement). The worst frequency and eigenvector difference are found in the mode pair 42 (22.5% and 28 MAC value respectively). These worst frequency value could be related to convergence error, the type of element formulation or the solver.

It is well known that the cross-orthogonallity and orthogonallity matrices provide similar information about the experimental accuracy, and they tend to indicate different things. Fifty and nineteen paired modes are illustrated in Fig. 6.6 (2D and 3D plots). The diagonal values of the orthogonality and cross-orthogonality matrices have the value of unity and the off-diagonal terms have the value around 30 in the full and reduced FE models using the pshell elements. These differences are observed comparing the off-diagonal terms of the SDTools full and reduced FE models in Fig. 6.6 versus the MSC/NASTRAN and ABAQUS full FE models, see Fig. 5.2.

The orthogonality matrix indicates the goodness of the mass distribution in the full FE and reduced model. Analyzing the orthogonallity and cross-orthogonallity matrices results, one can conclude the good mass distribution (orthogonallity) and the good accuracy of the reduced mode shapes (cross-orthogonallity). Several observations can be made:

1. The free interface method shows good agreement results in the lower frequency range. It is believed that this is due to the fact that the rigid body modes are explicitly present in the reduction basis[2].

2. The CBMOR method shows excellent results based on the basis Rayleigh-Ritz vectors, error estimations and residual iterations of substructure modes, the SVD and the AMLS.

3. The reduction basis is enhanced through the automatic generation interface, the SVD, the error estimates and residual iterations of substructure modes and the Rayleigh-Ritz vectors implemented in SDTools. It is possible to accurately describe a low and high number of eigenmodes of the assembled system.

[2]Due to the rigid body modes having a significant influence in the low frequency range, the free interface reduce model shows a very small error on the first eigenmodes and eigenfrequencies [198].

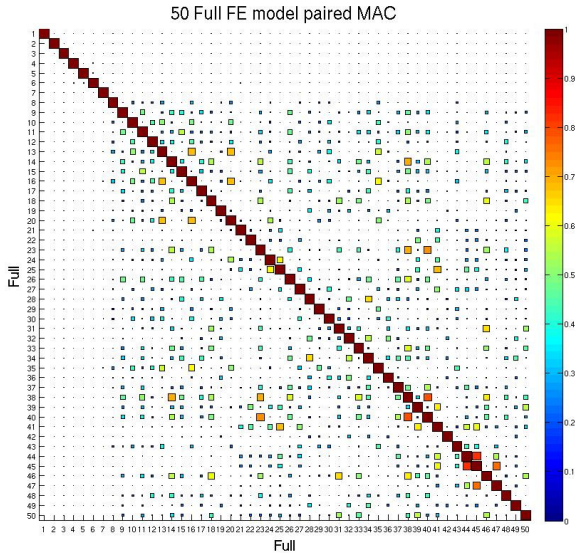

(a) XOR full FE model - 50 paired modes.

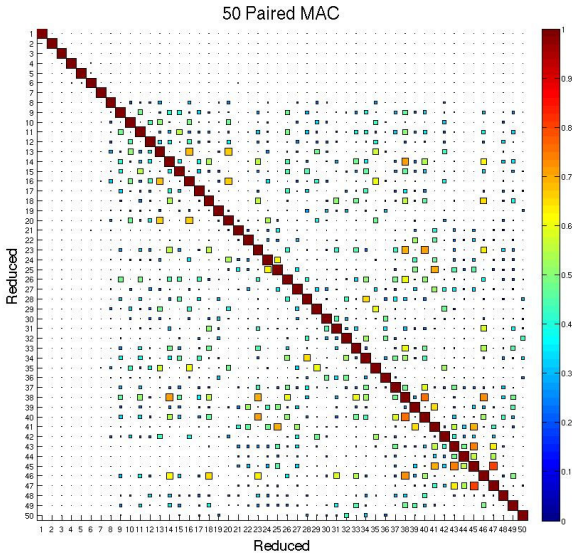

(b) XOR reduced FE model - 50 paired modes.

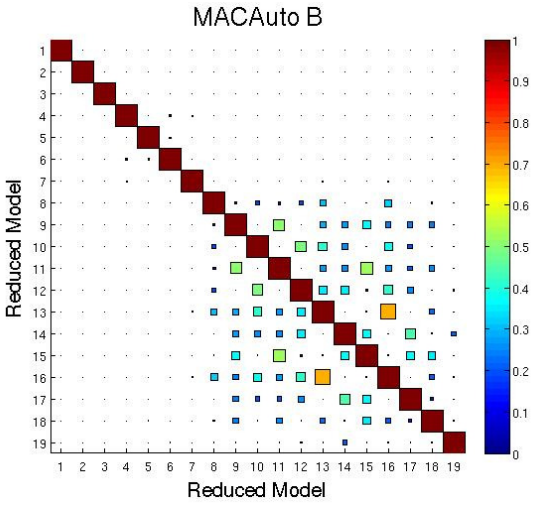

(c) XOR reduced FE model - 19 paired modes

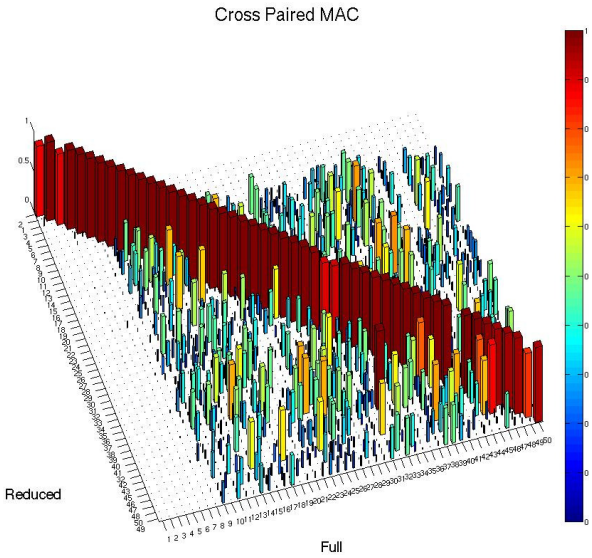

(d) 3D MAC reduced vs. full model - 50 paired modes

Fig. 6.6 XOR and MAC of the full and reduced models (MATLAB-SDTools).

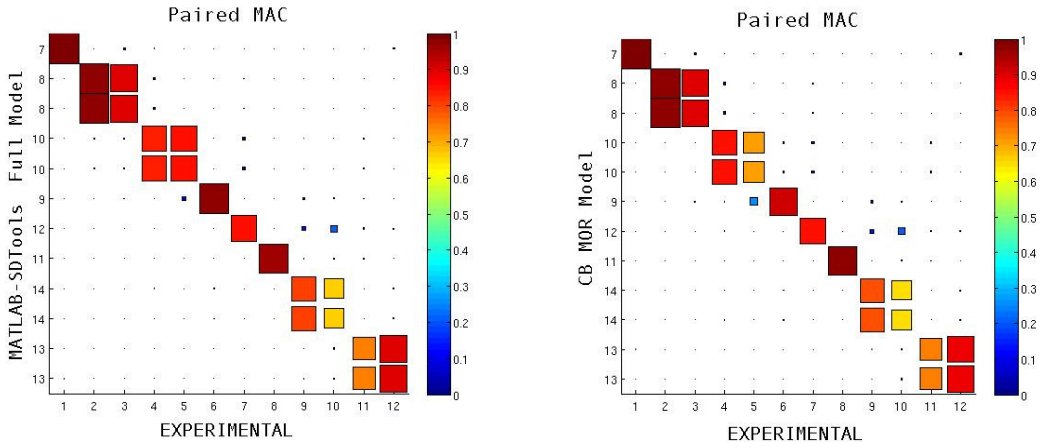

(a) (b)

Fig. 6.7 Comparison of MAC vs experimental measurements: a) SDTools Full model b) Reduced model.

After performing the XOR and MAC analysis of the reduced versus the full FE models, a MAC correlation can be performed between the experimental measurements and the reduced model for the same frequency ranges up to 400 Hz based on the curve-fitting model generated [106] [152]. Most of the paired modes show a good correlation between the reduced and full models (MAC over 80%) with the exception of pairs 5^{th}, 10^{th} and 11^{th} versus the experimental measurements. The nearly double correlations identified in the full FE model versus the experimental results suggesting the presence of the veering phenomenon (bending and torsional mode at the same frequency), identified in Fig. 6.7a. Moreover, it is also identified the veering phenomenon using the reduced FE model versus the experimental measurements, (see Fig. 6.7b). Table 6.2 shows the numerical MAC values versus the experimental measurements. It can be noticed that the MAC of the reduced model using the CBMOR method is slightly worse than the full model versus the experimental measurements in consistency with the literature.

6.2.1 Modal Assurance Criterion per pair-sensor (MACco) applied to a CFRP component using CMS

After performing the MAC with the updated material properties, the application of the MAC per paired-sensor (MACco) criterion can be also applied to the reduced FE model to comply with the sequential order of sensors that contribute most to the poor correlation [106] for comparative purposes.

Table 6.2 MAC Table reduced FE model vs. experimental measurements.

ID	Test (Hz)	ID	CBMOR FEM (Hz)	DF/FA %	MAC
1	49.243	7	57.218	16.2	100
2	92.265	8	106.21	15.1	97
3	93.756	8	106.21	13.3	90
4	145.29	10	168.29	15.8	84
5	160.05	10	168.29	5.1	71
6	164.18	9	167.79	2.2	92
7	226.36	12	236.93	4.7	85
8	243.4	11	235.12	-3.4	97
9	307.33	14	326.82	5.9	80
10	314.18	14	326.82	4.0	65
11	324.83	13	315.33	-2.9	74
12	329.67	13	315.33	-4.3	89

Table 6.3 Comparative MACco Table reduce and full FE models vs. experimental measurements

Pair number		7	8	9	10	11	12	13	14	15	16	17	18
EXPERIMENTAL		1	2	3	4	5	6	7	8	9	10	11	12
SDTools reduced FE model		7	8	8	10	10	9	12	11	14	14	13	13
Y-Sensors	Mean MAC												
All	85	100	97	90	84	71	92	85	97	80	65	74	89
16y	86	100	97	91	85	71	92	86	97	81	67	76	89
95y	86	100	97	91	85	71	92	87	97	82	68	77	89
96y	87	100	97	91	85	71	92	88	97	83	69	77	89
131y	87	100	97	92	86	72	92	89	98	83	70	77	89
129y	87	100	97	92	86	71	92	88	98	84	71	79	90
23y	87	100	97	93	86	72	91	88	97	84	73	78	90
17y	88	100	97	93	85	73	91	88	97	84	74	79	91
128y	88	100	97	93	84	72	92	89	97	85	76	80	91
21y	88	100	97	94	84	73	91	89	97	85	77	80	91
97y	88	100	97	94	84	73	91	90	97	85	78	80	92
EXPERIMENTAL		1	2	3	4	5	6	7	8	9	10	11	12
SDTools full FE model (updated)		7	8	8	10	10	9	12	11	14	14	13	13
Y-Sensors	Mean MAC												
All	87	100	97	90	83	86	98	86	96	81	66	74	90
16y	88	100	97	91	83	86	98	86	96	82	67	76	90
96y	88	99	97	91	82	87	98	87	97	83	69	77	90
95y	88	100	97	91	82	87	98	88	97	84	70	78	90
23y	89	99	97	92	84	87	97	88	96	84	73	77	90
131y	89	100	97	93	85	88	97	89	96	85	73	77	90
17y	89	100	97	93	84	89	97	89	97	85	74	78	91
21y	90	100	97	94	85	89	97	89	97	85	76	78	91
129y	90	100	97	94	85	89	97	89	97	86	77	79	92
128y	90	100	97	94	84	89	97	89	97	86	79	80	92
97y	91	100	97	94	84	89	97	90	97	87	79	81	92

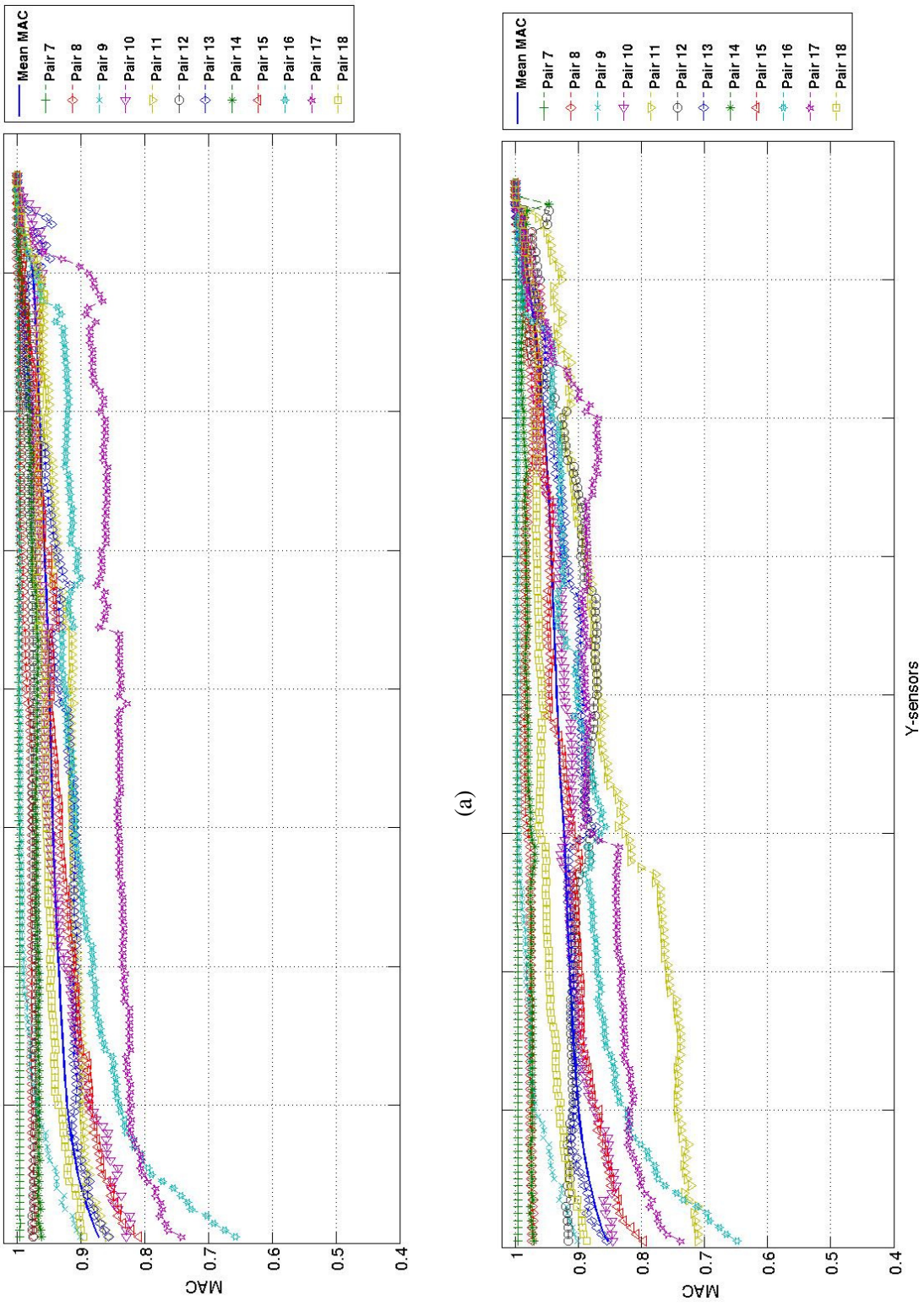

Fig. 6.8 Comparison of MACco vs. exp.: a) SDTools full model b) Reduced models.

This criterion is implemented by computing the MAC while ordering one sensor at a time introduced in subsection 2.1.1. Applying the sensor order used with the full FE model, the results will point to the best mean MAC using the CBMOR method versus the experimental results. The MACco results of the reduced FE model versus the full FE model (paired modes per sensor) present a slightly worst correlation values, illustrated in Table 6.3. It can be appreciated that the worst MACco results per paired-sensor in the reduced FE model are identified in the same sensors in respect to the full FE model, but in different order, (see Table 6.3 and Fig. 6.8 respectively). The worst paired modes obtained in the reduced FE model are observed in the pair number 11^{th}, 16^{th} and 17^{th} in respect to the full FE model. It can be observed also that the pair number 11^{th} shows a deterioration in the correlation in respect to the same pair number of the full FE model. The MACco of the reduced model in general showed a slightly worse results illustrated in Fig. E.3b. The values observed using the reduced FE model shows a slight decrease in consistency with the literature (the ROM model presents slightly worse values compared to the full FE model).

6.2.2 Coordinate Modal Assurance Criterion (COMAC)

The calculation of the COMAC values (in blue) at each sensor/coordinate over all the correlated paired modes was given in Eq.(2.2). It is important to note that the modes are also normalized, which gives equal weighting to all modes. The COMAC of the reduced FE model is also calculated over a set of the same mode pairs computed using the CBMOR method (19 mode pairs per superlement). The implementation of the COMAC technique with the reduced models requires also two stages of calculation, as was done with the full FE model[3]. The COMAC values of the reduced model shown similar values versus the full FE model displayed in the Fig. 6.9. The best COMAC value in the reduced model is found at sensor 84y=0.052. The worst value in the reduced model is also displayed at sensor 201y=0.423 as was identified in the full FE model (equal to 0.397). The COMAC's values obtained using the CBMOR method showed a slightly difference versus the full FE models COMAC's suggesting a good correlation, illustrated in Fig. 6.9.

[3]In the first stage, the modes from the two sets were matched using the MAC. After constructing the set of *NM* mode pairs, the second stage is the COMAC calculation of correlation values at each coordinate, over all the correlated mode pairs.

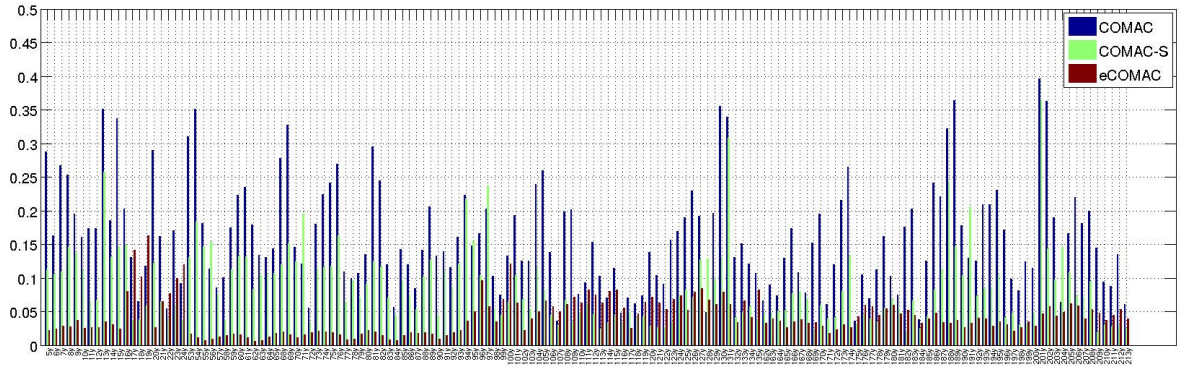

(a) COMAC's SDTools versus number of sensors

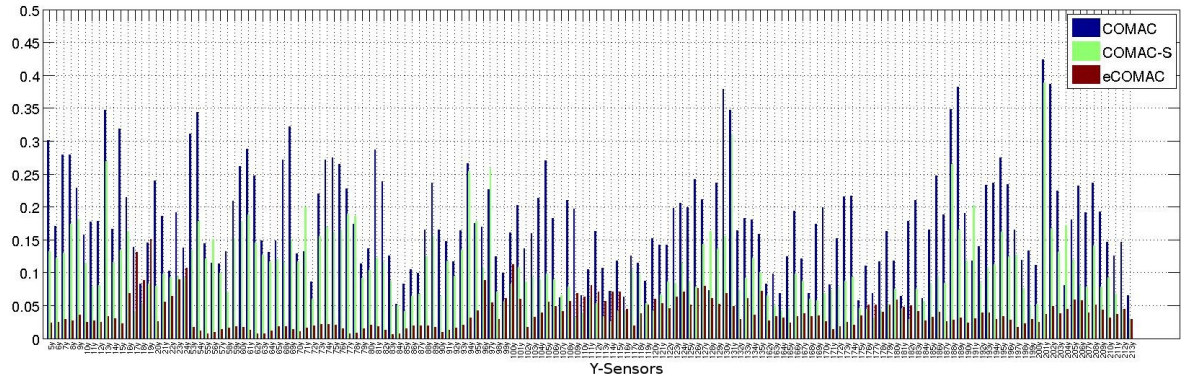

(b) COMAC's CBMOR versus number of sensors

Fig. 6.9 Comparison of COMAC's results.

6.2.3 Scale Coordinate Modal Assurance Criterion (COMAC-S)

The COMAC-S results show a similar patterns between the full and the reduced FE models. The COMAC-S is displayed in green in respect to the COMAC (in blue) and eCOMAC (in brown). Fig. 6.9 presents the worst COMAC-S value is found at sensor 201y=0.388 compared to the COMAC-S of the full FE model at the same sensor with a value of 0.366. The best COMAC-S is found at sensor 114y=0.026. The similar COMAC and COMAC-S values obtained with the CBMOR method show a good agreement per DOF according to each formulation.

6.2.4 Enhanced Coordinate Modal Assurance Criterion (eCOMAC)

The eCOMAC values of the reduced model are also identified in the CFRP component. The eCOMAC values range from zero to one (in brown), where the value closer to zero per DOF

will have the higher agreement. As was introduced, the formulation for an enhanced COMAC will overcome some of the limitations of the standard COMAC.

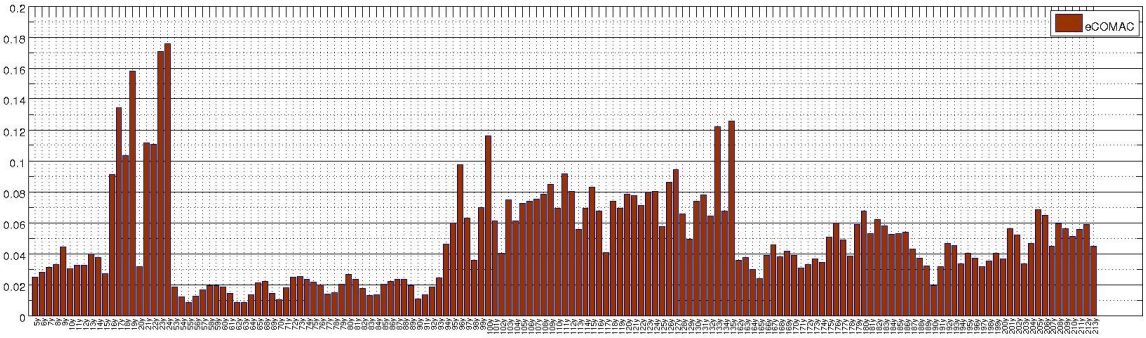

(a) eCOMAC's SDTools full FE model.

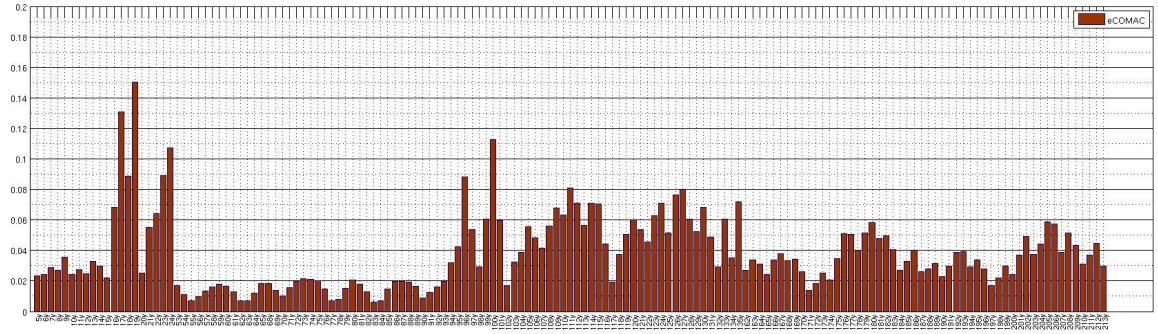

(b) eCOMAC's Reduced FE model.

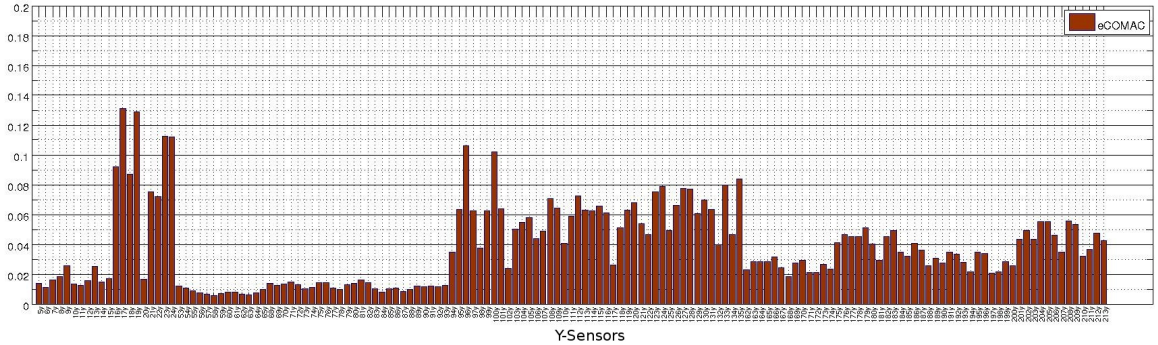

(c) eCOMAC's ABAQUS full FE model.

Fig. 6.10 Comparison of eCOMAC's vs. number of sensors

Lower eCOMAC values are obtained in most of the sensors of the reduced model respect to the other two coordinate modal assurance criteria with the exception of the sensors

$17y, 19y, 23y, 24y, 100y$, (see Fig. 6.10). The worst eCOMAC values of the reduced FE model is found at sensor $24y$=0.15 versus the eCOMAC values of the full FE model at sensor 24=0.176. The better eCOMAC value of the reduced FE model is identified at sensor $83y$=0.006 versus the full FE models. However, the ABAQUS model displays similar eCOMAC values obtained in the reduced model, (see Fig. 6.10). The lower eCOMAC results suggest an improvement obtained per DOF in the composite component assembly with the updated stiffness parameters. The eCOMAC values of the reduced model obtained are the best versus the eCOMAC results obtained with the SDTools full FE model, (see Fig. 6.10).

6.3 Conclusions

These results lead to the following conclusions:

- The CBMOR method based on Rayleigh-Ritz vectors basis is performed as an accurate and efficient description of the dynamic behaviour of the CFRP assembled system.
- The free-interface method shows results with good correlation in low-frequency ranges.
- The use of the CBMOR method, the AMLS, the SVD, the error estimations and residual iterations of substructure modes leads to an improvement of the accuracy-time ratio to find the ideal and accurate DOF interface reduction basis.
- The repeatability of the curve-veering phenomena using superelements is observed applying the CBMOR method in the CFRP component.
- High accuracy of the results are obtained in the full and reduced models applying the MAC, XOR, MACco, and COMACs criteria.

6.4 Application of mode shape expansion techniques to CFRP

6.4.1 MAC and verification of composite component assembly using mode shape expansion methods

The mode shapes and eigenfrequencies of the different MSE methods are compared to a full reference solution. The evaluation of the CFRP using MSE techniques can be performed combining the experimental measurements, the curve-fitting and the updated stiffness parameters

of the MATLAB-SDTools full FE model using the MAC performed in Chapters 4 and 5. The different MSE are calculated (MODAL/SEREP, STATIC, DYNAMIC, MDRE, MDRE-WE) using fe_exp command, (see Appendix A, from step 24 to 33).

The influence of the expansion methods in the correlation is observed calculating the K-MAC and M-MAC based on the stiffness and mass matrices updated in the full FE model respectively, (see Appendix A, step 29). The same number of paired modes are calculated (12 pairs) for all the MSE methods. An error of 0.1 is used in the interpolation of the MDRE-WE, (see Appendix A, step 28). The K-MAC and M-MAC results can be compared using the different MSE techniques, (see Tables 6.4 and 6.5 respectively). The best K-MAC results are obtained applying the MODAL and MDRE-WE MSE methods displayed in Table 6.4. The worst paired modes of the MODAL and MDRE-WE MSE methods are displayed at paired mode 10^{th} (K-MAC of 79) and at paired mode 11^{th} (K-MAC of 33), respectively. The other MSE methods display a decrease of the K-MAC results in respect to the MODAL/SEREP and MDRE-WE results. Moreover, in the column (DF/FA MSE %) of Tables 6.4 and 6.5 can be observed that the differences of the eigenfrequencies between the experimental measurements and MSE results are zero. The reason to have a null difference in the frequencies applying different MSE is because it is used in the same pole identification obtained with the curve-fitting for all the MSE methods defined in [106]. The M-MAC of all the MSE methods can be observed in Table 6.5. An improvement of the M-MAC results is observed in the MODAL/SEREP, DYNAMIC, MDRE and MDRE-WE in respect to the K-MAC results at paired modes $6^{th} - 10^{th}$, 12^{th} and M-MAC at paired modes $2^{th} - 6^{th}$, $8^{th} - 10^{th}$, 12^{th} respectively. This improvement in the K-MAC and M-MAC can be implicated as the influence of the defined MOR methods applying MSE in respect to the curve-fitting of the experimental measurements and the updated stiffness parameters. With the exception of the STATIC MSE method where the inertial forces are not included, a strong influence of the M-MAC results is observed in allmost of the subspace-basis expansion methods. The STATIC MSE method presents the worst M-MAC results in agreement with the literature, where the inertial terms contributing to the dynamic behaviour are ignored or not considered applying STATIC condensation.

Furthermore, MAC, XOR and MACco criteria are performed between the MSE results and the curve-fitting of the experimental measurements in order to check orthogonality, cross paired results and sensor correlation respectively, (see Figs. 6.11, 6.12 and 6.13). Figs. 6.11 and 6.12 displayed the first 12^{th} MAC paired between the curve-fitting and each MSE results obtained. The XOR analysis displayed values close to one for all MSE results. Performing

Table 6.4 K-MAC mode shape expansion methods.

# :	Test (Hz)	FE (Hz)	DF/FA %	MAC	#	DF/FA MSE %	K-MAC for MOD	K-MAC for STA	K-MAC for DYN	K-MAC MDRE	K-MAC MDRE-WE
1 :	49.24	57.22	16.2	100	1	0.0	98	31	31	31	100
2 :	92.27	106.02	14.9	97	2	0.0	96	74	74	58	95
3 :	93.76	106.02	13.1	90	3	0.0	92	51	51	38	78
4 :	145.29	168.2	15.8	83	4	0.0	88	81	81	45	89
5 :	160.05	168.2	5.1	86	5	0.0	87	84	84	49	87
6 :	164.18	167.5	2.0	98	6	0.0	94	89	89	56	99
7 :	226.36	236.83	4.6	86	7	0.0	88	79	79	49	89
8 :	243.4	234.99	-3.5	96	8	0.0	96	89	90	65	97
9 :	307.33	323.93	5.4	81	9	0.0	88	81	81	60	87
10 :	314.18	323.93	3.1	66	10	0.0	79	65	66	45	76
11 :	324.83	315.26	-2.9	74	11	0.0	87	70	71	16	33
12 :	329.67	315.26	-4.4	90	12	0.0	93	87	88	39	89

Table 6.5 M-MAC mode shape expansion methods.

# :	Test (Hz)	FE (Hz)	DF/FA %	MAC	#	DF/FA MSE %	M-MAC for MOD	M-MAC for STA	M-MAC for DYN	M-MAC MDRE	M-MAC MDRE-WE
1 :	49.24	57.22	16.2	100	1	0.0	100	3	100	100	100
2 :	92.27	106.02	14.9	97	2	0.0	99	4	98	98	99
3 :	93.76	106.02	13.1	90	3	0.0	93	2	92	92	93
4 :	145.29	168.2	15.8	83	4	0.0	83	8	82	82	86
5 :	160.05	168.2	5.1	86	5	0.0	86	5	86	86	88
6 :	164.18	167.5	2.0	98	6	0.0	98	11	98	97	99
7 :	226.36	236.83	4.6	86	7	0.0	83	2	82	81	86
8 :	243.4	234.99	-3.5	96	8	0.0	96	86	96	96	98
9 :	307.33	323.93	5.4	81	9	0.0	82	5	80	78	83
10 :	314.18	323.93	3.1	66	10	0.0	69	2	65	64	70
11 :	324.83	315.26	-2.9	74	11	0.0	80	49	73	6	71
12 :	329.67	315.26	-4.4	90	12	0.0	90	2	89	83	91

the XOR one can realised that some of the off-diagonal terms in all the MSE results do not fulfill the criteria of $\leq$ than ten. The missing of this criteria $\leq$ than ten might be due to the missing of the experimental measurements of the second component. Furthermore, some of the double pairs obtained in the experimental measurements (curve-veering phenomenon) are not displayed using the XOR of the different MOR subspace-basis calculated, (see Figs. 6.11f, 6.12a and 6.12d). The main differences applying the MSE techniques and the CBMOR method are observed comparing the sequential order in the MAC paired modes, the MAC diagonal terms equal to one and off-diagonal terms obtained versus the experimental measurements. Furthermore, comparing the off-diagonal terms of the XOR using MSE versus the XOR obtained with the CBMOR model is shown that some of the off-diagonal terms are not zero. The XOR of the reduced FE model using CBMOR method presents better off-diagonal results.

Fig. 6.13 displays the MACco results between the curve-fitting of the experimental mesurements and the MSE results obtained. Comparing these results with the CBMOR model one can notice an improvement in the number of mode pairs (up 0.94 for the MODAL/SEREP and up to 0.999 for the MDRE-WE) respectively, (see Figs. 6.13a and 6.13e). Due to assumption in the boundary conditions established in the SDTools[4], the MACco results per paired-sensor display values close to one in the STATIC, DYNAMIC and MDRE MSE methods, (see Figs. 6.13b, 6.13c and 6.13d respectively).

Comparing the eigenfrequencies and modeshapes obtained with the MSE techniques versus the curve-fitting of the experimental measurements can be made a number of conclusions:

- The computation of the modes with non-contact sensors (SLDV) gives a good indication of the type of motion in the frequency range 30 Hz to 400 Hz.
- The use of more than one expansion method leads to various estimates where good predictions were obtained.
- The use of observation matrices with accurate stiffness parameters obtained with MNET gives a fairly good theoretical basis to extend expansion methods to composite component test configuration.
- Almost all MSE methods implemented in SDTools showed excellent results versus the curve-fitting of the experimental measurements. Using the MAC criterion, most of the

[4] *The assumption that dynamic loads used for the expansion are only applied at sensor locations is not particularly realistic* [122].

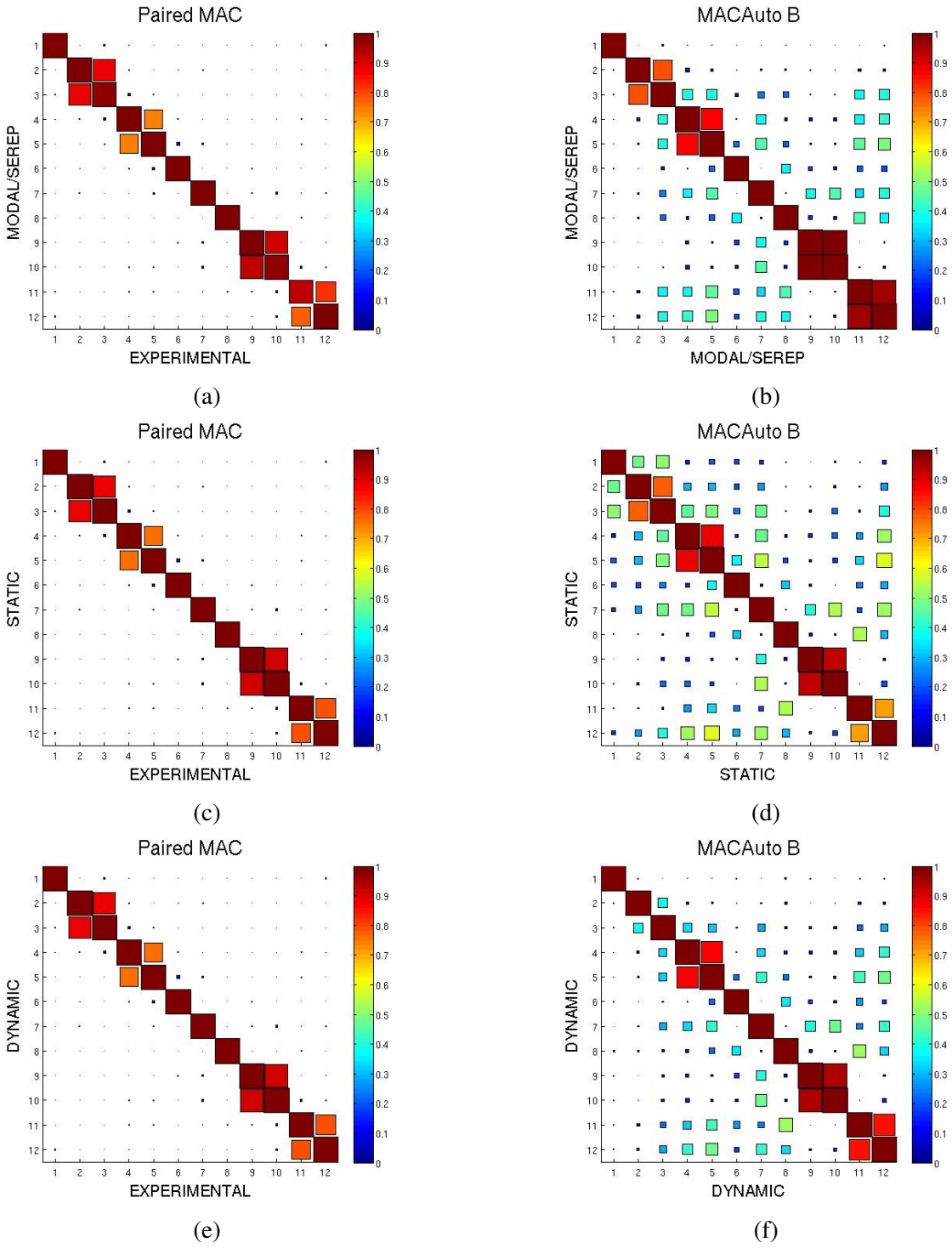

Fig. 6.11 Comparison of MAC and XOR: a) MSE MODAL/SEREP vs. exp., b) XOR MODAL/SEREP, c) MSE STATIC vs. exp., d) XOR MSE, e) MSE DYNAMIC vs. exp., f) XOR MSE.

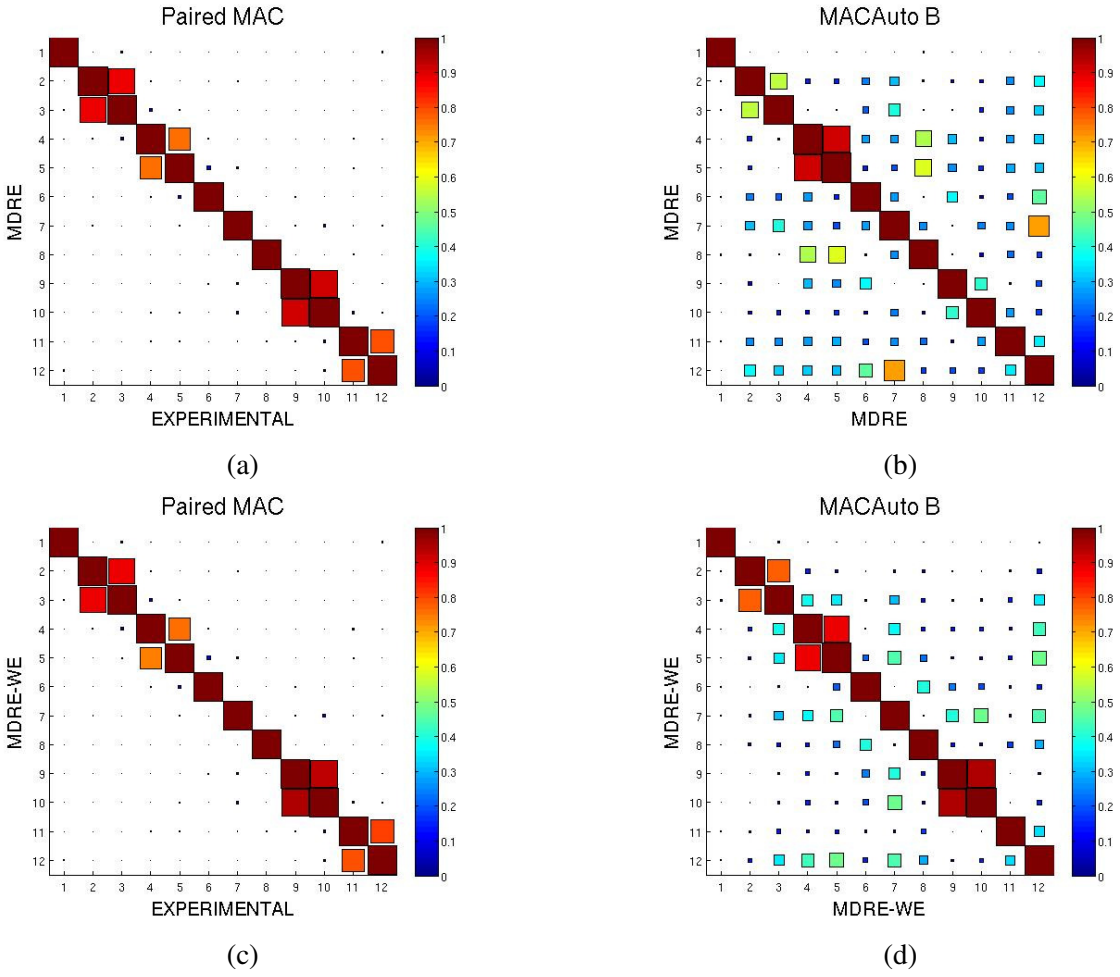

Fig. 6.12 Comparison of MAC and XOR: a) MSE MDRE vs. exp., b) XOR MDRE, c) MSE MDRE-WE vs. exp. d) XOR MDRE-WE.

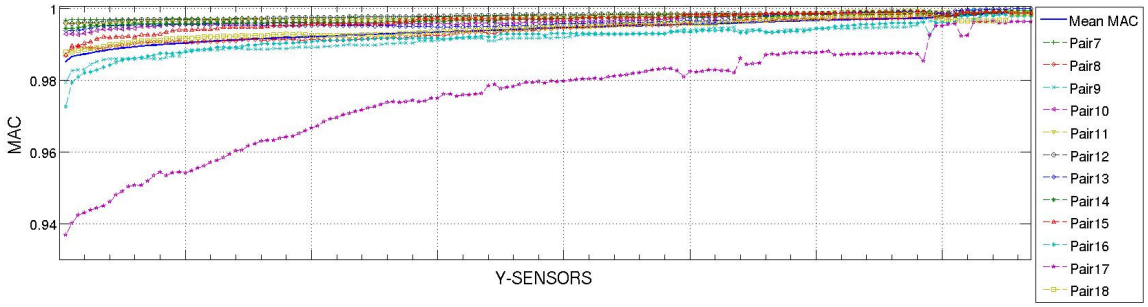

(a) MODAL/SEREP

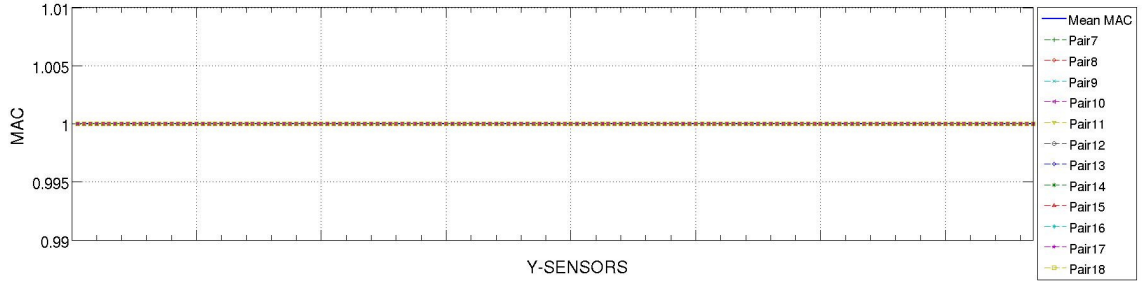

(b) STATIC

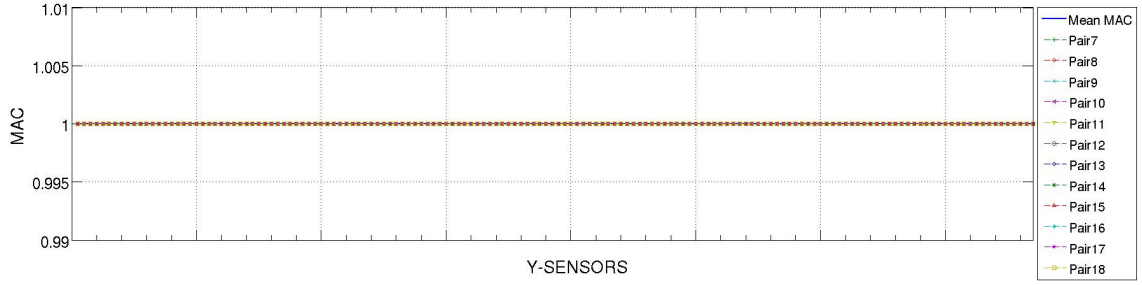

(c) DYNAMIC

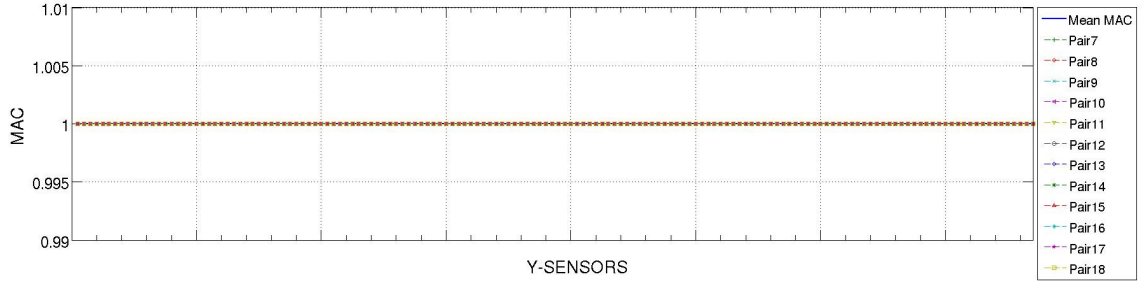

(d) MDRE

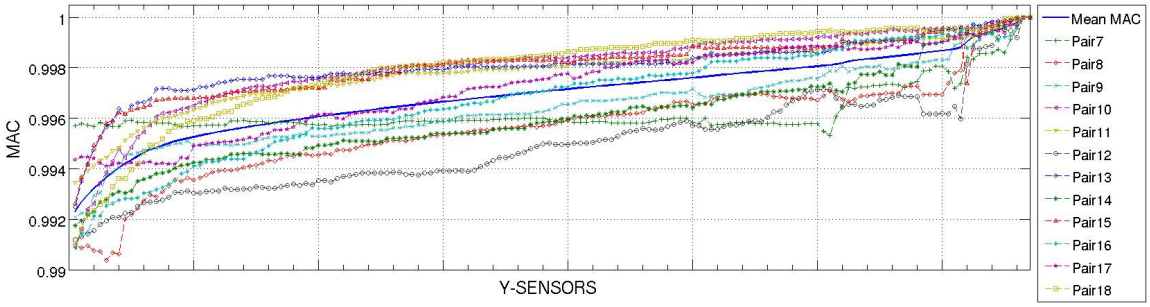

(e) MDRE-WE

Fig. 6.13 Comparison of MACco using mode shape expansion techniques versus exp.

MSE techniques presented a good M-MAC results. Low M-MAC results obtained with the STATIC MSE method might be due to the assumption of exclusion of the inertial terms.

- These mode shape expansion methods proved to be useful in obtaining valid predictions in a composite component.
- MODAL/SEREP, DYNAMIC, MDRE and MDRE-WE MSE methods tend to be sensible using K-MAC and M-MAC in terms of the updated stiffness parameters.
- MODAL/SEREP, and MDRE-WE methods showed the best K-MAC results.
- MODAL/SEREP, DYNAMIC and MDRE-WE methods showed the best M-MAC results.
- The SLVD measurements performed, the curve-fitting and the type of element formulation used in the FE full models as part of the MNET seem to show an important influence in the MSE as well as CBMOR results.
- The results obtained in Table 6.5 suggest a good correlation combining local FE model, classical theory of structural modification by coupling it with MSE technique and CMS with interface model reduction method (subspace selection) implemented in SDTools [106].

The results obtained suggest if the stiffness parameters used in the full FE model approach are really close to the physical model, the MSE results will display an improvement in the approximation. It is suggested, for further work to obtain the experimental measurements of the second component to perfom a comparison the off-diagonal terms obtained in this work applying MSE techniques implemented in [106].

Part III

Conclusions and Recomendations

Chapter 7

Conclusions and Recommendations

7.1 Conclusion using the MNET and CBMOR with basis on Rayleigh-Ritz vectors in a composite component assembly

A new MNET methodology was established in order to apply a CBMOR with Rayleigh-Ritz and AMLS methods in a composite component assembly introduced from Chapter 1 to 3. The objective of this work was fulfilled establishing two parts: The accurate identification of the stiffness parameters of a CFRP assembly and the feasibility to use the Craig-Bampton reduction technique (CBMOR) and AMLS allowing the generation of compact reduced model applied to a CFRP.

The experimental results performed in Chapter 4 with a SLDV and the curve-fitting performed using the IDRM and IDRC algorithms showed high correlation quality results of the measured FRFs. According to the curve-fitting, both algorithms are suitable to identify and parametrize the modal parameters in the CFRP and played and essential role to perform to obtain the modal parameters. The updating of the elastic material properties in the full FE model was performed using a DOE as part of the MNET. The updated mass and stiffness matrices in the full FE model have played an important role in this optimization procedure. The low Poisson ratio value ν_{12}, the moduli of elasticity E_1, E_2 and the shear modulus G_{12} are the stiffness parameters with more influence using the DMKT elements according the uncoded coefficients obtained with the ANOVA. These coefficients were used to generate the transfer

function. The main and interaction effects and the contour and surface plots obtained with the DOE are useful to visualize easily the impact and influence of the factors and interactions involved in the study, (see Figs. 4.21 and 4.22, respectively).

In Chapter 5 the MAC and MACco results have shown a good correlation agreement on the dynamic behaviour of the composite structure using orthotropic elements with PCOMP and MAT8 cards and different solvers (MATLAB-SDTools, MSC/NASTRAN and ABAQUS). It is well known that using thin elements may lead to the so-called phenomenon of shear lock-ing and that the transverse shear strains become small or even negligible studied by Reddy [77], [83]. The consequence of the shear lock-ing problem is that the stiffness matrix becomes stiff, which yields to erroneous results. The shear lock-ing is avoided in this work using the DMKT element with transverse shear effects included known as discrete shear triangular (DST) [76], [84], [99]. One of the characteristics of the DST element formulation is that if the shear effects are not significant, the DST element degenerate naturally to the DKT [84]. Another characteristic of the DST element is remark by Lardeur *et al.* [84] and Pagano *et al.* [85] that the transverse shear effects decrease with the increase of layers. The MAC and MACco values obtained with the MNET methodology have shown an improvement per paired mode and per paired-sensor respectively using the CTRIA3 and pshell elements based on the DMKT elements. It can be observed satisfactory results using the MAC and MACco criteria considering the plane and transverse shear effects according the number of layers defined using the finite elements selected. More research needs to be perform with another CFRP or sandwich components using the finite elements evaluated in this work to compare the performance and correlation with experimental measurements.

The different COMAC values of the full FE models obtained have also shown a good agreement on the phase correlation in respect to the experimental results. The material properties updated using the MAC and MACco and verified with the COMAC's values displayed high sensitive results.

Furthermore, the reduced model obtained in Chapter 6 based on the Craig-Bampton MOR and AMLS methods (the reduced model couples 2 substructures through 123 nodes and 579 DOF) has demonstrated a good agreement with the experimental results. The MAC values obtained with the FE models as well with the experimental results suggest a presence of mode veering phenomenon (bending and torsional mode at the same frequency in the considered composite structure). The MAC results in the reduced FE model obtained display a slightly improvement in some pair modes applying the CBMOR and AMLS methods. The different

COMAC values of the reduced FE model obtained have also shown a good agreement on the phase correlation in respect to the experimental results. The eCOMAC results in the reduced FE model display the best COMAC's results. The eCOMAC results with the ABAQUS FE model display similar values versus the reduced FE model.

The MODAL/SEREP and MDRE-WE showed the best results compared with the other MSE techniques based on the M-MAC obtained, (see Table 6.5).

In review, the correlation between the full FE model and ROM applying the CBMOR method in respect to the experimental results is validated through the use of different MACs, COMACs, MSE techniques, curve-fitting algorithms based on the updating of stiffness parameters applying the new MNET methodology.

It can, therefore, be concluded that this study successfully developed and implemented a MNET methodology to obtain the stiffness parameters that have enough accuracy to correlate experimental results and the application of CBMOR method to a CFRP assembly.

The achievements using the MNET and MOR method in a composite component can be summarized as follows:

- The proposed MNET using a DOE based on MAC and different COMACs, mode shape expansion methods, SLDV and curve-fitting algorithms have confirmed the influence of the stiffness parameters applying the CBMOR method to composite components.

- The application of the CBMOR with Rayleigh-Ritz basis, error estimations and residual iterations of substructures modes, the SVD and AMLS methods can be used to describe with enough accuracy the dynamic behaviour in a CFRP assembly.

- The experimental measurements results presented a good quality in low-frequency range (30-400 Hz).

- The IDRM and IDRC algorithms based on the pole/residues parametrization are suitable to validate and identify the modal parameters in a CFRP assembly.

- The use of CTRIA3 with PCOMP and MAT8 cards in MSC/NASTRAN and pshell in MATLAB-SDTools for a dynamic analysis can be used to describe with enough precision the stiffness parameters of a CFRP component in the frequency interval of interest (30-400 Hz) evaluating low Poisson's ratio values.

- The CTRIA3 element in MSC/NASTRAN and pshell in MATLAB-SDTools showed good predictive capabilities versus the experimental measurements as well as high computational efficiency using low Poisson's ratio values. The S3 element in ABAQUS with similar characteristics respect to the CTRIA3 element does not show the same results.
- The MNET established in this work is an efficient and robust tool that in combination with the experimental measurements and the finite element method is possible to obtain the stiffness parameters of a CFRP compared with the MNET established by Rikards *et al.* in [32], [33] and [39] that selected just some experimental measurements.
- The sensitivity of the stiffness parameters was observed using the MAC from a pool of candidates with respect to the available structural responses to identify the main, second and third interaction effects of the stiffness parameters and the error in a transfer function based on the ANOVA analysis.
- The analysis of variance (ANOVA) is a practical technique to determine the significance of the design parameters of CFRP that influence the MAC.
- It is important to highlight the number of interactions needed in order to reduce the error in the transfer function. This is not reported in the literature applying MNETs neither MOR methods.
- The selected parameters represented in the different element formulations affect the modal response significantly.
- The Young's modulus, shear modulus and low Poisson's ratio stiffness parameters evaluated were sufficient to have an accurate description of the dynamic behaviour of the assembled composite component using the full FE models.
- The updated laminate elastic constants using the DOE show a similar values obtained in the literature for high modulus carbon/epoxy.
- The results of the full and reduced FE models using the different MAC and COMACs show an accurate description of the dynamic behaviour of the CFRP assembled.
- It is observed how the accuracy of stiffness parameters obtained with the MNET influenced the different condensation algorithms implemented in the mode shape expansion techniques (MODAL, SEREP, STATIC, MDRE, MDRE-WE).

7.2 Suggestions for futher work using MNET and CBMOR with composite component assemblies

Considering the promising results applying CBMOR and AMLS methods to a composite component assembly working on a MNET methodology would lead to continue developing new projects as follows:

- Perform a central composite design (CCD) using the DOE perfomed in this work for building a second order (quadratic) model for the response variable (MAC) without needing to use a complete three-level factorial experiment.

- Analyze the stiffness parameters based on the variables of the manufacuring process and the selection of the carbon fiber material to monitor in real time the cure state of polymer gels applying: light scattering (photon correlation) spectroscopy, ultrasonic dynamic mechanical analysis (UDMA) dynamic mechanical thermal analysis (DMTA), Fourier transform (FT-IR) spectroscopy, near infrared spectroscopy (NIR), RAMAN spectroscopy and resonant utrasound spectroscopy (RUS).

- Evaluate other ESL and LWM using the new MNET methodology to apply the CBMOR and AMLS methods.

- Compare results obtained using the CTRIA3 or pshell with other elements (for example CQUAD4 or see Katili, 1993, A new discrete Kirchhoff-Mindlin element based on Mindlin-Reissner plate theory and assumed shear strain fields: Part 1: An extended DKT element for thick-plate bending analysis, International Journal for numerical methods in engineering, 36, 1859-1883) and then apply the CBMOR method.

- Evaluate the behaviour of the DST element in CFRP using MNET where the level of anisotropy is higher for comparative purposes.

- Extend the research of the veering phenomena identified with the DLR composite component assembly.

- Evaluate correlation of stress/displacement, damping, delamination, fracture (Puck criterion) and fatigue of composite materials using the DST element and MNET.

- Evaluate the temperature dependence of the Poisson ratio on composite materials using MNET.
- Perform and include the experimental measurements of the second component used in this work to analyze the higher frequencies.
- Use other experimental identification algorithms including residual modes to compare the MAC results.
- Perform a study using six-sigma in order to identify the critical steps in the manufacturing process of composite components that influence the quality of the stiffness parameters to control them.
- Compare results obtained with the CBMOR and AMLS methods of the CFRP in this work versus the enhanced AMLS method developed by Jin-Gyun [209].

Bibliography

[1] Gugercin, S., Antoulas, A. C., Bedrosian, N.,2001, *Approximation of the International Space Station 1R and 12A Model*, In Proc. Dec. Contr., pp.1515-1516.

[2] Hellard, G., *Composites in Airbus - A long story of innovations and experiences*, *Source: Airbus*.

[3] *Im CFK-Valley Stade stricken Spezialisten am Super-Leichtbau*, Source: *http://www.industrieanzeiger.de/home/-/article/32571342/33787629/*.

[4] Cunedioğlu, Y., 2011, *Analyses of laminated cantilever composite beams by model order reduction techniques*, Mechanics Based Design of Structures and Machines, Vol. 39, Iss. 1, 2011.

[5] Courant, R, 1943, *Variational methods for the solution of problems of equilibrium and vibration*, Bull. Am. Math. Soc., 49, pp. 1-43.

[6] Argyris, J.H., and Kelsey, S., 1960, *Energy theorems and structural analysis*, Butterworth Scientific Publication.

[7] Turner, M., Clough, R., Martin, H., and Topp, L., 1956, *Stiffness and deflection analysis of complex structures*, J. Aero. Sci., 23(9), pp. 805-823.

[8] Hurty, W. C., 1965, *Dynamic analysis of structural systems using component modes*, AIAA Journal,3(4), pp. 678-685.

[9] Craig, R. J., and Bampton M.C.C.,1968, *Coupling of substructures for dynamic analysis*, AIAA J., 6(7), pp. 1313-1319.

[10] Craig, R. J.,1987, *A review of time-domain and frequency domain component mode synthesis*, Int. J. Anal. and Exp. Modal Analysis 2(2), pp. 59-72.

[11] MacNeal, R.H., 1971, *A hybrid method of component mode synthesis*, Computers and structures, 1(4), pp. 581-601.

[12] Rubin, S., 1975, *Improved component-mode representation for structural dynamic analysis*, AIAA, 13, pp. 995-1006.

[13] Sol. H., 1986,*Identification of anisotropic plate rigidities using free vibration data*, PhD Thesis.

[14] De Wilde, W.P., 1987, *Anisotropic material identification using measured resonant frequencies of rectangular composite plates*, Compos. struct. Elsevier, 4, pp. 2317-24.

[15] Pedersen, P., 1989, *Optimization method applied to identification of material parameters, in: Eschenauer, A., and Thierauf, G., (eds.)*, Discretization methods and structural optimization- Procedures and Applications, Springer Verlag, pp. 277-283.

[16] De Wilde, W.P., 1991, *Identification of the rigidities of composite systems by mixed numerical/experimental methods, in: Vautrin, A., and Sol, H., (eds.)*, Numerical identification of composites, pp. 1-15.

[17] Frederiksen, P.S., 1992, *Identification of temperature dependence for orthotropic material moduli*, Mech. Mater., 13, pp. 79-90.

[18] Frederiksen, P.S., 1992, *Identification of material parameters in anisotropic plates – a combined numerical-experimetal method*, PhD Thesis, Department of solid mechanics, The technical University of Denmark.

[19] Frederiksen, P.S., 1997, *Experimental procedure and results for the identification of elastic constants of thick orthotropic plates*, J. Compos. Mater., 35, pp. 1241-1260.

[20] Frederiksen, P.S., 1998, *Parameter uncertainty and design of optimal experiments for the estimation of elastic constants*, Int. J. Solids and structures, 31(4), pp. 360-382.

[21] De Visscher, J., Sol, H., De Wilde, W.P., and Vantomme, J., 1997, *Identification of damping properties of orthotropic composite materials using a mixed numerical experimental method*, Appl. Compos. Mater., 4(1), pp.13-33.

[22] Mota Soares, C.M., Moreira de Freitas, M.J., and Araujo A.L., 1993, *Identification of material properties of composite plate specimen*, Composite Structures , 25, pp. 277-285.

[23] Bolognini, L., Riccio, F., Bettianli, F., 1993, *A modal technique for identification of stiffness and mass parameters in large structures, in: Brebbia, C.A. and Carlomagno, G.M., (eds.)*, Computational Methods and experimental measurements VI, Vol. 2: Stress Analysis, Elsevier Applied Science, London - New York, pp. 337-352.

[24] Grediac, M., and Vautrin, A., 1993, *Mechanical characterization of anisotropic plates: experiments and results*, Eur. J. Mech., A/Solids, 12(6), pp. 819-838.

[25] Moussu, F., and Nivoit, M., 1993, *Determination of elastic constants of orthotropic plates by modal analysis method of superposition*, J. Sound Vibr., 165(1), pp.149-163.

[26] Sol, H., De Visscher, J., and De Wilde W.P., 1993, *Identification of viscoelastic material properties of orthotropic plates using a mixed numerical/experimental technique, in: Brebbia, C.A. and Carlomagno, G.M., (eds.)*, Computational Methods and experimental measurements VI, Vol. 2 :Stress Analysis Elsevier Applied Science, London – New York, pp. 131-142.

[27] Link, M., and Zou, Z., 1994, *A two-step precedure to identify physical parameters of composite material structures using vibration test data, in: Proc. Int. Conf. On Vibration Engineering, ICVE 94, Beijing*, International Academic Publishers, pp. 217-224.

[28] Lai, T.C., Ip, K.H., 1996, *Parameter estimation of orthotropic plates by Bayesian sensitivity analysis*, Composite Struct., 34, pp. 29-42.

[29] Araujo, A.L., Mota Soares, C.M., Moreira de Freitas, M.J., 1996, *Characterization of material parameters of composite plate specimens using optimization and experimental vibrational data*, Composites: Part B 1996; 27 B: 185-9.

[30] Pedersen, P., 1999, *Identification techniques in composite laminates. In: Mota Soares, C.A., Mota Soares, C.M., Moreira de Freitas, M.J., editors* , Mechanics of composite materials and structures. Dordrecht: Kluwer Academic Publishers., pp. 443-452.

[31] Araujo, A.L., Mota Soares, C.M., Moreira de Freitas, M.J., Pedersen, P., and Herskovits, J., 2000, *Combined numerical-experimental model for the indentification of mechanical properties of laminated structures*, Composites structures 50, pp. 363-372.

[32] Rikards, R. and Chate, A., 1998, *Identification of mechanical properties of composites based on design of experiments*, Mechanics of Composite materials, 34(1), pp. 1-11.

[33] Rikards, R. and Chate, A., Steinchen, W., Kessler, A., Bledzki, A.K.,1999, *Method for identification of elastic properties of laminates based on experiment design*, Composites Part B: engineering, 30(1), pp. 279-289.

[34] Rikards, R., Bledzki, A. K., Eglais, V., Chate,A., and Kurek, K., 1992, *Elaboration of optimal design models for composite materials from data of experiments Identification of composites based on design of experiment*, Mech. Compos. Mater., 28(3) ,pp. 435-445.

[35] Rikards, R., 1993, *Elaboration of optimal design models for objects from data of experiments,in: Pedersen, P.(ed.), Optimal Design with Advanced Materials*, Proceedings of the IUTAM Symposium, Lungby, Denmark, 18-20 August, 1992, Elsevier Science Publishers, Amsterdam, pp. 148-162.

[36] Rikards, R., Chate, A., and B*ü*cklund, J., 1995, *Optimal design of sandwich plates based on planning of experiments in: Olhoff N. and Rozvany, G. I., (eds.)*, Proc. 1st World Congress of Structural and Multidisciplinary Optimization,28 May - 2 June 1995, Goslar, Germany, Pergamon, pp. 569-574.

[37] Rikards, R., Chate, A., 1995, *Optimal design of sandwich and laminated composite plates based on planning of experiments*, Struct. Optimiz. 4(1), pp. 46-53.

[38] Rikards, R., 1995, *Minimum weight design of sandwich and laminated composite structures, mechanics of composite materials*, Mech. Compos. Mater., 31(1), pp. 51-64.

[39] Rikards, R., Chate, A., Gailis, G., 2001, *Identification of elastic properties of laminates based on experimental design*, Mech. Compos. Mater., 38, pp. 5097-5115.

[40] Alsharif, F., MacNaughton J.L., 1987, *Optimization analysis of a V-Twin motorcycle engine using wave cycle analysis and iSight optimization framework*, pp. 1-7.

[41] Xiaoping, C., Xiaoli, Y., and Binwei, J., 2010, *Study of crankshaft strength based on iSIGHT plataform and DOE methods*, Int. Conference on measuring Tech. and mechatronics automation, IEEE computer society, pp. 548-551.

[42] Cuhna, J., Piranda, J. 1999, *The use of model updating techniques in dynamics for identification of stiffness properties of sandwich composite structures*, J. Braz Soc. Mech Scis, XXI(2):313-21, in Portuguese.

[43] Cugnoni, J., Gm*ü*r, T., Schorderet A., 2004, *Identification by modal analysis of composite structures modelled with FSDT and HSDT laminated shell finite elements*, Composites: Part A 35, Applied science and manufacturing, pp. 977-987.

[44] Cugnoni, J., Gm*ü*r, T., Schorderet A., 2007, *Inverse method based on modal analysis for characterizing the constitutive properties of thick composite plates*, Computers and structures, 85, pp. 1310-1320.

[45] Matter, M., Gm*ü*r, T., Cugnoni , J., Schorderet A., 2007, *Improved modal characterization of the constitutive parameter in multilayered plates*, Composite science and technology, 67, pp. 1121-1131.

[46] Van den Abeele, F., De Oliveira, J.R., Huertos, F,J., 2013, *Identification of the complex moduli of orthotropic materials using modal analysis*, Excerpt from the proceeding of the COMSOL conference, Paris.

[47] Badshah, S., 2013,*Mixed numerical-experimental identification based on modal testing*, International Journal of Engineering and Advanced Technology (IJEAT) ISSN: 2249 – 8958, Volume-2, Issue-4, April 2013

[48] Ghanmi, S., Bouajila, S., Gruedi, M., 2013, *Numerical-experimental updating identification of elastic behavior of a composite plate using new multi-objective optimization procedure*, Journal of Surface Engineered Materials and Advanced Technology, 3(1), pp.13-20.

[49] Luczak, M., Vecchio, A., Gielen, L., Mucchi, E., and Peeters, B., 2009, *Variability in composite structure vibration measurement and numerical modal updating*, IMAC, pp. 1-15.

[50] Yang, P.C., Norris, C.H., Stavsky, Y., 1966,*Elastic wave propagation in heterogeneous plates*, Int. J. Solids Struct., 2, pp. 665-684.

[51] Ambartsumyan, S.A., 1969, *Theory of Anisotropic Plates*, Technomic Publising,

[52] Withney, J.M., 1969, *The effect of transverse shear deformation on the bending of laminated plates*, J. Compos. Mater., 3, pp. 534-547.

[53] Chou, P.C. and Carleone, J., 1973, *Transverse shear in laminated plate theories*, AIAA. J., 11, pp. 1333-1336.

[54] Lo, K.H., Chistensen, R.M., and Wu, E.M., 1977, *A high-order theory of plate deformation*, J. Appl. Mech. ASME, 99, pp. 663-676.

[55] Reddy, J.N., 1986, *A simple higher-order theory for laminated composite plates*, J. Appl. Mech. ASME, 51, pp. 745-752.

[56] Renn, J.G., 1986, *A new theory of laminated plate*, Compos. Sci. Technol., 26, pp. 225-239.

[57] Lekhnitskii, S.G., 1968, *Anisotropic plates*, Gordon and Breach, New York.

[58] Srinivas, S., 1973, *A refined analysis of composite laminates*, J. Sound Vib., 30, pp. 495-507

[59] Di Sciuva, M., 1985, *Development of an anisotropic, multilayered, shear deformable rectangular plate element*, Compos. Struct., 21, pp. 789-796

[60] Reissner, E., 1945, *The effect of transverse shear deformation on the bending of elastic plates*, J. Appl. Mech. ASME. 12, pp. A69-A77.

[61] Reissner, E., 1950, *On a variational theorem in elasticity*, J. Math. Phys., 29, pp. 90-95.

[62] Reissner, E., 1972, *A consistent treatment of transversal shear deformations in laminated anisotropic plates*, AIAA J. 10, pp. 716-718.

[63] Cohen, G.A., 1978, *Transverse shear stiffness of laminated anistropic shells*, Comp. Methods Appl. Mech. Eng., 13, pp. 205-220.

[64] Verchery, G., 1973, *Extremal theorems in term of mixed variables- Application to beams ans plates subjeted to transverse shears*, 15th Polish Solid Mechanics Conference, Zakopane.

[65] Lekhnitskii, S.G., 1935, *Strength calculation of composite beams*, Vestn. Inzh. Tekh., 9.

[66] Grigolyuk, E.I., and Kulikov, G.M., 1988, *General directions of the development of theory of shells*, Mechanics of Composite Materials, 24, Iss 2, pp. 231-241

[67] Reddy, J.N. and Robbins, D.H., 1994, *Theories and computational models for composite laminates*, Applied mechanics reviews 47(6), pp. 147-169.

[68] Vasilive, V.V., and Lur'e, S.A., 1992, *On refined theories of beams, plates and shells*, Journal of composite materials 26(4), pp. 546-557.

[69] Lur'e, S.A., and Shumova, N.P., 1996, *Kinematic models of refined theories concerning composite beams, plates and shells*, Mechanics of Composite Materials, 32(5), pp. 422-430.

[70] Qatu, M.S., 2002, *Recent research advances in the dynamic behavior of shells: 1989-2000, Part 1: Laminated composite shells*, Applied Mechanics Reviews 55(4), pp. 325-350.

[71] Qatu, M.S., 2002, *Recent research advances in the dynamic behavior of shells: 1989-2000, Part 2: Homogeneous shells* Applied Mechanics Reviews 55(5), pp. 415-434.

[72] Tessler, A.,and Hughes.T.J.R., 1985, *A three-node Mindlin plate element with improved transverse shear*, Comp. Methods Appl. Mech. Eng., 50, pp. 71-101.

[73] Tessler, A. and Hughes, T.J.R., 1983, *An improved treatment of transversal shear in a Mindlin-type four-node quadrilateral element*, Comp. Methods Appl. Mech. Eng., 39, pp. 311-335.

[74] Pryor, C.W. and Barker, R.M., 1970, *A finite element analysis including transverse shear effects for applications to laminated plates*, AIAA J., 9, pp. 912-917.

[75] Mohan, P., 1997, *Development and applications of flat triangular elements for thin laminated shells*, PhD Thesis

[76] Batoz, J.L., and Lardeur, P.,1989, *A discrete shear triangular nine dof element for the analysis of thick to very thin plates*, Int. J. Numer. Methods Eng., 28, pp. 533-560.

[77] Reddy, J.N., and Kupusamy, T., 1984, *Natural vibrations of laminated anisotropic plates*, J. Sound Vib., 94, pp. 63-69.

[78] Sanders J.L., 1959, *An improved first approximation theory for thin shell*, NASA report TR-R24,

[79] Murthy, S.S., 1983, *A triangular anisotropic thin shell element based on discrete Kirchhoff theory*, PhD Thesis.

[80] Zienkiewicz, O.C., Taylor R.L.,2000, *The finite element method, Fifth Edition*, Butterworth-Heinemann Linacre House, Jordan Hill,

[81] Cramer, D. R., Taggart D.F., Hypercar, Inc., 2002, *Design and manufacture of an affordable advanced-composite automotive body structure*, Proceedings of The 10th International Battery, Hybrid and fuel cell electric vehicle symposium and exhibition, pp. 1-12,

[82] Reuter, Robert, C. Jr., 1971, *Concise property transformation relations for an anisotropic lamina*, J. Composite Materials, Vol. 5, pp. 270-272.

[83] Reddy J.N, 2005, *Mechanics of laminate composite plates and shells. Theory and Analysis*, Department of Mechanical Engineering Texas A&M University, College Station, Texas USA 77843.

[84] Lardeur P., Batoz J.L, 1989, *Composite plate analysis using a new discrete shear triangular finite element*, Int. J. Num. Meth. in Eng., 27, pp. 343-359.

[85] Pagano, N.J., Hatfield, S.J., 1972, *Elastic behaviour of multilayered bidirectional composites*, AIAA J., 10, pp. 931-933.

[86] Kirchhoff , G., 1876, *Vorlesungen über Mathematische Physik*, Mechanik, Vol.1.

[87] Wempner, G.a., Oden, J.T., Kross, D.A., 1968, , *Finite element analysis of thin shells*, Proc. ASCE. J. Engng. Mech. Div. No. EM6, pp. 1273-1294.

[88] Mindlin, R.D., 1951, *Influence of rotatory inertia and shear in flexural motions of isotropic elastic plates*, J. Appl. Mech. ASME , 18,pp. 1031-1036.

[89] Reissner, E., 1945, *The effect of transverse shear deformation on the bending of elastic plates* , J. Appl. Mech. ASME 12, pp. 69-76.

[90] Whitney, J.M., and Pagano, N.J., 1970, *Shear deformation in heterogeneous anisotropic plates*, J. Appl. Mech. ASME., 37, pp. 1031-1036.

[91] Kress, G., 2006, *Mechanik der Faserverbundwerkstoffe*, IMES, October.

[92] Rao, S.S., 2004, *The finite elmenent method in enginnering*, Elsevier Science and Technology books.

[93] Carrera, E., 1996, C^0 *Reissner-Mindlin multilayered plate elements including Zig-Zag and Interlaminar stress continuity*, Int. J. for Numer. Methods in Eng., 39, pp. 1797-1820.

[94] Carrera, E., 2004, *Assessment of theories for free vibration analysis of homogeneous and multilayered plates*, Shock and Vibration., 11(3), pp. 261-270.

[95] Carrera, E., 2002, *Theories and finite elements for multilayered plates and shells: A unified compact formulation with numerical and benchmarking*, Archives of computational methods in Engineering., 9(2), pp. 87-40.

[96] Carrera, E., 2003, *Theories and finite elements for multilayered plates and shells: A unified compact formulation with numerical and benchmarking*, Archives of computational methods in Engineering., 10(3), pp. 215-296.

[97] Greaves, G.N., Greer, A.L., Lakes, R.S., and Rouxel, T., E., 2011, *Poisson's ratio and modern materials*, Nature Materials, 10, pp. 823-837.

[98] Herakovich, C.T., 1984, *Composite laminate with negative through-the-thickness Poisson's ratio*, Journal of composite materials, 18, pp. 447-455.

[99] Oñate, E., 2013, *Structural analysis with the finite element method. Linear statics.,* Vol. 2, Beams, plates and shells, First edition, Springer.

[100] Antonucci, V., Hsiao, K.T., Advani, S. G., 2002, *A methodology to reduce thermal gradients due to the exothermic reactions in composites processing*, International Journal of Heat and Mass Transfer, 48(5), pp. 1675-1684.

[101] Whitney, J.M., 1987, *Structural analysis of laminated anistropic plates*, Technomic Publishing Co.

[102] Whitney, J.M., 1973, *Shear correction factors for orthotropic laminates under static load*, J. of Appl. mech., 40, pp. 302-304.

[103] Lalonde, S., 2000, *Investigation into the static and fatigue behavior of a Helicopter main rotor yoke made of composite materials*, M.Sc. Thesis, McGill university, Montreal.

[104] Batoz, J.L, Bathe, K., and Ho, L., 1980, *A study of tree-node triangular plate bending elements*, Int. J. Num. Meth. in Eng., 15, 1771-1812.

[105] Roos, R., 2008, *Model for interlaminar normal stresses in doubly curve laminates*, PhD Thesis, Swiss Federal Institut of Technology Zurich, Switzerland.

[106] SDTools Inc., 2011, *SDTools Version 6.3*, Structural Dynamics Toolbox and FEMLink User's Guide.

[107] Reddy, J.N., and Kuppusamy, T., 1984, *Natural vibrations of anisotropic plates*, Journal of Sound and Vibrations, 94, pp. 63–69.

[108] Guyan, R.J.(1965). *Reduction of mass and stiffness matrices*, AIAA. Journal, 3, pp. 380.

[109] Irons, B. M., 1965, *Structural eigenvalue problems - elimination of unwanted variables*, AIAA. Journal, 3(5), pp. 96-96.

[110] Leung, A. Y. T., 1978, *An accurate method of dynamic condensation in structural analysis*, Int. Journal for Numerical Methods in Engineering, 12(11), pp.170-1715.

[111] O'Callahan, J., Avitabile, P. and Riemer, 1989, *System equivalent reduction expansion process (SEREP)*, IMAC VII., 1, pp. 29-37.

[112] Kammer, D .1987. *Test-Analysis model development using and exact modal reduction*, International Journal of Analytical and Experimental Modal Analysis., 2(4), pp. 174-179.

[113] Gu, J., 2000, *Efficient model reduction methods for structural dynamics analyses*, Doctoral Thesis, The University of Michigan, U.S.A.

[114] Koutsovasilis, P, 2009, *Model order reduction in structural mechanics*, PhD Thesis, Technical University of Dresden, Germany.

[115] Antoulas, A. C., Sorensen, D. C., Gugercin, S., 2004, *A survey of model reduction methods for large-scale systems*, Technical report, Rice University, Houston, Texas. 2(4), pp. 174-179.

[116] Cunedioğlu, Y., Muğan, A., Akcay, H., 2006, *Frequency domain analysis of model order reduction techniques*, Finite Elements in Analysis and Design, 42, pp. 367-403.

[117] Balmès, E., 1996, *Optimal ritz vectors for component mode synthesis using the singular value decomposition*, AIAA J., 34(6), pp. 1256-1260.

[118] Balmès, E., 2005, *Modes and regular shapes. How to extend component mode synthesis theory*, International Seminar on Modal Analysis, Leuven, September, 42, pp. 367-403.

[119] Balmès E.,1996, *Parametric families of reduced finite element models. Theory and applications*, Mechanical Systems and signal processing, 10(4), pp. 381-394.

[120] Balmès, E.,1998, *Efficient sensitivity analysis based on finite element model reduction*, IMAC, pp. 1168-1174.

[121] Balmès, E., 1999, *Use of generalized interface degree of freedom in component mode synthesis*, DRET A/C, ONERA, Structures Direction, pp. 1-7.

[122] Balmès, E., 1999, *Sensors, Degrees of freedom, and generalized modeshape expansion methods*, IMAC, pp. 1-8.

[123] Balmès, E., 2000, *Review and evaluation of shape expansion methods*, IMAC, pp. 555-561.

[124] Levine-West, M., Mihnan, M., Kissil , A.,1994, *Evaluation of mode shape expansion techniques on the micro-precision*, interferometer truss, IMAC, pp. 212-218.

[125] Allemang, R.J., and Brown, D.L., 1982, *A Correlation Coeffiecient for Modal Vector Analysis*, IMAC, USA, pp.110-116.

[126] Guillaume, M. Balmès, E., Chancelier, T., 2014, *Improved modal assurance criterion using a quantification of idenfication errors per mode sensor*, International Conference on Noise and Vibration Engineering, Belgium pp. 1-12.

[127] Brughmans, M., Leuridan, J., Blauwkamp, K., 1993, *The application of FEM-EMA correlation and validation techniques on a body-in-white*, IMAC, pp. 646-654.

[128] Lieven, N., A.J, Ewins, D.J, 1988, *Spatial correlation of mode shapes, The coordinate modal assurance criterion (COMAC)*, IMAC, pp. 690-695.

[129] Hunt, D.L., 1992, *Application of an enhanced coordinate modal assurance criteria (ECOMAC)*, IMAC, pp. 66-71.

[130] Hatch, C., Skingle G.W., Greaves, C.H., Lieven, N.A.J, Coot, J.E., Friswell, M.I., Mottershead, J.E., Shaverdi, H., Mares, C., McLaughlin, A., Link, M., Piet-Lahanier, N., Van Houten, M.H., Goege, D., Rottmayr, H., 2006, *Methods for refinement of structural finite element models: Summary of the Gateur AF14 collaborative programme*, European Rotorcraft Forum (DY09), pp. 1-28.

[131] Ewins, D.J., 1984, *Modal testing: Theory and practice*, John Wiley and Sons Inc., New York, U.S.A.

[132] Catbas, F.N., Aktan, A.E., Allemang, R.J., Brown, D.L, 1998, *Correlation function for spatial locations of scaled mode shapes (COMEF)*, IMAC, pp. 1550-1555.

[133] Allemang, R.J., 2003, *The modal assurene criterion - Twenty years of use and abuse*, Sound and vibration, pp. 14-21.

[134] Kidder, R., 1973, *Reduction of structural frequency equations*, AIAA J., 11(6), pp. 892-892.

[135] Kammer, D.,(1991). *A hybrid approach to test-analytical model development for large structures*, Journal of Vibrations and Acoustics, 11(3), pp. 325-332.

[136] Roy, N. Girard, A. and Bugeat, L.-P.,1993, *Expansion of experimental modeshapes - An improvement of the projection technique*, IMAC, 11(6), 152-158.

[137] Balmès E., Billet, L., 2001. *Using expansion and interface reduction to enhance structural modification methods*, IMAC, pp. 615-621.

[138] Corus, M., and Balmes, E., 2003,*Improvement of a structural modification method using data expansion and model reduction techniques*, IMAC, pp. 1-7.

[139] Gade, S., Moller, N.B., Jacobsen, N.J., and Hardonk. B., 2000, *Modal analysis using a scanning laser Doppler vibrometer*, Sound and Vibration Measurements, pp. 1015-1019.

[140] Avitabile, P., Niezrecki, C., Helfrick, M., Warren and Pingle , P., 2010, *Noncontact measurement techniques for model correlation*, Sound and Vibration, pp. 8-12.

[141] Pingle, P, Sailhammer, J. and Avitabile, P. 2009, *Comparision of 3D laser vibrometer and accelerometer frequency measurements*, IMAC, pp. 1-13.

[142] Stanbridge, A.B., and Ewins, D.J.,1996, *Using a continuous-scanning laser doppler vibrometer for modal testing*, IMAC, pp. 816-822.

[143] Stanbridge, A.B., and Ewins, D.J., 2002, *Modal testing using a scanning laser doppler vibrometer*, Mechanical Systems and Signal Processing, 13(2), pp. 255-270.

[144] SDRC I-deas level 3, 1986, *User's guide, Section VI, Universal file datasets*, SDRC, pp. 306-470.

[145] Montgomery, D.C., 2001, *Design and Anlysis of Experiments*, Arizona State University, John Wiley and Sons Inc., U.S.A.

[146] Ross, P.J., 1988, *Taguchi techniques for quality engineerig*, McGraw-Hill Book Company, New York, U.S.A.

[147] Minitab 17 Statistical Software, 2010, Computer software, State Collage, PA:Minitab, Inc. (www.minitab.com).

[148] MSC/NASTRAN, 2012, *MSC/NASTRAN User's Guide*, MSC.Software Corporation.

[149] MacNeal R.J., 1986, *The evolution of lower order plate and shell elements in MSC/Nastran*, Finite element methods for plate and shell structures, 1, Pineridge Press, Swansca, pp. 316-347.

[150] MSC/NASTRAN V68 *Reference Manual*, MacNeal-Schwendler Corporation.

[151] ABAQUS 6.9 *Reference Manual*, Dassault Systemes Simulia Corp.

[152] Balmès E., 1996, *Frequency domain identification of structural dynamics using the pole/residue*, IMAC, pp. 540-546.

[153] Roy N., Girard A., 2005, *Impact of residual modes in structural dynamics*, Proceedings, European Conference of Spacecraft Structures, Materials & Mechanical Testing, Noordwijk, The Netherlands. IMAC, pp. 540-546.

[154] Balmès, E., 1999, *Sensor, degrees of freedom, and generalized modeshape expansion methods*, IMAC 1999, reproduced with permission from SEM, 1(1), pp. 1-12.

[155] Balmès, E., 1993, *Integration of existing methods and user knowledge in a MIMO identification algorithm for structures with high density*, IMAC, pp. 613–619.

[156] Hirotsu, S., 1990, *Elastic anomaly near the critical point of volume phase transition in polymer gels*, Macromolecules, 23(3), pp. 903-905.

[157] McKnight, R.E.A. et al, 2008, *Grain size dependence of elastic anomalies accompanying the alpha-beta phase transition in polycrystalline quartz*, J. Phys. Cond. Mat., 20, pp. 903-905.

[158] Li, C., Hu, Z., and Li, Y., 1993, *Poisson's ratio in polymer gels near the phase-transition point*, Phys. Rev. E., 48, pp. 603-606.

[159] Grima, J.N. *et al*, 2010, *Hexagonal honeycombs with zero Poisson's ratios and enhanced stiffness*, Adv. Eng. Matter. 12, pp. 855-862.

[160] Wang, Y.C., and Lakes, R.S., 2005, *Composites with inclusions of negative bulk modulus: extreme damping and negative Poisson's ratio*, J. Comp. Mater. 39, pp. 1645-1657.

[161] Tsai S.W., and Hahn H.T., 1980, Introduction to composite materials, Technomic, Lancaster, PA.

[162] Lakes R., 1993, Advanced in negative Poisson's ratio materials, adapted from Advanced Materials, 5, pp. 293-296.

[163] Mounier D., Poilane C., Bucher C., Picart P., 2012, *Evaluation of transverse elastic properties of fibers used in composite materials by laser resonant ultrasound spectroscopy*, Proceeding of the acoustics 2012, Nantes Conference 23-27 April 2012, Nantes France.

[164] Maistros G.M., Patridge I., 1998, *Monitoring autoclave cure in commercial carbon fibre/epoxy composites*, Composites Part B: Engineering, 29(3), pp. 245-250.

[165] Whitney T.M. Green Jr R.E., 1995, *Cure monitoring of carbon epoxy composites: an application of resonant ultrasound sprectroscopy*, Ultrasonics, 34(2-5), pp. 347-353.

[166] VanPaepegem W., De Baere I., Lamkanfi E., DeGrieck J., 2006, *Poisson's ratio as a sensitive indicator of (fatigue) damage in fibre-reinforced plastics*, Fatigue Fract. Engng. Mater. Struct., 30, pp. 269-276.

[167] Meuwissen, M.H.H, 1998, *An inverse method for the mechanical characterization of metals.* PhD Technische University Eindhoven, The Netherlands.

[168] Van Ratingen, M.R., 1994, *Mechanical identification of inhomogeneous solids*, PhD Thesis Eindhoven University of Technology, The Netherlands.

[169] Ledesma, A., and Gens, A., 1997, *Inverse analysis of tunnel excavation problem from displacement and pore water pressure measurements*, In Sol, H., and Oomens, C.W.J., editors, Material identification using mixed numerical experimental methods (EUROMECH 357), pp. 163-172.

[170] Lauwagie, T., 2005, *Vibration-Based Methods for the Identification of the Elastic Properties of Layered Materials*, PhD Thesis, Catholic University of Leuven, Belgium.

[171] Michino, M., and Tanaka, M., 1995, *Determination of flow stresses by inverse solution using finite element method*, Computational Mechanics, 16, pp. 290-296.

[172] Knipprath, C., 2010, *Mechanical performance of binder yarn composites*, PhD Thesis, Cranfield University.

[173] Khan, M.A., 2009, *Numerical and experimental forming analyses of textile composites reiforcements based on a Hypoelastic behavior*, PhD Thesis, Institut National des Sciences Appliquees de Lyon, France.

[174] Biswas, Sandhyarani., 2010, *Processing, characterization and wear response of particulate filled epoxy based hybrid composites*, PhD Thesis, Department of mechanical engineering National Institute of Technology, Rourkela, India.

[175] Patnaik, Amar, 2008, *Development, characterization and solid particle erosion response of polyester based hybrid composites*, PhD Thesis, Department of Mechanical Engineering National Institute of Technology, Rourkela, India.

[176] Balvers, J. M., 2014, *In situ and cure monitoring in liquid composite moulding by fibre Bragg grating sensors*, PhD Thesis, TU Delf.

[177] Tochukwu, G., 2014, *Carbon fiber composite cellular structures*, PhD Thesis, University of Virginia, U.S.A.

[178] Giorelli, M., 2002, *Methodology for correlating experimental and finite element modal analysis on valve trains*, M.Sc Thesis, Worcester Polytechnic Institute, U.S.A.

[179] Hörnlund, M., Papazoglu, A., 2005, *Analysis and measurements of vehicle door structural dynamic response*, M.Sc Thesis, Division of Structural Mechanics, LTH, Lund University, Sweden.

[180] Balmès E., 2011, *Methods for vibration design and validation*, ENSAM/PIMM, ECP/MSSMAT SDTools, Course notes ENSAM/Ecole Centrale Paris, 1997-2012.

[181] Balmès, E., Chapelier, C., Lubrina, P., Fargette, P., 1995, *An evaluation of modal testing results based on the force appropriation method*, Proc. IMAC 13 Int. Modal Analysis Conf.

[182] Richardson, M.H., 1977, *Derivation of mass, stiffness and damping parameters from experimental modal data*, Hewlett Packard Company, Santa Clara Division, 1, pp. 1-6.

[183] Richardson, M.H., 2000, *Modal Mass, stiffness and damping*, Vibrant Technology, Inc, 31, pp. 1-6.

[184] Potter, R., and Richardson, M., 1974, *Mass, stiffness, and damping matrices from measured modal parameters*, ISA Int. Instrumentation-Automation conference and Exhibit, pp. 1-5.

[185] Schwarz, B.J., Richardson, M.H.,1999, *Experimental modal analysis*, CSI Reliability Week, Vibrant technology, 1(1), pp. 1-12.

[186] Meirovitch, L.,1986, *Elements of Vibration Analysis*, *Second Edition McGraw-Hill*.

[187] Schwarz, B.J., Richardson, M.H., 2003, *Scaling mode shapes obtained from operating data*, Presented at IMAC XXI, 1(1), pp. 1-8.

[188] Schwarz, B.J, Richardson, M.H.,2006, *Using FEA Modes to Scale Experimental Mode Shapes*, Presented at IMAC 2006, 1(1), pp. 1-8.

[189] Cooley, J. W., and Tukey, J.W., 1965, *An algorithm for the machine calculation of complex fourier series*, Mathematics of Computation, 19(90), pp. 297-311.

[190] Brigham, EO., 1988, *The fast Fourier transform and its application. Experimental Modal Analysis*, Prentice Hall.

[191] Welaratna, S., 1997, *Thirty years of FFT analyzers*, Sound and Vibration, pp. 1-5.

[192] Formenti, D.L., Richardson M.H., 1982, *Parameter estimation from frequency response measurements using rational fraction polynomials*, IMAC 1st, pp. 1-8.

[193] Richardson, M.H., Formenti, D.L., 1985, *Global curve fitting of frequency response measurements using rational fraction polynomials*, IMAC 3rd, pp. 1-8.

[194] Richardson, M.H., 1986, *Global Frequency and damping estimates from frequency response measurements*, IMAC 4th., pp. 1-7.

[195] Rikards, R., 1995, *Elaboration of optimal design models for objects from data of experiments*, In: Pedersen, P., ed. Optimal design with advanced materials. Proceedings of the IUTAM symposium, Lyngby, Denmark. Elsevier Science Publishers.

[196] Chambers, L.D, 2000, *The practical handbook of genetic algorithms: Applications*, Chapman and Hall/CRC, USA.

[197] Maletta, C., and Pagnotta, L., 2004, *On determination of mechanical properties of composite laminates using genetic algorithms*, Int. Journal of Mechanics and Materials in Design, 1, 199-211.

[198] Van der Valk, P.L.C., 2010, *Model Reduction & Interface modeling in dynamic substructuring - Application to a multi-megawatt wind turbine*, M.Sc. Thesis, TU-Delft. The Netherlands.

[199] de Klerk D., Rixen D.J., Voormeeren S.N., 2008. *General framework for dynamic substructuring: History, review and Classification techniques*, AIAA. Journal, 46(5), pp. 1169-1181.

[200] de Klerk D., Rixen D.J., de Jong J., 2006. *The frequency based substructuring (FBS) method reformulated according to the dual domain decomposition method*, In: Proceeding of 24th IMAC, St. Louise Missouri, U.S.A.

[201] Kaplan, M., 2001, *Implementation of Automated Multilevel Substructuring for frequency response Analysis of Structures*, PhD Thesis, The University of Texas at Austin, U.S.A.

[202] Belsky, V., Crivelli, L., Dunbar, M., Belyi, M., Wood, M., Ianculescu, C., Kim, M., Bajer, A., Krawezik, G., 2015, *Accelerating commercial linear and non-linear implicit FEA software through high-performance computing*, Dassault Systemes Simulia Corp.

[203] Vermot des Roches, G., 2011, *Frequency and time simulation of squeal instabilities.- Application to the design of industrial automotive brakes*, PhD Thesis, École Centrale Des Arts Et Manufactures, Paris.

[204] Saad Y., 2000, *Iterative methods for Sparse Linear Systems*, Self-published, second edition.

[205] Ashcraft C., 1999, *Ordering sparse matrices and transforming front trees*, Boeing Shared Services Group.

[206] Karypis, G. and Kumar, V., 1998, *METIS. A software package for partitioning unstructured graphs, partitioning meshes, and computing fill-reducing ordering of sparse matrices, Version 4.0.*, Self published.

[207] Ashcraft, C. and Grimes, R., 1999, *Spooles. An object-oriented sparse matrix library*, In proceedings of the 1999 SIAM Conference on Parallel Processing for Scientific Computing.

[208] Bennighof, J., Kaplan M., Muller, M., and Kim, M., 2000, *Meeting the NVH computational challenge: Automated multi-level substructuring*, IMAC, pp. 909-915.

[209] Kim, J.G., K., Boo, S.H., Lee, P.S., 2015, *An enhanced AMLS method and its performance*, Computer methods in applied mechanics and engineering, 287, pp. 90-111.

[210] Vermot des Roches G.,Bianchi J.P., Balmès E., Lemaire R. and Pasquet T., 2010, *Using component modes in a system design process*, IMAC XXVIII, 2, pp. 683-688.

[211] Corus, M., 2003, *Amelioration des methodes de modification structurale par utilisation de techniques d'expansion et de reduction de modele*, PhD Thesis, École Centrale Paris, France.

[212] Sternchüss, A., 2009, *Multi-level parametric reduced models of rotating blade disk assemblies*, PhD Thesis, École Centrale Paris, France.

[213] Bobillot, A., 2002, *Méthodes de réduction pour le recalage. Application au cas d'Ariane 5*, PhD Thesis, École Centrale Paris, France.

[214] Florens C., 2009, *Modeling of the viscoelastic honeycomb panel equipped with piezoelectric patches in view of vibroacoustic active control design*, PhD Thesis, École Centrale Paris, France.

[215] Maia, N., Silva. J., 1997, *Theoretical and experimental modal analysis*, Research Studies Press, First edition.

[216] Herman, G.T., 1980, *Image Reconstruction from projections*, Academic Press, First edition.

[217] Shyu, W.H.,1996, *Quasi-static mode compensation for component mode synthesis of dynamical systems*, Doctoral Thesis, The University of Michigan, U.S.A.

[218] Shyu, W.H.Ma, Z.D., Hulbert, G.H., 1997, *A new component mode synthesis method: Quasi-static mode compensation*, Finite Element Anal. Des. 24(29), pp. 27-281.

[219] Shyu, W.H., Gu, J.,Hulbert, G.H.,Ma Z.D., 2000, *On the use of multiple Quasi-static mode compensation sets for component mode synthesis of complex structures*, Finite Element Anal. Des. 35, pp. 11-140.

[220] Gu, J.,.Ma, Z.D., Hulbert, G.H., 2000, *A new load dependent Ritz vector method for structural dynamic analyses: quasi-static Ritz vector method*, Finite Element Anal. Des. 36, pp. 26-278.

[221] Joo, K.J., Wilson P., Leger P., 1989) *Ritz vectors and generation criteria for mode superposition analysis*, J. Earthquake Eng.Struct. Dyn. 18, pp. 149-167.

[222] Wilson, E.L., Bayo, E.P., 1986, *Use of special Ritz vectors in dynamic substructure analysis*, J. Struct. Eng., 112, pp. 1944-1953.

[223] Gu, J., Ma, Z.D., Hulbert, G.H., 2001, *Quasi-static data recovery for dynamic analyses of structural systems Ritz vector method*, Finite Element Anal. Des., 37. pp. 825–841.

[224] National Aerospace University "KhAI", 2013, *Advanced in composite structures design and simulation*, Institute of Aerospace Engineering , Brno University of Technology IAE-BUT ERA Consortium, 2013, Volume 2, Training modules for researches.

[225] Halme, J., 2002, *Development testing of a composite wing rib*, Thesis - Master of Science in Technology - Helsinki University of Technologie, Finnland.

[226] Farhat, C., Hemezt F.M., 1993, *Updating finite element dynamic models using an element-by-element sensitivity methodology*, AIAA. J., 31,(9), pp. 1702-1711.

[227] Pierre, C., 1988, *Mode localization and eigenvalue loci of bridges with aeroelastic effects*, J. of Engineering Mechanics, 126(3), pp. 485-502.

[228] Balmés, C., 1993, *High modal density, curve veering, localization: a different perspective on the structural response*, J. of Sound and Vibration, 161(2), pp. 358-363.

[229] Bonisoli, E., Delprete, C., Espoito, M., Mottershead, J.E., 2011, *Structural dynamics with coincident eigenvalues: Modeling and Testing*, Modal Analysis topics 3, pp. 325-337.

[230] Du Bois, J.L., Adhikari, S., Lieven, N.A.J., 2009, *Eigenvalue curve veering in stressed structures: An experimental study*, J. of Sound and Vibration, 322, pp. 1117-1124.

Appendix A

Application of the Craig-Bampton MOR method to CFRP

Commands

1. Open and xterm and run matlab

   ```
   ./matlab
   ```

2. load the SDTools environment and set the path for the work directory

   ```
   cd ../toolbox/sdt
   sdtcheck('path');
   cd DLR
   ```

3. Read the UFF58 data and plot the model

   ```
   UFS=ufread('Scan_low.uff');
   modelexp=UFS(1);
   cf=feplot(modelexp);
   cf.def=UFS(2);
   ```

4. Plot the UFF58 data and load the curve-fitting file '05082012low400_t93.mat'

   ```
   idcom(UFS(2))
   ci=iicom('curveload','05082012low400_t93.mat');
   ```

5. On the "idcom properties" window select "Ident" and double click over the frequency in order to visualize the results
6. Save the results in a set

```
defexp28=cf.def;
```

7. Create the TEST set of the sensors

```
TEST.Node = modelexp.Node;
TEST.Elt = modelexp.Elt;
TEST.tdof = defexp28.DOF(:,1);
```

8. Open the FEM model File->Open with the material properties updated using the DOE

```
model_trix6beste_last_01_24.mat
```

9. Plot the FEM model

```
cf=feplot(modelabaq);
```

10. Solve the FEM model (19 modes)

```
defabaq=fe_eig(modelabaq,[5 19 1e3 11]);
```

11. Plot the results

```
feplot(modelabaq,defabaq)
```

12. Define sensors - - -

```
cf=feplot(modelabaq);
cf.mdl=fe_case(cf.mdl,'sensdof','test',TEST);
fecom('curtab Cases','Test');fecom('ProViewOn') %
% fe_sens('basis estimate',cf,'test'); % not needed for coincident mesh
fe_case(cf.mdl,'SensMatch','test')
sens=fe_case(cf.mdl,'sens');
```

13. Define MAC and MAC error of the TEST and full FEM model- - -

```
figure(1);clf;
subplot(211);     %comment this line if you dont want subplots
ii_mac(defexp28,defabaq, ...    % define data
```

```
'sens',sens, ...    % define sensors
'labela','Test','labelb','FEM', ...% set labels
'mac pair plot');   % desired plot for current axes
 subplot(212);ii_mac(1,'mac error');
```

14. Plot COMAC,ECOMAC and S-COMAC of the TEST and full FEM model- - -

```
ii_mac(1,'comac '); %plots all comac's in one graph
ii_mac(1,'comac n'); %plots only COMAC
ii_mac(1,'comac e'); %plots only ECOMAC
ii_mac(1,'comac s'); %plots only SCOMAC
```

15. Plot MACco of the TEST and full FEM model- - - and obtain the table with the data

```
ii_mac(1,'macco 153 plot');
ii_mac(1,'macco 153 table');
```

16. Builds CMS shapes with unit sensor response based on element groups defined in "modelabaq"

```
cf=feplot(modelabaq);
Sel={'Group 3:5';
'Group 1:2'};
mSE=fesuper('SESelAsSE-dispatch',modelabaq,Sel);
feplot(mSE)
feutil('infoelt',mSE)
cf=feplot(mSE);mSE=cf.mdl;
fecom(cf,'curtabModel')
```

17. Define the two superelements, the number of model to solve per superlement and assembly them

```
SE1=stack_get(mSE,'SE','se1','getdata');
SE1=stack_set(SE1,'info','EigOpt',[5 19 1e3 11]);
SE1=fe_reduc('CraigBampton -SE -UseDof',SE1);
cf.Stack{'se1'}=SE1;
SE2=stack_get(mSE,'SE','se2','getdata');
SE2=stack_set(SE2,'info','EigOpt',[5 19 1e3 11]);
```

```
SE2=fe_reduc('CraigBampton -SE -UseDof',SE2);
cf.Stack{'se2'}=SE2;
[m,k,mdof]=fe_mknl(cf.mdl);def=fe_eig({m,k,mdof},[5 19 1e3]);%
```

18. Solve the assembly reduced FEM model

```
defCB=fe_eig(cf.mdl,[5 19 1e3 11]);     % reduced model
```

19. Defined the results of the full FEM model solved below to compare the results of the reduced model

```
dfull=defabaq;
dfull.label='Full'; def.label='Reduced';
cf.def(1)=dfull;
fesuper('sedefinit',cf.mdl); % reinit restitution info
cf.def(2)=fesuper('sedef',cf,def);
fecom(';show2def;ch 7');
```

20. Plot the MAC results of the full and reduced model

```
figure(3);
ii_mac(dfull,cf.def(2),'inda',7:19,'macerrorplot');
```

21. Plot the MAC results of the TEST and reduced model

```
figure(4);
ii_mac(defexp28,cf.def(2), ...
'sens',sens, ...                    % define sensors
'labela','Test','labelb','FEM CB reduce', ...% set labels
'mac pair plot');
```

22. Plot COMAC,ECOMAC and S-COMAC of the TEST and reduced FEM model- - -

```
ii_mac(4,'comac'); %plots all
ii_mac(4,'comac n'); %plots only COMAC
ii_mac(4,'comac e'); %plots only ECOMAC
ii_mac(4,'comac s'); %plots only SCOMAC
```

23. Plot MACco of the TEST and reduced FEM model- - -

```
ii_mac(4,'macco 153 plot');
```

24. For a modal expansion on the basis of the full model, first 12 modes

```
cf=feplot(modelabaq);
cf.mdl=fe_case(cf.mdl,'sensdof','test',TEST);
fecom('curtab Cases','Test');fecom('ProViewOn') %
% fe_sens('basis estimate',cf,'test'); % not needed for coincident mesh
fe_case(cf.mdl,'SensMatch','test')
sens=fe_case(cf.mdl,'sens');
figure(1);clf;
subplot(211);     %comment this line if you dont want subplots
ii_mac(defexp28,defabaq, ...    % define data
'sens',sens, ...    % define sensors
'labela','Test','labelb','FEM', ...% set labels
'mac pair plot');   % desired plot for current axes
 subplot(212);ii_mac(1,'mac error');
dex1 = fe_exp(defexp28,sens,fe_def('subdef',defabaq,7:19));
MACPAIR=ii_mac(1,'macpair'); % get the MACPAIR data to allow sorting
cf.def(1)=dex1;
cf.def(2)=fe_def('subdef',defabaq,MACPAIR.indb);
fecom(';sub1 1;sel1egid>0;show2def;ScaleMatch;ch1');
```

25. For more robustness you will prefer a static expansion builds subspace of static shapes with unit sensor response

```
TR=fe_exp('static',modelabaq,sens);
dex2=fe_exp(defexp28,sens,TR);
cf.def(1)=dex2;
```

26. Using a Reduced Basis Dynamic Expansion (RBDE) combining static and modal expansion the results show an improvement.

```
modelabaq=stack_set(modelabaq,'info','EigOpt',[5 19 1e2]);
modelabaq=fe_mknl(modelabaq);
TR=fe_exp('mode+sens',modelabaq,sens); % basis with modes & static
dex3 = fe_exp('dynamic',defexp28,sens,modelabaq,TR);
cf.def(1)=dex3; fecom(';sel1egid>0;show2def;ch11');
```

27. You could also compute Minimum Dynamic Residual Expansion (MDRE) with

```
dex4 = fe_exp('mdre',defexp28,sens,modelabaq,TR);
```

28. And MDRE with measurement error (MDRE-WE) using

```
opt=struct('type','mdrewe','gamma',1,'MeasErr',.1);
dex5 = fe_exp('mdre',defexp28,sens,modelabaq,TR,opt);
```

29. To visualize the influence of the expansion method on the quality of the correlation you can take a look at the mass wheighted MAC

```
aa = ii_mac(1,'mac pair');
dref = fe_def('subdef',defabaq,aa.indb);
a1=ii_mac(dref,dex1,modelabaq.K{strcmp(modelabaq.Klab,'m')});
a2=ii_mac(dref,dex2,modelabaq.K{strcmp(modelabaq.Klab,'m')});
a3=ii_mac(dref,dex3,modelabaq.K{strcmp(modelabaq.Klab,'m')});
a4=ii_mac(dref,dex4,modelabaq.K{strcmp(modelabaq.Klab,'m')});
a5=ii_mac(dref,dex5,modelabaq.K{strcmp(modelabaq.Klab,'m')});
aa = [(1:size(defexp28.po,1))' defexp28.po(:,1) dref.data(:,1) ...
   (defexp28.po(:,1)./dref.data(:,1)-1)*100 ...
    diag(aa.data(aa.inda,aa.indb)) ...
    diag(a1.data) diag(a2.data) diag(a3.data)  ...
    diag(a4.data) diag(a5.data)];
fprintf(1,' # :  Test   FE    (Delta F , MAC, M-MAC for MOD,  ...
               STA,  DYN,  MDRE, MDRE-WE)\n');
fprintf(1,'%2i : %6.2f %6.2f (%6.1f %%, %4.2f,  %11.2f, %4.2f, ...
               %4.2f ,  %4.2f, %4.2f)\n',aa')
```

30. To illustrate the MAC of the modal mode shape expansion method

```
figure(6);
ii_mac(defexp28,dex1, ...
'sens',sens, ...                    % define sensors
'labela','Test','labelb','dex1', ...% set labels
'mac pair plot')
```

31. Plot MACco of the TEST and mode shape results based on the modal expansion - - -

```
ii_mac(6,'macco 153 plot');
```

32. To visualize the results of the MDRE W/E mode shape expansion method using the MAC

```
figure(7);
ii_mac(defexp28,dex5, ...
'sens',sens, ...                    % define sensors
'labela','Test','labelb','dex5', ...% set labels
'mac pair plot')
```

33. Plot MACco of the TEST and mode shape results based on the MDRE W/E - - -

```
ii_mac(7,'macco 153 plot');
```

34. To import the results from ABAQUS - - -

```
modelaS4=abaqus('read',fullfile('DLR_last_50_S4.inp')); % For reading
            %the models elaborated with S4 elements of ABAQUS
resabaqusS4=abaqus('read DLR_last_50_S4.fil')  % For reading results
cf=feplot(modelaS4);
cf.mdl=stack_set(cf.mdl,a.Stack);
cf.def=stack_get(resabaqusS4,'curve','Mode','get');
            % Displays the results
defnas=cf.def;    % save the results in MATLAB to perform the MAC
```

35. To import the results from MSC/NASTRAN

```
modelnas=nasread(fullfile('MODEL000.dat')); % For reading the models
            %elaborated with CTRIA3 elements of MSC/NASTRAN
cf=feplot(modelnas);                  % For reading results
resnastranCTRIA3=nasread(fullfile('MODEL000.op2'));
cf.mdl=stack_set(cf.mdl,a.Stack);
cf.def=stack_get(resnastranCTRIA3,'curve','OUG(1)','get')
           % Displays the results
defnas=cf.def;   % save the results in MATLAB to perform the MAC
```

36. To import the substructures (SE1) and (SE2) results from ABAQUS - - -

```
modelaS4SE1=abaqus('read',fullfile('DLR_sub1_2.inp')); % For reading
```

```
                % the models elaborated with S4 elements of ABAQUS
        resabaqusSE1S4=abaqus('read DLR_sub1_2.fil')  % For reading results
        cf=feplot(modelaS4SE1);
        cf.mdl=stack_set(cf.mdl,a.Stack);
        cf.def=stack_get( resabaqusSE1S4,'curve','Mode','get');
                % Displays the results
        defabaqusSE1=cf.def;    % save the results in MATLAB to perform the MAC
        modelaS4SE2=abaqus('read',fullfile('DLR_sub2_2.inp')); % For reading
              % the models elaborated with S4 elements of ABAQUS
        resabaqusSE2S4=abaqus('read DLR_sub2_2.fil')  % For reading results
        cf=feplot(modelaS4SE2);
        cf.mdl=stack_set(cf.mdl,a.Stack);
        cf.def=stack_get( resabaqusSE2S4,'curve','Mode','get');
% Displays the results
        defabaqusSE2=cf.def;    % save the results in MATLAB to perform the MAC
```

37. To combine the results files (.odb) of SE1 and SE2 - - -

```
abaqus substructureCombine
baseodb=DLR_sub1_2.odb copyodb=DLR_sub2_2.odb
```

Appendix B

Measures of variation and convergency analysis table

Table B.1 Measures of variation

n	MAC	Mean	Deviation	Deviation Squares	Sample Variance	Population Variance	Sample Sdt deviation	Population Sdt deviation
	(Y_i)	$\bar{x} = \sum_{i=1}^{n} \frac{Y_i}{n}$	$x_i - \bar{x}$	$(x_i - \bar{x})^2$	$s^2 = \frac{\sum (x_i - \bar{x})^2}{n-1}$	$\sigma^2 = \frac{\sum (x_i - \bar{x})^2}{n}$	$s = \sqrt{s^2}$	$\sigma = \sqrt{\sigma^2}$
1	87	81.015625	-5.984375	35.8127441406	10.3648313492	10.2028808594	3.219445814	3.1941948687
2	83	81.015625	-1.984375	3.9377441406				
3	77	81.015625	4.015625	16.1252441406				
4	82	81.015625	-0.984375	0.9689941406				
5	80	81.015625	1.015625	1.0314941406				
6	77	81.015625	4.015625	16.1252441406				
7	83	81.015625	-1.984375	3.9377441406				
8	80	81.015625	1.015625	1.0314941406				
9	83	81.015625	-1.984375	3.9377441406				
10	80	81.015625	1.015625	1.0314941406				
11	87	81.015625	-5.984375	35.8127441406				
12	80	81.015625	1.015625	1.0314941406				
13	82	81.015625	-0.984375	0.9689941406				
14	83	81.015625	-1.984375	3.9377441406				
15	82	81.015625	-0.984375	0.9689941406				
16	80	81.015625	1.015625	1.0314941406				
17	80	81.015625	1.015625	1.0314941406				
18	82	81.015625	-0.984375	0.9689941406				
19	76	81.015625	5.015625	25.1564941406				
20	77	81.015625	4.015625	16.1252441406				
21	83	81.015625	-1.984375	3.9377441406				
22	77	81.015625	4.015625	16.1252441406				
23	84	81.015625	-2.984375	8.9064941406				
24	83	81.015625	-1.984375	3.9377441406				
25	83	81.015625	-1.984375	3.9377441406				
26	84	81.015625	-2.984375	8.9064941406				
27	76	81.015625	5.015625	25.1564941406				
28	84	81.015625	-2.984375	8.9064941406				
29	77	81.015625	4.015625	16.1252441406				
30	83	81.015625	-1.984375	3.9377441406				
31	80	81.015625	1.015625	1.0314941406				
32	87	81.015625	-5.984375	35.8127441406				
33	80	81.015625	1.015625	1.0314941406				
34	84	81.015625	-2.984375	8.9064941406				
35	82	81.015625	-0.984375	0.9689941406				
36	77	81.015625	4.015625	16.1252441406				
37	80	81.015625	1.015625	1.0314941406				
38	77	81.015625	4.015625	16.1252441406				
39	80	81.015625	1.015625	1.0314941406				
40	87	81.015625	-5.984375	35.8127441406				
41	87	81.015625	-5.984375	35.8127441406				
42	77	81.015625	4.015625	16.1252441406				
43	82	81.015625	-0.984375	0.9689941406				
44	83	81.015625	-1.984375	3.9377441406				
45	80	81.015625	1.015625	1.0314941406				
46	77	81.015625	4.015625	16.1252441406				
47	83	81.015625	-1.984375	3.9377441406				
48	80	81.015625	1.015625	1.0314941406				
49	82	81.015625	-0.984375	0.9689941406				
50	87	81.015625	-5.984375	35.8127441406				
51	76	81.015625	5.015625	25.1564941406				
52	76	81.015625	5.015625	25.1564941406				
53	80	81.015625	1.015625	1.0314941406				
54	80	81.015625	1.015625	1.0314941406				
55	80	81.015625	1.015625	1.0314941406				
56	80	81.015625	1.015625	1.0314941406				
57	80	81.015625	1.015625	1.0314941406				
58	83	81.015625	-1.984375	3.9377441406				
59	87	81.015625	-5.984375	35.8127441406				
60	83	81.015625	-1.984375	3.9377441406				
61	82	81.015625	-0.984375	0.9689941406				
62	77	81.015625	4.015625	16.1252441406				
63	77	81.015625	4.015625	16.1252441406				
64	77	81.015625	4.015625	16.1252441406				
TOTAL Seq-SS= 652.984375								

Table B.2 Convergency study

Number of modes	Model 1 (Hz)	Model 2 (Hz)	Model 3 (Hz)	Difference freq. between Model 2 and 3 (Hz)
1	0	0	0	0
2	0	0	0	0
3	0.0012729527	0.0004512738	0.0003519775	-9.929623470819E-005
4	2.5650192583	0.4447173721	0.4447174399	6.78922330021869E-008
5	9.1855606633	1.2193482986	1.2193483154	1.67655800353828E-008
6	16.4788259642	1.9084835158	1.9084835855	6.97161202101171E-008
7	60.4085607205	57.2178522019	57.2181616045	0.0003094026
8	107.7434653919	106.0159913306	106.0184422224	0.0024508918
9	166.7078574294	167.4985180386	167.5218453579	0.0233273194
10	192.6007901701	168.1976908574	168.2031420071	0.0054511497
11	195.452878994	234.9896215835	235.0211598418	0.0315382584
12	207.4931981416	236.8306882202	236.8500881865	0.0193999663
13	229.1223916842	315.2561192208	315.2674816416	0.0113624208
14	243.1205995801	323.9287505984	324.3403208829	0.4115702845
15	300.4433670183	401.7150658411	401.7304660224	0.0154001814
16	345.6052106178	408.3878011355	408.3942114787	0.0064103432
17	384.3258236379	432.8885476722	432.9249702757	0.0364226035
18	397.5621368247	494.9042950249	495.4830440677	0.5787490428
19	414.7216741893	497.0441353055	497.3161125824	0.2719772769
20	426.3092317864	516.1119223113	516.1483706648	0.0364483535
21	484.3597917079	538.8484163481	539.1718926797	0.3234763316
22	497.9132277383	559.4688846108	559.8701067416	0.4012221308
23	502.4682935927	571.8477206668	572.5122739163	0.6645532495
24	550.5428900724	607.0379437768	607.1836493824	0.1457056056
25	587.2431759991	637.2919994683	637.4869340054	0.1949345371
26	599.5882173013	657.0620962248	658.1772876822	1.1151914573
27	612.0467461313	678.44378711	678.6585405308	0.2147534208
28	644.89596893	787.1232434896	789.5251746558	2.4019311662
29	659.4420887743	812.0220887311	813.7280456256	1.7059568945
30	681.2319790825	814.7483875678	855.8979941898	41.1496066219
31	701.4119773232	861.9419311451	867.716208024	5.7742768789
32	736.5842818786	882.3213852278	925.010342533	42.6889573052
33	762.3561437471	921.4069644664	967.7265909906	46.3196265242
34	793.8250416075	956.1984250517	978.1945915349	21.9961664831
35	803.9829606929	977.9572102022	987.6882273925	9.7310171903
36	814.2767883673	987.4871169665	997.1924163561	9.7052993896
37	848.2223485374	1012.3846260879	1044.8036854477	32.4190593598
38	913.2628353651	1044.4278431115	1061.0609559657	16.6331128543
39	920.0285070041	1051.4588840045	1096.8897475447	45.4308635402
40	939.1487940712	1085.7627404262	1124.1677418063	38.4050013801
41	1024.8452060772	1121.6546369128	1159.8478194585	38.1931825458
42	1056.9846787635	1145.5531350058	1163.1853289448	17.632193939
43	1077.0286817295	1157.0920876494	1172.3023246902	15.2102370407
44	1085.563416768	1159.7375423798	1187.6238635953	27.8863212155
45	1100.3969726275	1182.8260424836	1192.0208351697	9.1947926861
46	1110.0066767565	1190.0286307633	1213.9878414301	23.9592106668
47	1125.7039933897	1206.4925513149	1224.8275272976	18.3349759826
48	1134.94869145	1213.5287710594	1239.190996954	25.6622258946
49	1142.9358981706	1223.2325554209	1263.1736944486	39.9411390277
50	1162.1798118818	1234.1711859284	1298.4658344078	64.2946484793

Appendix C

Substructuring in ABAQUS and DOE analysis of parameters

It initially was applied and generated to the substructures using ABAQUS, before applying the CBMOR using Ritz vectors methodology developed by Balmès in MATLAB.

A DOE methodology was also used to obtain the qualitative and quantitative parameters of the CFRP introduced in Chapter 2 using a MNET. The stages of the MNET study established in this research were: experimental measurements, elaboration of FE models, DOE, and different MCC. The same MNET methodology was used with the small difference that was performed as

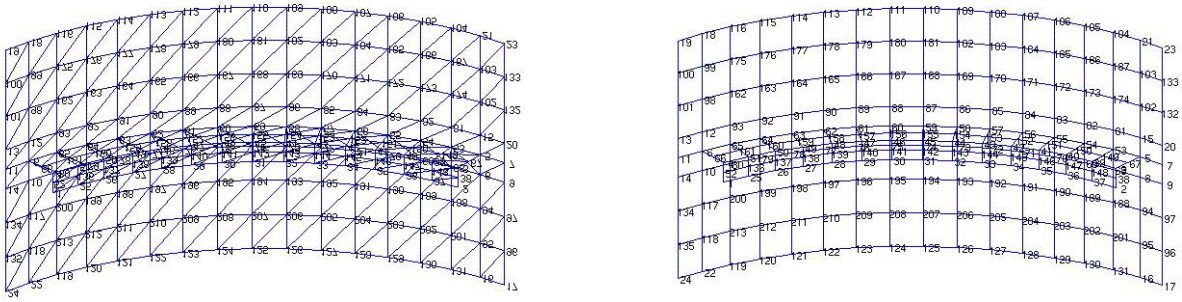

(a) Full FE model S3. (b) Full FE model S4.

Fig. C.1 Initial FE models used to generate substructures.

additional step for the number of factors: a fractional factorial design [145]. This is the main

difference between the study presented in this work using the CBMOR methodology established in SDTools versus the CBMOR methodology established in ABAQUS in Appendix 3.

	C5	C6	C7	C8	C9	C10	C11	C12	C13	C14
	Thickness1	Angle	Thickness2	Density	Substructures	Nodexsubstr	Gshear	E1	Numberplies	Lenght1
1	1,6	22,5	3,5	1300	0	12	375	1,80000E+11	6	8,4
2	4,8	22,5	3,5	1300	0	4	125	6,00000E+10	2	8,4
3	1,6	67,5	3,5	1300	0	4	125	6,00000E+10	6	2,8
4	4,8	67,5	3,5	1300	0	12	375	1,80000E+11	2	2,8
5	1,6	22,5	10,5	1300	0	4	125	1,80000E+11	2	2,8
6	4,8	22,5	10,5	1300	0	12	375	6,00000E+10	6	2,8
7	1,6	67,5	10,5	1300	0	12	375	6,00000E+10	2	8,4
8	4,8	67,5	10,5	1300	0	4	125	1,80000E+11	6	8,4
9	1,6	22,5	3,5	3900	0	4	375	6,00000E+10	2	2,8
10	4,8	22,5	3,5	3900	0	12	125	1,80000E+11	6	2,8
11	1,6	67,5	3,5	3900	0	12	125	1,80000E+11	2	8,4
12	4,8	67,5	3,5	3900	0	4	375	6,00000E+10	6	8,4
13	1,6	22,5	10,5	3900	0	12	125	6,00000E+10	6	8,4
14	4,8	22,5	10,5	3900	0	4	375	1,80000E+11	2	8,4
15	1,6	67,5	10,5	3900	0	4	375	1,80000E+11	6	2,8
16	4,8	67,5	10,5	3900	0	12	125	6,00000E+10	2	2,8
17	1,6	22,5	3,5	1300	4	12	125	6,00000E+10	2	2,8
18	4,8	22,5	3,5	1300	4	4	375	1,80000E+11	6	2,8
19	1,6	67,5	3,5	1300	4	4	375	1,80000E+11	2	8,4
20	4,8	67,5	3,5	1300	4	12	125	6,00000E+10	6	8,4
21	1,6	22,5	10,5	1300	4	4	375	6,00000E+10	6	8,4
22	4,8	22,5	10,5	1300	4	12	125	1,80000E+11	2	8,4
23	1,6	67,5	10,5	1300	4	12	125	1,80000E+11	6	2,8
24	4,8	67,5	10,5	1300	4	4	375	6,00000E+10	2	2,8
25	1,6	22,5	3,5	3900	4	4	125	1,80000E+11	6	8,4
26	4,8	22,5	3,5	3900	4	12	375	6,00000E+10	2	8,4
27	1,6	67,5	3,5	3900	4	12	375	6,00000E+10	6	2,8
28	4,8	67,5	3,5	3900	4	4	125	1,80000E+11	2	2,8
29	1,6	22,5	10,5	3900	4	12	375	1,80000E+11	2	2,8
30	4,8	22,5	10,5	3900	4	4	125	6,00000E+10	6	2,8
31	1,6	67,5	10,5	3900	4	4	125	6,00000E+10	2	8,4
32	4,8	67,5	10,5	3900	4	12	375	1,80000E+11	6	8,4

Fig. C.2 Parameters .

The experimental measurements used were established in section Chapter 4, see Fig. 4.3. The number of sensors are displayed in Fig. C.3. Two FE models were elaborated using shells elements (quadrilaterals and triangles), (see Fig. C.1 for comparative purposes).

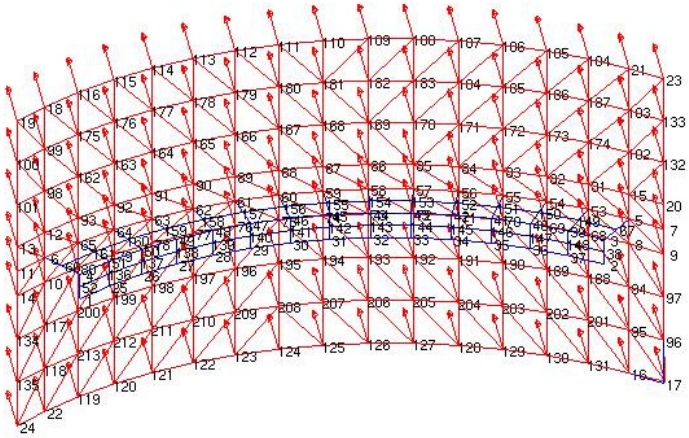

Fig. C.3 FEM model and sensors.

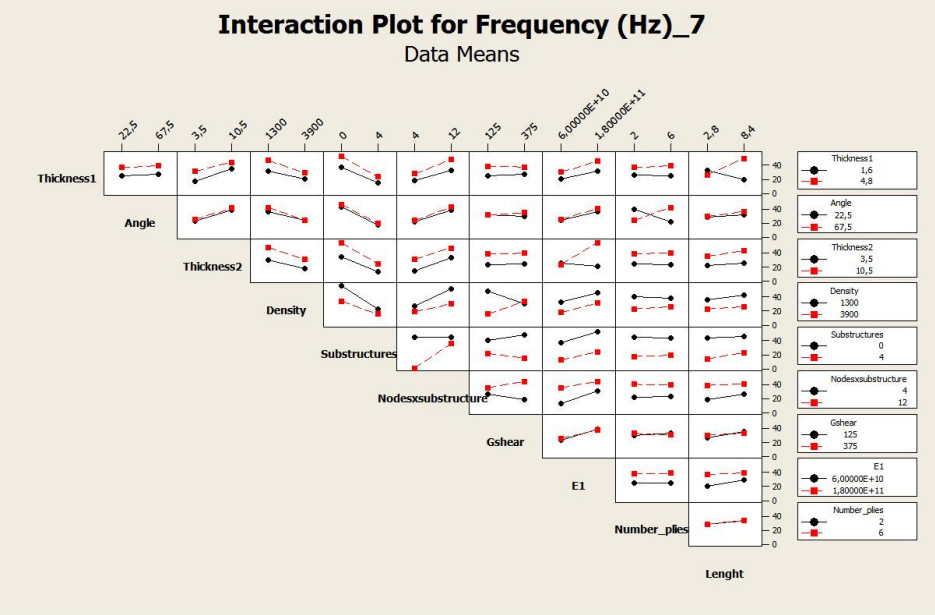

Fig. C.4 Full Interaction.

A total of 10 parameters were evaluated including some geometrical parts[1]. However, the DOE array performed was a reduced full factorial 2^{10-5} for the number of parameters to analyze the CFRP using the CBMOR. The main advantage of the reduced full factorial is to reduce the number of runs of the main parameters.

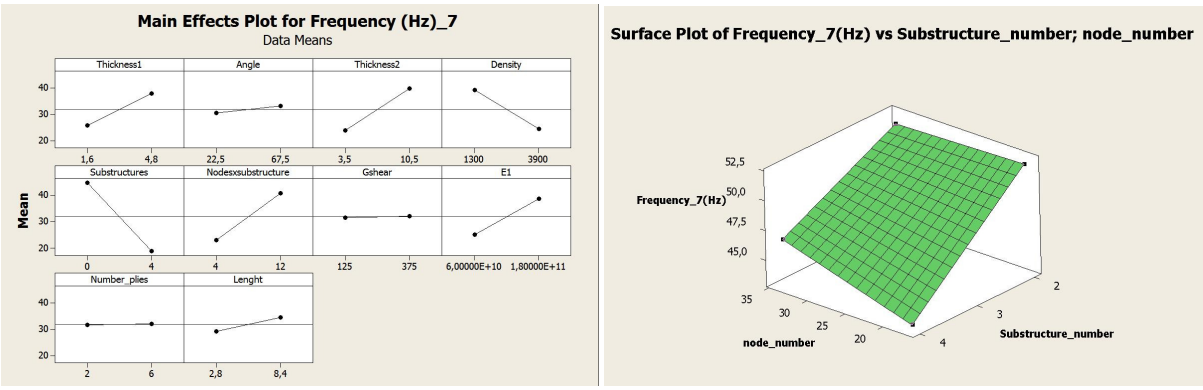

(a) Main Effects.

(b) Full FE model S4.

Fig. C.5 Main effects and Surface response - nodes × substructure.

[1]The two thicknesses are displayed in Table 4.11. The lenght is related to the rib in the center of the CFRP. A number of nodes and substructures are displayed in Fig. C.5a and included in the electronic files.

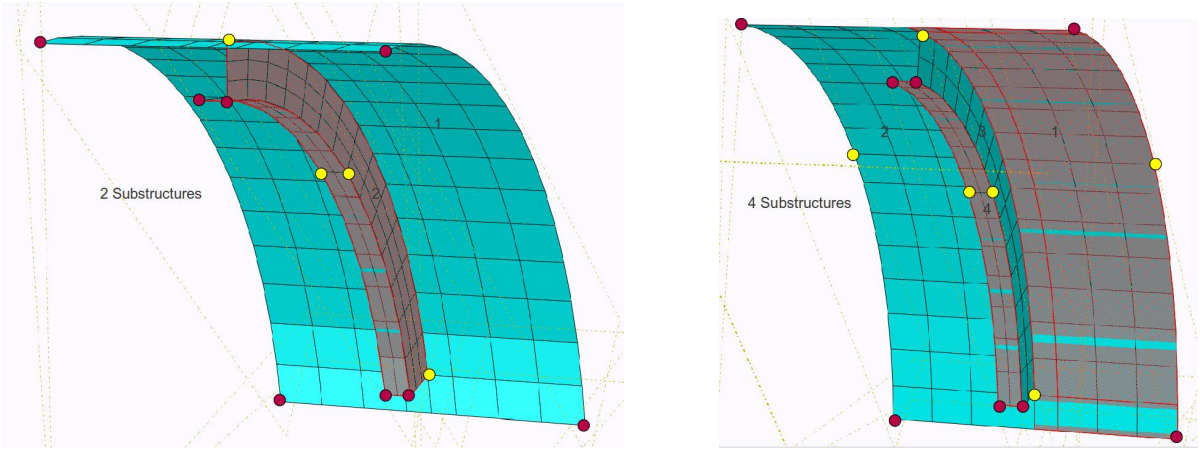

(a) Two substructures and selected nodes .

(b) Four substructures and selected nodes.

Fig. C.6 Nodes used in the substructures (in red and yellow) and substructures (grey and cyan) analyzed with ABAQUS.

The main disadvantage was that some interactions can be mixed and it is not possible to obtain an accurate approximation. Fig. C.5a shows the main effects are identified through the slope generated due to the eigenfrequency values between the limits defined for each parameter – a bigger slope means a strong parameter effect. The upper and lower limits are displayed in Fig. C.2.

The results shown in Fig. C.5 (vertical left side) are eigenfrequencies. The Young's modulus, density, number of nodes and substructure parameters have a strong influence reflected in the slope, (see Figs. C.4 and C.5a). Once we have selected the main parameters based on the DOE-screening, can be obtained a surface response, (see Fig. C.5b), that help us find the best model for the parameter limits selected. Several reduced full factorial were performed changing the number of nodes and substructures to improve the MAC response. The MAC correlation between the full FE model and experimental measurement was useful to validate the MOR results, (see Fig. 5.1c).

The MAC results of the reduced model (substructure 1) evaluating S4 elements are displayed in Fig. C.7 using the material properties of Table 4.11. It is possible to observe some mode shapes of the superlements in Figs. C.8 and C.9 respectively. Due to the lower MAC values obtained and the considerably time spend after several reduced full factorials using ABAQUS, then was proposed to use other elements with similar finite element properties and AMLS methodology introduced in Chapter 3 to compare results. The finite element properties of Table

Table C.1 MAC results with material properties of Table 4.11 of SE1 vs. experimental measurements.

	EXPERIMENTAL (Hz)		SE1 ABAQUS (Hz)	DF/FA %	MAC
1	49.243	8	58.518	18.8	99
2	92.265	10	108.26	17.3	96
3	93.756	10	108.26	15.5	89
4	145.29	11	173	19.1	55
5	160.05	11	173	8.1	61
6	164.18	7	30.644	-81.3	75
7	226.36	13	249.62	10.3	57
8	243.4	13	249.62	2.6	42
9	307.33	16	321.53	4.6	34
10	314.18	12	176.55	-43.8	24
11	324.83	17	343.14	5.6	73
12	329.67	17	343.14	4.1	86

4.11 were obtained applying a DOE using pshell elements in MATLAB-SDTools. The change of finite elements was essential to obtain improvement in the results. The same number of mode pairs were calculated per substructure (19 mode pairs) for illustrative purposes.

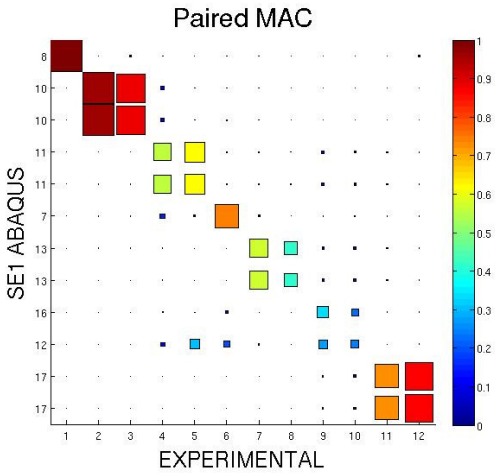

Fig. C.7 MAC of SE1 using substructuring in ABAQUS vs. experimental measurements.

The Table C.2 displays the results obtained per superlement and the combination of both superelements for the coarse mesh. The combination of results was performed with the *abaqus substructureCombine* command. The best response obtained with ABAQUS was calculated

Table C.2 Eigenfrequencies results with material properties of Table 4.11 of SE1, SE2 and combination.

	SE1 (Hz)	SE2 (Hz)	SE1 + SE 2 (Hz)
1	0	0	0
2	0	0	0
3	0	0	0
4	2.96198E-04	2.34027E-04	4.71645E-05
5	7.91667E-04	2.76216E-04	9.75939E-05
6	1.00950E-03	3.17778E-04	1.24310E-04
7	30.644	246.03	59.501
8	58.518	290.76	109.53
9	88.115	418.54	124.09
10	108.26	452.94	176.38
11	173.00	644.52	204.92
12	176.55	889.65	241.88
13	249.62	946.22	243.77
14	285.85	1037.1	252.65
15	321.20	1171.0	258.02
16	321.53	1514.9	301.74
17	343.14	1687.5	343.88
18	423.18	1890.1	355.86
19	460.84	1960.7	371.83

with two super-elements and 43 nodes distributed in both superelements. In Fig. 5.1c one can observe the MAC results increasing the number of nodes.

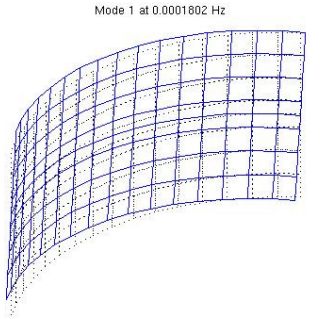

(a) Mode 1=0 Hz.

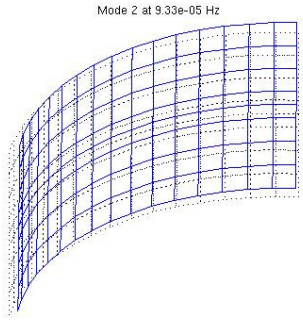

(b) Mode 2=0 Hz.

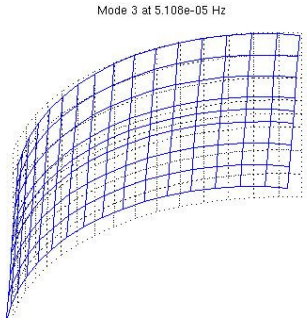

(c) Mode 3=0 Hz.

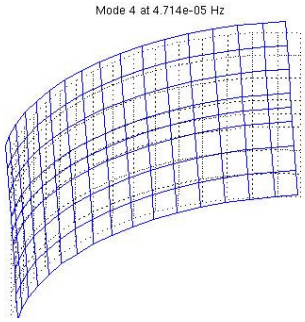

(d) Mode 4 = 2.96198E-04 Hz.

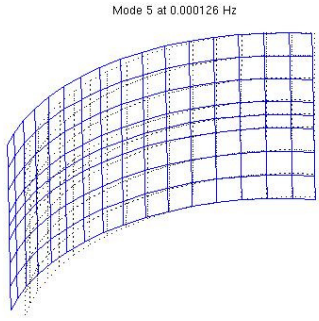

(e) Mode 5= 7.91667E-04 Hz.

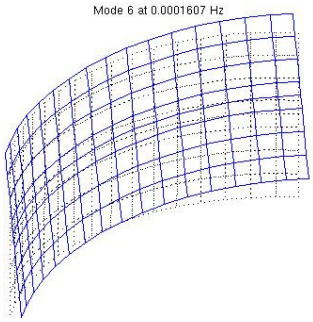

(f) Mode 6=1.00950E-03 Hz.

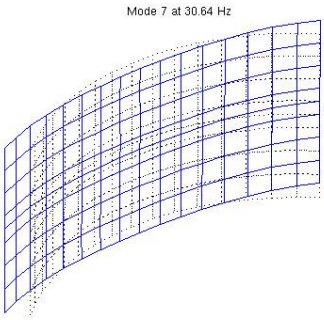

(g) Mode 7=30.644 Hz.

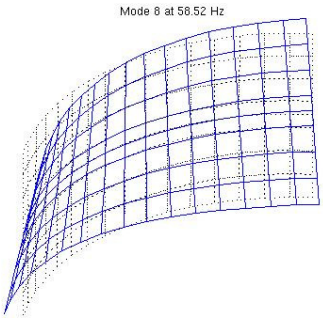

(h) Mode 8=58.518 Hz.

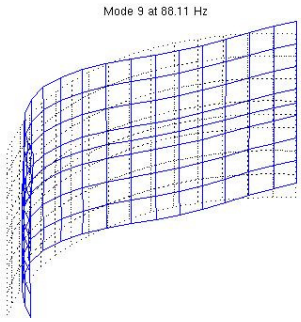

(i) Mode 9=88.115 Hz.

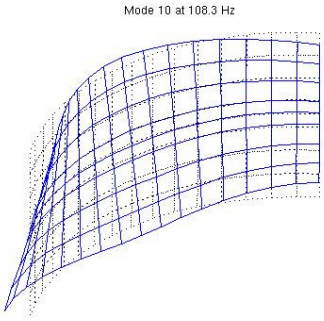

(j) Mode 10=108.26 Hz.

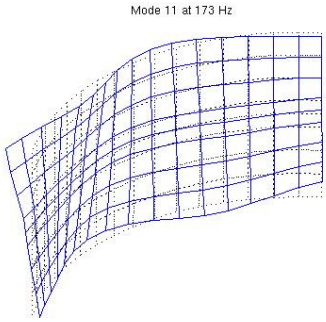

(k) Mode 11=173.00 Hz.

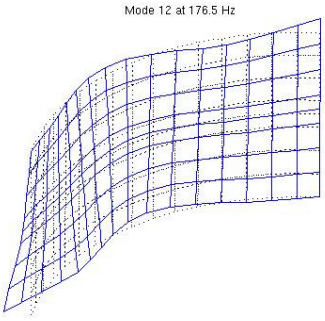

(l) Mode 12=176.55 Hz.

Fig. C.8 SE 1 free-free.

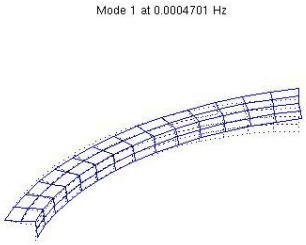

(a) Mode 1=0 Hz.

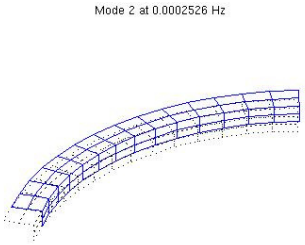

(b) Mode 2=0 Hz.

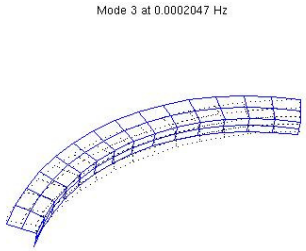

(c) Mode 3=0 Hz.

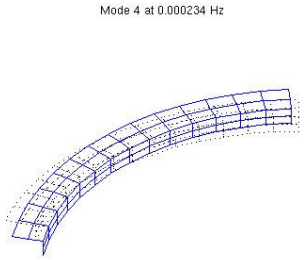

(d) Mode 4 = 2.34027E-04 Hz.

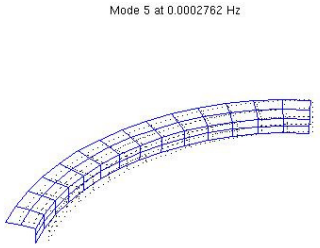

(e) Mode 5=2.76216E-04 Hz.

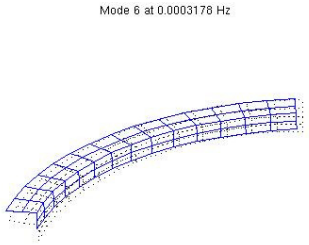

(f) Mode 6=3.17778E-04 Hz.

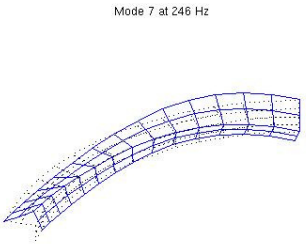

(g) Mode 7=246.03 Hz.

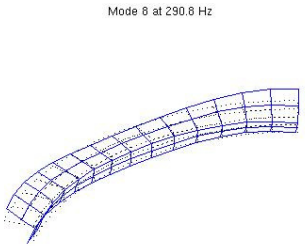

(h) Mode 8=290.76 Hz.

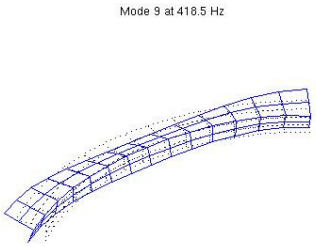

(i) Mode 9=418.54 Hz.

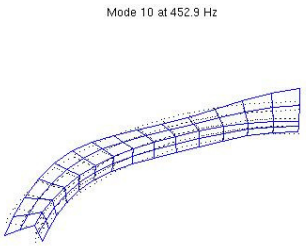

(j) Mode 10=452.94 Hz.

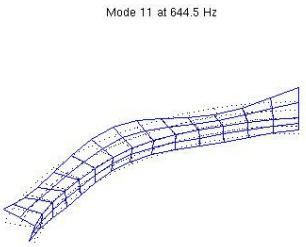

(k) Mode 11=644.52 Hz.

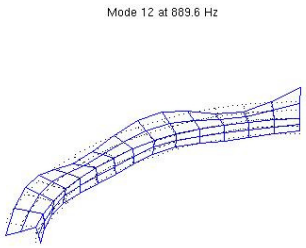

(l) Mode 12=889.65 Hz.

Fig. C.9 SE 2 free-free.

Appendix D

Product data of the raw materials used in the elaboration of the CFRP

Link- Araldite Ly 564 / Aradur 2954 source:
http://www.mouldlife.net/ekmps/shops/mouldlife/resources/Other/araldite-ly564-aradur-2954-eur-e-1-.pdf
Link- C-faser-Gewebe source:
http://www.hadeg-recycling.de/c-faser-gewebe.php
Link- IM7 HexTow source:
https://compositeenvisions.com/documents/tds/Model-f-1647-hexcel-im7-tds.pdf
Link- HexMC Moulding concept source:
http://info.lindberg-lund.no/produktblad/Tekniske datablad/HEXMC-M77-TD.pdf
Link- Saertex Multi-Axial-Gelege source:
http://alumag.com/wp-content/uploads/2013/11/RCOM11.2011SAERTEXLecture.pdf

Appendix E

Sensibility comparison using CLT and FSDT vs. Exp. measurements

The Discrete Kirchhoff (DK) constraint, which refers to the satisfaction of the Kirchhoff constraint at discrete points on the shell surface, is imposed in all thin shell elements in ABAQUS. For element type STRI3 the constraint is imposed analytically and involves no transverse shear strain energy calculation. Solutions obtained with these elements converge to those corresponding to classical shell theory, see ABAQUS theory manual section 3.6.1 shell element overview.

In Abaqus/Standard curved elements (STRI65, S8R5, S9R5) are preferable for modeling bending of a thin curved shell. Element type STRI3 is a flat facet element. If this element

Table E.1 Raw elastic mechanical properties C-faser-gewebe, see Appendix D.(*th=thickness)

Part 1(m)	***Modulus***	***E(GPa)***	***ν* (-)**	**Shear**	***G(GPa)***	***ρ*** (Kgm^{-3})
**th=0.0035*	E_1	68.0	0.3	G_1	5	2600
	E_2	68.0	0.3	G_2	5	
				G_3	5	
Part 2(m)	***Modulus***	***E(GPa)***	***ν* (-)**	**Shear**	***G(GPa)***	***ρ*** (Kgm^{-3})
**th=0.007*	E_1	68.0	0.3	G_1	5	1500
	E_2	68.0	0.3	G_2	5	
				G_3	5	
Part 3(m)	***Modulus***	***E(GPa)***	***ν*(-)**	**Shear**	***G(GPa)***	***ρ*** (Kgm^{-3})
**th=0.0035*	E_1	68.0	0.3	G_1	5	1500
	E_2	68.0	0.3	G_2	5	
				G_3	5	

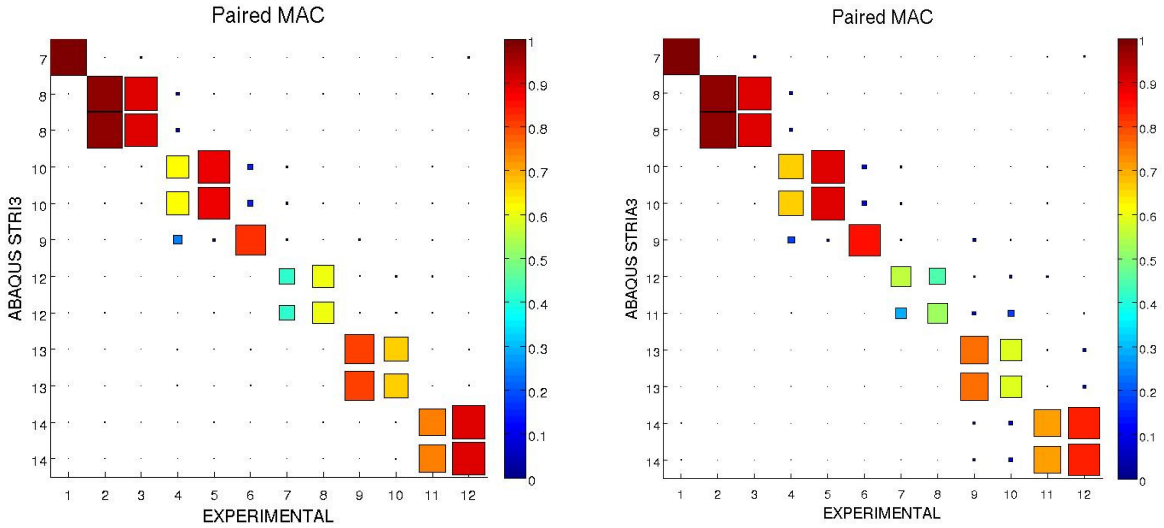

(a) Updated stiffness parameters.

(b) Raw stiffness parameters.

Fig. E.1 MAC sensibility comparison based on CLT(STRI3) vs. experimental measurements: a) Updated stiffness parameters (see Table 4.11) b) Raw stiffness parameters (see Table E.1).

Table E.2 MAC sensibility comparison based on CLT(STRI3) vs. experimental measurements: left side: Updated stiffness parameters (see Table 4.11) right side: Raw stiffness parameters (see Table E.1).

		CLT (STRI3)				CLT(STRI3)			
ID	Test (Hz)	ID	FE model (Hz)	DF/FA %	MAC	ID	FE model (Hz)	DF/FA %	MAC
1	49.243	7	60.581	23.0	99	7	51.613	4.8	99
2	92.265	8	109.23	18.4	97	8	93.691	1.5	97
3	93.756	8	109.23	16.5	90	8	93.691	-0.1	90
4	145.29	10	171.39	18.0	62	10	148.02	1.9	67
5	160.05	10	171.39	7.1	89	10	148.02	-7.5	90
6	164.18	9	158.99	-3.2	82	9	146.75	-10.6	86
7	226.36	12	239.04	5.6	42	12	208.66	-7.8	56
8	243.4	12	239.04	-1.8	60	11	203.72	-16.3	53
9	307.33	13	309.01	0.5	81	13	277.48	-9.7	75
10	314.18	13	309.01	-1.6	67	13	277.48	-11.7	59
11	324.83	14	317.63	-2.2	75	14	281.3	-13.4	72
12	329.67	14	317.63	-3.7	90	14	281.3	-14.7	84

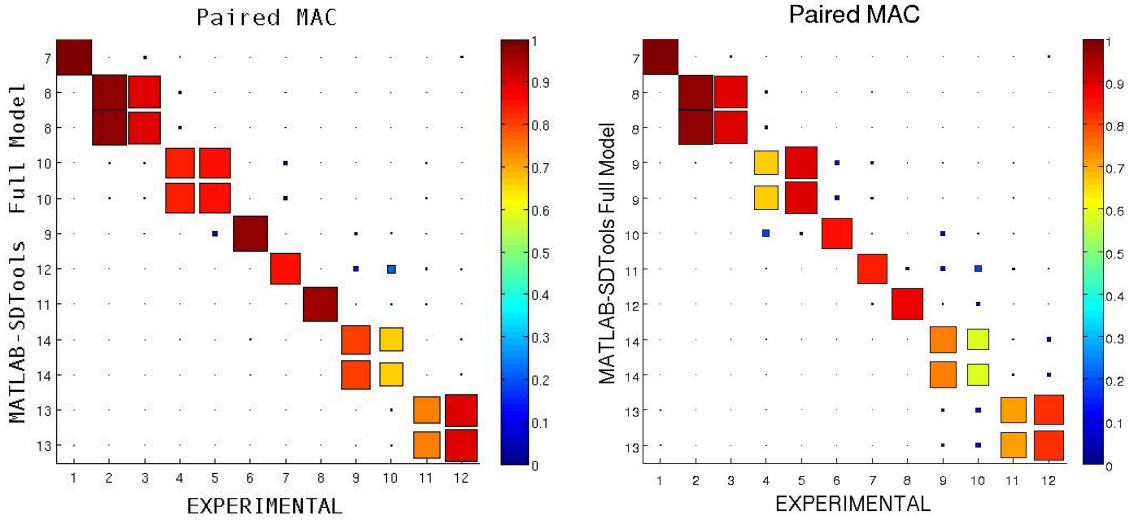

(a) Updated stiffness parameters.

(b) Raw stiffness parameters.

Fig. E.2 MAC sensibility comparison based on FSDT(pshell) vs. experimental measurements: a) Updated stiffness parameters (see Table 4.11) b) Raw stiffness parameters (see Table E.1).

Table E.3 MAC sensibility comparison based on FSDT(pshell) vs. experimental measurements: left side: Updated stiffness parameters (see Table 4.11) right side: Raw stiffness parameters (see Table E.1).

		FSDT (pshell)				FSDT(pshell)			
ID	Test (Hz)	ID	FE model (Hz)	DF/FA %	MAC	ID	FE model (Hz)	DF/FA %	MAC
1	49.243	7	57.218	16.2	100	7	48.953	-0.6	99
2	92.265	8	106.02	14.9	97	8	91.379	-1.0	97
3	93.756	8	106.02	13.1	90	8	91.379	-2.5	90
4	145.29	10	168.2	15.8	83	9	145.95	0.5	67
5	160.05	10	168.2	5.1	86	9	145.95	-8.8	90
6	164.18	9	167.5	2.0	98	10	154.16	-6.1	85
7	226.36	12	236.83	4.6	86	11	207.34	-8.4	83
8	243.4	11	234.99	-3.5	96	12	208.53	-14.3	88
9	307.33	14	323.93	5.4	81	14	291.79	-5.1	74
10	314.18	14	323.93	3.1	66	14	291.79	-7.1	58
11	324.83	13	315.26	-2.9	74	13	281.28	-13.4	71
12	329.67	13	315.26	-4.4	90	13	281.28	-14.7	83

is used to model bending of a curved shell, a dense mesh may be required to obtain accurate results, see ABAQUS analysis user's manual section 25.6.2 choosing a shell element.

It can be appreciated in Tables E.2 and E.3 the difference in frequency between the updated and the raw stiffness parameters based on the laminate theory (CLT or FSDT) using the STRI3 elements in ABAQUS and the pshell in MATLAB-SDTools respectively. Using the raw stiffness parametes for both laminate theory the difference between the experimental and analytical eigenfrequencies obtained is not bigger than 5 %. However, it is observed that the difference increase in the eigenfrequencies using the updated stiffness parameters in both laminate theories represented in each element formulation according the ABAQUS theory manual section 3.6.1. It is necesary to highlight the poor MAC correlation in paired modes 4^{th}, 7^{th}, 8^{th}, and 10^{th} using the CLT theory with the raw or updated stiffness parameters, (see Fig. E.1).

Furthermore, it is observed an inverse behaviour in the eigenfrequencies with the CLT and/or FSDT comparing the updated stiffness parameters obtained with the MNET versus the raw stiffness parameters, see Tables E.2 and E.3. Thus, it is displayed and improvement in the MAC correlation values based on the FSDT, see paired modes 4^{th}, 7^{th}, 8^{th}, and 10^{th} with the updated stiffness parameters, however it is observed a bigger difference in the first fourth eigenfrequencies. Based on the updated stiffness parameters versus raw stiffness parameters comparing the CLT and FSDT, it is observed a good eigenfrequency in the first paired modes using the CLT and a poor MAC correlation sensitivity in the paired modes 4^{th}, and from 6^{th} to 8^{th} respect to the FSDT.

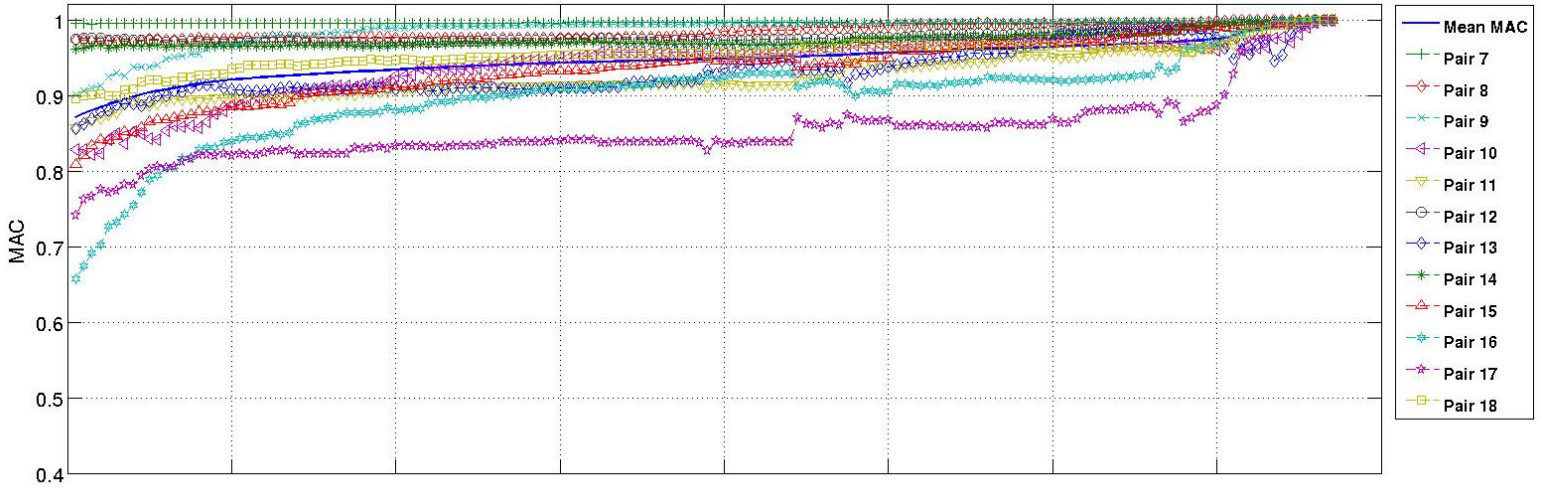

(a)

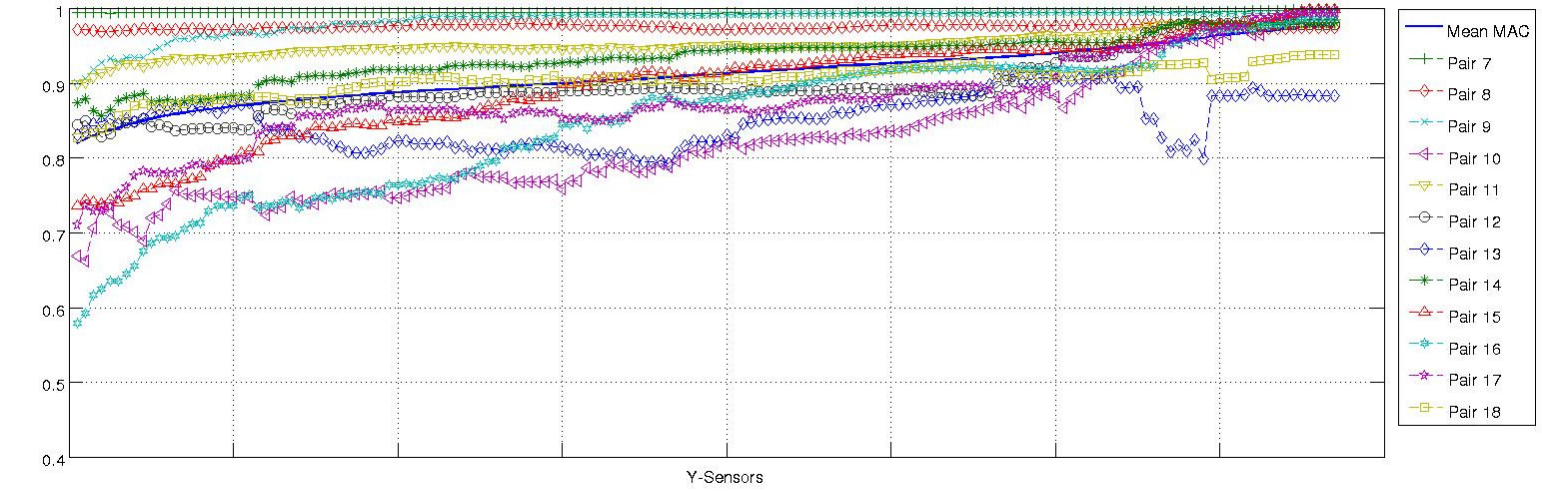

(b)

Fig. E.3 Comparison of MACco based on FSDT using FE model(pshell) vs. Exp.: a) SDTools updated b) SDTools raw material data C-faser-gewebe.

Appendix F

Modeling of composite component assembly (CFRP)

Composites can be modeled using single layer shells, multi-layer shells (continuum shells) and/or solids. Majority of real life parts are modeled with single layer shells elements. Analysis of composite shells is very similar to the solution of standard shell elements. A single shell element is modeled as composite by assigning a composite property (e.g. PCOMP) to it [148].

PCOMP defines the structure properties of a composite lay-up which is then assigned to an element. The ply is only defined for that particular property and there is not relationship of a ply that is common across several properties [148].

Composite materials properties in general are modeled with an orthotropic material model (e.g. MAT8- MSC/NASTRAN solver). The typical material model used for composites is MAT8, which is planar orthotropic material [148].

The parameters for modeling composites defined in MAT8 consist of: the number of plies, matrix and core (HOMOGENIZATION), the material coordinate system to establish the reference for defining the ply angle, the element normal to establish the reference for defining ply stacking and the individual laminate property (PCOMP) introduced in Chapter 1, section 1.2. PCOMP defines all the laminate properties like ply material, thickness (number of plies), ply angle, orientation and also the stacking sequence and order in ONE property card defined. Each ply is associated with a material property. The use of MAT1 or general anostropic MAT2 for ply properties is also available [148].

The definition of material properties, MAT8 in MATLAB-SDTools and MSC/NASTRAN is established in the Table F.1.

Table F.1 Ply-Based Laminate Modeling Concept

(1)	(2)	(3)	(4)	(5)	(6)	(7)	(8)	(9)	(10)
PCOMP	PID	Z0	NSM	SB	d	TREF	GE	LAM	
	MID1	T1	THETA1	SOUT1	MID2	T2	THETA2	SOUT2	
	MID3	T3	THETA3	SOUT3	MID4	etc			

The description of the composite card follows the NASTRAN's PCOMP format as following:

- ProID Type Z0 NSM SB d TREF GE f MatId1 T1 THETA1 SOUT1 ...
- ProID Type: $fe_{mat}('pshell','SI',2)$
- Z0: distance from the reference plane to the bottom surface default -(total thickness)/2
- NSM : non structural mass per unit area
- SB: allowable shear stress (unused)
- d: -1 no drilling stiffness, If d==0 d is set to 1. d>0 drilling DOF stiffness coefficient
- TREF: reference temperature (unused)
- GE: loss factor
- LAM: formulation
- MatID1: material idenfier for the layer (ply number)
- T1 : Layer thickness
- THETA1: Ply angle orientation
- SOUT1 layer options (unused)
- k : shear factor (default value is 5/6)
- $12I/T^3$: Ratio of bending moment of inertia to nominal $T^3/12$ (default 1)

Element's normal direction defines the stacking sequence. Plies are listed from the bottom surface upwards, with respect to the element's normal direction.

The material orientation is important to estalish the reference for ply angles. Ply angles can be specified relative to a:

- Element coordinate system,
- Vector projeted onto elements,

Table F.2 Nastran Property 1 : LAMINATE Property

(1)	(2)	(3)	(4)	(5)	(6)	(7)	(8)	(9)	(10)
PCOMP	1	0	NSM	SB	d	TREF	GE	LAM	
+	2	2.5E-4	-45	YES	2	2.5E-4	45.	YES+	
+	2	2.5E-4	-45	YES	2	2.5E-4	45.	YES+	
+	2	2.5E-4	-45	YES	2	2.5E-4	45.	YES+	
+	2	2.5E-4	-45	YES	2	2.5E-4	45.	YES	

Table F.3 Nastran Property 2 : LAMINATE Property

(1)	(2)	(3)	(4)	(5)	(6)	(7)	(8)	(9)	(10)
PCOMP	2	0	NSM	SB	d	TREF	GE	LAM	
+	2	4.E-4	-45	YES	2	4.E-4	45.	YES+	
+	2	4.E-4	-45	YES	2	4.E-4	45.	YES+	
+	2	4.E-4	-45	YES	2	4.E-4	45.	YES+	
+	2	4.E-4	-45	YES	2	4.E-4	45.	YES	

Table F.4 Nastran Property 3 : LAMINATE Property

(1)	(2)	(3)	(4)	(5)	(6)	(7)	(8)	(9)	(10)
PCOMP	3	0	NSM	SB	d	TREF	GE	LAM	
+	1	4.E-4	-45	YES	1	4.E-4	45.	YES+	
+	1	4.E-4	-45	YES	1	4.E-4	45.	YES+	
+	1	4.E-4	-45	YES	1	4.E-4	45.	YES+	
+	1	4.E-4	-45	YES	1	4.E-4	45.	YES	

Table F.5 Nastran Property 4 : LAMINATE Property

(1)	(2)	(3)	(4)	(5)	(6)	(7)	(8)	(9)	(10)
PCOMP	4	0	NSM	SB	d	TREF	GE	LAM	
+	3	4.375E-4	-45	YES	3	4.375E-4	45.	YES+	
+	3	4.375E-4	-45	YES	3	4.375E-4	45.	YES+	
+	3	4.375E-4	-45	YES	3	4.375E-4	45.	YES+	
+	3	4.375E-4	-45	YES	3	4.375E-4	45.	YES+	
+	3	4.375E-4	-45	YES	3	4.375E-4	45.	YES+	
+	3	4.375E-4	-45	YES	3	4.375E-4	45.	YES+	
+	3	4.375E-4	-45	YES	3	4.375E-4	45.	YES+	
+	3	4.375E-4	-45	YES	3	4.375E-4	45.	YES	

Table F.6 Nastran Property 5 : LAMINATE Property

(1)	(2)	(3)	(4)	(5)	(6)	(7)	(8)	(9)	(10)
PCOMP	5	0	NSM	SB	d	TREF	GE	LAM	
+	3	4.375E-4	-45	YES	3	4.375E-4	45.	YES+	
+	3	4.375E-4	-45	YES	3	4.375E-4	45.	YES+	
+	3	4.375E-4	-45	YES	3	4.375E-4	45.	YES+	
+	3	4.375E-4	-45	YES	3	4.375E-4	45.	YES+	
+	3	4.375E-4	-45	YES	3	4.375E-4	45.	YES+	
+	3	4.375E-4	-45	YES	3	4.375E-4	45.	YES+	
+	3	4.375E-4	-45	YES	3	4.375E-4	45.	YES+	
+	3	4.375E-4	-45	YES	3	4.375E-4	45.	YES	

Table F.7 Nastran Material 1 : 2D ORTHOTROPIC Material

(1)	(2)	(3)	(4)	(5)	(6)	(7)	(8)	(9)	(10)
MAT8	1	7.13E+10	9.73E+10	0.03	7.E+9	5.E+9	7.E+9	2600.	+MT 1
+MT 1	0	0	0			+MA 1			
+MA 1									

Table F.8 Nastran Material 2 : 2D ORTHOTROPIC Material

(1)	(2)	(3)	(4)	(5)	(6)	(7)	(8)	(9)	(10)
MAT8	2	7.13E+10	6.83E+10	0.02	6.E+9	5.E+9	6.E+9	1500.	+MT 2
+MT 2	0	0	0			+MA 2			
+MA 2									

Table F.9 Nastran Material 3 : 2D ORTHOTROPIC Material

(1)	(2)	(3)	(4)	(5)	(6)	(7)	(8)	(9)	(10)
MAT8	3	7.13E+10	6.83E+10	0.02	6.E+9	5.E+9	6.E+9	1500.	+MT 3
+MT 3	0	0	0			+MA 3			
+MA 3									

- Coordinate system.

Since element coordinate system is strongly dependent upon the node numbering in individual elements, it is advisible to prescribe a coordinate system for composite elements and specify ply angles relative to this system. Material orientation is very important because it defines the direction for E_1 and E_2. It also establishes the reference for the definition of ply angle [148].

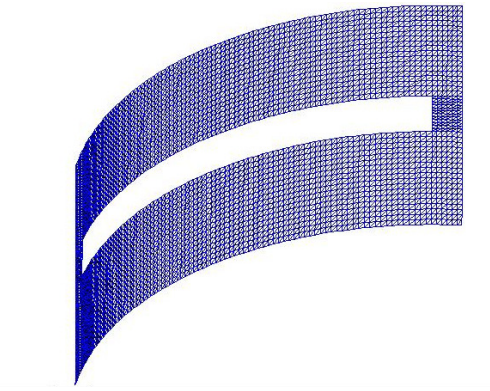

Fig. F.1 Material properties see Table F.7 with laminate properties see Table F.4.

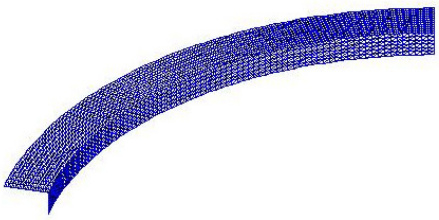

Fig. F.2 Material properties see Table F.8 with laminate properties see Tables F.2 and F.4.

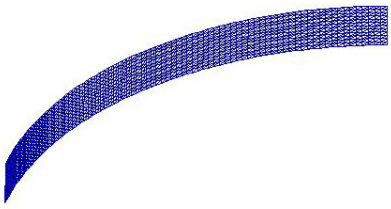

Fig. F.3 Material properties see Table F.9 with laminate properties see Tables F.5 and F.6.

Appendix G

Publications, thesis support and Presentations

- Peredo Fuentes, H., Model reduction of components and assemblies made of composite materials as part of complex technical systems to simulate the overall dynamic behaviour, PhD thesis, 2017, TU-Berlin, Berlin.
- Peredo Fuentes, H., Zehn, M., Application of the Craig-Bampton model order reduction to a composite structure: MAC and XOR. Facta Universitatis, series: Mechanical Engineering Vol. 12, No 1, 2014, pp. 37 – 50, This work is licensed under the Creative Commons Attribution-NonCommercial-NoDerivatives 4.0 International License (CC-BY-NC-ND) 4.0, from:http://casopisi.junis.ni.ac.rs/index.php/FUMechEng/article/download/182/50, Retrieved 27 Nov. 2017 15:29:28 AM.
- Peredo Fuentes, H., Zehn, M., Application of the Craig-Bampton model order reduction to a composite structure: COMAC, ECOMAC, S-COMAC and MACco. Open Engineering J., 6, 2016, pp. 185-198, This work is licensed under the Creative Commons Attribution-NonCommercial-NoDerivatives 3.0 International License (CC-BY-NC-ND) 3.0, from DOI:https://doi.org/10.1515/eng-2016-0024
- Peredo Fuentes, H., Application of the mode-shape expansion based on model order reduction methods to a composite structure. Open Engineering J., 7(1), pp. 199-212, This work is licensed under the Creative Commons Attribution-NonCommercial-NoDerivatives 3.0 International License (CC-BY-NC-ND) 3.0, from DOI:https://doi.org/10.1515/eng-2017-0026

- Marian Schücker, Generierung und Reduktion der Steifigkeits- und Massenmatrix in Scilab und Matlab, Diplomarbeit, TU-Berlin, Germany, 2013.
- Peredo Fuentes, H., Zehn, M., Application of Modal Assurance Criterion (MAC), Coordinate Modal Assurance (COMAC), Enhanced COMAC and Scale-COMAC criteria in a Composite Assembly using a Laser Scanning Vibrometer. International Meeting on Optical Measurement Techniques and Industrial Applications, November 2013, The Hague, Netherlands.

FACTA UNIVERSITATIS
Series: **Mechanical Engineering** Vol. 12, N° 1, 2014, pp. 37 - 50

APPLICATION OF THE CRAIG-BAMPTON MODEL ORDER REDUCTION METHOD TO A COMPOSITE STRUCTURE: MAC AND XOR

UDC (531+624.01)

Humberto Peredo Fuentes, Manfred Zehn

Institute of Mechanics, Technical University Berlin, Germany

Abstract *The Craig-Bampton model order reduction (CBMOR) method based on the Rayleigh-Ritz approach is applied to dynamic behavior simulation of a composite structure in order to verify the method's feasibility and accuracy. The principle of this method is to represent a coupled component model based on the mass, damping and stiffness matrices. The methodology consists of a finite element model based on the classical laminate theory (CLT), a design of experiment to improve the modal assurance criteria (MAC) and experimental results in order to validate the reduced model based on CBMOR method and substructures (super-elements). Experimental modal analysis has been performed using a scanner laser Doppler vibrometer (SLDV) in order to assess the quality of the finite element models. The MAC and cross orthogonality MAC (XOR) values are computed to verify the eigenfrequencies and eigenvectors. This approach demonstrates the feasibility of using CBMOR for composite structures. The example is prepared and solved with MSC/NASTRAN SOL103. The design of experiments (DOE) method has been applied in order to identify the critical parameters and thus obtain high MAC values.*

Key Words: *SDTools-MATLAB, NASTRAN, Modal Analysis, Composites*

1. INTRODUCTION

Many techniques have been proposed to obtain reduced order finite element models (known as model order reduction (MOR) methods) by reducing the order of mass and stiffness matrices of structures made of conventional materials [1-3]. The substitution of conventional materials by composite materials in the aeronautic, space and automotive industry is becoming increasingly important today for the production of industrial high-performance components [11-13]. The state-of-the-art MOR techniques are classified in

Received November 27, 2013
Corresponding author: Humberto Peredo Fuentes
Technical University Berlin, Institute of Mechanics, Berlin, Germany
E-mail: hperedo@mailbox.tu-berlin.de

four groups [19]: direct reduction, modal methods, reduction with Ritz vectors and the component mode synthesis (CMS). According to this classification, the last two groups yield the best results. The Ritz vectors improve the accuracy-cost ratio and the CMS combines the first three classes of methods. Hence the MOR method based on the Rayleigh-Ritz approach is used to improve the accuracy-time ratio in civil and aeronautical engineering applications in many areas of structural dynamics [6, 14, 19, 22, 23]. Thus, it is necessary to study the feasibility and efficiency of using the CMS with the Rayleigh-Ritz reduction basis in order to describe the dynamic behavior of a composite structure [14, 19]. The sections 2-4 introduce to MOR based on the Ritz vectors, classical CMS and substructures, respectively. The classical laminate theory (CLT) is introduced in Section 5. Sections 6-8 demonstrate a sensitivity analysis performed by using different tools – design of experiment (DOE), finite element method (FEM) and modal assurance criteria (MAC).

2. Model Order Reduction with Ritz Vectors

It is typical for coupled problems with model sub-structuring [6, 14, 22, 23] to have an accurate second order representation in the form:

$$\begin{array}{c}([M]s^2+[C]s+[K])\{q\}=[b]\{u\}\\ \{y\}=[c]\{q\}\end{array}, \tag{1}$$

where s is the Laplace variable, $[M]$, $[C]$, $[K]$ are mass, damping and stiffness matrices, respectively, $\{q\}$ are generalized degrees of freedom (DOFs), $[b]$ and $[c]$ are input and output matrices, respectively, $\{u\}$ are the inputs describing the time/frequency dependence, and $\{y\}$ are the physical outputs.

In this description, two - not very classical and yet important - assumptions are made:

1) The decomposition of discretized loads $F(s)$ as the product of the fixed input shape matrix specifying the spatial localization of loads $[b]$ and inputs $\{u\}$.
2) The definition of physical outputs $\{y\}$ is a linear combination of DOFs $\{q\}$.

The Ritz/Galerkin displacement methods seek approximations of the response within a subspace characterized by matrix $[T]$ associated with generalized DOFs $\{q_R\}$:

$$\{q\}=[T]\{q_R\}, \tag{2}$$

where $\{q\}$ is the original set of DOF and $\{q_R\}$ is the reduced set of DOF, substituting Eq. (2) into Eq. (1) leading to an overdetermined set of equations. The Ritz approximation assumes that the virtual work of displacements in the dual subspace generated by $[T]^T$ is also zero, thus leading to a reduced model:

$$\begin{array}{c}\left([T]^T[M][T]\ \ s^2+[T]^T[C]\,[T]\,s+[T]^T[K]\,[T]\right)\ \{q_R(s)\}=[T]^T[B]\,\{u(s)\}\\ \{y(s)\}=[c]\,[T]\,\{q_R(s)\}\end{array}. \tag{3}$$

3. Classical CMS Bases as Approximation of the Frequency Response

The method was first developed by Walter Hurty in 1964 [1] and later expanded by Roy Craig and Mervyn Bampton [2] in 1968. Component mode synthesis and model reduction methods provide for the means for building appropriate [*T*] bases (the subspace spanned rectangular matrix). There are many ways of proving classical bases [22]. Their validity is associated with two assumptions: the model needs to be valid over a restricted frequency band and the number of inputs is limited. One needs to translate this hypothesis into the requirement to include mode shapes and static responses into [*T*] basis. Most of the literature on CMS implies the fundamental assumption for coupling, which states that the displacement is continuous at the interfaces. Considering the response of an elastic structure to applied loads $F(s)=[b]\{u(s)\}$, the exact response at a given frequency $[H(s)]$ is given by:

$$[H(s)]=[c]\{[M]s^2+[K]\}^{-1}[b]=[c][Z(s)]^{-1}[b], \tag{4}$$

where $[Z(s)]$ is the dynamic stiffness. If there is no external excitation:

$$[Z(\lambda_j)]^{-1}\{\phi_j\}=\{0\}, \tag{5}$$

and the solutions are known as free modes of the structure, where λ_j is j^{th} eigenvalue of the matrix and $\{\phi_j\}$ is j^{th} eigenvector. A reduction model should include these shapes to allow for an accurate representation of the resonances which are associated with the singularities of the dynamic stiffness. A point of particular interest is the static response at $s=0$. The associated deformation is:

$$\{q(s=0)\}=[Z(0)]^{-1}[b]\{u(0)\}=[T_s]\{u(0)\}. \tag{6}$$

The columns of $[T_s]$ are also called attachment modes [22]. For the case of free floating structures (structures with rigid modes), $[Z(0)]$ is singular and one defines attachment modes as responses of all modes except for the rigid body modes.

The bases combining free modes and attachment modes are valid over a certain frequency range (truncation of the series of free modes) and certain inputs characterized by [*b*].

One, thus, considers the response of the structure with enforced displacements on a subset of DOFs. Division of the DOFs in two groups – active or interface DOFs denoted by *I* in the subscript, and complementary, denoted by *C* in the subscript, leads to:

$$\begin{bmatrix}[Z_{II}(s)] & [Z_{IC}(s)]\\ [Z_{CI}(s)] & [Z_{CC}(s)]\end{bmatrix}\begin{Bmatrix}<\{q_I(s)\}>\\ q_C(s)\end{Bmatrix}=\begin{Bmatrix}R_I(s)\\ <\{0\}>\end{Bmatrix}, \tag{7}$$

where $<\{q_I(s)\}>$ and $<\{0\}>$ denotes a known quantity. The exact solution to this problem is:

$$\{q\}=[T(s)]\{q_I\}=\begin{bmatrix}[I]\\ -[Z_{CC}(s)]^{-1}[Z_{CI}(s)]\end{bmatrix}\{q_I\}. \tag{8}$$

The subspace found here is frequency dependent and can only be used in very restricted applications [23]. A classical approximation is to evaluate the static ($s=0$) value in this subspace for the active or interface DOFs denoted by *CI* in the subscript, and complementary, *CC* in the subscript:

$$[T]=\begin{bmatrix} [I] \\ \left[[-K_{CC}]^{-1}[K_{CI}]\right] \end{bmatrix}. \tag{9}$$

Reduction on this basis is known as static or Guyan condensation [4]. The columns of $[T]$ are called constraint modes [22]. They correspond to unit displacements of the interface DOFs. Significant deviations can be expected when $[Z_{CC}(s)]^{-1}$ differs from $[Z_{CC}(0)]^{-1}=[K_{CC}]^{-1}$ Such difference is significant for singularities of $[Z_{CC}(s)]^{-1}$ which are computed by the eigenvalue problem:

$$\begin{bmatrix} [0] & [0] \\ [0] & [Z_{CC}(\omega_j)] \end{bmatrix}\begin{Bmatrix} 0 \\ \phi_{j,c} \end{Bmatrix}=0. \tag{10}$$

The use of a basis combining constraint, Eq. (9), and fixed-interface modes, Eq. (10), is proposed in [2]. It yields the Craig-Bampton method:

$$[T]=\begin{bmatrix} [I] & [0] \\ \left[[-K_{CC}]^{-1}[K_{CI}]\right] & [\phi_{NM,C}] \end{bmatrix}, \tag{11}$$

where $[\phi_{NM,C}]$ is the interior part of the matrix of kept fixed-interface modes. There are many results reported by Balmès *et al.* [6, 14, 15] obtained by the Craig-Bampton model order reduction (CBMOR) and the Rayleigh-Ritz vectors approach in order to solve coupled problems related to model sub-structuring (also known as component mode synthesis).

One should be aware of the fact that the use of Raleigh-Ritz vectors leads to dense matrices, as opposed to not reduced FEM models characterized by a sparse form of the matrices.

4. SUBSTRUCTURES OR SUPER-ELEMENTS

Sub-structuring is a procedure that condenses a group of finite elements into one element. It implies that the whole structure is divided into smaller structures (see Figs. 1 and 2), and the resulting elements are referred to as super-elements. In the considered case (Fig. 1), the structure is divided into two substructures using 123 nodes at the interface. The model size is reduced from 37,698 DOF to 579 DOF.

a) b)

Fig. 1 Prototype and FEM model in NASTRAN and SDTools:
a) Composite structure – front and back; b) FEM model

The basic sub-structuring idea is to consider a part of the model separately and extract the degrees of freedom needed to connect this part to the rest of the model. Therefore, the result of sub-structuring is a collection of finite elements whose response is defined by the stiffness and mass of the retained degrees of freedom. The categories of modal truncation sub-structuring and static condensation approaches have been widely applied relying on the eigenfrequency information [3, 23].

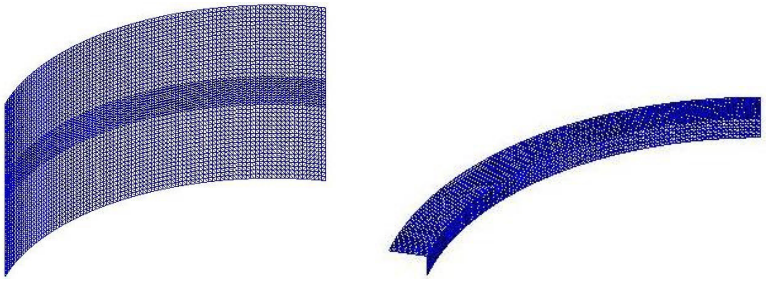

a) b)

Fig. 2 Sub-structuring: a) Substructure 1; b) Substructure 2

5. LAMINATE THEORY

The classical laminate theory is applicable to linear and composite elastic materials [21] by means of the Discrete Kirchhoff Theory (DKT) elements [20]. The CLT has been used extensively to predict elastic behavior of the traditional fiber-reinforced polymers (FRP). FRP materials (carbon or glass FRP) are widely used in aerospace and construction applications. One important consideration is to have perfectly bonded layers with a uniform thickness (see Fig. 3). The mechanical properties measured in ply level experiments are used to populate the stiffness matrix for each ply. The stiffness matrices for the individual plies are combined to form the laminate stiffness matrix – the ABC matrix:

$$\begin{pmatrix} N_x \\ N_y \\ N_{xy} \\ M_x \\ M_y \\ M_z \end{pmatrix} = \begin{pmatrix} A & B \\ B & C \end{pmatrix} \times \begin{pmatrix} \varepsilon_x \\ \varepsilon_y \\ \gamma_{xy} \\ \kappa_x \\ \kappa_y \\ \kappa_{xy} \end{pmatrix}. \tag{6}$$

The ABC matrix relates forces (N_i) and moments (M_i) to strains (ε_i) and curvatures (κ_i). The components of the ABC matrix are given in Eqs. (7-9), where N is the number of plies, Q_k is the stiffness matrix of each ply, and Z_k denotes the distance from the laminate's mid-plane to the edges of single plies:

$$A = \sum_{k=1}^{N} Q_k \times [Z_k - Z_{k-1}], \text{ in-plane stiffness matrix,} \tag{7}$$

$$B = \frac{1}{2}\sum_{k=1}^{N} Q_k \times [Z_k^2 - Z_{k-1}^2], \text{ bending-stretching coupling matrix,} \tag{8}$$

$$C = \frac{1}{3}\sum_{k=1}^{N} Q_k \times [Z_k^3 - Z_{k-1}^3], \text{ bending-stiffness matrix.} \tag{9}$$

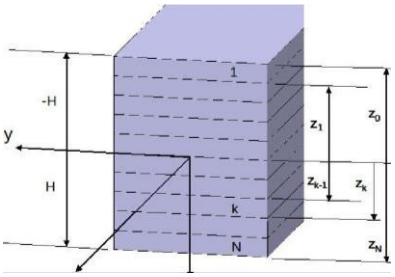

Fig. 3 Configuration of composite layers

The prototype and the finite element (FE) model are shown in Fig. 1. The composite structure incorporates three parts (properties in Table 1). The first component is made of Hunts-man Ly 564 + Hexcel Gewebe G0926 (HTA-Faser) with dimensions of 0.390m × 0.810m (Fig. 2). The middle shell that connects the two principal parts (Fig. 2a) has dimensions of 0.710m × 0.030m. Finally, there is the C-section Hexcel RTM6 + Saertex Multi-Axial-Gelege (MAG) with a IM7-Faser with dimensions of 0.710m × 0.030m. All the parts have symmetric layer distribution $[45/-45/45/-45/]_S$.

6. Design via Finite Element Analysis (Full and Reduced Model)

Our study is divided into two parts.

The first part is a full modal analysis using the same model but with two different solvers for reference purposes. Two types of elements have been used: CTRIA3 shell (from MSC/NASTRAN) and PSHELL (from SDTools).

The second part is setting the reduced model by using SDTools for MATLAB. The reduced model is built up defining two super-elements. Super-element 1 (Fig. 2a) has 4,753 nodes and 9,219 elements, while super-element 2, (Fig. 2b) has 1,615 nodes and 3,026 elements. The defined super-elements share 579 DOF distributed in 123 nodes along the common border with different DOF per node, according to the CMS that has defined an appropriate [*T*] matrix, used in [3]. We have calculated the same number of modes in each super-element and performed a cross orthogonality MAC (XOR) evaluation to verify the approximation of the MOR used in low (12 mode pairs) and/or high frequency range (29 mode pairs) versus the full model.

In order to estimate the main parameters (qualitative and quantitative) that affect our MOR based on the number of substructures and nodes, we have performed a DOE using first the full model and the experimental analysis. The DOE study is performed using the methodology implemented in Minitab 16 [7]. Fig. 4a shows the main effects of each parameter in the composite structure based on the physical characteristics selected. The

main effect is identified through the slope generated due to the eigenfrequency values between the limits defined for each parameter – a bigger slope means a strong parameter effect. Due to the number of parameters, it is necessary to perform first a DOE-screening with 2^{10-5}=32 "runs" and then a full factorial with the identified principal parameters based on the DOE-screening.

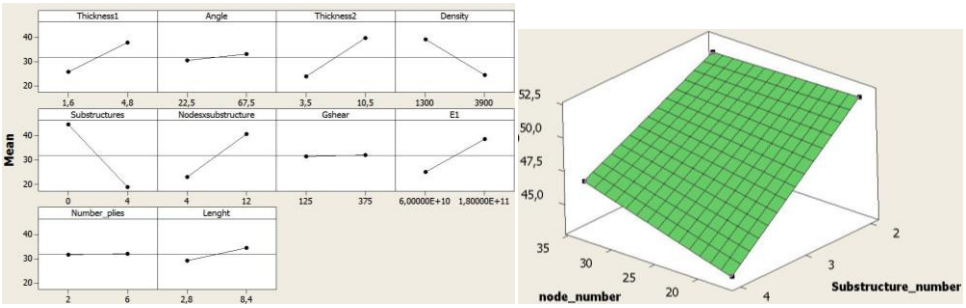

a) b)

Fig. 4 DOE: a) Parameters main effects, b) Surface response

The results shown in Fig. 5a (vertical left side) are eigenfrequencies. The MAC correlation between the full model and experimental data help us validate the MOR results. The Young Modulus, density, number of nodes and substructure parameters have a strong influence reflected in the slope (Fig. 4b) and in the MAC values (section 7). Once we have selected the main parameters based on the DOE-screening, we perform a DOE full factorial 2^4 and obtain a surface response (see Fig. 4b) that help us find the best model for the parameter limits selected. This process is known in literature as updating. Jing [8], Barner [9] and Xiaoping *et al.* [10] reported the use of design of experiments in order to quantify and qualify different key parameters in mechanical components (stresses, displacements, low and high cycle fatigue, and frequencies). The DOE is a sensitivity analysis tool used to estimate the critical input parameters.

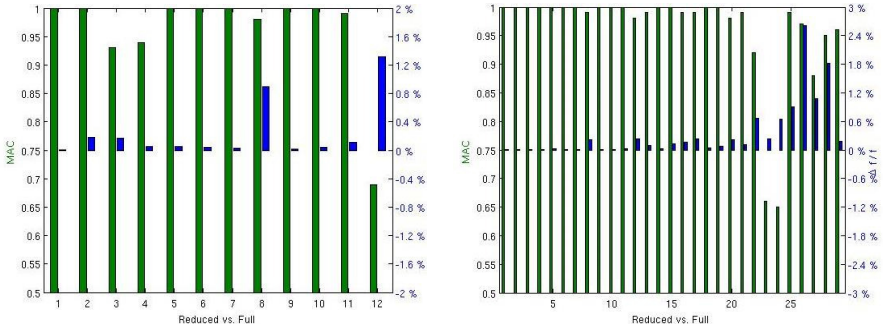

a) b)

Fig. 5 Cross orthogonality MAC reduced vs. full model: (a) low frequencies (b) higher frequencies (green bars MAC, blue bars frequency difference)

In Fig. 5, we can see the low and high mode pairs selected between the full and reduced model (12 and 29 mode pairs), respectively. The green bars show the eigenvector criteria and the blue bars the eigenfrequency difference between the reduced and the full model. The low frequencies show a larger difference in the 3rd, 4th and 12th mode pair. The largest difference in the frequencies is about 1.2% (low eigenfrequencies) between the full and reduced model. Increasing the number of pairs, the eigenfrequency difference increases up to 3% for 29 pairs. However, the mode pairs 3, 4 and 12 have improved suggesting that the accuracy using CBMOR method depends on the number of retained constraint modes. Most of the pair selections have a correlation above 90%, except for the 12th mode pair in the low frequency range and the 23rd and 24th pair in a high frequency range. Table 2 shows the values comparing the full with a reduced model for low frequency. A 3D plot of the XOR for high frequency pairs is given in Fig. 6.

Table 1 Orthotropic elastic mechanical properties per thickness

Modulus	Th_1(m)	E(GPa)	ν(-)	Shear	G(GPa)	ρ(Kgm^{-3})
E_1	0.035	71.3	0.3	G1	7.0	2600
E_2		97.3	0.3	G2	5.0	
				G3	7.0	
Modulus	Th_2(m)	E(GPa)	ν(-)	Shear	G(GPa)	ρ(Kgm^{-3})
E_1	0.007	71.3	0.2	G1	6.0	1500
E_2		68.3	0.2	G2	5.0	
				G3	6.0	
Modulus	Th_3(m)	E(GPa)	ν(-)	Shear	G(GPa)	ρ(Kgm^{-3})
E_1	0.035	71.3	0.2	G1	6.0	1500
E_2		68.3	0.2	G2	5.0	
				G3	6.0	

Table 2 MAC values: full versus CBROM reduced model

#	Full	#	Reduced	DF/FA	MAC
7	57.218	7	57.218	0.0	100
8	106.02	8	106.21	0.2	100
9	167.50	9	167.79	0.2	93
10	168.2	10	168.29	0.1	94
11	234.99	11	235.12	0.1	100
12	236.83	12	236.93	0.0	100
13	315.26	13	315.33	0.0	100
14	323.93	14	326.82	0.9	98
15	401.72	15	401.77	0.0	100
16	408.39	16	408.57	0.0	100
17	432.89	17	433.39	0.1	99
18	494.90	18	501.41	1.3	69

The correlation of nearly double modes 9-10,11-12,13-14 and 15-16 in Table 2 suggests the possibility of having bending and torsional modes at close frequencies in the composite structure (mode veering) [24]. Thus, a lower MAC value is expected in some mode pairs in the experimental validation. There are only three types of structures made of

the conventional materials that have been identified to exhibit veering: symmetric or cyclic structures, multi-dimensional structures such as plates having bending and torsion at close frequencies and structures with fully uncoupled substructures. The considered structure corresponds to the second type – multi-dimensional plate structures.

7. MODAL ASSURANCE CRITERION (MAC)

There are two general categories for correlation criteria: eigenfrequencies and eigenvectors [18]. The MAC is one of the most useful comparison methods that relies on the eigenvector information according to Eq. (10). The MAC is a known vector correlation between the experimental and the FE model. To approximate the measurements through a polynomial function, (Fig. 9), we use the frequency domain identification of structural dynamics applying the pole/residue parameterization [15].

$$MAC(i) = \frac{\left| \left(\sum_{j=1}^{l} (c_j \varphi_{id})^H (c_j \varphi_k) \right) \right|^2}{\left| \sum_{j=1}^{l} (c_j \varphi_{id})^H (c_j \varphi_{id}) \right| \left| \sum_{j=1}^{l} (c_j \varphi_k)^H (c_j \varphi_k) \right|} \tag{10}$$

The MAC value of 100 % corresponds to an absolute correlation. The less this value becomes, the worse the eigenvector correlation is ($c_j\varphi_{id}$ is the j^{th} mode shape at sensors and $c_j\varphi_k$ is the j^{th} analytical mode shape), provided that the observability law for the selection of DOFs is not violated. A MAC coefficient of a magnitude larger or equal than 90% implies a satisfactory correlation. In Fig. 8, we observe some mode shapes of the reduced and full models. Figs. 10a, 10b, and 10c, show the MAC between the full and the experimental measurements in MATLAB, NASTRAN, and CBMOR model, respectively. The correlation is performed for a low frequency range (up to 400 Hz), based on the fitting model generated from the experimental measurements [3, 15].

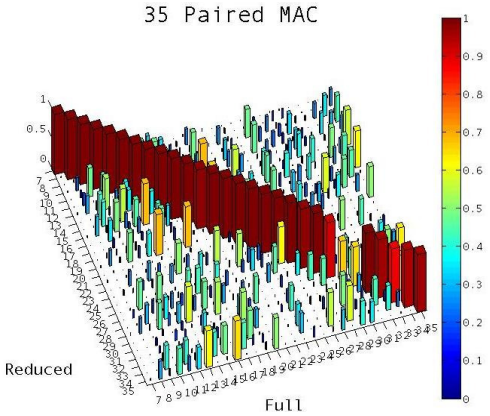

Fig. 6 Cross orthogonality MAC (XOR): higher frequencies – reduced vs. full model

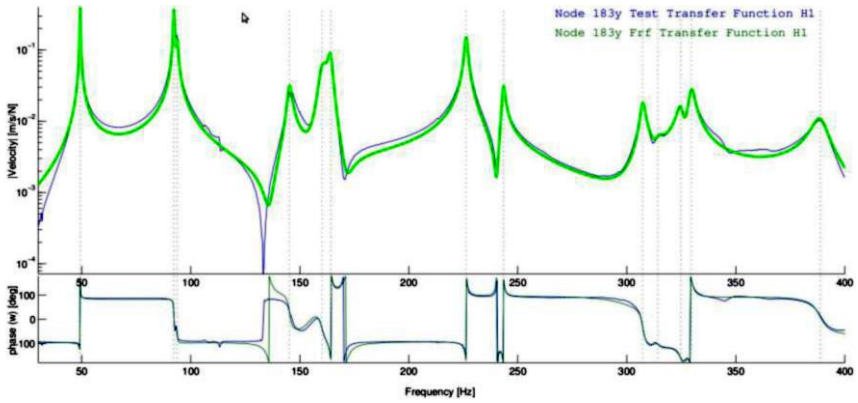

Fig. 7 FRF(blue) and fitting curve (green) of composite model at node 183y

8. EXPERIMENTAL MODAL ANALYSIS

All the measurements are performed with the Scanning Laser Doppler Vibrometer (SLDV) PSV 840 (Fig. 9a). It is a complete and compact system including a sensor head, a PC with DSP boards and Windows NT-based application software packages [16]. Discrete Fourier transform is applied to response $x(t)$ and excitation $f(t)$ to give $X(\omega_i)$ and $F(\omega_i)$, respectively [17]. The frequency response function (FRF), $H(\omega_i)$, is defined as the ratio of the transformed excitation [18]:

$$H(\omega_i) = \frac{X(\omega_i)}{F(\omega_i)}, \tag{11}$$

where $H(\omega_i)$ is the identified (predicted) FRF transfer function matrix , $H(\omega_i)$ the measured FRF transfer function matrix, $X(\omega_i)$ the Fourier spectrum of response, and $F(\omega_i)$ is the Fourier spectrum of excitation force. The FRF in Eq. (11) is the inverse of the dynamic stiffness matrix:

$$H(\omega_i) = [-\omega_i^2[M] + \omega_i[C] + [K]]^{-1}. \tag{12}$$

Mass $[M]$, damping $[C]$ and stiffness $[K]$ matrices in Eq. (12) are dependent on physical parameters such as material's density, Young's and shear moduli and Poisson ratio.

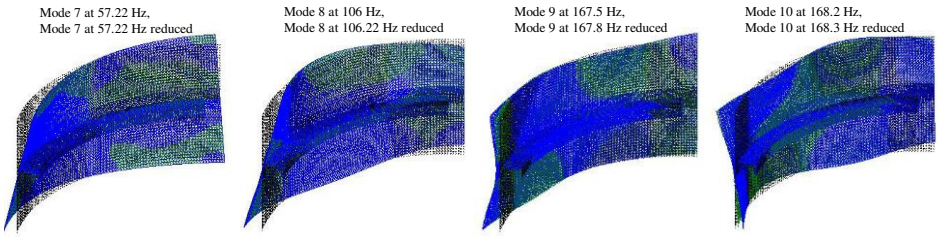

Fig. 8 CBMOR (in green) vs full model in MATLAB (in blue)

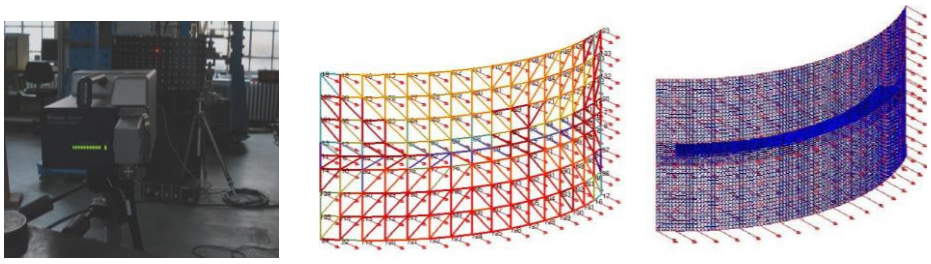

a) b) c)

Fig. 9 Experiment: a) Experimental set-up; b) 153 Y-direction sensors; c) 153 sensors in the FEM model

The SLDV employs a laser to sweep over the structure continuously while measuring, capturing the response of the structure from a moving measurement point. Various methods have been devised to determine the mode shapes of the structure everywhere along the scan path measurement [16]. A bandwidth of 2% is used in order to localize the eigenfrequencies. The composite structure has rather small internal damping and the experimental modal analysis below 400 Hz is performed. The structure is excited by means of a shaker at node 17 (Fig. 9a and Fig. 9b) that is located in the right bottom corner. The input force is measured using a force transducer type 8200 in combination with a charge to CCLD converter Type 2646 in order to record the excitation in the transverse direction.

The interpolation between the experimental measurements uses Frequency Response Functions (FRF) [15], (Fig. 7). The FRFs allow comparison of the experimental modal parameters (frequency, damping, and mode shape) with those of the FE model. The Fast Fourier Transform (FFT) is a fundamental procedure that isolates the inherent dynamic properties of a mechanical structure and in our case with respect to the full and reduced FE model. The MAC analysis (Fig.10) shows a high correlation between the full model, the reduced model and the experimental measurements. The nearly double correlation in the experimental results identified in Table 3 (previously identified applying the CBMOR method in Table 2), suggests the presence of the veering phenomena (bending and torsional mode at the same frequency) in the considered composite structure. This is reflected in the MAC values for the corresponding modes.

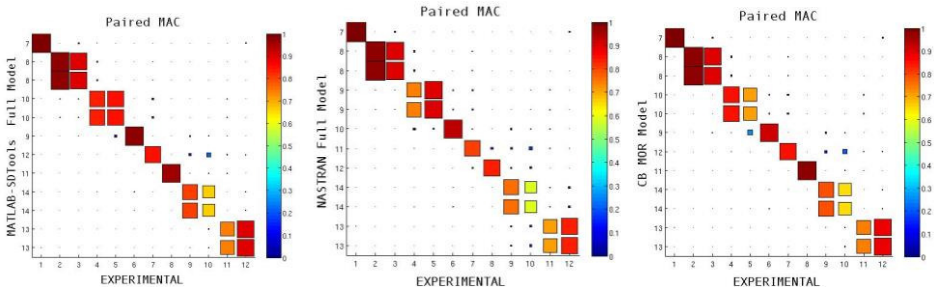

a) b) c)

Fig. 10 Comparative MAC: a) SDtools-Exp, b) MSC/NASTRAN-Exp, c) CBMOR-Exp

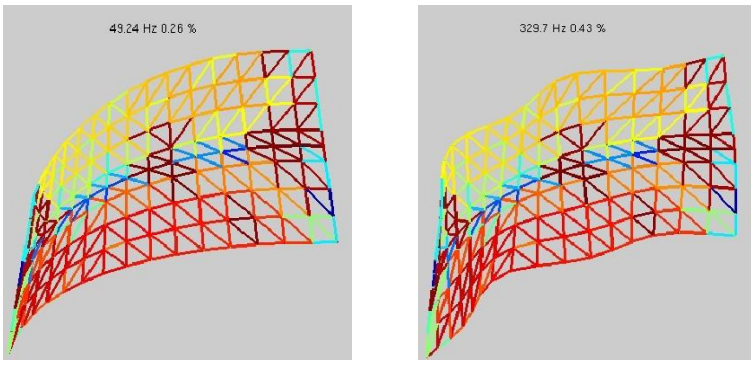

Fig. 11 Experimental mode shapes

Pierre [25] reported how localization and veering are related to two kinds of "coupling": the physical coupling between structural components, and the modal coupling set up between mode shapes through parameter perturbations.

His studies show that, in structures with close eigenvalues, small structural irregularities (could be our case) result in both strong localization of modes and abrupt veering away of the loci of the eigenvalues when these are plotted against a parameter representing the system disorder. The study of the presence of this phenomenon in the composite structure is beyond the scope of this work.

Table 3 shows the MAC values obtained for each case between the full and reduced model versus the experimental results. The mode shapes depicted in Fig. 11 are the experimental results.

Table 3 Full and reduced FEM model results versus experimental results

#	Experimental	#	Full	DF/FA	MAC	CBMOR	DF/FA	MAC
1	49.243	7	57.218	16.2	100	57.218	16.2	100
2	92.265	8	106.02	14.9	97	106.21	15.1	97
3	93.756	8	106.02	13.1	90	106.21	13.3	90
4	145.29	10	168.20	15.8	83	168.29	15.8	84
5	160.05	10	168.20	5.1	86	168.29	5.1	71
6	164.18	9	167.50	2.0	98	167.79	2.2	92
7	226.36	12	236.83	4.6	86	236.93	4.7	85
8	243.40	11	234.99	-3.5	96	235.12	-3.4	97
9	307.33	14	323.93	5.4	81	326.82	5.4	80
10	314.18	14	323.93	3.1	66	326.82	4.0	65
11	324.83	13	315.26	-2.9	74	315.33	-2.9	74
12	329.67	13	315.26	-4.4	90	315.33	-4.3	89

9. CONCLUSIONS

The results have shown a good correlation in dynamic behavior of the composite structure model using the DKT elements with different solvers. The MAC values with the full and reduced models have also shown a good agreement with the experimental results. In order to achieve high quality models that can adequately capture the dynamic behavior, the material properties are updated through the DOE and are crucial in the MOR correlation with the experimental results. The updated mass and stiffness matrices in the full model play an important roll in this procedure. Furthermore, the reduced model obtained by means of the Craig-Bampton MOR method (the reduced model couples 2 substructures through 123 nodes and 579 DOF) has demonstrated a good agreement with the experimental results. The MAC values for the FEM models as well with the experimental results suggest a presence of mode veering phenomenon (bending and torsional mode at the same frequency in the considered composite structure). And finally, the experimental results using a SLDV as well as the identification of pole/residues used in [15], are suitable to validate the dynamic analysis using modal order reduction. It is improper to draw conclusions from a single example, but the obtained results using two different solvers are coherent. This conducted work obviously leaves much room for further research. Other modal assurance criteria need to be performed, such as coordinate modal assurance criteria (COMAC), enhanced modal assurance criteria (ECOMAC) and scale coordinate assurance criteria (S-COMAC) and also other model order reduction and/or mode shape expansion methods should be assessed.

REFERENCES

1. Hurty, W. C., 1965, *Dynamic analysis of structural systems using component modes*, AIAA Journal, 3(4), pp. 678-685.
2. Craig R. J. and Bampton M., 1968, *Coupling of substructures for dynamic analyses*, AIAA Journal 6(7), pp.1313-1319.
3. SDTools Inc. 2011, *Structural dynamics toolbox and FEMLink, User's Guide*, SDTools, Ver. 6.4, Paris, France.
4. Guyan, J. 1965, *Reduction of stiffness and mass matrices*, AIAA Journal, 3(380). pp.
5. Irons, B. M.., 1965, *Structural eigenvalue problems - elimination of unwanted variables*, AIAA Journal, 3(5): pp. 961-962.
6. Balmès E., 1996, *Use of generalized interface degrees of freedom in component mode synthesis*, International Modal Analysis Conference, pp. 204-210.
7. Montgomery, D. C., 2000, *Design and analysis of experiments*, John Wiley & Sons.
8. Fan J., Zeng, W., Wang R., Sherr X., Chen Z., 2010, *Research on design and optimization of the turbine blade shroud*, 2nd International Conference on Engineering Optimization, Lisbon, Portugal.
9. Barner, N., 2010, *Isight-Abaqus optimization of a ring-stiffened Cylinder*, SIMULIA Customer Conference.
10. Chen, X., Yu, X., and Ji B., 2010, *Study of crankshaft strength based on iSIGHT platform and DOE methods,* International Conference on Measuring Technology and Mechatronics Automation, pp. 548-551.
11. Lauwagie, T., 2005, *Vibration-Based Methods for the Identification of the Elastic Properties of Layered Materials*, PhD thesis, Catholic University of Leuven, Belgium.
12. Reddy, J. N., 2005, *Mechanics of Laminated Composite Plates and Shells Theory and Analysis*, CRC, Press Second edition.
13. Berthelot, J. M., 1992, *Materiaux composites: Comportement mecanique et analyse des structures*, Lavoisier, Paris, France
14. Balmès E., 1997, *Efficient Sensitivity Analysis Based on Finite Element Model Reduction*, International Modal Analysis Conference, IMAC, pp.1-7.
15. Balmès E., 1996, *Frequency domain identification of structural dynamics using the pole/residue parametrization*, International Modal Analysis Conference, pp. 540-546.

16. Gade, S., Møller, N.B., Jacobsen, N.J., and Hardonk. B., 2000, *Modal analysis using a scanning laser Doppler vibrometer,* Sound and Vibration Measurements, pp. 1015-1019.
17. Newland, D.E., 1993, *An Introduction to random vibration, spectral and wavelet Analysis*, New York, Longman, Harlow and John Wiley.
18. Ewings, D. J., 1995, *Modal testing: Theory and practice,* Research Studies Press, Letchworth, United Kingdom.
19. Cunedioğlu, Y., Muğan, A., Akçay, H., 2006, *Frequency domain analysis of model order reduction techniques,* Finite Elements in Analzsis and Design, 42, pp. 367-403.
20. Batoz, J.L., Bathe, K.J., Ho, L.W., 1980, *A Study of three node triangular plate bending elements*, International Journal for Numerical Methods in Engineering, 15, pp. 1771-1812.
21. Batoz, J.L., Lardeur, P., 1989, *Composite plate analysis using a new discrete shear triangular finite element*, International Journal for Numerical Methods in Engineering, 27, pp. 343-359.
22. Craig, R.J., 1987, *A review of time-domain and frequency domain component mode synthesis methods*. Int. J. Anal. and Exp. Modal Analysis, 2(2), pp. 59-72.
23. Balmès, E., 2000, *Review and Evaluation of shape expansion methods*, International Modal Analysis Conference, pp. 555-561.
24. Bonisoli E, Delprete C., Espoito M., Mottershead J. E., 2011, *Structural Dynamics with conicident Eigenvalues: Modeling and Testing*, Modal Analysis Topics 3, pp 325-337.
25. Pierre C., 1988, *Mode Localization and eigenvalue loci of Bridges with Aeroeslastic effects*, Journal of Engineering Mechanics 126(3), pp. 485-502.

PRIMENA CRAIG-BAMPTON REDUKCIJE MODELA NA STRUKTURU OD KOMPOZITNOG MATERIJALA: MAC I XOR

Craig-Bampton metoda za redukciju modela (*CBMOR*) *zasnovana na Rayleigh-Ritz pristupu je primenjena u simulaciji dinamičkog ponašanja kompozitnih struktura u cilju verifikacije izvodljivosti i tačnosti ove metode. Princip ove metode je da predstavi model spregnutih komponenti preko matrica inercije, prigušenja i krutosti. Metodologija uključuje model primenom konačnih elemenata* (*MKE*) *na osnovu klasične teorije laminata* (*CLT*)*, zatim postavku eksperimenta sa ciljem poboljšanja vrednosti koeficijenata poređenja modova* (*MAC*)*, kao i eksperimentalne rezultate sa ciljem validacije redukovanog modela primenom CBMOR metode i substruktura* (*superelemenata*)*. Eksperimentalna modalna analiza je sprovedena korišćenjem laserskog Doplerovog vibrometra da bi se ocenio kvalitet MKE modela. MAC vrednosti za pripadajuće i nepripadajuće modove su sračunate da bi se verifikovale sopstvene frekvence i modovi. Ovaj postupak pokazuje izvodljivost primene CBMOR redukcije modela u slučaju kompozitnih struktura. Model je pripremljen i rešen primenom programskog paketa MSC/NASTRAN SOL103. Metodom dizajna eksperimenta identifikovani su kritični parametri, što je kasnije omogućilo dobijanje visokih MAC vrednosti.*

Ključne reči: *SDTools-MATLAB, NASTRAN, modalna analiza, kompozitni materijali*

Research Article **Open Access**

Humberto Peredo Fuentes* and Manfred Zehn

Application of the Craig-Bampton model order reduction method to a composite structure: MACco, COMAC, COMAC-S and eCOMAC

DOI 10.1515/eng-2016-0024
Received Mar 01, 2016; accepted Jun 06, 2016

Abstract: The Craig-Bampton model order reduction (CBMOR) method based on the Rayleigh-Ritz approach was applied in a previous work to simulate dynamic behavior of a composite structure (CFRP) using the modal assurance criteria (MAC) and cross orthogonality (XOR) to validate the correlation. Different coordinate modal assurance criteria are applied to complement and verify the eigenfrequencies and eigenvectors obtained of the full and reduced models using substructures (super-elements). An improvement is observed per paired mode-sensor with the MAC per coordinates criterion (MACco) in a CFRP once the stiffness parameters are updated in the full model applying a mix-numerical experimental technique (MNET) using a design of experiments (DOE). The coordinate modal assurance criteria (COMAC) and the scale COMAC (COMAC-S) results of the full models display the best results respect to the reduced model. Furthermore, slight improvement of the enhanced COMAC (eCOMAC) results are observed in the reduced model despite having lower MAC performance. This approach complements the results of the previous work using several COMAC techniques, and demostrates the feasibility to achieve low COMACs results in the reduced finite element model once the stiffness parameters of the full element model are updated. The example was prepared and solved with MSC/NASTRAN SOL103 and SDTools-MATLAB for comparative purposes.

Keywords: CBMOR; AMLS; Modal Analysis; Composites; MAC; MACco; COMACs

1 Introduction

Many techniques have been proposed to obtain reduced order finite element models (known as model order reduction (MOR) methods) by reducing the order of mass and stiffness matrices of structures made of conventional [1–15] or carbon fiber reinforced polymer (CFRP). The Craig-Bampton model order reduction (CBMOR) method based on the Rayleigh-Ritz approach implemented in [3] was performed in [17] to simulate the dynamic behavior of a CFRP. The simulation of the dynamics of the CFRP was divided into two steps: a mix-numerical experimental technique [18, 19] (MNET) and the reduced model using the CBMOR method. In the first part several techniques were combined using a design of experiments [22, 33] (DOE): experimental results [20], parametric curve-fitting [10], computed FEM results, and the modal assurance criteria [21] (MAC) to obtain the stiffness parameters in a composite assembly (CFRP). The obtaining of the stiffness parameters of a CFRP is one of the most challenging problems in experimental analysis. The second part was setting the reduced model using the CBMOR, superelements, the automated multi-level substructuring [14] (AMLS) and the residual iteration [13] methods implemented in SDTools [3] once the stiffness parameters were obtained. It is documented in the literature that the combination of CBMOR, AMLS, and residual mode effects can improve the accuracy of the original transformation matrix [3, 7, 15]. This study is based on the stiffness parameters obtained in [17] with the MNET and it is an extension to validate the MAC and XOR results of the full and reduced models using different coordinate modal assurance criterias. The application of these criterias to a CFRP is not documented in the literature. The different modal assurance criterias used in this study are introduced in sections 2-6, and are implemented in SDTools. In section 7 the results are discussed.

***Corresponding Author: Humberto Peredo Fuentes:** Institute of Mechanics, Technical University Berlin, Strasse des 17. Juni 135, 10623 Berlin, Germany; Email: hperedo@mailbox.tu-berlin.de
Manfred Zehn: Institute of Mechanics, Technical University Berlin

2 Modal Correlation Criterion

There are two general categories for correlation criteria: the eigenfrequencies and eigenvectors [21]. The modal assurace criteria [23] (MAC) is one of the most useful comparison methods that relies on the eigenvector information, see Eq. (1):

$$MAC(i) = \frac{\left|\left(\sum_{j=1}^{l}(c_j\phi_{id})^H(c_j\phi_k)\right)\right|^2}{\left|\sum_{j=1}^{l}(c_j\phi_{id})^H(c_j\phi_{id})\right|\left|\sum_{j=1}^{l}(c_j\phi_k)^H(c_j\phi_k)\right|} \quad (1)$$

where $c_j\phi_{id}$ is the jth mode shape at sensors and $c_j\phi_k$ is the jth analytical mode shape. The MAC value of 1 corresponds to an absolute correlation. The less this value becomes, the worst the eigenvector correlation will be. In the modal community a MAC coefficient of a magnitude larger or equal than 0.90 in the diagonal and less or equal than 0.05 in the off-diagonal implies a satisfactory correlation.

3 Coordinate modal assurance criterion

The coordinate modal assurance criteria (COMAC) is an extension of the MAC developed by Lieven and Ewins [24]. The implementation of the COMAC criterion requieres two stages of calculation. In the first stage, the modes from the two sets are matched using the MAC. After constructing the set of *NM* mode pairs to be correlated, the second stage of the COMAC is the calculation of the correlation values at each coordinate, over all the correlated pairs [25], see Eq. (2):

$$COMAC_{(l)} = 1 - \frac{\left|\left(\sum_{j=1}^{NM}(c_l\phi_{jA})(c_l\phi_{jB})\right)\right|^2}{\left|\sum_{j=1}^{NM}(c_l\phi_{jA})\right|^2\left|\sum_{j=1}^{NM}(c_l\phi_{jB})\right|^2} \quad (2)$$

where $c_l\phi_{jA}$ is the jth mode shape at sensors and $c_l\phi_{jB}$ is the jth analytical mode shape selected. It is important to note that the modes have to be normalized as this gives equal weighting to all modes. Unfortunatly, the standard COMAC cannot identify differences that occur due to fairly common problems during modal testing. These problems include orientation of the accelerometers and transducers scale factor errors [26]. Additionally, the COMAC is equally sensitive to large and small motion of DOF, which can make COMAC results more difficult to interpret. COMAC values closer to zero per DOF represent a higher agreement.

4 Scale coordinate modal assurance criterion

The scale coordinate modal assurance criterion (COMAC-S) is computed with shapes in set B scaled using the modal scale factor (MSF) [3, 23] (see Eq. (3)). The MSF provides a qualitative way of comparing two modal vector sets. This criterion has been used by Ewins [21], Allemang [23], Catbas [25], and Balmés [3] for a variety of different analyses including structural modifications and frequency response function (FRF) synthesis for comparison with experimental data [32].

$$COMAC - S_{(l)} = 1 - \frac{\left|\left(\sum_{j=1}^{NM}(c_l\phi_{jA})(c_l\hat{\phi}_{jB})\right)\right|^2}{\sum_{j=1}^{NM}\left|(c_l\phi_{jA})\right|^2\sum_{j=1}^{NM}\left|(c_l\hat{\phi}_{jB})\right|^2}$$

$$(c_l\hat{\phi}_{jB}) = (c_l\phi_{jB})MSF = (c_l\phi_{jB})\frac{(c_l\phi_{jB})^T(c_l\phi_{jA})}{(c_l\phi_{jB})^T(c_l\phi_{jB})} \quad (3)$$

This COMAC-S criterion sets the scaling of vectors in set B to minimize the quadratic norm of the difference between $(c_l\phi_{jA})$ and $(c_l\hat{\phi}_{jB})$ [3]. Scaling assumes that each experimental mode shape is already correlated with an analytical shape. When two modal vectors are scaled similarly, elements of each vector can be averaged, differentiated or sorted to provide an indication of the type of error vector superimposed on the modal vector [27]. The lower values of the COMAC-S represent also a higher agreement per DOF.

5 Enhanced coordinate modal assurance criterion

The formulation of the enhanced COMAC (eCOMAC), introduced by Hunt [26], overcome some of the limitations of the standard COMAC, expressed as:

$$eCOMAC_{(l)} = \frac{\sum_{j=1}^{NM}\left\|(c_l\tilde{\phi}_{jA}) - (c_l\hat{\phi}_{jB})\right\|}{2NM} \quad (4)$$

The comparation is done using mode shapes that are vector normalized to 1 and there must be phase correlation

between pair modes, see Eq. (5)

$$(c_l\tilde{\phi}_{jA}) = \frac{(c_l\phi_{jA})}{\|c_l\phi_{jA}\|} \tag{5}$$

This can be accomplished by examining the high coefficient DOF in the mode pairs or by using the MSF to determine if the normalization mode should be multiplied by –1. The use of eCOMAC requires this extra step in mode shape normalization, namely a check for phase consistency between each mode pair using the MSF [26]. The unit normalization and correct phasing are interpreted in the same way as the COMAC. The eCOMAC values are obtained from zero to one, similar to COMAC, where a value closer to zero per DOF will have a higher correlation agreement. Furthermore, Hunt reported in [26] that the eCOMAC can successfully identify measurement errors such as scaling and polarity. This is because the eCOMAC is less sensitive to errors at small motion of DOF and it is considered more robust than the standard COMAC.

6 Modal assurance criteria per pair-sensor (MACco)

The MAC per pair-sensor (MACco) criterion consists in the sequential order of sensors that contribute most to the poor correlation. The MACco is known with different names in the literature: the MAC coordinate criterion [3] or the MAC variation technique [28]. It is an iterative algorithm that takes the modes in $c_j\phi_{id}$ and $c_j\phi_k$ and computes the pair MAC with one sensor "removed" that contribute to low MAC values. The MACco algorithms leads to the best mean MAC for the paired modes, and is a direct indication of where the poorest correlation is located. In this work is suggested the possibility of applying the MACco criterion implemented in [3] to identify the improvement per pair-sensor using the updated stiffness parameters of the FE model obtained in [17].

7 Results

A summary of the results in [17] is introduced to present the initial COMAC results from this study. All the measurements were performed with the Scanning Laser Doppler Vibrometer (SLDV) PSV840 by suspending the CFRP component from very soft cords (free condition), (see Fig. 1), provided by the DLR Braunschweig. The shaker LDS V406 and the stinger with length of 65 mm at node 17 are used to

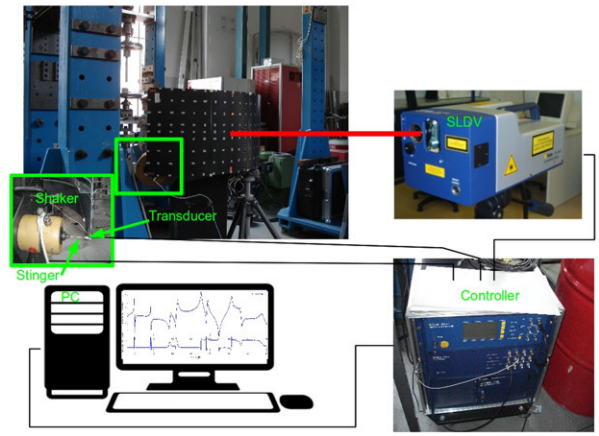

(a)

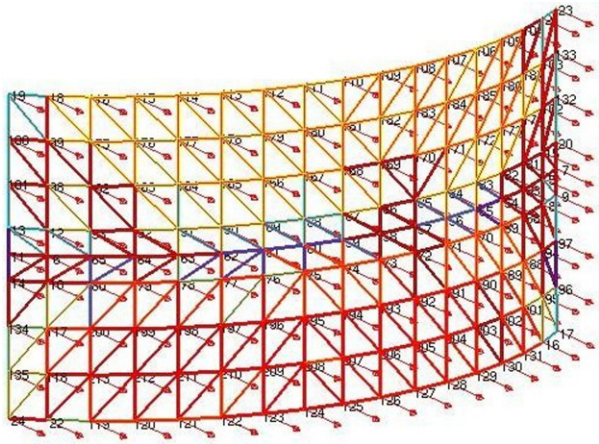

(b)

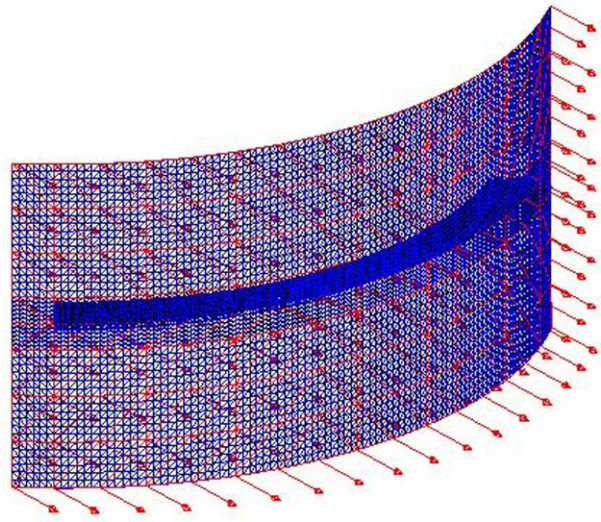

(c)

Figure 1: Experiment: a) Experimental set-up; b) 153 Y-direction sensors; c) 153 sensors in the FEM model [17].

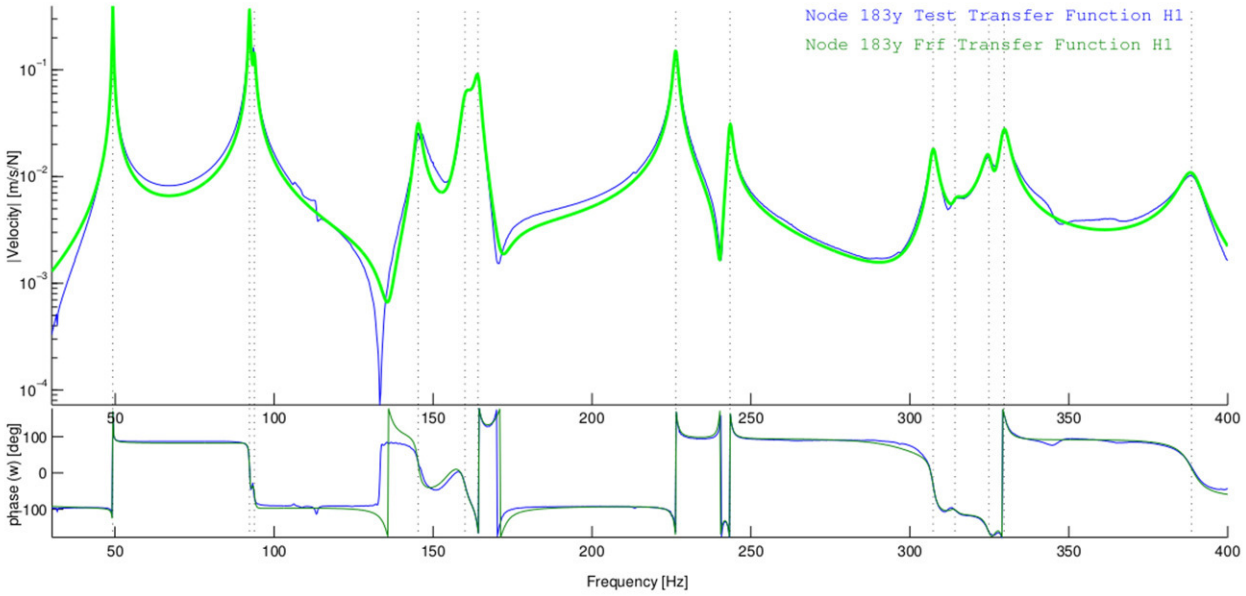

Figure 2: FRF (blue) and fitting curve (green) of composite model at node 183y [17].

excite the structure that produce a sinusoidal vibration velocity signal on the line of sight of the SLDV (out-of-plane). The reason to use a stinger is to ensure that the shaker will only impart force to the structure along the axis of the stinger. The excitation signal selected is a periodic chirp (with frequency span 30–400 Hz, 6400 lines of resolution, with complex average type and number of average per Frequency Response Function (FRF) equal to 10), and reflective foil is used to acquire the response measurement location. The input force is measured using a force transducer Dytran 1051V3 and power amplifier LDS PA 100 in order to record the excitation in the transverse direction.

The interpolation between the experimental measurements uses FRFs [10]. The FRF, (see Fig. 2), allowed us to compare the experimental modal parameters (frequency, damping, and mode shape) with the FE model. The Fast Fourier Transform (FFT) is a fundamental procedure that isolates the inherent dynamic properties of a mechanical structure and in our case with respect to the full and reduce FE model performed in [17].

To approximate the measurements (blue line) through a polynomial function (green line), we used the frequency domain identification of structural dynamics applying the pole/residue parameterization [10], (see Fig. 2). The correlation results vs the experimental model was performed at low frequency (up to 400 Hz), based on the curve-fitting generated from the experimental measurements [10]. A bandwith of 2% is used to localize the eigenfrequencies.

The MAC analysis of the full and reduced FE models obtained in [17] can be observed in Fig. 3 (MATLAB, NASTRAN, and CBMOR model respectively) versus the experimental measurements. Two different elements and solvers were used for reference purposes: CTRIA3 shell (from MSC/NASTRAN) and pshell (from SDTools) [29, 30]. The same number of modes were calculated for both the full and reduced FE models, using super-elements. Cross orthogonality MAC (XOR) was performed to verify the approximation of the MOR in low frequency range (12 mode pairs) versus the full model, see [17].

A good MAC correlation was obtained between the three models and the MAC results displayed an agreement with the literature (the MAC results in the reduced FE model are slightly lower). These MAC results of the full FE models were calculated with the stiffness parameters obtained in [17] performing a DOE full factorial in MINITAB [33]. The nearly double correlation in the experimetal results identified in Fig. 3 and Table 1 for the full and reduced models suggest the presence of the veering phenomena [16, 31] (bending and torsional mode at the same frequency) in our composite component assembly. Thus, lower MAC results in 4, 9, 10 and 11 paired modes (see Fig. 3b) and 5, 9, 10 and 11 paired modes (see Fig. 3c) were archieved and identified using the experimental results.

Furthermore, the reduced model was performed using CMS in terms of substructure /super-element technique, AMLS and residual iteration methods implemented in [3]. The reduced model was built up defining two super-elements.

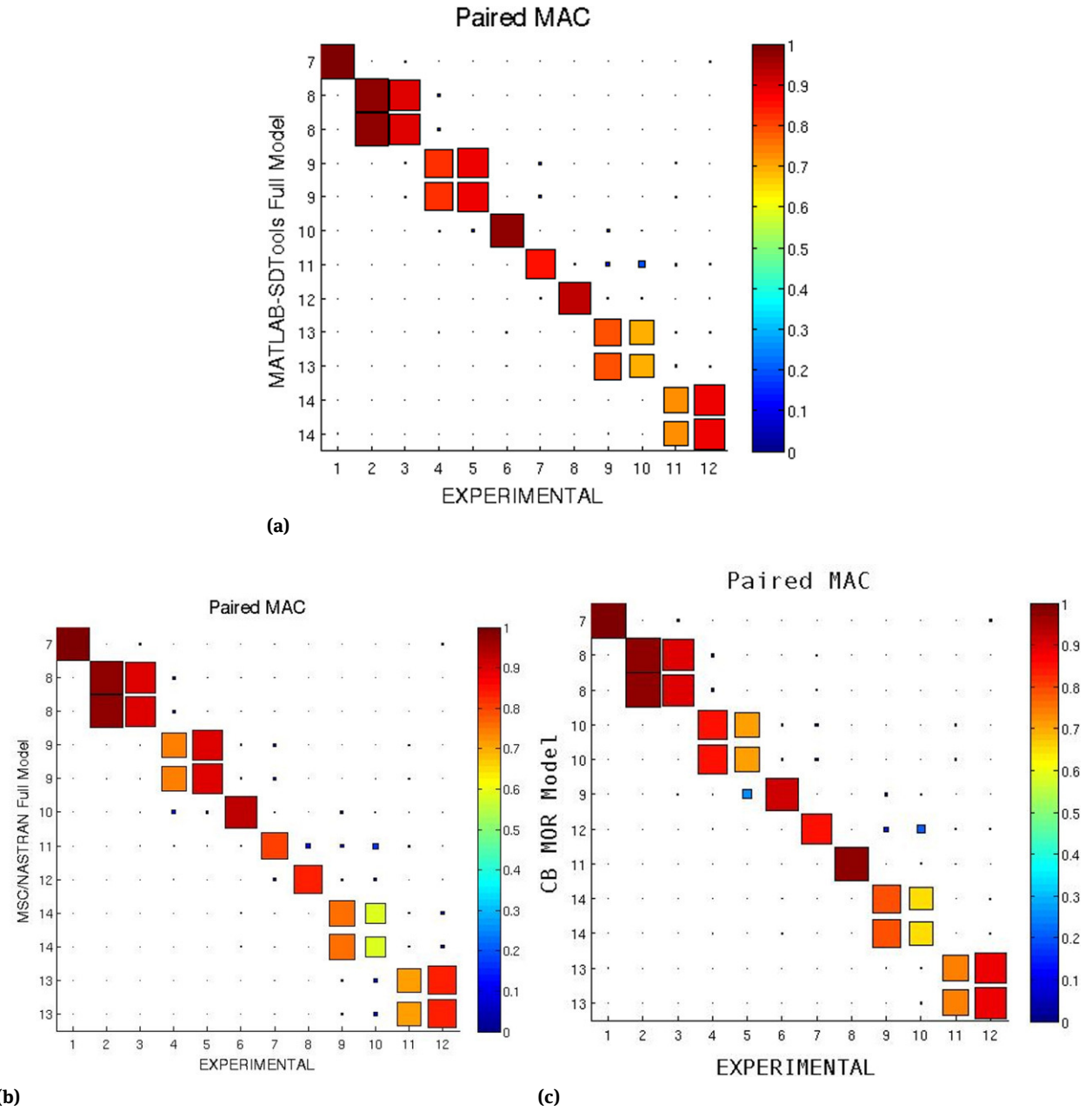

Figure 3: Comparative MAC: a) SDtools-Exp, b) MSC/NASTRAN-Exp, c) CBMOR-Exp [17].

Super-element 1 has 4,753 nodes and 9,219 elements, while super-element 2, has 1,615 nodes and 3,026 elements. The defined super-elements shared 579 DOF distributed in 123 nodes along the common border with different DOF per node, according to the CMS that has defined an appropriate [T] matrix [3]. Some mode shapes of the reduced and full models can be observed (see Fig. 4) as well as experimental measurements (see Fig. 5).

After constructing the set of NM mode pairs, the next step is the calculation of the COMAC values over all the correlated mode pairs, as given in the Eq. (2). Different COMAC results (in blue) can be visualized in Fig. 6 (MATLAB (non-updated), MATLAB (updated), NASTRAN (updated), and CBMOR model, respectively) with respect to the number of sensors (x-axis). Fig. 6a is included as a reference to visualze the improvement between the FE models using the different COMACs. The COMAC values are calculated and displayed an improvement after updating the material properties with similar pattern and values between FE models, (see Figs. 6b, 6c, 6d). The best COMAC result of the full FE models are obtained on sensor 107y=0.036 ,and the worst result on sensor 201y=0.397 (see Fig. 6b). Further-

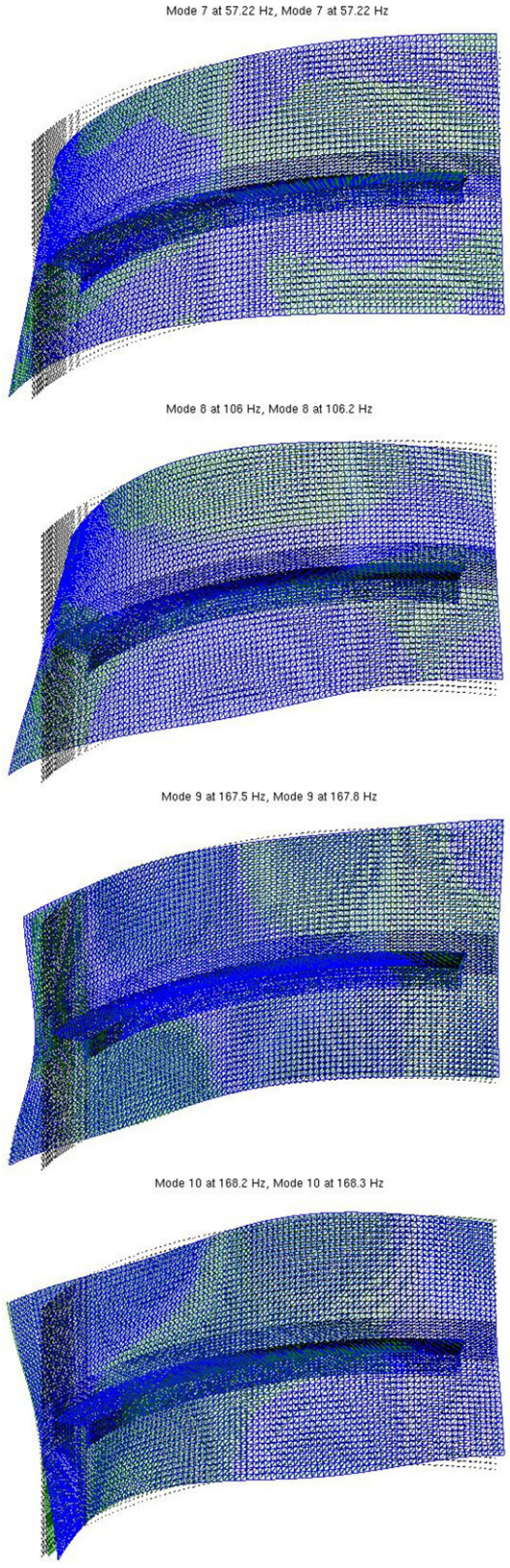

Figure 4: Full model in MATLAB (in blue) vs CBMOR (in green) [17], for values see Table 1.

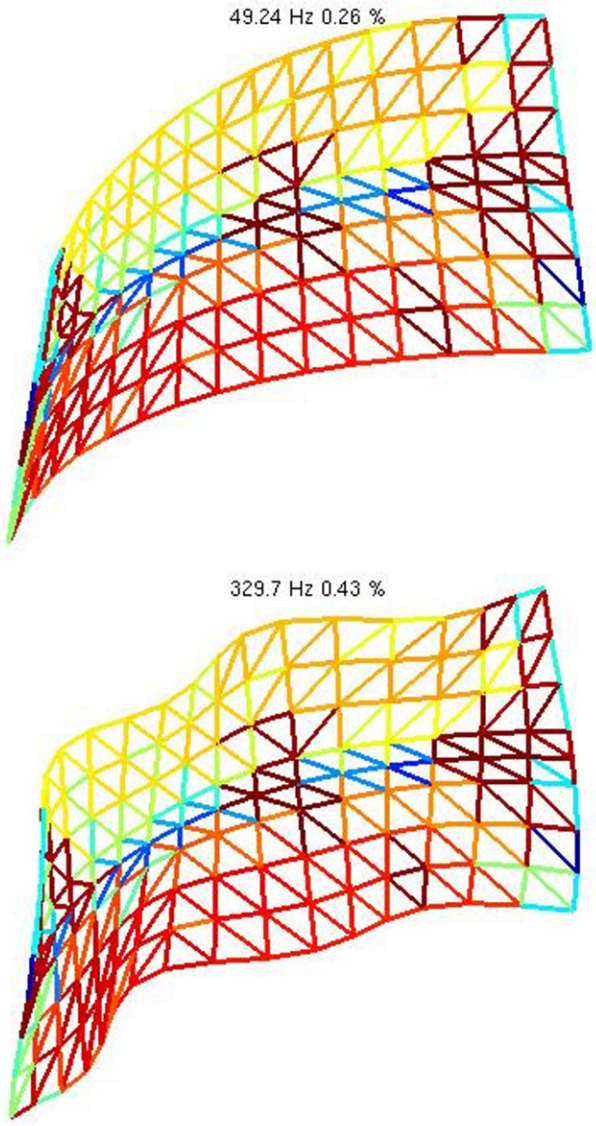

Figure 5: Experimental mode shapes [17].

more, in the reduced FE model the best and worst COMAC results are found on sensors 84y=0.052 and 201y=0.423 respectively.

A pattern in the results can be visualized using the COMAC criterion (see Fig. 6) with slight differences (except for the non-updated FE model). The COMAC-S results, for all the FE models, display an improvement respect to the COMAC values (green line). The best COMAC-S value is displayed in the full FE model in Fig. 6b on sensor 209y=0.019, and the worst value on sensor 201y=0.366. In the reduced FE model the best and the worst COMAC-S values are obtained on sensors 114y=0.026 and 201y=0.388 respectively.

The eCOMAC results (in brown) of the full and reduced FE models show a much lower values respect to the COMAC and COMAC-S results. The eCOMAC criterion displays

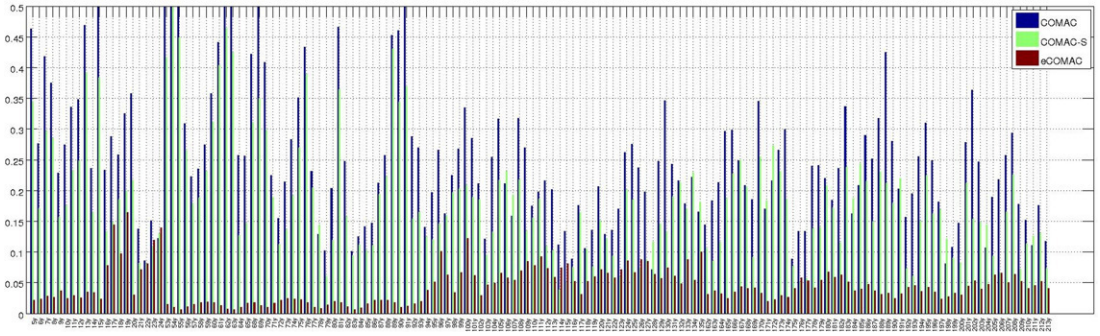

(a)

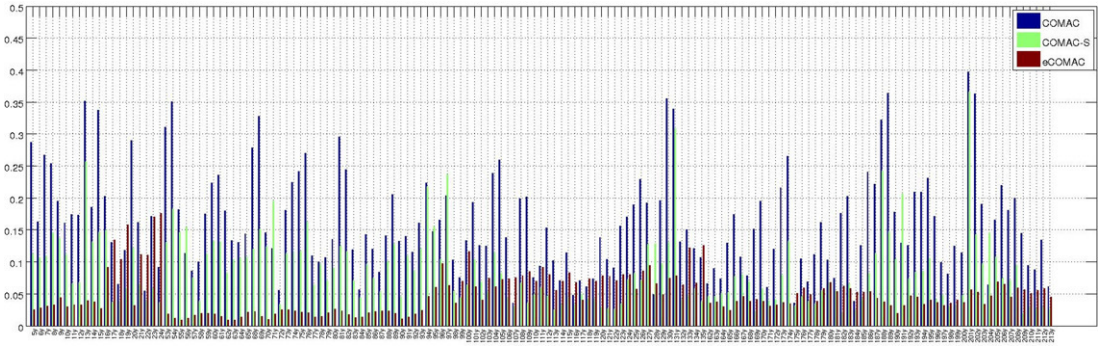

(b)

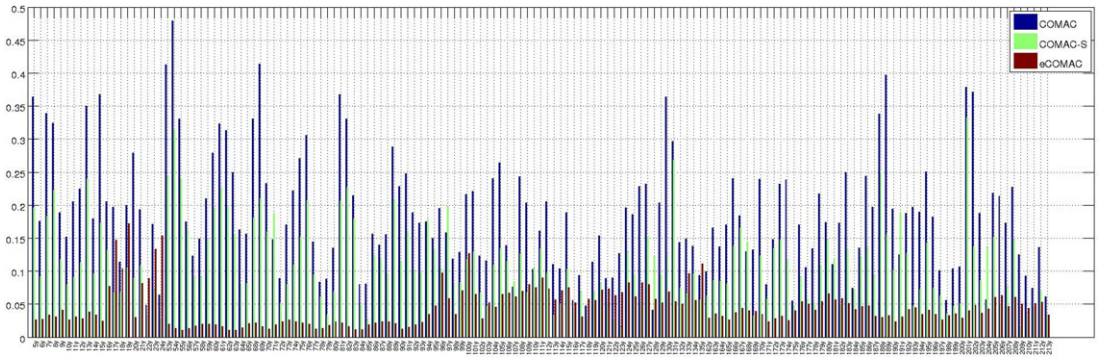

(c)

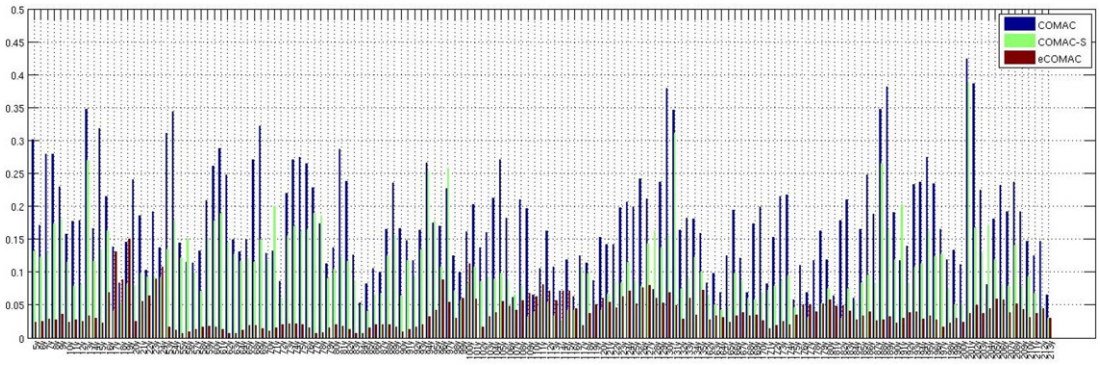

(d)

Y-SENSORS

Figure 6: Comparison of COMACs: a) SDtools-Exp (non-updated), b) SDtools-Exp(updated) c) MSC/NASTRAN-Exp (updated), d) CBMOR-Exp.

Table 1: Full and reduced model results versus experimental results [17].

#	Experimental	#	Full	DF/FA	MAC	CBMOR	DF/FA	MAC
1	49.243	7	57.218	16.2	100	57.218	16.2	100
2	92.265	8	106.02	14.9	97	106.21	15.1	97
3	93.756	8	106.02	13.1	90	106.21	13.3	90
4	145.29	10	168.20	15.8	83	168.29	15.8	84
5	160.05	10	168.20	5.1	86	168.29	5.1	71
6	164.18	9	167.50	2.0	98	167.79	2.2	92
7	226.36	12	236.83	4.6	86	236.93	4.7	85
8	243.40	11	234.99	−3.5	96	235.12	−3.4	97
9	307.33	14	323.93	5.4	81	326.82	5.4	80
10	314.18	14	323.93	3.1	66	326.82	4.0	65
11	324.83	13	315.26	−2.9	74	315.33	−2.9	74
12	329.67	13	315.26	−4.4	90	315.33	−4.3	89

the best results with the exception of few sensors (16y-19y and 21y-24y) for all the FE models. The updated full FE model shown in Fig. 6b, displays the best eCOMAC value at sensor 83y (0.009), with the worst eCOMAC value found at sensors 24y (0.176). Furthermore, in the reduced FE model the worst and the best eCOMAC values are found in the same sensors (24y=0.15 and 83y=0.006 respectively). It can be appreciated that the eCOMAC in the reduced FE model displays slightly enhanced results versus the full FE models (see Fig. 7). The lower eCOMAC values suggest a good normalization and phase correlation between pair coordinates of the full and reduced FE model with the experimental results.

The lower COMACs values obtained with different criterias suggest a good agreement of the full and reduced FE models versus the experimental measurements. It is necessary to mention the good agreement between different COMAC, COMAC-S and eCOMAC using two types of elements and solvers.

Applying the MACco criterion it is possible to analyze the paired mode per sensors ordered in ascending order leading to the best "mean MAC" for the paired modes, see Fig. 8. The MACco criterion and COMAC criteria also display a significant improvement per mode paired-sensor, which contribute to high MAC values using the stiffness parameters obtained in [17]. The "mean MAC" (represented as a solid line in blue in Fig. 8) is obtained by calculating the mean of the MAC per mode paired-sensor selected of each FE model. The x-axis of each graph in Fig. 8 represents the total number of sensors (153 sensors) used with the MACco algorithm. Only the worst ten MAC results per paired mode-sensor of each FE model are displayed in Tables 2 and 3.

Table 2 is divided into three sections, displaying the MACco results of the non-updated and updated full FE models respectively. The values of the "mean MAC" can be observed in Table 2 of each FE model. In Table 3 the MACco results of the reduced model are displayed. In both tables an improvement using the updated stiffness parameters is observed. Before updating the material properties, the sensors 16y displays the worst "mean MAC" = 77. After updating the stiffness parameters, the sensors 16y shows a considerable improvement when applying the MACco criterion in the full and reduced models ("mean MAC" of 88, 85 and 87 respectively). The worst paired mode per sensor is identified in the pair number 16 of each updated FE model (MAC per paired-sensor of 67, 60, 67 respectively) on sensor 16y. The worst paired mode per sensor of the non-updated FE model is identified in the pair number 10 on the sensor 16y with "mean MAC" value of 58. With the exception of the sensors 104y and 133y in Tables 2 and 3, the worst MACco results in the updated FE models are identified in the same sensors, (see Fig. 9), per paired mode on the edge of the CFRP.

8 Conclusions

The results have shown a good correlation in dynamic behavior of the composite component assembly model using the pshell and CTRIA3 elements applying different solvers for comparative purposes in the FE models. The MAC values obtained (eigenfrequencies and eigenvectors) for the full and reduced FE models versus the experimental measurements in the previous work are consistent applying different coordinate criteria (COMACs and MACco). The im-

Table 2: MACco results - Full models versus experimental results.

Pair number		7	8	9	10	11	12	13	14	15	16	17	18
Experimental		1	2	3	4	5	6	7	8	9	10	11	12
SDTools FEM (non-updated)		7	8	8	9	9	10	12	11	14	14	13	13
Sensor	Mean MAC												
All	77	99	97	90	58	87	73	65	63	73	61	72	86
16y	77	99	97	91	57	87	73	65	63	73	62	75	87
23y	78	99	97	92	62	88	71	69	59	72	63	74	86
21y	78	99	97	93	66	89	70	71	57	72	63	74	87
129y	78	99	97	93	65	89	70	70	58	72	65	75	88
96y	79	99	97	93	64	89	70	70	60	73	66	76	88
95y	79	99	97	94	64	89	71	70	60	73	66	77	88
17y	79	99	97	94	62	90	72	68	63	73	66	78	90
128y	80	99	97	94	61	89	73	68	63	73	68	79	90
133y	80	99	97	94	64	90	71	70	60	73	69	79	90
104y	80	99	97	95	66	90	71	70	61	74	69	79	90
Experimental		1	2	3	4	5	6	7	8	9	10	11	12
SDTools FEM (updated)		7	8	8	10	10	9	12	11	14	14	13	13
Sensor	Mean MAC												
All	87	100	97	90	83	86	98	86	96	81	66	74	90
16y	88	100	97	91	83	86	98	86	96	82	67	76	90
96y	88	99	97	91	82	87	98	87	97	83	69	77	90
95y	88	100	97	91	82	87	98	88	97	84	70	78	90
23y	89	99	97	92	84	87	97	88	96	84	73	77	90
131y	89	100	97	93	85	88	97	89	96	85	73	77	90
17y	89	100	97	93	84	89	97	89	97	85	74	78	91
21y	90	100	97	94	85	89	97	89	97	85	76	78	91
129y	90	100	97	94	85	89	97	89	97	86	77	79	92
128y	90	100	97	94	84	89	97	89	97	86	79	80	92
97y	91	100	97	94	84	89	97	90	97	87	79	81	92
Experimental		1	2	3	4	5	6	7	8	9	10	11	12
MSC/NASTRAN FEM (updated)		7	8	8	9	9	10	11	12	14	14	13	13
Sensor	Mean MAC												
All	83	100	97	90	74	90	93	81	84	76	59	71	84
16y	84	99	97	91	74	91	93	81	85	77	60	74	84
23y	84	99	97	92	77	91	92	82	83	76	63	73	84
96y	85	99	97	92	76	92	93	82	84	77	64	74	85
21y	85	99	97	93	79	92	92	83	83	77	65	74	85
95y	85	100	97	93	79	92	92	84	83	78	66	74	85
17y	86	100	97	93	77	93	93	83	85	78	67	76	87
129y	86	100	97	93	77	93	93	82	85	78	68	78	88
131y	86	100	97	94	77	93	93	83	86	79	69	78	88
128y	87	100	97	94	76	93	93	83	86	80	71	79	88
133y	87	100	97	95	79	93	93	84	85	80	72	78	88

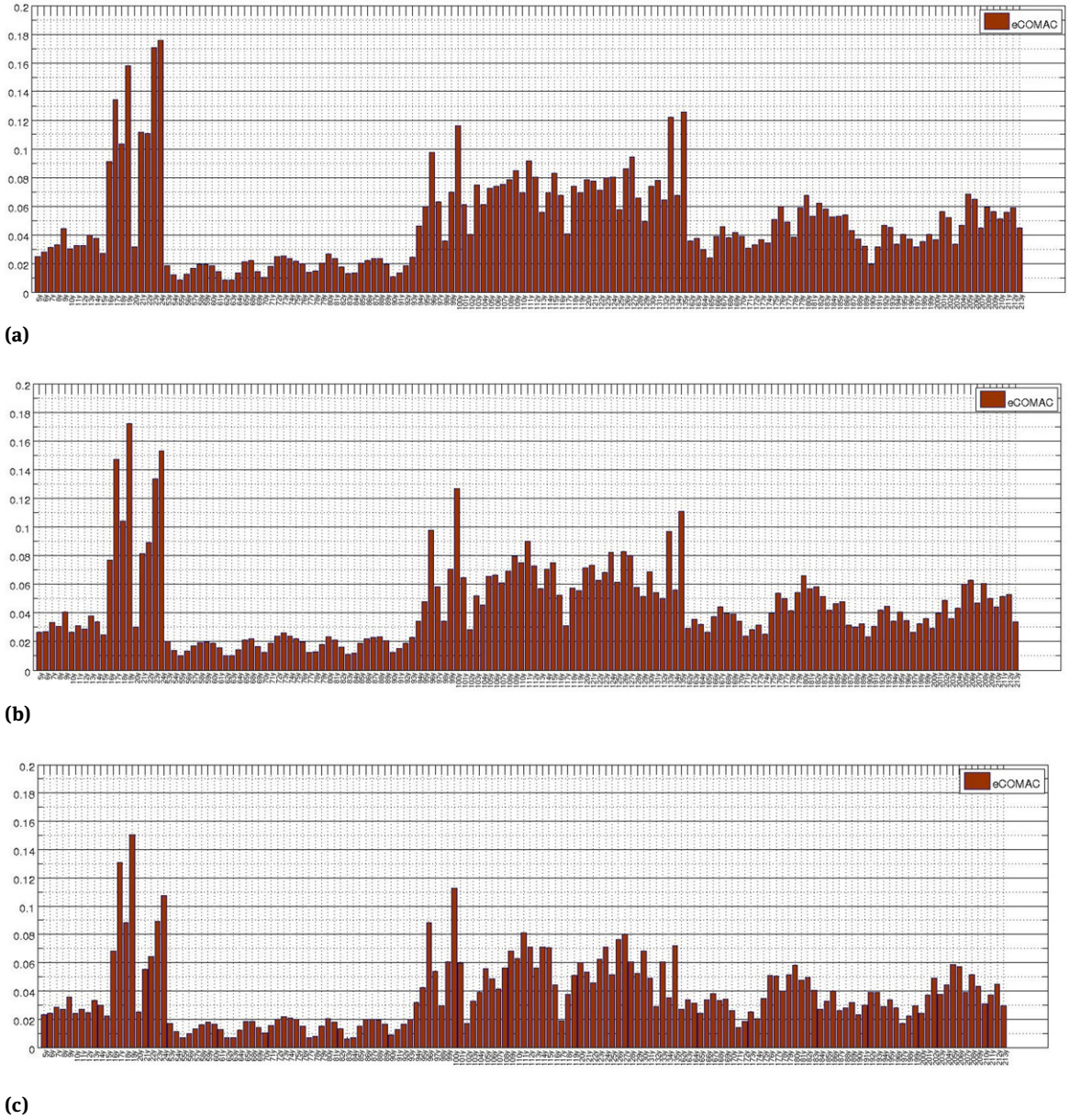

Figure 7: Comparison of eCOMACs: a) SDtools-Exp(updated) b) MSC/NASTRAN-Exp (updated), c) CBMOR-Exp.

provement of the COMACs results is observed in all the FE models once the stiffness parameters were updated. The full FE model with pshell elements displays the best COMAC, COMAC-S and MACco results between full FE models. The reduced model obtained by means of the Craig-Bampton MOR method (the reduced model has 123 nodes with 2 substructures and 579 DOF) has demonstrated a good agreement with the experimental results using different COMACs. The eCOMAC values of the reduced model present a slight enhancement in the results and are the best values versus the eCOMAC results obtained in the full models. The MACco results of the reduced FE model also show a good agreement with the experimental measurements with respect to the full FE model. The experimental results performed with an SLDV and the identification of pole/residues used are suitable to validate the dynamic analysis of CFRP using coordinate assurance criteria applying modal order reduction. In order to achieve high quality COMACs results in the FE models that can adequately capture the dynamic behavior, the material properties were updated by applying a DOE and are crucial in the MOR correlation with the experimental results. The

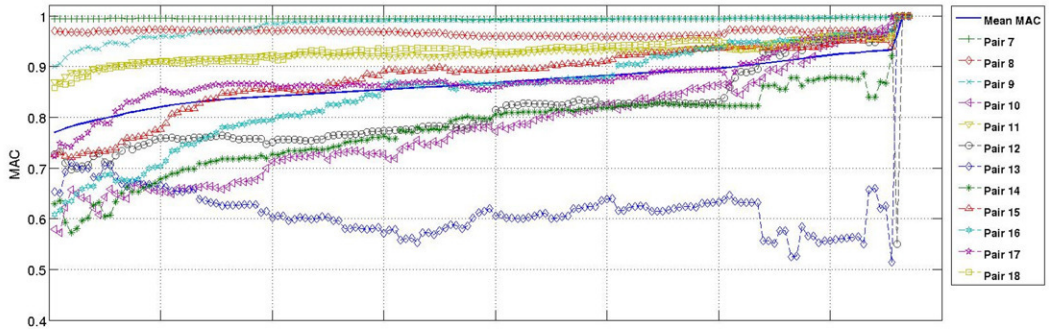

(a)

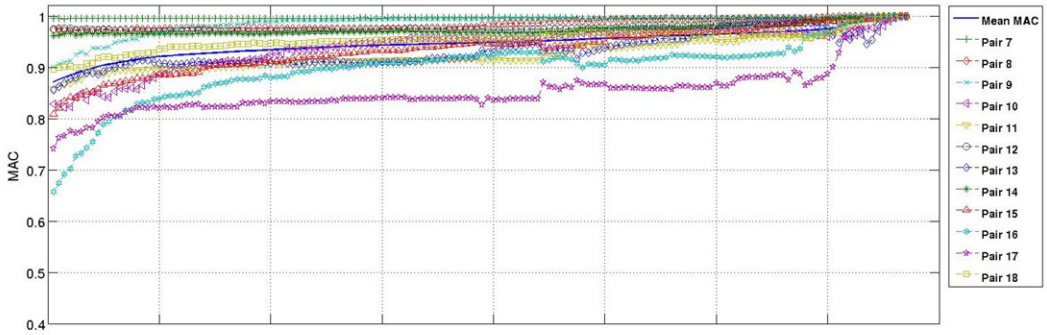

(b)

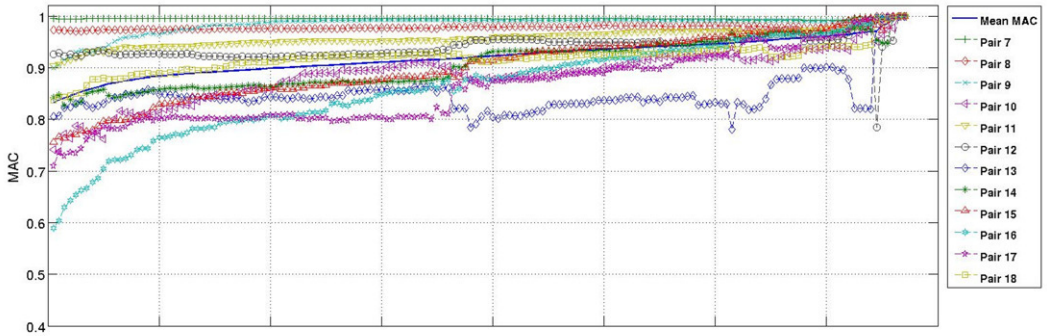

(c)

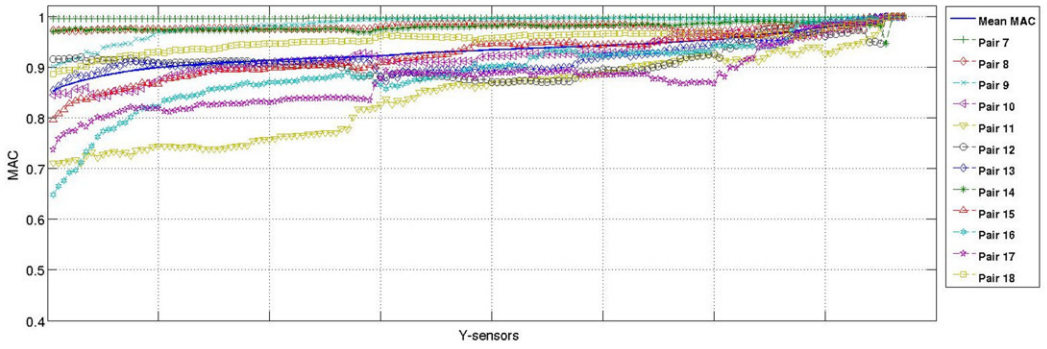

(d)

Figure 8: Comparison of MACcos: a) SDtools-Exp (non-updated), b) SDtools-Exp (updated), c) MSC/NASTRAN-Exp (updated), d) CBMOR-Exp.

Table 3: MACco results - Reduced model versus experimental results.

Pair number		7	8	9	10	11	12	13	14	15	16	17	18
Experimental		1	2	3	4	5	6	7	8	9	10	11	12
Reduced FE model CBMOR		7	8	8	10	10	9	12	11	14	14	13	13
Sensor	Mean MAC												
All	85	100	97	90	84	71	92	85	97	80	65	74	89
16y	86	100	97	91	85	71	92	86	97	81	67	76	89
95y	86	100	97	91	85	71	92	87	97	82	68	77	89
96y	87	100	97	91	85	71	92	88	97	83	69	77	89
131y	87	100	97	92	86	72	92	89	98	83	70	77	89
129y	87	100	97	92	86	71	92	88	98	84	71	79	89
23y	87	100	97	93	86	72	91	88	97	84	73	78	90
17y	88	100	97	93	85	73	91	88	97	84	74	79	91
128y	88	100	97	93	84	72	92	89	97	85	76	80	91
21y	88	100	97	94	84	73	91	89	97	85	77	80	91
97y	88	100	97	94	84	73	91	90	97	85	78	80	92

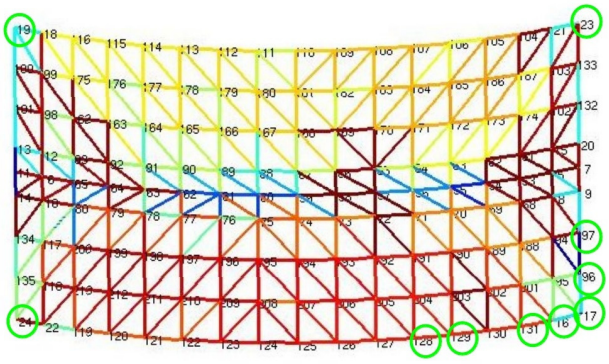

Figure 9: Identification of the "worst Y-sensors" (green) using MACco.

COMACs and MACco results obtained in full and reduced FE models based on the Rayleigh-Ritz approach to simulate dynamic behavior of a CFRP assembly suggest the following conclusions. A high accuracy in the updated stiffness parameters obtained that might be used to verify the mechanical properties, such as the Poisson ratio, along the measured CFRP. The updated mass and stiffness matrices in the full model played an important roll in the MNET procedure to perform the CBMOR method. The identification of the veering phenomena in the CFRP component assembly looked at the full and reduced FE models using the MAC. The application of the MACco to identify the improvement per pair-sensor once it was updated the FE model. The validation of the correlation proved applying different COMACs based on the type of finite elements used. Finally, the slightly improvement of the transformation matrix of the reduced model observed in the eCOMAC using superlements, the AMLS and residual iteration methods implemented in SDTools that show a good normalization and phase correlation with the experimental results.

It is needed to perform an assesment with other elements of similar characteristics for accuracy and sensitivity purposes applied to different CFRP. Different mode shape expansion methods of coupled predictions consisting of local FE model, enhanced AMLS, classical theory of structural modification by coupling, and CMS with interface model order reduction should be assessed for future work to validate the MNET results.

References

[1] Hurty W.C., Dynamic analysis of structural systems using component modes, AIAA J., 3(4), 1965, 678–685

[2] Craig R.J., Bampton M., Coupling of substructures for dynamic analyses, AIAA J., 6(7), 1968, 1313–1319

[3] Balmès E., Structural dynamics toolbox and FEMLink, User's Guide, SDTools, Paris, France, 2016, http://www.sdtools.com/help/sdt.pdf

[4] Van der Valk P.L.C., Model Reduction & interface modeling in dynamic substructuring, MSc. thesis, TU Delf, Netherlands, 2010.

[5] Reddy J. N., Mechanics of Laminated Composite Plates and Shells: Theory and Analysis, CRC, Press Second edition, 2004

[6] Cunedioğlu Y., Muğan A., Akçay H., Frequency domain analysis of model order reduction techniques, Finite Elements in Analysis and Design, 42, 2006, 367–403

[7] Balmès E., Optimal Ritz vectors for component mode synthesis using singular value decomposition, AIAA J., 34(5), 1996, 1256–1260

[8] Balmès E., Use of generalized interface degrees of freedom in component mode synthesis, IMAC 1996, 204–210
[9] Balmès E., Efficient Sensitivity Analysis Based on Finite Element Model Reduction, IMAC 1997, 1–7
[10] Balmès E., Frequency domain identification of structural dynamics using the pole/residue parametrization, IMAC 1996, 540–546
[11] Balmès E., Review and Evaluation of shape expansion methods, IMAC 2000, 555–561
[12] Balmès E., Modes and regular shapes. How to extend component mode synthesis theory, XI DINAME, 28th February-4th March 2005, 1–14
[13] Bobillot A., Balmès E., Iterative computation of modal sensitivities. AIAA J., 44(6), 2006, 1332–1338
[14] Kaplan M., Implementation of Automated Multilevel Substructuring for frequency response Analysis of structures, PhD thesis, The University of Texas at Austin, U.S.A.
[15] Jin-Gyun K., Seung-Hwan B., Phill-Seung L., An enhanced AMLS method and its performance. Computed methods in applied mechanics and engineering, 287, 2015, 90–111
[16] Bonisoli E., Delprete C., Espoito M., Mottershead J. E., Structural Dynamics with conicident Eigenvalues: Modeling and Testing, Modal Analysis Topics, 3, Conferencing Proceedings of the Society for Experimental Mechanics Series 6, 2011, 325–337
[17] Peredo Fuentes H., Zehn M., Application of the Craig-Bampton model order reduction method to a composite component assembly, Facta Universitatis, series: Mechanical Engineering, 12(1), 2014, 37–50
[18] Meuwissen M.H.H., An inverse method for the mechanical characterization of metals, PhD thesis, Technische University Eindhoven, Netherlands, 1998
[19] Van Ratingen M.R., Mechanical identification of inhomogeneous solids, PhD thesis, Technische University Eindhoven. Netherlands, 1994
[20] Gade S., Møller N.B., Jacobsen N.J., and Hardonk B., Modal analysis using a scanning laser Doppler vibrometer, Sound and Vibration Measurements A/S, 2000, 1015–1019
[21] Ewins D. J., Modal testing: Theory and practice, Research Studies Press, Letchworth, U. K., 1995
[22] Montgomery D. C., Design and analysis of experiments, 5th ed., John Wiley & Sons Inc., USA, 2000
[23] Allemang R.J., Brown D.L., A correlation coefficient for modal vector analysis, IMAC 1982, 110–116
[24] Lieven N. A.J., Ewins D.J., Spatial correlation of mode shapes, The coordinate modal assurance criterion *(COMAC)*, IMAC 1988, 690–695
[25] Catbas F.N., Aktan A.E., Allemang R.J., Brown D.L., Correlation function for spatial locations of scaled mode shapes (COMEF), IMAC 1998, 1550–1555
[26] Hunt D.L., Application of an enhanced coordinate modal assurance criteria (ECOMAC), IMAC 1992, 66–71
[27] Allemang R.J, The modal assurance criterion – twenty years of use and abuse, Sound and vibration, 2003, 14–21
[28] Brughmans M., Leuridan J., Blauwkamp K., The application of FEM-EMA correlation and validation techniques on a body-in-white. IMAC 1993, 646–654
[29] Batoz J.L., Bathe K.J., Ho L.W., A Study of three node triangular plate bending elements, International Journal for Numerical Methods in Engineering, 15, 1980, 1771–1812
[30] Batoz J.L., Lardeur P., Composite plate analysis using a new discrete shear triangular finite element, International Journal for Numerical Methods in Engineering, 27, 1989, 343–359
[31] Pierre C., Mode Localization and eigenvalue loci of Bridges with Aeroeslastic effects, Journal of Engineering Mechanics 126(3), 1988, 485–502
[32] Schwarz B., Richardson M., Scaling mode shapes obtained from operating data, IMAC 2003, 1–8
[33] Minitab 17 Statistical Software, Computer software, State College, PA:Minitab, Inc., 2010, (www.minitab.com)

Research Article

Humberto Peredo Fuentes*

Application of the mode-shape expansion based on model order reduction methods to a composite structure

https://doi.org/10.1515/eng-2017-0026
Received Jul 09, 2016; accepted May 31, 2017

Abstract: The application of different mode-shape expansion (MSE) methods to a CFRP based on model order reduction (MOR) and component mode synthesis (CMS) methods is evaluated combining the updated stiffness parameters of the full FE model obtained with a mix-numerical experimental technique (MNET) in a previous work. The eigenvectors and eigenfrequencies of the different MSE methods obtained are compared with respect to the experimental measurements and with a full FE model solutions using the modal assurance criteria (MAC). Furthermore, the stiffness and mass weighted coefficients (K-MAC and M-MAC respectively) are calculated and compared to observe the influence of the different subspace based expansion methods applying the MAC criteria. The K-MAC and M-MAC are basically the MAC coefficients weighted by a partition of the global stiffness and mass matrices respectively. The best K-MAC and M-MAC results per paired mode-sensor are observed in the subspace based expansion MODAL/SEREP and MDRE-WE methods using the updated stiffness parameters. A strong influence of the subspace based on MOR using MSE methods is observed in the K-MAC and M-MAC criteria implemented in SDTools evaluating the stiffness parameters in a contrieved example.

Keywords: Composites, Mode-shape expansion, GUYAN, MODAL, SEREP, DYNAMIC, MDRE, MDRE-WE, MAC, K-MAC, M-MAC

1 Introduction

The concept of mode-shape expansion (MSE), model order reduction (MOR) and component mode synthesis (CMS) methods play a significant role in the dynamic analysis of conventional materials or carbon fiber reinforced polymer (CFRP), especially comparing large analytical set of degree of freedom (DOF) versus experimental models with relatively small number of sensors [1–34]. The experimental measurements (EM) are critical for the success of any structural dynamic analysis and contain characteristics that cannot be obtained analytically [1]. Traditionally, interface model reductions [1–3, 5–9, 29] are used to estimate the motion at interfaces DOFs by the motion of sensors using EM, where the EM played a significant role in the correlation and updating of analytical models. Many approaches to correlate analytical models require measured vectors to be available at the full set of finite element DOF. Likewise, model updating in the set of tested DOF requires the large model to be reduced to a much smaller size but without distortion of the reduced model. Coupled predictions can also be estimated using MSE methods [1]. Two groups can basically be distinguished to characterize coupled predictions: unmodified structures, see [5] for further details, and modified structures illustrated in [1–3, 5–9, 29]. The difference between the two groups is basically that the first group needed to impose some of the measurement points on the interface while in the second group, it is not needed. The methodology presented by Corus *et al.* in [6] and Balmès [1–3, 8, 9, 29] combined techniques offering the advantages of the second group of coupled predictions consisting of: a local FE model, classical theory of structural modification by coupling it with MSE and CMS with several interface MOR methods (subspace selection) [1–3, 8]. The use or not of modifications in this methodology [1] is distinguished as an indicator for the validity of coupled predictions. The MSE methodology concept is used in this work to estimate the responses of all degrees of freedom of the interface of a CFRP component defined by the motion of sensors evaluating the stiffness parameters of a full finite element (FE) model obtained in [10]. The accuracy of the experimental measurements obtained in [10] and verified in [11] using discrete Kirchhoff triangular (DKT) elements including transversal shear effects [26], also know as discrete shear triangular (DST) [27, 28] and a reduced finite element model using superlements

***Corresponding Author: Humberto Peredo Fuentes:** Institute of Mechanics, Technical University Berlin, Strasse des 17. Juni 135, 10623 Berlin, Germany; Email: hperedo@mailbox.tu-berlin.de

applying the Craig-Bampton model order reduction based in Ritz vectors defined in [29]. Different advance interpolation MSE methods implemented in [29] are performed to determine the coupled predictions in the CFRP component such as: MODAL [12], SEREP [13], STATIC (based on Guyan reduction [14]), DYNAMIC [15], minimum residual dynamic expansion (MRDE) [16], and minimum residual dynamic expansion with test-error (MRDE-WE) [17]. The MRDE and MRDE-WE are also known as hybrid methods. The MSE methods are calculated using EM, curve-fitting algorithms, and a FE model to obtain the interpolation results. Thus, these advance MSE interpolation methods can be evaluated to determine the paired accuracy predictions in the CFRP component for unmeasured DOFs in a CFRP component applying the modal assurance criterion [19] (MAC) based on the EM, the curve-fitting algorithms, and the updated stiffness parameters of the full FE model obtained with a MNET. The impact of the accuracy in the results using MSE is documented in the literature for conventional materials taking in consideration residual modes [18]. The application of these MSE methods and it's accuracy to a CFRP is not documented in the literature. The influence of the MOR applying MSE methods implemented in [29] is evaluated using the stiffness and mass weighted criteria or K-MAC and M-MAC (normalized stiffness and mass cross-orthogonality criteria respectively) based on the MAC. In section 2, it is introduced a brief theoretical background of this MSE methodology developed by Corus and Balmès. In section 3, the results are discussed based on the updated stiffness parameters obtained of the FE model versus the modification of these stiffness parameters (contrieved example). The conclusions are discussed in section 4.

2 Theoretical background

Initially, the theoretical background of the MSE methodologies combining different techniques introduced in [1, 2, 4, 6, 9, 29] was established as a close loop prediction problem for structural modifications. The knowledge of the close loop prediction problem between the physical and the analytical model is used in the industry applying experimental measurements and the finite element method (FEM) to reduce the cost of prototypes components. A number of steps are described in [29] such as: EM, curve-fitting algorithms, laminate theory, form of the lineal differential equation, dealing with continuous interfaces and the evaluation of the error. These steps are briefly introduced and adapted for the objective of this work in the next sections.

2.1 Experimental measurements

The experimental measurements described by the frequency response functions (FRF). $H(\omega_i)$, is defined as the ratio of the transformed excitation [19]:

$$H(\omega_i) = \frac{X(\omega_i)}{F(\omega_i)}, \tag{1}$$

where $H(\omega_i)$ is the measured (predicted) FRF transfer function matrix, $X(\omega_i)$ the Fourier spectrum of response, and $F(\omega_i)$ is the Fourier spectrum of excitation force. The FRF in Eq. (1) is the inverse of the dynamic stiffness:

$$H(\omega_i) = \left[-\omega_i^2[M] + \omega_i[C] + [K]\right]^{-1}, \tag{2}$$

where the mass $[M]$, damping $[C]$ and stiffness $[K]$ matrices in Eq. (2) are dependent of physical parameters such as material's density, Young's and shear moduli and Poisson's ratio [10].

2.2 Curve-fitting Algorithms

The goal of using the curve-fitting algorithms is to produce an accurate estimation of the modal parameters of the CFRP component using the FRF. There are several methods that can be used to estimate the modal parameters based on one mode at a time (SDOF) or more modes at a time (MDOF, global and multi-reference) [30]. The global curve-fitting expression called the rational fraction polynomial (RFP) or partial fraction expansion (PFE) is received with great interest and attention for its simplicity and easy implemention in personal computers (PC) [31] for the last 20 years [32–34]. The RFP form of poles and residues, illustrated in Eq. (3), offers advantages over other forms documented in literature [30, 31, 34].

$$H(s) = \sum_{k=1}^{modes} \left(\frac{[R_k]}{s - \lambda_1} + \frac{[R_k^\star]}{s - \lambda_2^\star} \right) \tag{3}$$

The residue matrices $[R_k]$ and $[R_k^\star]$ are defined as the constant numerators of the transfer function matrix, "modes" are the number of modes of vibration, λ_r is the pole location and (s) is the Laplace variable. The RFP form in Eq. (3) is typically used when the modal data is obtained from experimental transfer function measurements (FRF's). Traditionally the relationship between residues and mode shapes are expressed in terms of FRF or modal parameters. The identification of experimental measurements is determined obtaining modes whose poles are located in the test frequency range selected. A characteristic of the curve-fitting algorithms *identification De Résidus*

Complexes (IDRC) and *Identification De Résidus Multiples* (IDRM) used in this work are the residual terms $[R_k(\lambda_r)]$, $[E(s)]$ and $[F(s)]$ defined in [21]. The contributions of the residual terms in the transfer functions are used to evaluate the high and low frequency mode terms respectively, see Eq. (4).

$$H(s) = \sum_{k=1}^{modes} \left(\frac{[R_k]}{s-\lambda_1} + \frac{[R_k^\star]}{s-\lambda_2^\star} \right) + [E(s)] + \frac{[F(s)]}{s^2} \quad (4)$$

The residual terms are known also a residual modes or residual vectors [21] and it is documented the advantages of the application of the residual terms in the literature [18]. Thus, the estimation of the poles depends linearly on the residual terms $[R_k(\lambda_r), E(s), F(s)]$ solving the linear least squares problem associated with the frequency domain output error illustrated in Eq. (5).

$$\left[R_k(\lambda_r), E(s), F(s)\right] = arg\ min\ \left|[H(s)]_{test} - H(s)\right|^2 \quad (5)$$

where the residue matrix $[R_k] = \{c\phi_j\}\{\phi_j^T b\}$ is given by the product of a column observability $\{c\phi_j\}$ and row controllability $\{\phi_j^T b\}$ defined in [21]. The residue matrix $[R_k]$ is often expressed as $[A_j] = \{\phi_j\}\{L_j\}$ in the structural dynamics community, where $[A_j]$ is commonly called *modal participation factor*, $\{\phi_j\}$ is the modeshape and $\{L_j\}$ is the controllability [29]. Assuming that the complex poles come in conjugate pairs and the residue matrices too, the normal mode residue with symmetric pole structure can be defined as a rational fraction expression (to determine the damping ratios that are different for each pole using the normal mode model format proposed by Balmès in [21] of the form:

$$H(s) = \sum_{j=1}^{N} \frac{\{[c]\phi_j\}\{\phi_j^T[b]\}}{s^2 + 2\zeta_j\omega_j s + \omega_j^2} = \sum_{j=1}^{N} \frac{[T_j]}{s^2 + 2\zeta_j\omega_j s + \omega_j^2} \quad (6)$$

where the contribution of each mode is characterized by the pole frequency ω_j, damping ratio ζ_j, and the normal mode residues matrix $[T_j]$ with symmetric pole structure [21]. The matrix $[T_j]$ is equal to the product of the normal mode output shape matrix $\{[c]\phi_j\}$ by the normal mode input shape matrix $\{[b]\phi_j^T\}$. The matrix $[b]$ is called the input shape matrix and the matrix $[c]$ is called the output shape matrix. This matrix description is established based on several assumptions in [29] and it can be applied considering second order models of the form introduced in subsection 2.4.

2.3 Laminate Theory

The classical laminate theory (CLT) and the first-order shear deformation laminate theory (FSDT) are applicable to linear and composite elastic materials [26], by means of the Discrete Mindlin Kirchhoff Triangle (DMKT) elements also known as Discrete Shear Triangle (DST) elements [27, 28]. One characteristic of these triangle elements is that the Mindlin/Reissner plate theory can be reduced theoretically to the Kirchhoff plate theory if the transverse shear effects are not important [28]. These laminate theories have been used extensively to predict elastic behavior of the traditional fiber-reinforced polymers (FRP). FRP materials (carbon or glass FRP) are widely used in aerospace and construction applications. One important consideration is to have perfectly bonded layers with a uniform thickness (see Figure 1). The mechanical properties measured in ply level experiments are used to populate the stiffness matrix for each ply. The stiffness matrices for the individual plies are combined to form the laminate stiffness matrix $ABD-\tilde{S}$ in:

$$\begin{Bmatrix} N_i \\ M_i \\ S_{ij} \end{Bmatrix} = \begin{bmatrix} A & B & 0 \\ B & D & 0 \\ 0 & 0 & \tilde{S} \end{bmatrix} \begin{Bmatrix} \epsilon_i \\ \kappa_i \\ \gamma_{ij} \end{Bmatrix}. \quad (7)$$

The $ABD-\tilde{S}$ matrix in Eq. (7) relates forces (N_i), moments

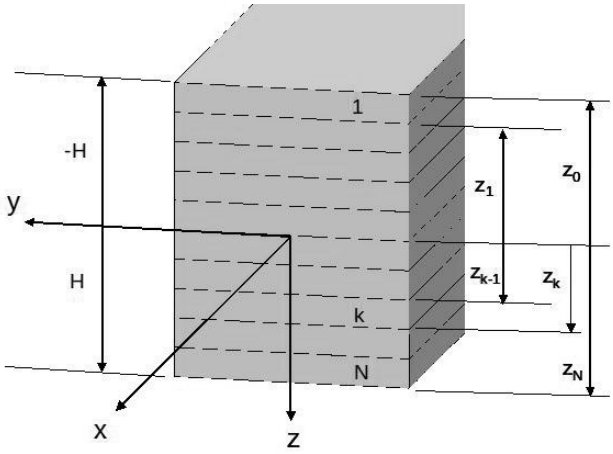

Figure 1: Configuration of composite layers [10].

(M_i) and shear stresses (S_{ij}) to strains (ϵ_i), curvatures (κ_i) and shear strains (γ_{ij}). The components of the $ABD-\tilde{S}$ matrix are given in Eqs. (8)-(11), where N is the number of plies, $[Q_k]$ is the stiffness matrix of each ply, z_k denotes the distance from the laminate's mid-plane to the edges of single plies, and K is the shear correction factor usually taken as 5/6:

$$[A] = \sum_{K=1}^{N} [\bar{Q}_k]^{(k)}(z_{k+1} - z_k), \quad (8)$$

$$[B] = \frac{1}{2}\sum_{K=1}^{N}[\bar{Q}_k]^{(k)}(z_{k+1}^2 - z_k^2), \tag{9}$$

$$[D] = \frac{1}{3}\sum_{K=1}^{N}[\bar{Q}_k]^{(k)}(z_{k+1}^3 - z_k^3), \tag{10}$$

$$[\tilde{S}] = K\sum_{K=1}^{N}[\bar{Q}_k]^{(k)}(z_{k+1} - z_k), \tag{11}$$

2.4 Form of the linear differential equation

It is considered only second order models of the form, see [10] and [29], and reintroduced in this section to perform MSE to a composite component assembly) in Eq. (12):

$$\begin{aligned}\left[[M]s^2 + [C]s + [K]\right]_B \{q_B(s)\} &= [b_{IB}]\{u_{IB}(s)\} \\ \{y_{IB}(s)\} &= [c_{IB}]\{q_B(s)\}\end{aligned} \tag{12}$$

where (s) is the Laplace variable, $[M]$, $[C]$, $[K]$ are the mass, damping and stiffness matrices, respectively, $\{q_B(s)\}$ are the generalised degrees of freedom (DOFs) of the base, $[b_{IB}]$ and $[c_{IB}]$ are the input and output matrices of the base interface, respectively, $\{u_{IB}(s)\}$ are the inputs describing the time/frequency dependence, and $\{y_{IB}(s)\}$ are the physical outputs of the base interface defined in [1–3, 5–9, 21, 29]. Note that the input/output shape matrix formalism decouples the choice of DOF $\{q_B(s)\}$ from the choice of $\{u_{IB}(s)\}$ and $\{y_{IB}(s)\}$ [1]. The $[b_{IB}]$ and $[c_{IB}]$ are Boolean matrices of the base interface of the full FE models with compatible interface meshes. Considering the response of an elastic structure to applied loads $F(s) = [b_{IB}]\{u_{IB}(s)\}$, the exact response at a given frequency $[H(s)]$ is given in Eq. (13) by:

$$\begin{aligned}[H(s)] &= [c_{IB}]\left[[M]s^2 + [C]s + [K]\right]_B^{-1}[b_{IB}] \\ &= [c_{IB}]\left[Z_B(s)\right]^{-1}[b_{IB}],\end{aligned} \tag{13}$$

where $[Z(s)]$ is the dynamic stiffness. The interest of writing the transformation of the DOFs in this way, per Balmès [3], Corus [6] and Billet [1], is the easy translation of $[b_{IB}]$ and $[c_{IB}]$ denoted by IB in the subscript. For the coupled prediction in the CFRP component one assumes that the modification of the stiffness parameters can be modeled with the FE model in the base interface (denoted as IM subscript and M superscript). Thus, one can write the modification of the model in the form

$$\begin{bmatrix}\begin{bmatrix}Z_{II}^M(s)\end{bmatrix} & \begin{bmatrix}Z_{IC}^M(s)\end{bmatrix} \\ \begin{bmatrix}Z_{CI}^M(s)\end{bmatrix} & \begin{bmatrix}Z_{CC}^M(s)\end{bmatrix}\end{bmatrix}\begin{Bmatrix}\{y_{IM}(s)\} \\ q_C(s)\end{Bmatrix} = \begin{Bmatrix}\{u_{IM}(s)\} \\ \{0\}\end{Bmatrix}, \tag{14}$$

where the interface of DOFs explicitly appears as DOFs of the model, see [9]. The Division of the DOFs is divided into two groups: active or interface DOFs denoted by I in the subscript, and complementary, denoted by C in the subscript – observed in Eqs. (14) and (15). *Using the framework of Ritz methods, the coupled prediction is obtained by imposing displacement continuity on the base interface* ($\{y_{IB}(s)\} = \{y_{IM}(s)\}$), *and projecting the associated model on loads dual to the displacement subspace admissible under the continuity constrain. The projection thus combines continuity and dynamic equilibrium loads* ($\{u_{IB}(s)\} = \{u_{IM}(s)\}$). *The base model given by Eq.* (12) *and a modification described by Eq.* (14) *in [1] leads to*

$$\begin{aligned}&\begin{bmatrix}[Z_B(s)] & 0 \\ 0 & \begin{bmatrix}Z_{CC}^M(s)\end{bmatrix}\end{bmatrix} + \begin{bmatrix}b_{IB}(s) \\ 0\end{bmatrix}\begin{bmatrix}Z_{II}^M(s)\end{bmatrix}\begin{bmatrix}c_{IB} & 0\end{bmatrix} \\ &+ \begin{bmatrix}b_{IB}(s) \\ 0\end{bmatrix}\begin{bmatrix}0 & Z_{IC}^M(s)\end{bmatrix} \\ &+ \begin{bmatrix}0 \\ Z_{IC}^M(s)\end{bmatrix}\begin{bmatrix}c_{IB} & 0\end{bmatrix}\begin{Bmatrix}q_B(s) \\ q_C(s)\end{Bmatrix} = F(s)\end{aligned} \tag{15}$$

For $\{q_B(s)\}$ and $\{q_C(s)\}$ corresponding to FEM DOFs, $[b_{IB}]$ and $[c_{IB}]$ are the input and output Boolean matrices of the base interface respectively. Equation (15) corresponds to the standard assembly process established in [29]. For the applications considered in [29], the $\{q_B(s)\}$ are defined in modal coordinates and $\{q_C(s)\}$ corresponds to fixed interface modes of a Craig-Bampton model [1].

2.5 Dealing with continuous interfaces

The incompatibiliy between the discretisation of the FE model $\{y_I(s)\}$ and the experimental measurements $\{y_T(s)\}$ is documented in [1]. A highlight of this methodology assumes that exists a constant coefficient linear combination $[c_{IT}]$ relating the interface $\{y_I(s)\}$ and the test displacements $\{y_T(s)\}$ for the coupled response in Eq. (16):

$$\{y_I(s)\} \approx [c_{IT}]\{y_T(s)\}. \tag{16}$$

This relation imposes a strong constraint on the interface kinematics since $\{y_I(s)\}$ must be approximated by a subspace of basis $[T_G]$ with a dimension that is smaller than the number of sensors used. The choice of this subspace $[T_G]$, and the justification of its ability to represent the coupled response, is a key aspect proposed in [1]. The construction of a reduced interface model ($[T_G]$ subspace) is a classical extension of CMS addressed in the literature [2, 4, 29] using a Craig-Bampton type reduction of the modification where the constraint modes are replaced by the

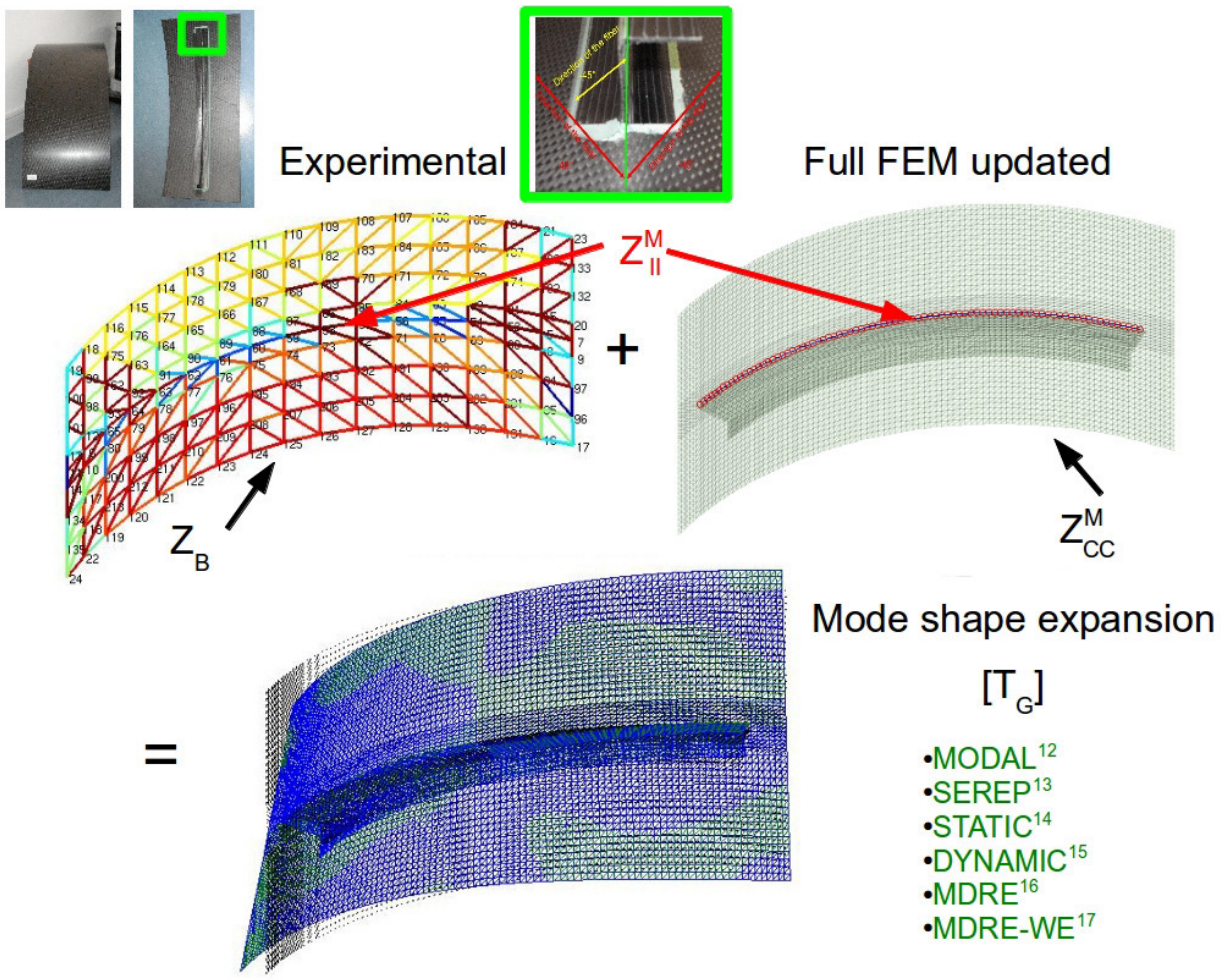

Figure 2: MSE process plot.

low order modes of the model statically condensed on its interface [1], as originally proposed in [22].

For this study, the updated FE model elaborated with triangle elements [26–28] is used to deal with the incompatibility of the interface between the FE model and the experimental measurements. The main purpose of using this updated FE model is to allow the interpolation of test motion at an arbitrary number of DOF of the interface to analyze the influence of the subspace-basis $[T_G]$ based on MOR methods in the CFRP component, (see Table 1). The subspace $[T_G]$ is defined on the DOFs of a local part of the updated FE model $[c_{IL}]$ including or not the modification, (see Figure 2).

The extraction of the interface of motion $\{y_I(s)\}$ using the updated FE model is thus written in Eq. (17) as

$$\{y_I(s)\} = [c_{IT}][T_G]\{y_G(s)\}. \tag{17}$$

An observation matrix $[T_G]$ can be constructed relating the $\{q_L(s)\}$ (DOFs of the updated FE model) with measurements $\{y_T(s)\} = [c_{TL}]\{q_L(s)\} = [c_{TG}]\{y_G(s)\} = [c_{TL}][T_G]\{y_G(s)\}$, (see [9] for possible methods). The estimation of the generalised motion of the interface $\{y_G(s)\}$, denoted by G in the subscript, can be established as:

$$\{y_G(s)\} = [c_{GB}]\{q_B(s)\}. \tag{18}$$

The standard approach to estimate the full response using different subspace-based expansion methods [1] established in [29] is then obtained by minimising the test error (distance between the test data and the associated re-

Table 1: Operator $[T_G]$ using different model order reduction methods applied to mode shape expansion methods.

MODAL/SEREP	$\{q_I(s)\}=[c_{IT}][T_G]_{MODAL/SEREP}\{y_T(s)\}$
STATIC	$\{q_I(s)\}=[c_{IT}][T_G]_{GUYAN}\{y_T(s)\}$
DYNAMIC	$\{q_I(s)\}=[c_{IT}][T_G]_{DYNAMIC}\{y_T(s)\}$
MDRE	$\{q_I(s)\}=[c_{IT}][T_G]_{MDRE}\{y_T(s)\}$
MDRE-WE	$\{q_I(s)\}=[c_{IT}][T_G]_{MDRE-WE}\{y_T(s)\}$

sponse for the expanded shape). The minimum is generally obtained by solving the least squares problem as

$$\{y_G(s)\} = \underbrace{Arg\ min}_{\{y_G\}} || [c_{TG}] \{y_G(s)\} - [c_{TB}] \{q_B(s)\} ||^2 \tag{19}$$

whose solution is given by

$$[c_{GB}] = [c_{TG}^T c_{TG}]^{-1} [c_{TG}^T c_{TB}] \tag{20}$$

which leads to the observation Eq. (16) *with* $[c_{IT}] = [c_{IL}][T_G][c_{GB}]$. *The given assumption* (17)*, the second block row of Eq.* (14)*, describes the motion of the modification*

$$[Z_{CC}]\{q_C(s)\} = -[Z_{CI}^M(s)][T_G]\{y_G(s)\}. \tag{21}$$

For the first block row it is assumed that the generalised loads are defined by projection on the subspace $[T_G]$ *of the form in*

$$\{u_{GM}\} = [c_{IG}]^T [Z_{IC}^M(s)]\{q_C(s)\} + [c_{IG}]^T [Z_{II}^M(s)][c_{IG}]\{y_G(s)\}. \tag{22}$$

The coupled response is obtained assuming dynamic equilibrium of generalised loads $\{u_{GB}\} = \{u_{GM}\}$ *established in* [1].

2.6 Evaluation of the error using the Modal Assurance Criterion (MAC)

Evaluation tools [1] are needed to evaluate the predictions based on many assumptions that introduce error. The evaluation of the error in the correlation in this study is analyzed applying a modal assurance criteria (MAC) based on the eigenfrequencies and eigenvectors divided into four parts. There are two general categories for correlation criteria: the eigenfrequencies and eigenvectors [19]. The MAC is one of the most useful comparison methods that relies on the eigenvector information, see Eq. (23) :

$$MAC = \frac{|\sum_{j=1}^{l} \{c_j\phi_{id}\}^H \{c_j\phi_k\}|^2}{|\sum_{j=1}^{l} \{c_j\phi_{id}\}^H \{c_j\phi_{id}\}|\,|\sum_{j=1}^{l} \{c_j\phi_k\}^H \{c_j\phi_k\}|}, \tag{23}$$

where $c_j\phi_{id}$ is the jth mode shape at sensors and $c_j\phi_k$ is the jth analytical mode shape. The MAC value of 1 corresponds to an absolute correlation. The less this value becomes, the worst the eigenvector correlation will be. In the modal community a MAC coefficient of a magnitude larger or equal than 0.90 in the diagonal and less or equal than 0.05 in the off-diagonal implies a satisfactory correlation. In the first part, the MAC of experimental measurements versus the updated stiffness parameters of the full FE model is analyzed. In the second part, the MSE methods are calculated to estimate the interface motion $\{y_I(s)\}$ using the experimental measurements, curve-fitting performed with the IDRC and IDRM algorithms, set-up of sensors and full FE model results. In the third part, once $\{c_j\phi_{id}\}$ and $\{c_j\phi_k\}$ are defined at sensors, it is proposed to obtain the stiffness and mass-weighted criterias, K-MAC and M-MAC, (see Eqs. (24) and (25) respectively), also called cross-generalised mass (CGM) and the less used cross-generalised stiffness (CGK) to observe the influence of the MOR using MSE methods.

The K-MAC=

$$\frac{|\sum_{j=1}^{l} \{c_j\phi_{id}\}^H [K] \{c_j\phi_k\}|^2}{|\sum_{j=1}^{l} \{c_j\phi_{id}\}^H [K] \{c_j\phi_{id}\}|\,|\sum_{j=1}^{l} \{c_j\phi_k\}^H [K] \{c_j\phi_k\}|}, \tag{24}$$

and M-MAC=

$$\frac{|\sum_{j=1}^{l} \{c_j\phi_{id}\}^H [M] \{c_j\phi_k\}|^2}{|\sum_{j=1}^{l} \{c_j\phi_{id}\}^H [M] \{c_j\phi_{id}\}|\,|\sum_{j=1}^{l} \{c_j\phi_k\}^H [M] \{c_j\phi_k\}|}, \tag{25}$$

values closer to 1 represent a higher agreement, and these values are being interpreted in the same way as the MAC [29].

The implementation of these criteria supports an original method for reducing the mass on the sensor set that used vectors defined at DOFs implemented in [29] based on the mass and stiffness matrices of the full FE model. The fourth part is evaluated modifying E_1 and E_2 equal to 97.3 GPa of all the parts defined in [10] to observe the impact of the stiffness and mass matrices in the interface motion of the full FE model applying subspace based expansion methods using the K-MACand M- MAC criteria based on the MAC.

3 Results and Discussion

The composite structure incorporates three parts, see Figures 3 and 4. The first component is made of Hunts-man

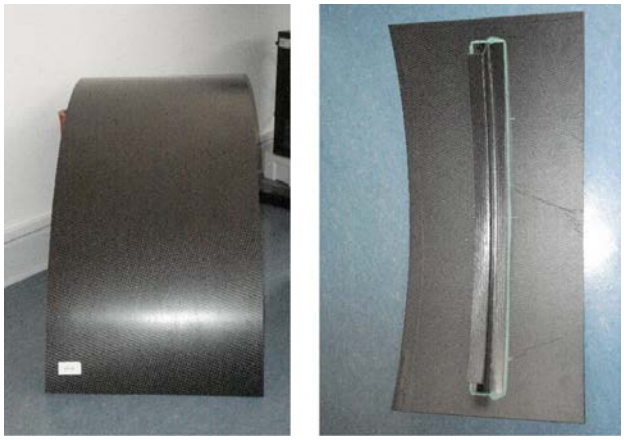

Figure 3: RTM Composite component assembly [10]

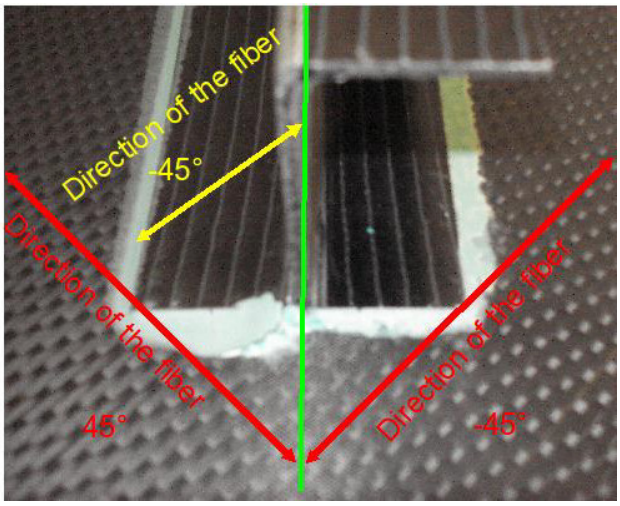

Figure 4: Composite component assembly detail [10].

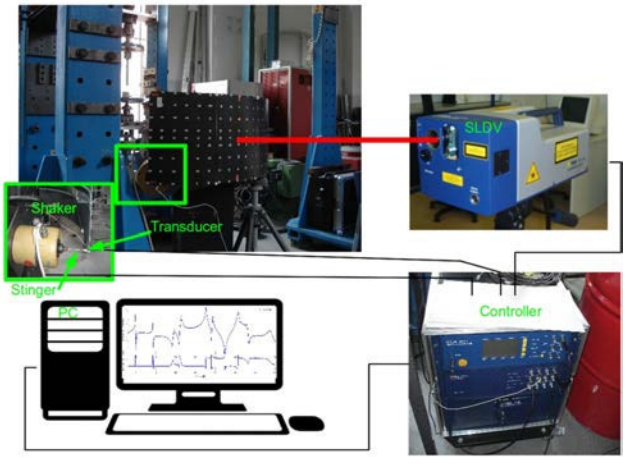

Figure 5: Experimental Set-up [11].

Ly 564 + Hexcel Gewebe G0926 (HTA-Faser) with dimensions of 0.390m × 0.810m (Figure 3 front and back part).

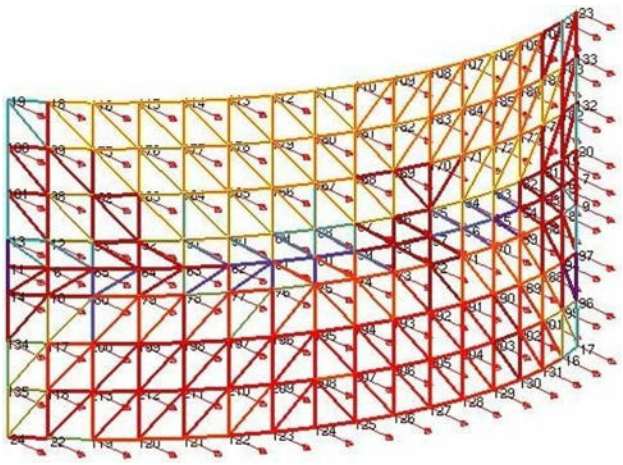

Figure 6: 153 Y-direction sensors [10].

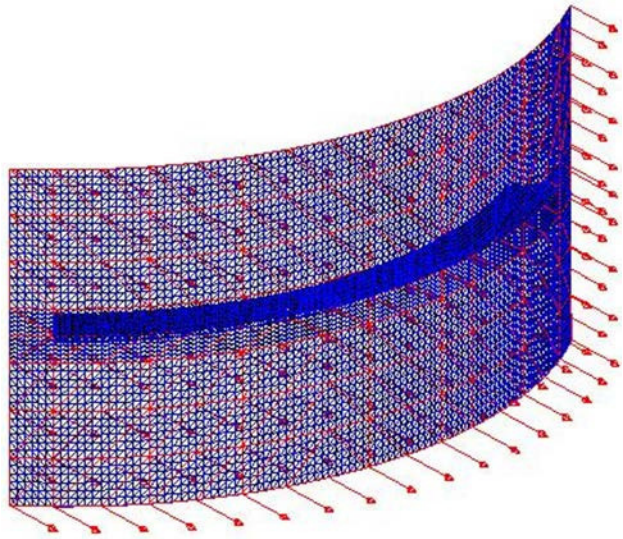

Figure 7: 153 Sensors in the FEM model [10].

The middle shell that connects the two principal parts with epoxic (Figure 4 has dimensions of 0.710m × 0.030m. Finally, there is the C-section Hexcel RTM6 + Saertex Multi-Axial-Gelege (MAG) with a IM7-Faser with dimensions of 0.710m × 0.030m. All the parts have symmetric layer distribution $[45/-45/45/-45/]_S$. All the measurements were performed with the Scanning Laser Doppler Vibrometer (SLDV) PSV840 by suspending the CFRP component from very soft cords (free condition), (see Figures 5-7).

The shaker LDS V406 and the stinger with length of 65 mm at node 17 are used to excite the structure that produce a sinusoidal vibration velocity signal on the line of sight of the SLDV (out-of-plane). The reason to use a stinger is to ensure that the shaker will only impart force to the structure along the axis of the stinger. The excitation signal selected is a periodic chirp (with frequency span 30-400

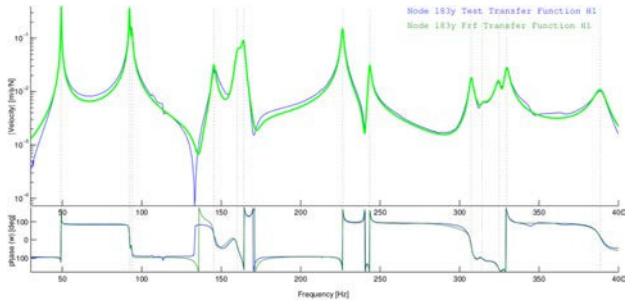

Figure 8: FRF(blue) and fitting curve (green) of composite model at node 183y [10].

Hz, 6400 lines of resolution, with complex average type and number of average per Frequency Response Function (FRF) equal to 10) and reflective foil is used to acquire the response measurement location. The input force is measured using a force transducer Dytran 1051V3 and power amplifier LDS PA 100 in order to record the excitation in the transverse direction. The interpolation between the experimental measurements uses FRFs [21]. The FRF, (see Figure 8), allowed us to compare the experimental modal parameters (frequency, damping, and mode shape) with the FE model. The Fast Fourier Transform (FFT) is a fundamental procedure that isolates the inherent dynamic properties of a mechanical structure and in our case with respect to the full FE models. To approximate the measurements (blue line) through a polynomial function (green line), it was used the frequency domain identification of structural dynamics applying the pole/residue parameterization [21], (see Figure 8). The experimental measurements were performed at low frequency (up to 400 Hz), and the curve-fitting generated from the experimental measurements [10]. A bandwith of 2% is used to localize the eigenfrequencies.

The CFRP provided by the DLR Braunschweig was measured, elaborated the FEM model and imported into SDTools using primarily triangular shells in the mesh (pshell). An appropiate assessment was perfomed to evaluate the mesh density of the FE model. Normal modes were computed using the FE model to obtain the natural frequencies and normal mode shapes of a CFRP structure. The model was divided in three parts, (see Figure 9), for convienience to modify the physical parameters per group of elements. The FE model is composed by triangular elements with a fairly regular shape and pattern.

A good practice in modal analysis using FE model assemblies is to couple the components using rigid body elements (RBE) or couplings as a boundary conditions to perform a modal analysis in the assembly. In this work, the FE model is prepared as a continuous body between

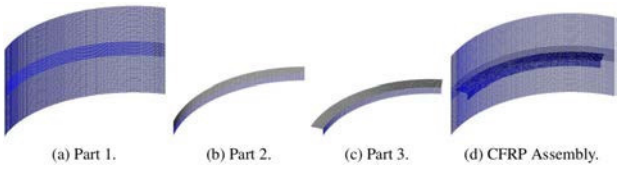

Figure 9: FEM groups.

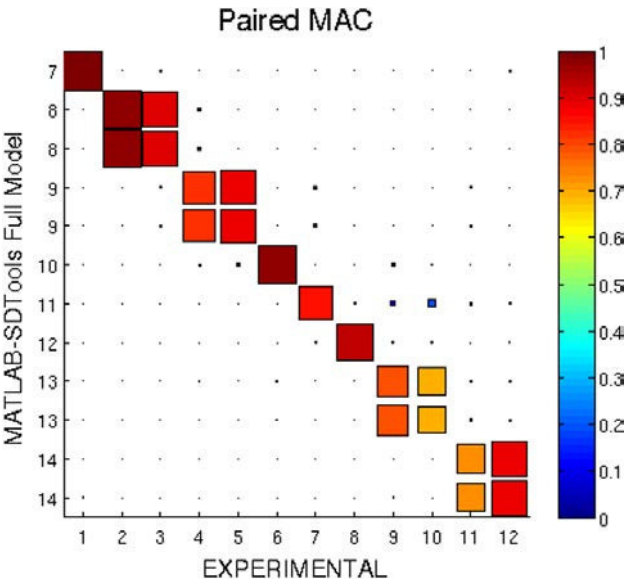

Figure 10: MAC: SDTools vs. Exp. [10]

the three components for convienience to simplify the FE model. The number of nodes and elements per group are listed in Table 3. After the FE model was developed, a number of validity checks were performed on the model prior to conduct the modal analysis. These check ups are units, mass comparation, layer stack-up, material and element properties and input and output coodinate systems.

The MAC analysis of the full FE model can be observed in Figure 10 (SDTools-MATLAB model versus the experimental measurements). The same number of modes was calculated in the full FE model. It was performed a cross orthogonality MAC (XOR) to verify the approximation of the full in low frequency range (12 mode pairs) versus the full model, see [10]. A good MAC correlation was obtained between updated full FE model and the experimental measurements in [10]. The nearly double correlation in the experimetal results identified in Figure 10 for the full models suggest the presence of the veering phenomena [23–25] (bending and torsional mode at the same frequency) in our composite component assembly. Thus, lower MAC results in 4,9,10 and 11 paired modes (see Figure 10) were archieved and identified using the experimental results.

Table 2: Comparative MAC: Updated full model (SDTools) and MSE results vs. experimental measurements.

ID	Test (Hz)	ID	FE model SDTools (Hz)	DF/FA %	MAC	ID	MAC MODAL /SEREP	MAC STATIC	MAC DYNAMIC	MAC MDRE	MAC MDRE-WE
1	49.243	7	57.218	16.2	100	1	100	100	100	100	100
2	92.265	8	106.02	14.9	97	2	99	100	100	100	99
3	93.756	8	106.02	13.1	90	3	98	100	100	100	99
4	145.29	10	168.2	15.8	83	4	99	100	100	100	99
5	160.05	10	168.2	5.1	86	5	100	100	100	100	99
6	164.18	9	167.5	2.0	98	6	100	100	100	100	99
7	226.36	12	236.83	4.6	86	7	99	100	100	100	99
8	243.4	11	234.99	−3.5	96	8	99	100	100	100	99
9	307.33	14	323.93	5.4	81	9	99	100	100	100	99
10	314.18	14	323.93	3.1	66	10	97	100	100	100	99
11	324.83	13	315.26	−2.9	74	11	94	100	100	100	99
12	329.67	13	315.26	−4.4	90	12	99	100	100	100	99

Table 3: FE model — elements, nodes and DOFs

Component	Element Type	Number of Elements	Number of Nodes
Part 1	pshell	7,200	3,840
Part 2	pshell	2,016	1,105
Part 3	pshell	3,024	1,615
Assembly		12,240	6,283
Total DOF			37,698

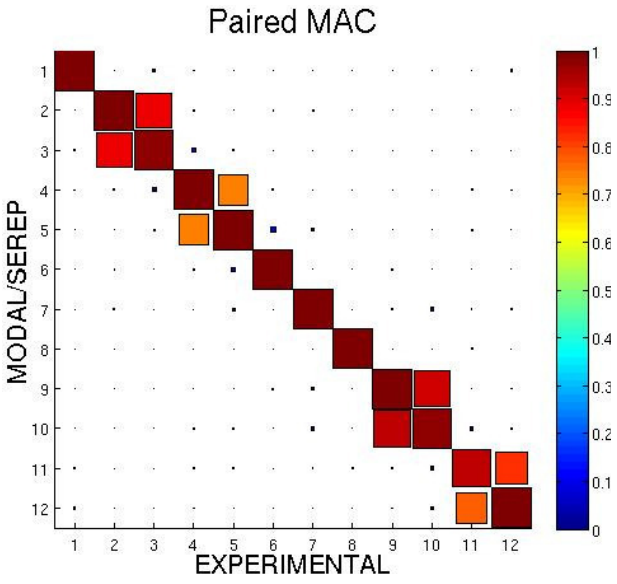

Figure 11: MAC: MSE MODAL/SEREP vs. Exp.

Furthermore, the different MSE are calculated (MODAL / SEREP, STATIC, DYNAMIC, MDRE, MDRE-WE) based on the updated full FE model, the experimental measurements and curve-fitting according the methodology implemented in [29] using fe_exp command, (see Figures 11-15). The same number of paired modes are calculated (12 pairs) for all the MSE methods. An error of 0.1 is used in the interpolation of the MDRE-WE. In Figures 11-15, an improvement of the double correlation is identified using the MSE methods versus the experimental measurements.

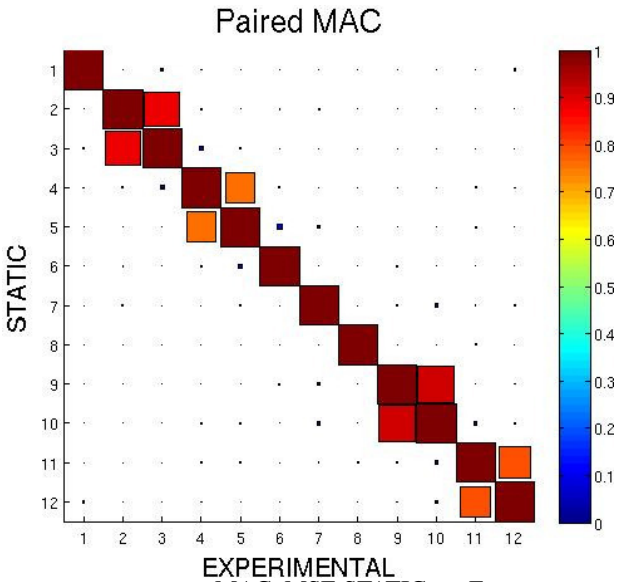

Figure 12: MAC: MSE STATIC vs. Exp.

The same number of DOF are obtained applying the MSE interpolation based on MOR methods according the number of DOF defined in the full model (37,698 DOF). In

Table 4: Comparative MAC: Updated full model (SDTools) and K-MAC MSE results vs. experimental measurements.

ID	Test (Hz)	ID	FE model SDTools (Hz)	DF/FA %	MAC	ID	K-MAC MODAL /SEREP	K-MAC STATIC	K-MAC DYNAMIC	K-MAC MDRE	K-MAC MDRE-WE
1	49.243	7	57.218	16.2	100	1	98	31	31	31	100
2	92.265	8	106.02	14.9	97	2	96	74	74	58	95
3	93.756	8	106.02	13.1	90	3	92	51	51	38	78
4	145.29	10	168.2	15.8	83	4	88	81	81	45	89
5	160.05	10	168.2	5.1	86	5	87	84	84	49	87
6	164.18	9	167.5	2.0	98	6	94	89	89	56	99
7	226.36	12	236.83	4.6	86	7	88	79	79	49	89
8	243.4	11	234.99	−3.5	96	8	96	89	90	65	97
9	307.33	14	323.93	5.4	81	9	88	81	81	60	87
10	314.18	14	323.93	3.1	66	10	79	65	66	45	76
11	324.83	13	315.26	−2.9	74	11	87	70	71	16	33
12	329.67	13	315.26	−4.4	90	12	93	87	88	39	89

Table 5: Comparative MAC: Updated full model (SDTools) and M-MAC MSE results vs. experimental measurements.

ID	Test (Hz)	ID	FE model SDTools (Hz)	DF/FA %	MAC	ID	M-MAC MODAL /SEREP	M-MAC STATIC	M-MAC DYNAMIC	M-MAC MDRE	M-MAC MDRE-WE
1	49.243	7	57.218	16.2	100	1	100	3	100	100	100
2	92.265	8	106.02	14.9	97	2	99	4	98	98	99
3	93.756	8	106.02	13.1	90	3	93	2	92	92	93
4	145.29	10	168.2	15.8	83	4	83	8	82	82	86
5	160.05	10	168.2	5.1	86	5	86	5	86	86	88
6	164.18	9	167.5	2.0	98	6	98	11	98	97	99
7	226.36	12	236.83	4.6	86	7	83	2	82	81	86
8	243.4	11	234.99	−3.5	96	8	96	86	96	96	98
9	307.33	14	323.93	5.4	81	9	82	5	80	78	83
10	314.18	14	323.93	3.1	66	10	69	2	65	64	70
11	324.83	13	315.26	−2.9	74	11	80	49	73	60	71
12	329.67	13	315.26	−4.4	90	12	90	2	89	83	91

Table 2 can be observed the improvement of the MAC values in all the paired modes of the MSE based on MOR versus the experimental measurements. The MAC values of the full FE model versus the experimental measurements can be observed in the left part of the Table 2.

Furthermore, the influence of the MOR methods using MSE can be analyzed obtaining the K-MAC and M-MAC displayed in Tables 4 and 5 respectively. The best K-MAC results are obtained applying the MODAL and MDRE-WE MSE methods displayed in Table 4. The worst paired modes of the MODAL and MDRE-WE MSE methods are displayed at paired mode 10 (K-MAC of 79) and at paired mode 11 (K-MAC of 33) respectively. The others MSE methods display a decrease of the K-MAC respect to the MODAL and MDRE-WE results. Furthermore, in Tables 2 to 5 are not displayed the differences of the eigenfrequencies between the experimental measurements and MSE results because there differences are zero.

There is a null difference in the frequencies applying different MSE because it is used the same pole identification obtained with the curve-fitting for all the MSE methods defined in [29]. The M-MAC of all the MSE methods can be observed in Table 5. A strong influence of the M-MAC results is observed in the subspace based expansion methods with the exception of the STATIC MSE method (the STATIC MOR is not taking in consideration the inertial forces). Using the contrieved example (modifying only the Young 's modulus E_1 and E_2 for all the three parts in the

Table 6: Comparative MAC: Contrieved full model (SDTools) and MSE results vs. experimental measurements.

ID	Test (Hz)	ID	FE model SDTools (Hz)	DF/FA %	MAC	ID	MAC MODAL /SEREP	MAC STATIC	MAC DYNAMIC	MAC MDRE	MAC MDRE-WE
1	49.243	7	64.497	31.0	100	1	100	100	100	100	100
2	92.265	8	117.86	27.7	97	2	99	100	100	100	99
3	93.756	8	117.86	25.7	90	3	98	100	100	100	99
4	145.29	10	184.66	27.1	61	4	99	100	100	100	99
5	160.05	10	184.66	15.4	88	5	100	100	100	100	99
6	164.18	9	177.54	8.1	81	6	100	100	100	100	99
7	226.36	12	257.19	13.6	47	7	99	100	100	100	99
8	243.4	11	257.19	5.7	55	8	99	100	100	100	99
9	307.33	14	344.15	12.0	66	9	99	100	100	100	99
10	314.18	14	344.15	9.5	49	10	97	100	100	100	99
11	324.83	13	340.81	4.9	64	11	94	100	100	100	99
12	329.67	13	340.81	3.4	73	12	99	100	100	100	99

Table 7: Comparative MAC: Contrieved full model (SDTools) and K-MAC MSE results vs. experimental measurements.

ID	Test (Hz)	ID	FE model SDTools (Hz)	DF/FA %	MAC	ID	K-MAC MODAL /SEREP	K-MAC STATIC	K-MAC DYNAMIC	K-MAC MDRE	K-MAC MDRE-WE
1	49.243	7	64.497	31.0	100	1	98	33	33	33	100
2	92.265	8	117.86	27.7	97	2	96	74	74	62	96
3	93.756	8	117.86	25.7	90	3	93	52	53	41	81
4	145.29	10	184.66	27.1	61	4	66	60	60	36	66
5	160.05	10	184.66	15.4	88	5	91	85	85	54	91
6	164.18	9	177.54	8.1	81	6	79	74	74	48	82
7	226.36	12	257.19	13.6	47	7	52	46	46	29	53
8	243.4	11	257.19	5.7	55	8	58	52	53	39	58
9	307.33	14	344.15	12.0	66	9	72	65	66	49	71
10	314.18	14	344.15	9.5	49	10	59	48	49	34	57
11	324.83	13	340.81	4.9	64	11	77	61	62	15	33
12	329.67	13	340.81	3.4	73	12	75	69	70	32	73

full FE model, $E_1 = E_2 = 97.3$ GPa), a decrese of the eigenvectors per paired mode as well as of the eigenfrequencies of the full FE model can be observed applying the MAC in the paired modes 4,6-12 in Figure 16 and Table 6, column (DF/FA). Furthermore, the MAC obtained in Figure 16 is used to calculate the MSE results modifying the E_1 and E_2 stiffness parameters. A good eigenvector correlation between the MSE and the experimental measurements can be observed between Tables 2 and 6 evaluating the stiffness parameters of the contrieved example respect to the updated stiffness parameters. Howerver, it can be identified the difference in the eigenvector correlation using the contrieved stiffness parameters. The MAC results in Table 6 suggest a robustness in the interpolation using MSE methods even though the MAC results of the contrieved full FE model displayed poor results, see Figure 16. However, the influence of the MOR methods using MSE methods can be analyzed using the K-MAC and M-MAC criteria. A negative impact in K-MAC and M-MAC is displayed in Tables 7 and 8 respectively using the stiffness parameters of the contrieved example. In Table 7 can be observed that the K-MAC results displayed a significative decrease in all the paired modes applying the different MSE methods respect to the K-MAC results displayed in Table 4. The STATIC, DYNAMIC and MDRE MSE methods display similar K-MAC and M-MAC values in the paired modes 1-3 in Tables 7 and 8 respect to the same paired modes in Tables 4 and 5 respectively. However, the rest of the paired modes obtained in

Table 8: Compartive MAC: Contrieved full model (SDTools) and M-MAC MSE results vs. experimental measurements.

ID	Test (Hz)	ID	FE model SDTools (Hz)	DF/FA %	MAC	ID	M-MAC MODAL /SEREP	M-MAC STATIC	M-MAC DYNAMIC	M-MAC MDRE	M-MAC MDRE-WE
1	49.243	7	64.497	31.0	100	1	100	2	100	100	100
2	92.265	8	117.86	27.7	97	2	99	3	98	98	99
3	93.756	8	117.86	25.7	90	3	94	1	92	92	93
4	145.29	10	184.66	27.1	61	4	62	5	61	60	62
5	160.05	10	184.66	15.4	88	5	89	5	89	89	90
6	164.18	9	177.54	8.1	81	6	83	18	83	83	84
7	226.36	12	257.19	13.6	47	7	49	1	48	47	50
8	243.4	11	257.19	5.7	55	8	57	54	56	56	57
9	307.33	14	344.15	12.0	66	9	67	3	65	65	68
10	314.18	14	344.15	9.5	49	10	52	1	50	49	52
11	324.83	13	340.81	4.9	64	11	70	48	65	57	64
12	329.67	13	340.81	3.4	73	12	73	1	72	69	74

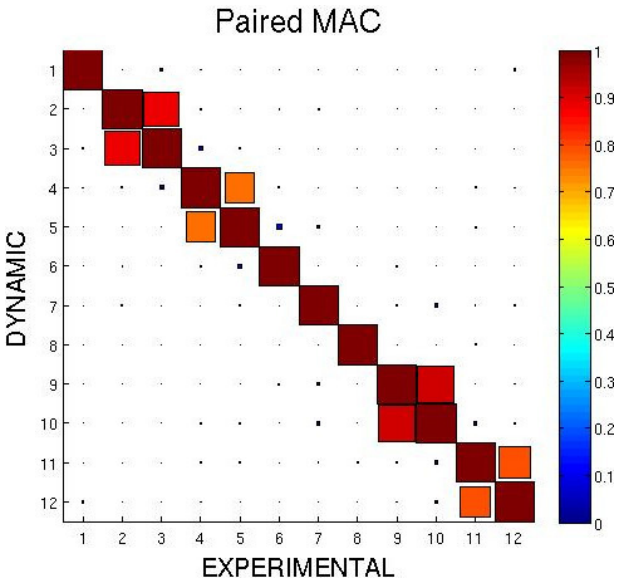

Figure 13: MAC: MSE DYNAMIC vs. Exp.

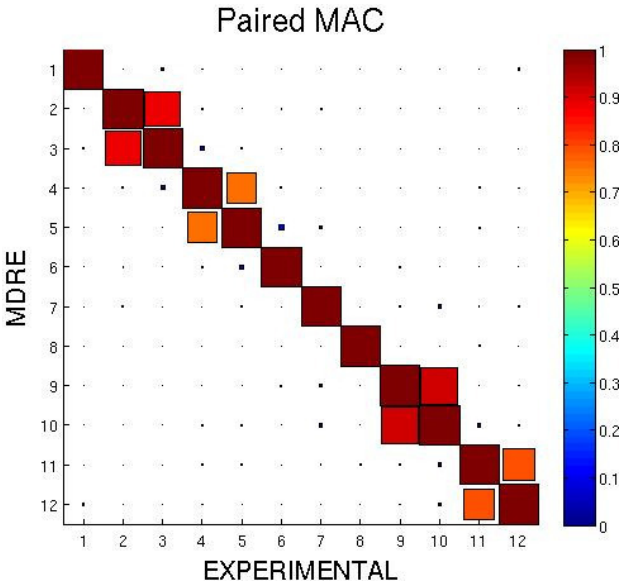

Figure 14: MAC: MSE MDRE vs. Exp.

Tables 7 and 8 using the K-MAC and M-MAC applying different MSE methods display a deterioration respect to the K-MAC and M-MAC results of Tables 4 and 5, with exception of the paired mode 5 with value of 91 in the K-MAC applying the MODAL and MDRE-WE MSE methods.

3.1 Conclusions

The application of MSE based on MOR methods using CMS to a CFRP component have shown good predictive capabilities of the dynamic behaviour in a CFRP combining experimental results, curve-fitting and an updated FE model. The experimental measurements performed with a SLDV and the identification of pole/residues used in a previous work are suitable to apply MSE methods to a CFRP according the results. It was observed an improvement in the MAC results between the experimental measurements and the MSE methods using the updated or modifying the stiffness parameters of the full model(contrieved model). However, the influence of the MOR using MSE can be identified comparing of K-MAC and M-MAC results (eigenfrequencies and eigenvectors) based on the modification of the stiffness parametes of the updated FE model. It is no-

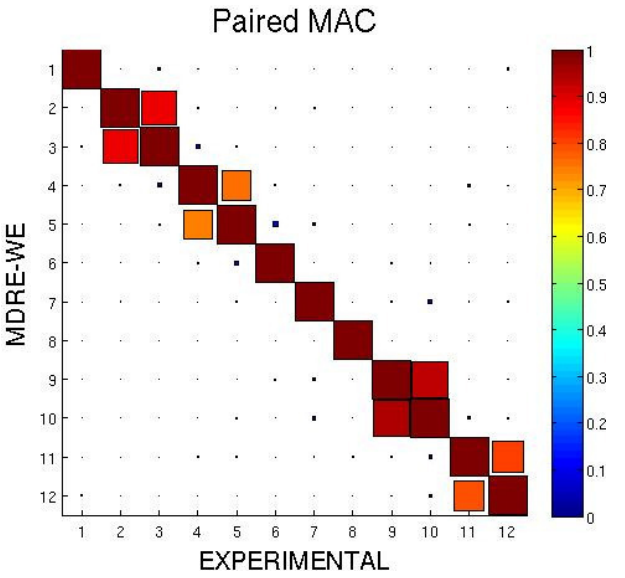

Figure 15: MAC: MSE MDRE-WE vs. Exp.

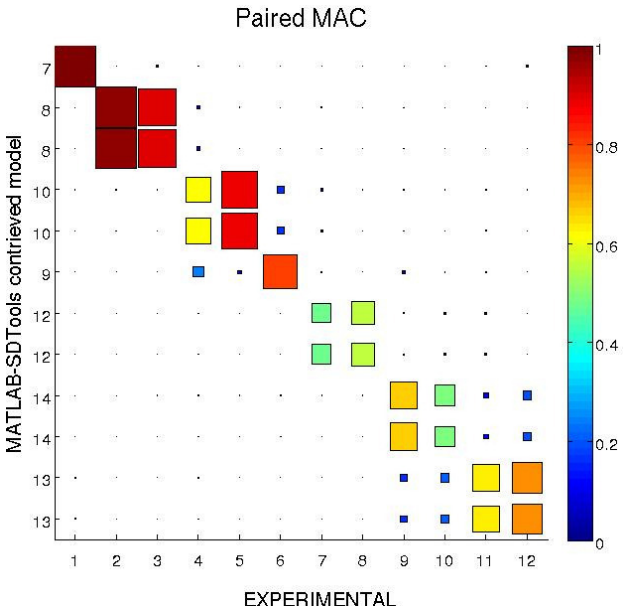

Figure 16: MAC: Contrieved vs. Exp.

ticed a strong influence of the stiffness parameters in the K-MAC and M-MAC criteria using MSE methods to a CFRP based on the MAC correlation between the experimental measurements and the full FE model. The best K-MAC and M-MAC results are observed using the MODAL/SEREP and MDRE-WE MSE methods implemented in SDTools based on the experimental measurements, curve-fitting and updated stiffness parameters obtained in a previous work. The strong influence of the stiffness parameters suggests that the distorsion of the subspace based expansion methods can be controlled applying the K- MAC and M-MAC using the MAC criteria. Furthermore, the general framework methodology of Ritz vectors, the updated stiffness parameters of the CFRP, the quality of experimental measurements, the curve-fitting algorithms based in the classical Laplace method and the type of element selected played an essential role in the dynamic correlation applying MSE, MOR and CMS methods to a CFRP.

Acknowledgement: This work has been supported by the DAAD-CONACYT Mexico with DAAD number: A/09/72544 and CONACYT Mexico number: 211983/306778. This support is gratefully acknowledged.

References

[1] Balmès E., Billet, L., Using expansion and interface reduction to enhance structural modification methods. IMAC XIX, 2001, 615-621

[2] Balmès E., Modes and regular shapes. How to extend component mode synthesis theory, XI DINAME, 28th February-4th March 2005, 1-14

[3] Balmès E., Review and Evaluation of shape expansion methods, IMAC 2000, 555-561

[4] Balmès E., Optimal Ritz vectors for component mode synthesis using singular value decomposition, AIAA J., 34(5), 1996, 1256-1260

[5] Maia N., Silva J., Theoretical and experiemental modal analysis, Mechanical engineering research studies, Engineering dynamics series, Research Studies Press, First edition, 1997

[6] Corus M., Balmès E., Improvement of structural modification method using data expansion and model reduction techniques. IMAC, 2003, pp. 1-7.

[7] Urgueia A., Using the SVD for the selection of independent connetions coordinates in the coupling of substructures. IMAC 1991, 919-925

[8] Balmès E., Sensors, degrees of freedom, and generalized mode-shape expasion methods, IMAC 1999, 628-634

[9] Balmès E., Use of generalized interface degrees of freedom in component mode synthesis, IMAC 1996, 204-210

[10] Peredo Fuentes H., Zehn M., Application of the Craig-Bampton model order reduction method to a composite component assembly: MAC and XOR, Facta Universitatis, series: Mechanical Engineering, 12(1), 2014, 37-50

[11] Peredo Fuentes H., Zehn M., Application of the Craig-Bampton model order reduction method to a composite component assembly: MACCO, COMAC, S-COMAC and ECOMAC, Open Eng.,6, 2016, 1-13

[12] Kammer D., Testing-analysis model development using an exact modal reduction, International Journal of Analytical and Experimental Analysis, 174-179

[13] O'Callahan J., Avitabile P., and Riemer R., System equivalent reduction expansion process (SEREP), IMAC VII, 1989, 29-37

[14] Guyan R., Reduction of Mass and Stiffness Matrices, AIAA Journal, 3, 1985, 380

[15] Kidder R., Reduction of structural frequency equations, AIAA Journal, 11(6), 1973
[16] Kammer D., A hybrid approach to test-analysis model development for large space structures, Journal of vibrations and acustics, 113(3), 1991, 325-332
[17] Roy N., Girard A. And Bugeat L.-P. Expansion of experimental modeshapes – An improvement of the projection technique, IMAC 1993, 152-158.
[18] Roy N., Girard A., Impact of residual modes in structural dynamics, Proceedings, European Conference of Spacecraft Structures, Materials & Mechanical Testing, Noordwijk, The Netherlands, 2005
[19] Ewins D. J., Modal testing: Theory and practice, Research Studies Press, Letchworth, U. K., 1995
[20] Gade S., Moller N.B., Jacobsen N.J., and Hardonk B., Modal analysis using a scanning laser Doppler vibrometer, Sound and Vibration Measurements A/S, 2000, 1015-1019
[21] Balmès E., Frequency domain identification of structural dynamics using the pole/residue parametrization, IMAC 1996, 540-546
[22] Craig, R.J., Bampton, M., Coupling of substructures for dynamic analyses, AIAA J., 6(7), 1968, 1313-1319.
[23] Bonisoli E., Delprete C., Espoito M., Mottershead J. E., Structural Dynamics with conicident Eigenvalues: Modeling and Testing, Modal Analysis Topics, 3, Conferencing Proceedings of the Society for Experimental Mechanics Series 6, 2011, 325-337
[24] Pierre C., Mode Localization and eigenvalue loci of Bridges with Aeroeslastic effects, Journal of Engineering Mechanics 126(3), 1988, 485-502
[25] Mounier D., Poilane C., Bucher C., Picart P., Evaluation of transverse elastic properties of fibers used in composite materials by laser resonant ultrasound spectroscopy, Proceeding of the acoustics 2012, Nantes Conference 23-27 April 2012, Nantes France
[26] Batoz J.L., Lardeur P., Composite plate analysis using a new discrete shear triangular finite element, International Journal for Numerical Methods in Engineering, 27, 1989, 343-359
[27] Batoz J.L., Bathe K.J., Ho L.W., A Study of three node triangular plate bending elements, International Journal for Numerical Methods in Engineering, 15, 1980, 1771-1812
[28] Batoz J.L., Lardeur P., A discrete shear triangular nine D.O.F element for the analysis of thick to very thin plates, International Journal for Numerical Methods in Engineering, 28, 1989, 533-560
[29] Balmès E., Structural dynamics toolbox and FEM-Link, User's Guide, SDTools, Paris, France, 2016, http://www.sdtools.com/help/sdt.pdf
[30] Schwarz, B.J., Richardson, M.H., Experimental modal analysis, CSI Reliability Week, Vibrant technology, 1(1), 1999, pp. 1-12.
[31] Formenti, D.L., Richardson M.H., Parameter estimation from frequency response measurements using rational fraction polynomials, IMAC 1st, 1982, pp. 1-8.
[32] Richardson, M.H., , Derivation of mass, stiffness and damping parameters from experimental modal data, Hewlett Packard Company, Santa Clara Division, 1, 1977, pp. 1-6.
[33] Richardson, M.H., Modal Mass, stiffness and damping, Vibrant Technology, Inc, 31, 2000, pp. 1-6.
[34] Richardson, M.H., Formenti, D.L., Global curve fitting of frequency response measurements using rational fraction polynomials, IMAC 3rd, 1985, pp. 1-8.